4-1-1998

Confinement Effectiveness of High Strength Spiral Reinforcement in Prestressed Concrete Piles

Benjamin Graybeal

Stephen P. Pessiki

Follow this and additional works at: http://preserve.lehigh.edu/engr-civil-environmental-atlss-reports

CONFINEMENT EFFECTIVENESS
OF HIGH STRENGTH SPIRAL REINFORCEMENT
IN PRESTRESSED CONCRETE PILES

by

Benjamin Graybeal
Graduate Research Assistant
Civil and Environmental Engineering

Stephen Pessiki
Associate Professor
Civil and Environmental Engineering

ATLSS Report No. 98-01

April 1998

CONFINEMENT EFFECTIVENESS
OF HIGH STRENGTH SPIRAL REINFORCEMENT
IN PRESTRESSED CONCRETE PILES

by

Benjamin Graybeal
Graduate Research Assistant
Civil and Environmental Engineering

Stephen Pessiki
Associate Professor
Civil and Environmental Engineering

ATLSS Report No. 98-01

April 1998

ACKNOWLEDGMENTS

TABLE OF CONTENTS

LIST OF TABLES

LIST OF FIGURES

x

ABSTRACT

Spiral reinforcement is used in prestressed concrete piles to create a state of triaxial compression in the confined concrete core, thus increasing both the strength and ductility of the concrete core. Increases in unconfined concrete strengths have led to the need for greater confining pressures to be exerted by the spiral reinforcement. This can be achieved through the use of a greater volumetric ratio of spiral reinforcement or through the use of higher yield strength spiral reinforcement. However, reinforcement congestion problems frequently occur if the volumetric ratio is increased. The objective of this research is to evaluate the confinement effectiveness of high strength spiral reinforcement in precast, prestressed concrete piles. The research included eight large-scale axial load tests of spirally reinforced piles, an experimental and analytical investigation of the properties of the spiral reinforcement, and the development of a proposed method for the design of high strength spiral reinforcement in piles.

It was found that, for the pile geometries and material strengths treated in this study, current code provisions that limit the design yield strength of spiral reinforcement to 60 ksi (414 MPa) are overly conservative. The use of a fixed, predefined value of design yield stress for a particular wire reinforcement is not an adequate way to approach the design of spiral reinforcement. The value of spiral stress that can be used in design depends upon a number of factors including the in situ spiral stress-strain curve, pile diameter, cover distance, and concrete strength. The proposed method for the design of high strength spiral reinforcement provides a means to determine the useable stress in a given spiral wire for a particular combination of pile geometric parameters and material properties. Using the proposed design method, spiral steel stresses in excess of 60 ksi (414 MPa) can be used in design.

1

CHAPTER 1
INTRODUCTION

1.1 INTRODUCTION
The concept of confining concrete into a state of triaxial compression in order to increase its strength and ductility is well understood. Spiral reinforcement used in a compression member produces a state of triaxial compression by restraining the lateral expansion of the concrete as the member is compressed axially. The lateral confinement created by the spiral increases both the strength and deformation capacity of the concrete.

Spiral reinforcement is often used as transverse reinforcement in precast, prestressed concrete piles. As will be discussed in Section 2.2, spiral reinforcement is proportioned in part based on the concrete compressive strength. In short, spiral reinforcement is designed so that, in the event that the pile is overloaded, the spiral provides enough strength enhancement to the core concrete to replace the strength lost as the cover concrete spalls away. For a given pile cross-sectional geometry, a higher compressive strength concrete requires a greater volume fraction of spiral reinforcement. Thus, as concrete strengths have increased in recent years, the amount of spiral reinforcement required has increased as well. This increased amount of spiral reinforcement is provided through the use of a larger diameter spiral bar and/or through smaller pitch. This can create a problem during fabrication in that a small pitch, large bar diameter spiral can complicate concrete placement and consolidation. Additionally, restrictions on spiral pitch will be encountered based on concrete aggregate size.

One approach to minimize the reinforcement congestion problems created by the spiral reinforcement is to increase its yield strength. Assuming the steel has yielded, a higher yield strength spiral along with a smaller volume fraction of spiral reinforcement may be used to provide a given required amount of confining pressure to the concrete. In general, present design code requirements limit the design yield strength of spiral reinforcement to 60 ksi (414 MPa). This limit is based on a lack of evidence that steel with a greater yield strength will achieve its yield strength prior to the member reaching its ultimate strength. However, as discussed later in this report, steel stress is a function of many factors, including concrete lateral expansion, peak confined concrete strength, and spiral steel stress-strain relationship. Therefore, a fixed limit on design yield strength which does not account for the concrete properties or reinforcement parameters in addition to yield strength will not necessarily capture the factors that determine the effectiveness of the spiral.

1.2 OBJECTIVE
The objective of this research is to evaluate the confinement effectiveness of high strength spiral reinforcement in precast, prestressed concrete piles.

1.3 SUMMARY OF APPROACH
This research involved three phases of work. The first phase involved tests of eight large-scale spirally reinforced concrete piles loaded in concentric axial compression. Two pile diameters were treated. Four of the piles had a diameter of 24 in. (610 mm), and the remaining four piles had a

2

diameter of 14 in. (356 mm). The test piles were designed according to the requirements of ACI 318 Building Code Requirements for Structural Concrete (1995) and American Association of State Highway and Transportation Officials LRFD Bridge Design Specifications (1994). The design concrete compressive strength was 8.0 ksi (55 MPa). Within each set of four specimens, the design nominal yield strength of the spiral reinforcement varied from 78 ksi (538 MPa) to 140 ksi (965 MPa).

The second phase of the research focused on the material properties of the spiral reinforcement. Tension tests were performed on the reinforcement to determine the stress-strain properties, and analytical studies were performed to examine how these stress-strain properties are affected by the residual stresses introduced into the cross-section of the spiral wire as it is turned from a straight length of wire into a spiral.

The final phase of the research focused on the development of a proposed method for the design of high strength spiral reinforcement in piles.

1.4 SUMMARY OF FINDINGS
For the pile geometries and material strengths treated in this study, current code provisions that limit the design yield strength of spiral reinforcement in piles to 60 ksi (414 MPa) are overly conservative. Spiral steel stresses in excess of this limit can be used to design spiral reinforcement in piles similar to the piles treated in this study. However, the spiral reinforcement should be designed according to the proposed method presented in Chapter 7.

The use of a fixed, predefined value of design yield stress for a particular wire reinforcement is not an adequate way to approach the design of a spiral for a pile. This is because the value of stress in the spiral that can be used in design depends upon a number of factors including the in situ spiral stress-strain curve, pile diameter, cover distance, and concrete strength. The proposed method for the design of high strength spiral reinforcement provides a means to determine the useable stress in a given spiral wire for a particular combination of pile geometric parameters and material properties.

The spiraling process introduces residual stresses into the cross-section of a spiral wire. The magnitude of the residual stresses depends on a number of factors, including the diameter of the spiral, the wire diameter, and the stress-strain relationship of the wire. Residual stresses introduced by the spiraling process change the tension stress-strain properties of the wire.

1.5 OUTLINE OF REPORT
The remainder of this report is divided into seven chapters. Relevant background information is discussed in Chapter 2. Chapter 3 is a description of the experimental program, which includes the test matrix, specimen details, and material properties. The experimental results are presented in Chapter 4. Chapter 5 provides a detailed discussion of the spiral reinforcement properties. This includes an investigation of the in situ mechanical properties of spiral reinforcement in general as well as an approximation of the mechanical properties of the spiral reinforcement used in this

study. Chapter 6 presents an analysis of the results of this study. This analysis includes a discussion of spiral behavior, cover behavior, as well as the dilation ratio behavior of the confined core concrete. Comparisons between experimental results and predictions obtained from empirical equations are also included in this chapter. Chapter 7 proposes a method for the design of high strength spiral reinforcement in piles. Finally, Chapter 8 presents the conclusions of the research as well as the recommendations for future research.

1.6 NOTATION

The following notation is used in this report:

$A_{c,o-o}$ = core concrete area of pile measured to outside diameter of spiral, in.^{2} (mm^2)

$A_{c,total}$ = total cross-sectional area of concrete in the pile, in.^{2} (mm^2)

A_g = gross cross-sectional area of pile, in.^{2} (mm^2)

A_{lg} = total area of longitudinal reinforcement, in.^{2} (mm^2)

A_{sp} = total cross-sectional area of bundled spiral wires, in.^{2} (mm^2)

A_{ntan2} = area under the tangent dilation ratio curve between $\varepsilon_c = 0$ and ε_{c2}

$\overline{A}_{ntan2}$ = area under the tangent dilation ratio curve between normalized values of $\varepsilon_c = 0$ and ε_{c2}

d_{sp} = diameter of spiral measured out-to-out of wire, in. (mm)

d_{sw} = diameter of an individual spiral wire, in. (mm)

f_2 = lateral confining stress exerted on confined concrete, ksi (MPa)

f_{2-1} = lateral confining stress exerted on confined concrete at Δ_1, ksi (MPa)

f_{2-2} = lateral confining stress exerted on confined concrete at Δ_2, ksi (MPa)

f_{2-c} = lateral confining stress exerted on confined concrete at the confined concrete peak strength, ksi (MPa)

$f_{2-spall}$ = lateral confining stress exerted on confined concrete at Δ_{spall}, ksi (MPa)

f_c = axial compressive stress in concrete, ksi (MPa)

f_c' = compressive strength of prepared cylinders, ksi (MPa)

f_{c1} = compressive strength of confined concrete at Δ_1, ksi (MPa)

f_{c2} = compressive strength of confined concrete at Δ_2, ksi (MPa)

f_{cc} = peak confined concrete compressive strength, ksi (MPa)

f_{co} = compressive strength of unconfined concrete, ksi (MPa)

f_{lg} = stress in longitudinal reinforcement, ksi (MPa)

f_{ly} = yield strength of longitudinal reinforcement, ksi (MPa)

f_{pc} = concrete compressive stress due to effective prestress, ksi (MPa)

f_{sp} = stress in the spiral reinforcement, ksi (MPa)

$f_{sp,spall}$ = stress in the spiral reinforcement at Δ_{spall}, ksi (MPa)

f_{sp1} = stress in the spiral reinforcement at Δ_1, ksi (MPa)

f_{sp2} = stress in the spiral reinforcement at Δ_2, ksi (MPa)

f_{su} = ultimate strength of spiral reinforcement, ksi (MPa)

f_{sy} = yield strength of spiral reinforcement, ksi (MPa)

$f_{sy,nom}$	=	nominal yield strength of spiral reinforcement as reported by spiral manufacturer, ksi (MPa)
f_y	=	yield strength of reinforcement, ksi (MPa)
m	=	ε_{c2} normalized by ε_{co}
n_{fibers}	=	number of fibers in DRAIN-2DX model of wire cross-section
n_{lg}	=	number of longitudinal reinforcing bars in section
n_{sp}	=	number of spiral wires bundled to form a single turn of spiral
P	=	load on pile, kips (MN)
P_1	=	load on pile just prior to cover spalling, kips (MN)
P_2	=	load on pile at Δ_2, kips (MN)
P_{drop}	=	load on pile immediately after ΔP_{drop}, kips (MN)
$P_{failure}$	=	load on pile at failure, kips (MN)
P_o	=	nominal pile capacity, kips (MN)
P_{spall}	=	lowest load on pile between Δ_1 and Δ_2, kips (MN)
$R_{fsp2/fsy,nom}$	=	ratio of spiral stress at Δ_2 to nominal design spiral yield stress
$R(\Delta f_{c12})_{exp/dsgn}$	=	ratio of experimental to design increase in concrete stress from Δ_1 to Δ_2
$R(\Delta f_{c12})_{exp/rich}$	=	ratio of experimental to Richart et al. predicted increase in concrete stress from Δ_1 to Δ_2
$R(\varepsilon_{c2})_{exp/cus}$	=	ratio of experimental to Cusson and Paultre predicted longitudinal strain at Δ_2
$R(\varepsilon_{c2})_{exp/rich}$	=	ratio of experimental to Richart et al. predicted longitudinal strain at Δ_2
$R(\rho_{sp})_{nom/60}$	=	ratio of volumetric ratio from nominal design yield strength to volumetric ratio from 60 ksi (414 MPa) yield strength spiral steel
$R(\rho_{sp})_{redesign/60}$	=	ratio of volumetric ratio from redesign f_{sp2} to volumetric ratio from 60 ksi (414 MPa) yield strength spiral steel.
s	=	spiral pitch, in. (mm)
α	=	percentage of ε_{co} at which tangent dilation ratio beings to increase
β	=	percentage of ε_{c2} at which tangent dilation ratio stops increasing
Δf_{c12}	=	change in confined core stress between Δ_1 and Δ_2, ksi (MPa)
Δ_1	=	pile axial shortening corresponding to P_1, in. (mm)
Δ_2	=	pile axial shortening corresponding to P_2, in. (mm)
Δ_{spall}	=	pile axial shortening corresponding to P_{spall}, in. (mm)
$\Delta_{failure}$	=	pile axial shortening corresponding to $P_{failure}$, in. (mm)
ε_c	=	axial strain in concrete
ε_{c1}	=	axial strain in concrete corresponding to f_{c1}
ε_{c2}	=	axial strain in concrete corresponding to f_{c2}
ε_{cc}	=	axial strain in concrete corresponding to f_{cc}
ε_{co}	=	axial strain in concrete corresponding to f_{co}
ε_{ct}	=	transverse strain in the concrete core
ε_{ct2}	=	transverse strain in concrete core at Δ_2

5

ε_{ly}	=	strain in longitudinal reinforcement at f_{ly}
ε_{sp}	=	strain in the spiral reinforcement
ε_{sp2}	=	strain in the spiral reinforcement at Δ_2
ε_{su}	=	strain in the spiral reinforcement corresponding to f_{su}
ε_y	=	strain in reinforcement corresponding to f_y
η_{sec}	=	secant dilation ratio
η_{sec2}	=	secant dilation ratio at Δ_2
η_{tan}	=	tangent dilation ratio
$\eta_{tan,ini}$	=	proposed initial tangent dilation ratio
$\eta_{tan,lim}$	=	proposed limiting tangent dilation ratio
ρ_{lg}	=	longitudinal reinforcement ratio, computed as the ratio of the area of longitudinal reinforcement to the total area of concrete in section ($A_{c,total}$)
ρ_{sp}	=	volumetric steel ratio, computed as the ratio of the volume of spiral reinforcement to total volume of the core ($A_{c,o-o}$)

1.7 UNIT CONVERSION FACTORS

The following unit conversions are used in this report.

1 in.	=	25.4 mm
1 in.^{2}	=	645 mm^2
1 kip	=	4.448 kN
1 ksi	=	6.895 MPa
1 ft^3	=	0.02837 m^3

CHAPTER 2
BACKGROUND

2.1 INTRODUCTION

This chapter provides background information relevant to the study. The general behavior of axially loaded spirally reinforced members is discussed in Section 2.2. Section 2.3 reviews the initial studies of confinement of concrete by spiral reinforcement. More recent studies into this same topic are reviewed in Section 2.4. Finally, Section 2.5 summarizes current code provisions for the design of spiral reinforcement in an axially loaded concrete member.

2.2 GENERAL BEHAVIOR OF AXIALLY LOADED SPIRALLY REINFORCED MEMBERS

The general behavior of spirally reinforced concrete members has been thoroughly studied and documented over the past century. The initial studies within of this topic took place in the early 1900's when it was found that the compressive strength of concrete could be increased if a transverse confinement pressure was applied. This confining pressure, whether active (i.e. applied externally by a pressurized fluid) or passive (i.e. created by lateral expansion of the axially compressed concrete against a confining material), worked to resist the lateral expansion of concrete as it was loaded axially. The relationship between the unconfined concrete strength f_{co}, lateral pressure f_{2-c}, and the confined concrete strength f_{cc}, was found to be nearly represented by Equation 2.1, proposed by Richart, Brandzaeg, and Brown (1928, 1929, 1934).

$$f_{cc} = f_{co} + 4.1f_{2-c} \tag{2.1}$$

Richart et al. also proposed Equation 2.2 which relates the strain at the peak compressive strength, ε_{cc}, to the peak compressive stress, f_{cc}, the unconfined compressive stress, f_{co}, and the corresponding unconfined strain, ε_{co}.

$$\varepsilon_{cc} = \varepsilon_{co}\left(5\frac{f_{cc}}{f_{co}} - 4\right) \tag{2.2}$$

Richart et al. concluded that the presence of spiral reinforcement in an axially loaded member allows for increases in concrete compressive strength and increases member ductility. Thus, using a confining material to restrain the lateral expansion of a concrete member carrying axial load causes the load-shortening behavior of the member to improve significantly.

Figure 2.1 shows the idealized load-shortening behavior of a spirally reinforced concrete member. Several key load and shortening values in the response are indicated in the figure. P_1, P_{spall}, P_2, and $P_{failure}$ indicate the loads at the initiation of cover loss, the conclusion of cover loss, the confined peak, and the failure of the member, respectively. Δ_1, Δ_{spall}, Δ_2, and $\Delta_{failure}$ indicate the axial shortening values at the corresponding loads.

A concrete member without spiral reinforcement exhibits a load capacity approximately equal to P_1, and a continuous decrease in resistance with an increase in applied deformation beyond that point. Figure 2.1 shows that the presence of spiral reinforcement leads to a second peak in the response at the same carrying capacity. This second peak is reached at a much greater ductility than is achieved by an unconfined member.

The stress in the confined concrete at Δ_2, f_{c2}, is the maximum stress reached by the confined concrete and is thus equivalent to the f_{cc} shown in Equation 2.1. Similarly, the confining pressure on the confined concrete core at Δ_2, f_{2-2} is equivalent to f_{2-c}. Rewriting Equation 2.1 with f_{c2} and f_{2-2} gives Equation 2.3 shown below.

$$f_{c2} = f_{co} + 4.1f_{2-2} \tag{2.3}$$

Correspondingly, the strain at the second peak, ε_{c2}, is equivalent to the ε_{cc} shown in Equation 2.2. Rewriting Equation 2.2 with ε_{c2} gives Equation 2.4 shown below.

$$\varepsilon_{c2} = \varepsilon_{co}\left(5\frac{f_{c2}}{f_{co}} - 4\right) \tag{2.4}$$

2.3 INITIAL STUDIES OF CONFINEMENT BY SPIRAL REINFORCEMENT

As stated earlier, studies of the behavior of confined concrete began nearly a century ago. Considère (1903) discovered that the strength of confined concrete is proportional to the strength of the unconfined concrete plus an added strength related to the lateral restraint provided by the confining mechanism. Following this work, many studies were undertaken. However, it was not until the work of Richart, Brandzaeg, and Brown that significant knowledge of the behavior of spirally reinforced members was obtained.

The work performed by Richart et al. focused on axial load tests of concrete confined by fluid pressure as well as by spiral reinforcement. Literally hundreds of specimens were tested. Specimen sizes ranged from diameters of 4 in. (102 mm) to 28 in. (711 mm) with the majority of the fluid pressure specimens measuring 4 in. (102 mm) in diameter and the majority of the spirally reinforced specimens measuring 8 in. (203 mm) in diameter. Most specimens had unconfined concrete compressive strengths of 2 to 4 ksi (13.8 to 27.6 MPa), however some specimens had unconfined concrete compressive strengths of nearly 8 ksi (55.2 MPa). Additionally, in the spirally reinforced specimens, a number of different types and strengths of spiral reinforcing steel were used as confinement.

Equation 2.1 was the primary finding of the Richart et al. studies. This relationship between the unconfined and confined concrete strengths and the lateral pressure was first based on tests performed with confinement by fluid pressure. Analysis of additional tests on spirally reinforced members, with the core measured from the out-to-out of the spiral, showed that the same relation-

8

ship held. Equation 2.2, which can be used to estimate the compressive strain at the peak confined concrete stress, was also developed based on these tests. This equation is discussed further in Chapters 6 and 7, where a method is proposed for the design of high strength steel spiral reinforcement.

Richart et al. also reported a number of other findings which are of interest to the current study. The first deals with the material properties of spiral reinforcement in its in situ state within a compression member. The process of coiling a spiral from a straight length of bar influences the stress-strain properties of the reinforcement. The changes in the stress-strain properties are due to the residual stresses which are introduced in the coiling process. This is discussed further in Chapter 5. Richart et al. reported that, in general, as a coiled spiral is loaded in tension due to the expansion of the concrete core, the spiral provides less confining stress per strain over the strain range just preceding and following yield strain. However, Richart et al. also noted that in mild steel, the confining stress per strain can increase if the material properties of the steel allow it to exhibit a significant level of strain hardening.

Another important finding reported by Richart et al. deals with the dilation behavior of concrete. They found that, as a compression member is loaded, the overall volume of the member decreases until a certain stress is reached. Above this stress, the volume of the member ceases to decrease and eventually, as the ultimate load is approached, begins to increase. This finding is of importance in spirally reinforced members because lateral expansion of the confined core is required for the spiral to provide its confining stress. According to the Richart et al. findings, the spiral will not begin to provide significant confining pressure until the axial compressive stress in the concrete has reached the point where its dilation begins to increase.

2.4 RECENT STUDIES OF CONFINEMENT BY SPIRAL REINFORCEMENT

The work which has been performed in recent years with regard to confinement by spiral reinforcement has been wide ranging with many different and sometimes contradictory conclusions being drawn. One of the components of many of these studies is an attempt to determine limits on the amount and/or strength of spiral reinforcement which could be used to achieve a desired member response. However, it seems that many of these studies did not consider the transverse concrete strains which would be required in order to make full use of the spiral reinforcement. For example, as is concluded later in this study, some combinations of high yield strength spiral reinforcement and low volumetric ratio of spiral steel cannot be utilized because a very high transverse core concrete strain is required in order to reach the yield strength. The core concrete fails prior to reaching this strain and thus does not engage the full strength of the spiral. This is of particular concern with regard to limits on the use of high strength reinforcement.

The general conclusions of this body of research are stated below. A brief description of the experimental programs which led to these findings is as follows. Note that all tests cited were concentric axial load tests. Mugumura, Watanabe, Tanaka, Sakurai, and Nakamura (1979) tested small scale (6 in. (152 mm) diameter) spirally reinforced specimens. The spiral yield strengths tested were both 24 and 196 ksi (165 and 1350 MPa) and the unconfined concrete strengths ranged

from 4 to 9 ksi (28 to 62 MPa). Mander, Priestley, and Park (1988a) tested full scale (20 in. (508 mm) diameter) spirally reinforced specimens. The spiral yield strength in these specimens was approximately 45 ksi (310 MPa) and the unconfined concrete strength was approximately 4 ksi (28 MPa). Pessiki and Pieroni (1997) tested full scale (22 in. (559 mm) diameter) spirally reinforced specimens. The spiral yield strength was approximately 75 ksi (517 MPa) and the unconfined concrete strength ranged from 5 to 9 ksi (34 to 62 MPa). Martinez, Nilson, and Slate (1984) tested small scale specimens (4 and 6 in. (102 and 152 mm) diameter). The spiral yield strength in these specimens was between 55 and 60 ksi (380 to 414 MPa) and the unconfined concrete strengths ranged from 3 to 10 ksi (21 to 69 MPa). Sheikh and Toklucu (1993) tested three different diameter spirally reinforced specimens (8 in. (203 mm), 10 in. (254 mm), and 14 in. (356 mm)). The spiral yield strengths treated in this study ranged from 65 to 91 ksi (448 to 627 MPa) and the unconfined concrete strength was approximately 5 ksi (34 MPa). Finally, Cusson, De Larrard, Boulay, and Paultre (1996) tested small scale specimens (6 in. (152 mm) diameter). The spiral yield strength was 84 ksi (580 MPa) and the unconfined concrete strength ranged from 9.5 to 16 ksi (65 to 110 MPa).

The first set of conclusions deals with whether spiral reinforcement, either mild or high strength, will yield prior to the achievement of the confined strength of the core concrete. Mugumura et al., Mander et al., Pessiki and Pieroni, and Sheikh et al. all found that mild spiral steel does reach its yield strain prior to the confined core reaching its maximum strength. This conclusion supports the possibility that, in some compression members, a higher yield strength spiral may be permitted as increasing the spiral yield stress could increase the member strength. However, other researchers have found that the spiral steel does not yield even if it has a relatively low yield strength. In their tests, Martinez et al. found that the spiral steel exhibited strains very near or below the yield strain when the confined core reached its peak strength. Sheikh et al. reached this same conclusion for a number of their specimens which contained low volumetric steel ratios.

Conclusions with regard to axial deformations are more consistent than those pertaining to strength of reinforcement. Mugumura et al. showed that an increase in spiral yield stress will result in an increase in the ductility prior to the member reaching its ultimate load. This conclusion follows directly from the Mugumura et al. finding that the spiral steel did yield prior to the member reaching its confined concrete peak strength. Martinez et al. and Mugumura et al. found that increasing the steel yield strength will cause an increase in the post peak ductility of the column. This increase in ductility takes the form of a higher and more horizontal descending branch on the load-displacement curve. However, the deformation at ultimate failure is frequently smaller when a member contains this type of reinforcement. Cusson et al. also found this in their research and concluded that this behavior is the result of higher strength steels being able to undergo significantly less deformation prior to rupture as compared to lower strength steels.

Another finding of interest to the current study deals with the inclined failure plane which frequently develops in high strength concrete compression members. Studies on this topic have been performed by Torrenti, Desrues, Benaija, and Boulay (1991), Cusson et al. (1996), and Martinez et al. (1984). Torrenti et al. used stereophotogrammetry to determine when strain localizations, the

first signs of an inclined failure plane, begin to occur in confined concrete. They concluded that the localizations begin to occur when the confined concrete reaches its peak stress. Cusson et al. concluded from their research that an inclined failure plane is effectively a shear failure. They found that after the strain localizations begin to occur, the concrete blocks above and below the developing plane tend to slide along the localizations relative to one another. Additionally, they found that an increase in the level of confinement leads to an decrease in the angle of the failure plane, measured with respect to the horizontal. Martinez et al. studied the inclined failure plane using the Mohr-Coulomb Failure Criterion. A complete derivation is presented by Martinez et al., however, for the purposes of the current study, it is sufficient to state that the inclined failure plane is a function of the cohesion, internal friction angle, and confining stress of the concrete. They also found that increasing the level of confining pressure will decrease the angle of the failure plane. Finally, they conclude that highly confined concrete, in general, may not be able to develop the failure plane and may fail due to crushing.

The final finding of interest to the current study focuses on the dilation behavior of concrete. Figure 2.2 shows an idealized diagram of the axial, transverse, and volumetric strains in axially loaded unconfined concrete from load initiation until the unconfined peak strength (adapted from MacGregor 1992). As shown in the figure, throughout the initial increase in stress, the axial and the transverse stress-strain curves for the concrete are linear. Poisson's ratio for concrete in this range is generally accepted to be approximately 0.15 to 0.20. During this stage, bond cracks form in the concrete, however, the cracks are stable (i.e. they do not propagate). As the axial stress continues to increase to above approximately $0.5f_{co}$, the figure shows that the transverse strain per stress and the axial strain per stress both begin to increase slightly. This is the range of stable crack propagation where mortar cracks are beginning to form. Finally, once the axial stress increases over about $0.7f_{co}$ to $0.8f_{co}$, the transverse strain begins to increase at a much more rapid rate than the axial strain. This is the stage of unstable crack propagation where the bond and mortar cracks formed earlier in the loading grow larger and join together to form a continuous pattern of microcracks. At this point, the transverse to longitudinal dilation of the concrete is increasing. This increase in dilation continues until failure.

Due to the passive nature of confinement provided by spiral reinforcement, the initial dilation behavior of spirally confined concrete should be similar to that of unconfined concrete. However, as soon as the spiral begins to provide significant confining pressure to the concrete, the behavior will begin to differ from the unconfined case. Generally, this occurs when the concrete begins to undergo significant microcracking. However, if an extremely stiff confinement was provided, a reduced dilation could occur earlier in the response due to the higher confining pressures, as noted by Kestner, Harries, Pessiki, Sause, and Ricles (1997).

Once the confinement is engaged by the lateral expansion of the confined concrete, the dilation will continue to increase, but at a slower rate than that which occurred in the unconfined concrete. This increase in dilation may continue until failure or the ratio of the transverse to longitudinal strains may reach a limiting value. Harries, Ricles, Sause, and Pessiki (1998) state that if the confined concrete were to behave as unconfined concrete, the dilation ratio would continue in-

11

creasing until failure. They go on to say that if the confining pressure exerted on the confined concrete continues to increase, the increase in the confined concrete dilation would likely cease at a limiting value.

2.5 DESIGN CODE REQUIREMENTS FOR SPIRALLY REINFORCED COMPRESSION MEMBERS

Requirements for the design of spirally reinforced columns and piles are given in the ACI 318 Building Code Requirements for Structural Concrete (1995) (hereafter referred to as the ACI 318 Code) and in the American Association of State Highway and Transportation Officials LRFD Bridge Design Specifications (1994) (hereafter referred to as the AASTHO Design Specification). Provisions for the design of prestressed piles are also given in the Prestressed Concrete Institute Design Handbook (1992) (hereafter referred to as the PCI Manual).

The design load capacity of an axially loaded member is defined as follows. The ACI 318 Code and the AASHTO Design Specification both state that the nominal concentric axial load capacity, P_o, of an axially loaded non-prestressed member is given by

$$P_o = 0.85 f_{co} \left(A_g - A_{lg} \right) + f_{ly} A_{lg} \tag{2.5}$$

where A_g is the gross cross-sectional area of the pile, A_{lg} is the area of the longitudinal reinforcement, and f_{ly} is the yield strength of the longitudinal reinforcement. The PCI Manual provides a similar equation, except that it takes into account the prestress force present within a prestressed member through the equation

$$P_o = \left(0.85 f_{co} - 0.60 f_{pc} \right) A_{c,total} \tag{2.6}$$

where f_{pc} is the concrete compressive stress due to effective prestress and $A_{c,total}$ is the total area of concrete in the cross-section.

A pile is defined as an any axially loaded member which is embedded into the ground and, throughout its length, has sufficient lateral pressure surrounding it to prevent lateral buckling from occurring. If sufficient lateral ground pressure can be assured, then the member can be designed as a pile as defined in the AASHTO Design Specification and the PCI Manual. In the design of a pile through this method, the amount of spiral required is based solely the position of the spiral within the length of the pile. The amount of spiral is not dependent on the concrete cover, the strength of the reinforcement, or the strength of the concrete.

Generally, members designed as piles, although not strictly piles by the definition above, are designed through the specifications for non-pile compression members. This is due to, among other circumstances, the fact that it is difficult to assure that there will be sufficient surrounding ground pressure to prevent lateral buckling throughout the entire length of the pile. Also, piles frequently may protrude from the ground and thus would be required to be designed as columns.

A confining pressure which is applied to the concrete core by spiral reinforcement can be calculated from Equation 2.7.

$$f_2 = \tfrac{1}{2}\rho_{sp}f_{sp} \tag{2.7}$$

This equation is based on the forces exerted on a slice of the cross-section of the core concrete. The volumetric ratio of spiral reinforcement is denoted by ρ_{sp}. f_{sp} is the stress in the spiral reinforcement.

The volumetric ratio of steel required in order to provide sufficient confinement for the core concrete in a non-pile member is given as

$$\rho_{sp} \geq 0.45\left(\frac{A_g}{A_{c,o-o}} - 1\right)\left(\frac{f_{co}}{f_{sy}}\right) \tag{2.8}$$

where $A_{c,o-o}$ is the core concrete area measured to outside diameter of spiral and f_{sy} is the yield strength of the spiral reinforcement. This equation is based on Equations 2.3 and 2.7 as well as the design philosophy that the load carrying capacity which was lost at cover failure should be replaced by increased load carrying capacity of the core concrete. Such a member is expected to exhibit the behavior which was described in Section 2.2. In this formulation, the spiral reinforcement is assumed to reach its yield stress prior to Δ_2 being reached. However, in order to ensure sufficient confinement, there is an upper limit of $f_{sy} = 60$ ksi (414 MPa) placed on the yield strength of the spiral reinforcing steel. Through this means, the volumetric ratio of transverse reinforcement remains high and the confining pressure at the second peak is very likely at or above the expected level.

The volumetric ratio of spiral reinforcement in a pile is computed through the use of Equation 2.9.

$$\rho_{sp} = \frac{4A_{sp}}{d_{sp}s} \tag{2.9}$$

The out-to-out diameter of the spiral reinforcement is denoted by d_{sp}.

Within the design codes, there are also provisions relating to the spiral reinforcement bar size, the clear spacing between bars, and the cover concrete required. The purpose of the bar size and clear spacing requirements is to ensure that the confining pressure will be distributed throughout the length of the member while still allowing for easy flow of fresh concrete between the bars. For example, the ACI 318 Code specifies that the minimum bar size is a #3 bar, the minimum clear spacing between bars is the larger of 1 in. (25.4 mm) or 4/3 times the largest aggregate size, and

13

the maximum clear spacing between bars is 3 in. (76.2 mm). The AASHTO Design Specification contains similar requirements.

The clear cover requirements for concrete compression members are clearly defined in both the ACI 318 Code and the AASHTO Design Specification. In general for piles, the clear cover is to be 2 in. (50.8 mm) due to the member being placed in direct contact with the earth. However, in special cases such as exposure to a harsh environment, a cover of 3 in. (76.2 mm) may be specified. Additionally, note that prestressed members cast under factory controlled conditions sometimes are allowed reductions in the amount of cover required.
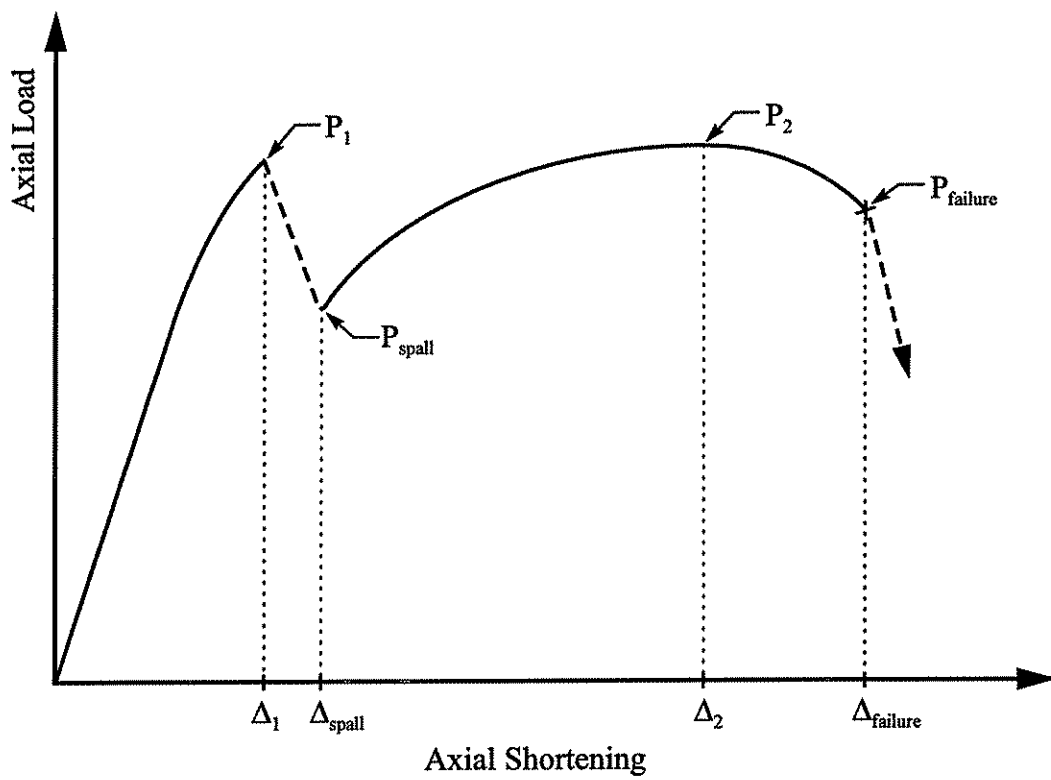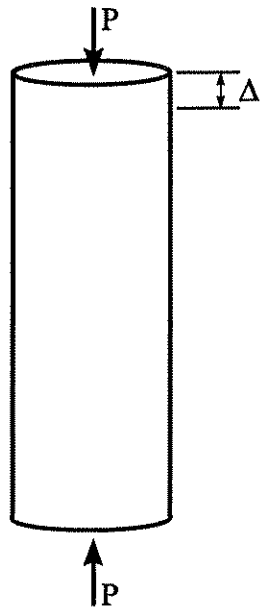
Figure 2.1   Idealized load-shortening behavior of a spirally reinforced member.
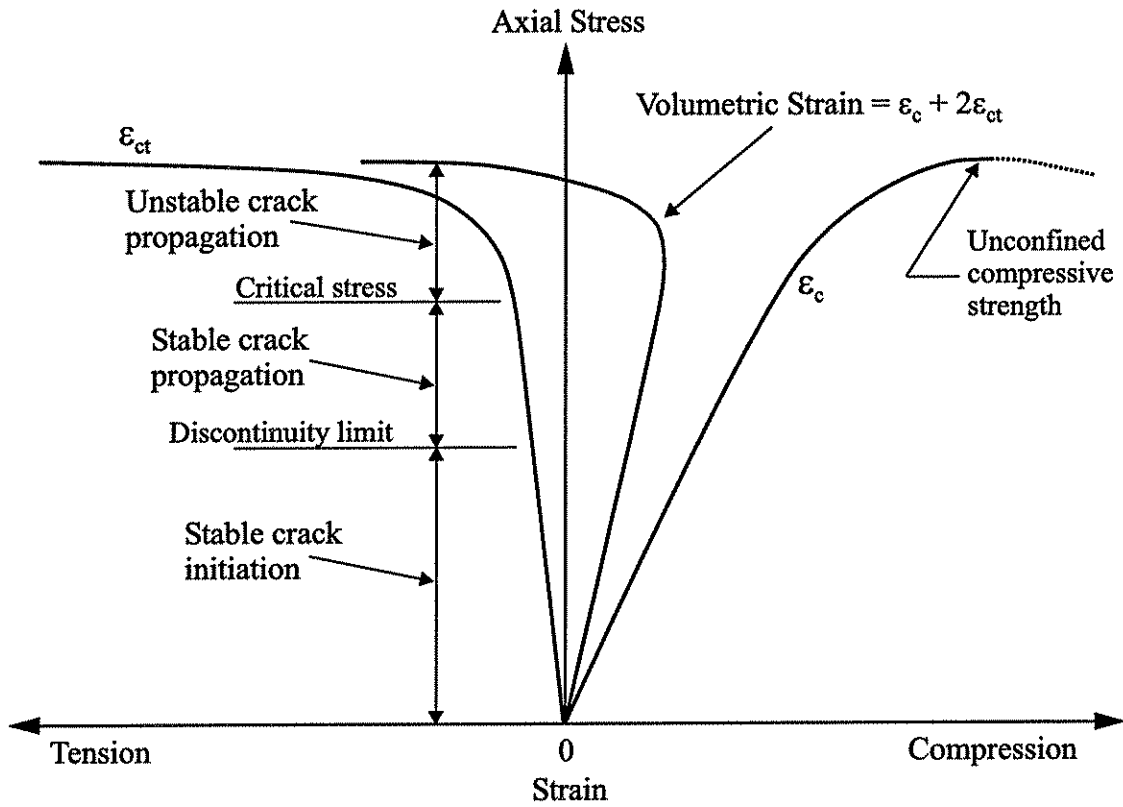
Figure 2.2   Transverse and volumetric strains in unconfined concrete with regard to the unconfined concrete stress-strain curve (adapted from MacGregor 1992).

CHAPTER 3
DESCRIPTION OF EXPERIMENTAL PROGRAM

3.1 INTRODUCTION

This chapter describes the experimental program. Section 3.2 presents the test matrix and Section 3.3 describes the details of each pile specimen. The instrumentation which was used to measure the response of each specimen is described in Section 3.4. Section 3.5 presents specimen fabrication details. Finally, Sections 3.6 and 3.7 describe the material properties of the concrete and the reinforcing steel, respectively.

3.2 TEST MATRIX

As stated in Chapter 1, the objective of the research is to evaluate the confinement effectiveness of high-strength spiral reinforcement in precast, prestressed concrete piles. The test matrix, presented in Table 3.1, was developed to investigate this objective. As shown in Table 3.1, a total of 8 specimens were included in the test program. The primary variables treated were pile diameter and spiral yield strength. Table 3.1 includes an alpha-numeric identifier for each pile. The prefixes '24' and '14' refer to piles with 24 in. (610 mm) and 14 in. (356 mm) diameters, respectively. The 'A', 'B', 'C', and 'D' in the alpha-numeric identifier are used to denote the nominal spiral steel yield strengths as follows: A = 78 ksi (538 MPa); B = 107 ksi (738 MPa); C = 121 ksi (834 MPa); and D = 140 ksi (965 MPa), respectively. These nominal yield strength values were provided by the spiral manufacturer.

3.3 SPECIMEN DETAILS

Table 3.2 summarizes the design parameters for each pile while Figure 3.1 shows schematic drawings of the specimen cross-sections and reinforcement layouts. The 24 in. (610 mm) diameter specimens all measured 96 in. (2.44 m) in height and the 14 in. (356 mm) diameter specimens all measured 56 in. (1.42 m) in height. Thus all specimens had a height-to-diameter aspect ratio of 4-to-1. All specimens had a 2 in. (51 mm) clear concrete cover between the outside of the spiral reinforcement and the outer surface of the specimen. The design concrete compressive strength was 8.0 ksi (55.2 MPa).

Figure 3.2 shows photographs of the completed reinforcement cages prior to placement in the formwork. As shown in Figure 3.2, the portion of each pile within one diameter of height from each end was provided with extra spiral reinforcement to increase the confinement in these end regions. The test region was defined as the section of the pile which was between the more heavily confined end regions.

Table 3.3 provides a summary of the reinforcement details. Six #4 Grade 60 bars provided the longitudinal reinforcement in the larger diameter piles while four #4 Grade 60 bars were used in the smaller diameter piles. Within each test region, the spiral reinforcement was proportioned according to the ACI 318 Code and AASHTO Specification based on the design concrete compressive strength and the manufacturer-supplied nominal spiral yield strengths as stated above. Standard deformed reinforcing bar was not available in all of the strengths required, so 0.35 in.

(8.89 mm) wire was used for all specimens. All spiral wires treated in the study had the same wire diameter (0.35 in). Also, in order to provide additional clear spacing between spiral turns, two wires were bundled to create the spiral in the two lower spiral yield strength specimens in each diameter (14-A, 14-B, 24-A, and 24-B). This is shown in Figure 3.2.

It is noted that the piles were not prestressed. This is not expected to affect axial load behavior as the effect of prestress is quickly overcome under concentric axial load.

3.4 INSTRUMENTATION

Three types of instruments were employed to evaluate the behavior of the piles during testing. Electrical resistance strain gages were used to monitor strains in both the spiral and longitudinal reinforcement. Linear potentiometers, anchored in the pile core, were used to measure axial short-ening of the pile over known gage lengths. These measurements, along with the known gage lengths, were used to compute average axial strains over the gage lengths. Finally, linear variable differential transformer (LVDT) displacement transducers were used to measure the travel of the testing machine head, and thus to provide an indication of overall axial shortening.

A total of twelve strain gages were used on each specimen. All gages were placed on reinforcing steel within the test region. The general layout of the gages on each pile was similar. The gage layout for a 14 in. (356 mm) diameter pile is shown in Figure 3.3. Strain gages S1 through S8 were placed on the spiral with S1 located in the top eighth of the test region and S8 located in the bottom eighth of the test region. The gages were placed in an alternating fashion at three locations approximately 120 degrees apart around the perimeter of the pile in the 24 in. (610 mm) diameter specimens and at four locations approximately 90 degrees apart in the 14 in. (356 mm) diameter specimens. Additionally, the gages were all placed midway between longitudinal reinforcement bars to avoid any possible influence of bending of the spiral reinforcement around the longitudinal bar. Where possible, the gages were placed on the bottom of the spiral, centered on the neutral axis about which the spiral was bent. This was done to reduce any bending effects and also to protect the gages from falling fresh concrete during concrete placement. In the specimens with bundled spirals, the gages were located alternately on each spiral in the bundle to capture any differences in strain between the two spirals.

Strain gages L1 through L4 were placed on the longitudinal reinforcing steel. As shown in Figure 3.3, L1 and L3 were placed on the same reinforcing bar in the top quarter and lower middle quarter of the test region, respectively. L2 and L4 were placed on the reinforcing bar opposite that of L1 and L3, with L2 and L4 located in the upper middle quarter and bottom quarter of the test region, respectively. All longitudinal reinforcing steel strain gages were located on a side of the bar whose normal was tangent to the circumference of the specimen. This was done to reduce any effects that may arise due to bending of the longitudinal reinforcement caused by expansion of the core.

Figure 3.4 shows the layout of the eight potentiometers and the LVDTs. Potentiometers 1-4 were positioned on one side of the specimen, each measuring axial shortening over a gage length equal to 1/4 of the height of the test region. As shown in Figure 3.4, Potentiometer 1 was located over

18

the top quarter of the test region, and Potentiometer 4 was located over the bottom quarter of the test region. Potentiometers 5-8 were positioned on the opposite side of the specimen from Potentiometers 1-4, and followed the same placement convention. Four LVDTs were placed on the testing machine head, one at each corner of the square head. The only exception was Pile 24-A in which only two LVDTs were used. For this pile, one LVDT was located just north of the specimen and the other LVDT was located on the southeast corner of the testing machine head. The LVDT placement for Pile 24-A confirmed that the measurement of head travel made at the corner of the testing machine head produced the same results as measurements of head travel made with a transducer positioned closer to the pile.

The output from all instruments, including the axial force output from the testing machine, was captured by a computer-based data acquisition system. This system processed the signals from the instruments, permanently recorded the data, and provided a real-time display of the various specimen parameters which were being measured.

3.5 SPECIMEN FABRICATION

The reinforcement cages were produced from collapsed helical spirals, each comprised of approximately 20 to 25 turns of wire, and straight longitudinal reinforcing bars. The longitudinal bars were placed in a template which held them in position while the spirals were tied to the correct pitch. The cages were produced in such a way that no spiral lap spliced occurred within the test region, although every specimen did have a number of lap splices outside of the test region. For each lap splice, the overlap of the two spirals was 1 to 1.5 turns. The ends of the spliced spirals were also bent into the confined core to aid in development of the spiral.

As noted earlier, extra confinement was provided near the ends of each pile specimen. One diameter of specimen height at each end of the specimen was heavily confined to prevent a failure due to end effects. This is shown in Figure 3.2. The extra confinement was provided by bundling one additional spiral into the cage over this region. Also, within approximately one quarter diameter from the end, the pitch of the spiral was decreased.

Reinforcement chairs were used to provide correct cage placement within the formwork, and thus the correct concrete cover. The chairs were placed on the outside of the heavily confined region both on the top and the bottom of the specimen at four locations around the perimeter.

The formwork consisted of cylindrical cardboard forms held in place by a wooden frame. The completed formwork for the pile specimens is shown in Figure 3.5. Ten 1.5 in. (38 mm) diameter by 1 in. (25 mm) thick polystyrene disks were glued to the inside of each cardboard form at the locations where the attachments for the potentiometers were to be placed. These disks were excavated from the hardened concrete once the formwork was removed. Thus, these disks provided a pocket in the concrete cover such that when cover concrete spalling occurred, the potentiometer embedded in the core would remain undisturbed. The cardboard forms were then placed over the cages and securely attached to the wooden frame. Lastly, the 0.25 in. (6.35 mm) diameter threaded

rods which served as the potentiometer attachments were screwed through the disks such that their interior end was embedded at least 2 in. (51 mm) into the core concrete.

One 24 in. (610 mm) diameter and one 14 in. (356 mm) diameter plain concrete specimen was also prepared along with the eight test specimens. These plain concrete specimens contained only two longitudinal reinforcing bars and did not contain any spiral reinforcement. They were cast to provide specimens in which the concrete had undergone the same curing history as the reinforced test specimens. Cores were cut from these plain concrete specimens and tested in compression to obtain information about the in-place concrete compressive strength. Additional tests were made on field-cured cylinders cast during the concrete pour. Concrete compressive strength testing is discussed in Section 3.6.3.

All specimens were oriented in a vertical position during concrete placement. The concrete was placed in 3 lifts for the 24 in. (610 mm) diameter specimens and in 2 lifts for the 14 in. (356 mm) diameter specimens. Each lift was consolidated with an electrically powered internal submersion vibrator. The 6 x 12 in. (152 x 305 mm) field-cured cylinders were made according to ASTM C-31.

The piles were cured in the cardboard forms for 21 days, during which time the tops of the specimens were covered with wet burlap and plastic sheeting. After this time, the formwork was removed from all 10 specimens. The field-cured cylinders were also covered with wet burlap and plastic sheeting for 21 days, after which they were stripped from their plastic molds.

3.6 CONCRETE MATERIAL PROPERTIES
This section discusses the concrete material properties. The concrete mixture proportions and the curing temperatures reached in the piles are briefly discussed first in Sections 3.6.1 and 3.6.2. The concrete material property of primary interest is the unconfined concrete compressive strength, f_{co}. This is discussed in Section 3.6.3. Finally, Section 3.6.4 describes the experimentally determined stress-strain curve of the unconfined concrete.

3.6.1 Mixture Proportions
The concrete for all eight piles, the two plain concrete specimens, and the field-cured cylinders came from the same batch of ready-mix concrete. The mixture proportions of the concrete, as reported by the ready-mix supplier, are shown in Table 3.4.

3.6.2 Curing Temperatures
Concrete temperatures were measured in the unreinforced 24 in. (610 mm) and 14 in. (356 mm) diameter piles, and also in one 6 x 12 in. (152 x 305 mm) field-cured cylinder for approximately the first 120 hours of curing. The ambient air temperature was also monitored during this period. The temperature of each monitored concrete specimen was measured using a thermocouple which was placed approximately at the center of the volume of the specimen during concrete placement. Figure 3.6 shows the temperature histories that were recorded. The 24 in. (610 mm) diameter pile reached the highest temperature at approximately 148 °F (64 °C), followed by the 14 in. (356 mm)

20

diameter pile at approximately 134 °F (57 °C), in turn followed by the field-cured cylinders at approximately 103 °F (39 °C).

3.6.3 Compressive Strength

As stated above, the concrete material property of primary interest is the unconfined concrete compressive strength. Three approaches were used to determine this value as follows:

1. Compression tests were performed on 6 x 12 in. (152 x 305 mm) field-cured cylinders;
2. Compression tests were performed on 6 x 12 in. (152 x 305 mm) cored cylinders cut from the unreinforced piles; and,
3. The unconfined concrete compressive strength was computed from the first peak (P_1) in the axial load response of each pile specimen.

The field-cured cylinders were cast from the same batch of concrete as the piles and were cured in the same manner as the piles. The cylinders were prepared according to ASTM C-31 procedures using plastic molds. They were cured using wet burlap and plastic sheeting for the same duration as the pile specimens.

The cored cylinders were extracted from the two unreinforced pile specimens, as per ASTM C-42, using an electric coring machine. The ends of cores were saw cut to obtain smooth and parallel faces. The cores had a diameter of 6 in. (152 mm) and a height which was within +/- 0.375 in. (10 mm) of 12 in. (305 mm). Figure 3.6 shows the locations at which the cores were extracted from the unreinforced piles. Three cores were extracted from each unreinforced pile. The cores were extracted and tested at approximately the same age that the piles were tested.

All field-cured and cored cylinders were tested in a 600 kip (2669 kN) capacity displacement controlled universal testing machine. The cylinders and cores were capped with a sulfur mortar compound according to ASTM C-617. Except for load rate, all cylinders and cores were tested according to ASTM C-39. The load rate for the majority of the specimens was within the ASTM prescribed range of 20 psi/sec. (138 kPa/sec.) to 50 psi/sec. (345 kPa/sec.). However, for two field-cured cylinders, the load rate was decreased to a rate more similar to the load rate applied to the pile specimens (approximately 2.6 psi/sec. (18 kPa/sec.)).

As stated above, the third method for determining the strength of the unconfined concrete was to compute the concrete strength from the first peak (P_1) on the load-shortening plot of the pile specimens. The basis for this approach is as follows. The pile concrete cross-section can be divided into two regions, the unconfined cover, and the confined core. At P_1, the spiral reinforcement does not provide significant restraint to lateral expansion. As a result, prior to P_1 the entire specimen cross-section is effectively behaving as if it were unconfined concrete. Based on this reasoning, the unconfined concrete strength can be calculated as follows:

$$f_{co} = \frac{P_1 - A_{lg}f_{ly}}{A_{c,total}}$$

(3.1)

21

where $A_{c,total}$ is the total area of concrete in the pile cross-section. This approach assumes that the longitudinal bars have yielded when P_1 is reached. This is shown to be the case in the individual test summaries in Chapter 4.

Many factors are expected to effect the concrete compressive strength determined using the three approaches described above. These factors include: (1) rate of loading; (2) concrete curing temperature (this may affect many things, including the distribution of porosity in the hydrated cement paste (Verbeck and Helmuth 1968), and the continued availability of moisture for hydration); (3) presence of voids due to bleed water (for example, cores nearer the top of the pile may contain more voids attributable to bleed water as compared to cores extracted nearer the bottom of the pile), to name a few. Thus, the different approaches used to estimate the unconfined concrete compressive strength were not necessarily expected to produce the same results.

Table 3.5 summarizes the results of the three approaches used to estimate the unconfined concrete compressive strength. The results are largely as expected. In particular, the following points are noted:

1. The results from the cored cylinders show that there is a variation of concrete strength over the height of the pile. In both the small and large diameter pile cores, there was an approximately 1.2 to 1.7 ksi (8.3 to 11.7 MPa) strength difference between the top core and the bottom core. This variation in strength with height is attributed to bleed water effects.
2. The three field-cured cylinders loaded at the ASTM load rate all exhibited similar compressive strengths, with an average value of 10.41 ksi (71.8 MPa). This is higher than the strengths computed from P_1. This result was anticipated, since a lower concrete strength can be expected in the piles due to, among other things, bleed-water effects, evaporation, voids, and loading rate. If a correction factor of 0.85 is applied to the strength of the field-cured cylinders, a modified strength of 8.85 ksi (61.0 MPa) is obtained. This value is consistent with the results of P_1.
3. The results of the five field-cured cylinder tests illustrate the influence of loading rate. As expected, a slower loading rate produced a lower concrete compressive strength. For the two load rates treated, a decrease in the load rate from an ASTM prescribed value of approximately 40 psi/sec. (276 kPa/sec.) to a value of 2.6 psi/sec. (18 kPa/sec.) led to a 6 percent reduction in concrete compressive strength.
4. The unconfined compressive strength values obtained from the first peak of the load-shortening response for all eight pile specimens varied within a narrow range of less than 0.2 ksi (1.4 MPa). This suggests that the concrete strength was very consistent between specimens.
5. Core strength comparisons between the two piles show that cores taken from the larger diameter piles have lower strengths. The reason for this is not clear. It is also noted that the unconfined concrete strength estimated from P_1 was the same for both the large and small diameter piles.

22

Based on the results presented in Table 3.5 and the discussion presented above, the unconfined concrete compressive strength, f_{co}, is taken as 8.5 ksi (58.6 MPa).

3.6.4 Stress-Strain Properties of Unconfined Concrete

The stress-strain properties of the unconfined concrete were determined from the field-cured and cored cylinders. Strain measurements were made using four clip gages attached 90 degrees apart around the circumference of the cylinder. The gage length for each clip gage was just over 6 in. (152 mm). The typical unconfined concrete stress-strain behavior is shown in Figure 3.8. Figure 3.8(a) shows the results from each individual clip gage, and Figure 3.8(b) shows the average of the four clip gage readings. This particular figure is for Core 24-2, however the same general behavior was observed in the stress-strain plot for all field-cured and cored cylinders. Additionally, through these tests, the axial concrete strain corresponding to the unconfined concrete stress, ε_{co}, was determined to be 0.0027.

3.7 REINFORCING STEEL MATERIAL PROPERTIES

The material properties of the longitudinal and spiral steel reinforcement used in the pile specimens is described below. The information relating to the longitudinal reinforcement was obtained from tests performed at Lehigh University. The information relating to the spiral reinforcement was obtained from the spiral manufacturer. Chapter 5 provides a more detailed look at the properties of the spiral reinforcement as they pertain to the spiral behavior in a spirally reinforced concrete member.

3.7.1 Longitudinal Reinforcing Steel

The longitudinal reinforcement was comprised of #4 steel reinforcing bars with a nominal diameter of 0.5 in. (12.7 mm) and a nominal yield strength of 60 ksi (414 MPa). From tension tests, this steel was found to have an actual yield stress of 71 ksi (490 MPa), and an ultimate strength of 118 ksi (814 MPa).

3.7.2 Spiral Reinforcing Steel

The spiral reinforcement was produced by a spiral reinforcement manufacturer. The four different grades of spiral reinforcement treated in the study were produced through a cold-drawing process from four different grades of undeformed steel wire. The spiral steel was then coiled such that the outer cage diameter was 20 in. (508 mm) and 10 in. (254 mm), respectively for the 24 in. (610 mm) and 14 in. (356 mm) diameter specimens. The grades of spiral are labeled A, B, C, and D with A having the lowest yield and ultimate strength. The nominal yield strength values as reported by the spiral manufacturer for the yield strength of the four grades of spiral were 78, 107, 121, and 140 ksi (538, 738, 834, and 965 MPa), respectively. The diameter of all spiral reinforcing wires was 0.350 in. (8.89 mm). The spiral manufacturer reported that no stress-relieving was performed either before or after the wire was turned into a spiral.

The spiral reinforcement manufacturer performed material testing on the spiral reinforcement. Tests were performed on all four strengths of spiral wire after the drawing process, but before the

wire had been turned into a spiral. This was done to determine the tensile yield and ultimate strength of the four grades of reinforcement. These results were supplied to the researchers and are summarized in Table 3.6.

The testing method used by the spiral manufacturer is basically an elongation under load method, as described in ASTM A370. This specification is referenced from ASTM A82 which defines standards for steel wire used as concrete reinforcement. The elongation under load method is generally used for determining the tensile yield properties of a steel tensile specimen which does not exhibit a well-defined yield point.

In this testing method, the wire is placed in the testing machine and the extensometer is attached to the wire. The wire is then loaded until a predefined displacement over the extensometer length is reached. At this displacement, the load divided by the original cross-sectional area is defined as the yield stress. Following this, the extensometer is removed and the wire is loaded until the ultimate load and subsequent failure load are reached.

The ASTM standard states that as long as the steel yield strength is not over 80 ksi (552 MPa), the strain at yield can be defined as 0.005. However, the standard continues by stating that if the yield strength is above 80 ksi (552 MPa), then the yield strain should be increased. This is due to the expected rounded nature of the stress-strain curve and a theoretical elastic-plastic steel wire of higher yield strength having a yield strain already close to or above 0.005.

The tests performed by spiral manufacturer deviated from the ASTM standard in two ways. First, the load applied to the wire prior to attaching the extensometer was 25 percent of the expected yield load. The spiral manufacturer reports that this load was applied solely to align the specimen. It therefore may be unnecessarily high. At this point, a preload strain of 0.0005 was assumed, which is also contrary to the ASTM standard. Based on the preload and the assumed strain value, the manufacturer defined yield strain is the strain at 25 percent of the expected f_{sy} plus 0.0045.

The second deviation from the specification is that the yield strain of 0.005 was used for all steel strengths. The lowest strength wire had a strength close to the ASTM limit of 80 ksi (552 MPa). The remaining three wires had strengths well above the yield stress at which at which a yield strain of 0.005 is permissible.

Because of the deviations from the ASTM standard, as well as the limitations inherent is the test method, the material properties obtained from the manufacturer may not be accurate representations of the actual spiral properties. However, these manufacturer supplied yield strength values were used in the design of the spiral reinforcement for the pile specimens.

24

Pile	Nominal Spiral Yield Strength (ksi)			
Diameter	78	107	121	140
24 in.	24-A	24-B	24-C	24-D
14 in.	14-A	14-B	14-C	14-D

1 ksi = 6.895 MPa

Table 3.1   Test matrix.

Pile	Diam. (in.)	Cover (in.)	Height (in.)	f_{co} (ksi)	f_{sy} (ksi)	ρ_{sp} %	f_{ly} (ksi)	ρ_{lg} %
24-A	24	2	96	8.0	78	2.04	60	0.26
24-B	24	2	96	8.0	107	1.49	60	0.26
24-C	24	2	96	8.0	121	1.31	60	0.26
24-D	24	2	96	8.0	140	1.13	60	0.26
14-A	14	2	56	8.0	78	4.47	60	0.51
14-B	14	2	56	8.0	107	3.26	60	0.51
14-C	14	2	56	8.0	121	2.88	60	0.51
14-D	14	2	56	8.0	140	2.49	60	0.51

1 ksi = 6.895 MPa
1 in. = 25.4 mm

Table 3.2   Summary of design parameters.

| Pile | Spiral Reinforcement | | | | | Longitudinal Reinforcement | | | |
	d_{sw} (in.)	n_{sp}	A_{sp} (in.^{2})	s (in.)	ρ_{sp} %	Bar Size	n_{lg}	A_{lg} (in.^{2})	ρ_{lg} %
24-A	0.35	2	0.1924	1.875	2.05	#4	6	1.18	0.26
24-B	0.35	2	0.1924	2.500	1.54	#4	6	1.18	0.26
24-C	0.35	1	0.0962	1.500	1.28	#4	6	1.18	0.26
24-D	0.35	1	0.0962	1.750	1.10	#4	6	1.18	0.26
14-A	0.35	2	0.1924	1.750	4.40	#4	4	0.79	0.51
14-B	0.35	2	0.1924	2.375	3.24	#4	4	0.79	0.51
14-C	0.35	1	0.0962	1.375	2.80	#4	4	0.79	0.51
14-D	0.35	1	0.0962	1.500	2.57	#4	4	0.79	0.51

1 in. = 25.4 mm

Table 3.3   Summary of reinforcement provided in each pile.

Item	Amount	Comment
Cement	0.132 yd^3	Keystone Cement - Type I
Cement	0.049 yd^3	JTM Industries - Type F
Fine Aggregate	0.290 yd^3	Hains & Kibblehouse - Chestnut Ridge
Coarse Aggregate	0.331 yd^3	Eastern Industries - Kutztown Quarry #8
Water	0.173 yd^3	
Air	0.025 yd^3	2.5% air entrainment
Total Volume	1.000 yd^3	
Admixture		Rheobuild 1000
Water/Cement Ratio	0.32	
Slump	7.0 in.	
Unit Weight	152.7 lb/ft^3	

1 yd^3 = 0.765 m^3
1 in. = 25.4 mm
1 lb/ft^3 = 0.157 kN/m^3

Table 3.4   Concrete mixture proportions per cubic yard as reported by the ready-mix supplier.

26

Specimen Type	ID	Load Rate (psi/sec.)	f_{co} (ksi)	Ave f_{co} (ksi)
Pile 1st Peak	14-A	2.6	8.51	8.53
	14-B	2.6	8.55	
	14-C	2.6	8.56	
	14-D	2.6	8.48	
Pile 1st Peak	24-A	2.6	8.48	8.55
	24-B	2.6	8.57	
	24-C	2.6	8.51	
	24-D	2.6	8.64	
14 Core	14-1	36.3	8.14	9.15
	14-2	37.0	9.35	
	14-3	37.7	9.96	
24 Core	24-1	39.9	7.55	8.26
	24-2	39.2	8.49	
	24-3	37.7	8.74	
Field-cured Cylinder	1	37.7	10.43	10.41
	2	39.9	10.28	
	3	41.3	10.51	
	4	2.6	9.77	9.82
	5	2.6	9.86	

1 psi/sec. = 6.895 kPa/sec.
1 ksi = 6.895 MPa

Table 3.5   Summary of concrete compressive strength test results.

Spiral Steel Type	Manufacturer Reported Yield Stress (ksi)	Manufacturer Reported Ultimate Stress (ksi)
A	78	84
B	107	116
C	121	143
D	140	174

1 ksi = 6.895 MPa

Table 3.6   Spiral reinforcing steel material properties as reported by the spiral reinforcement manufacturer.
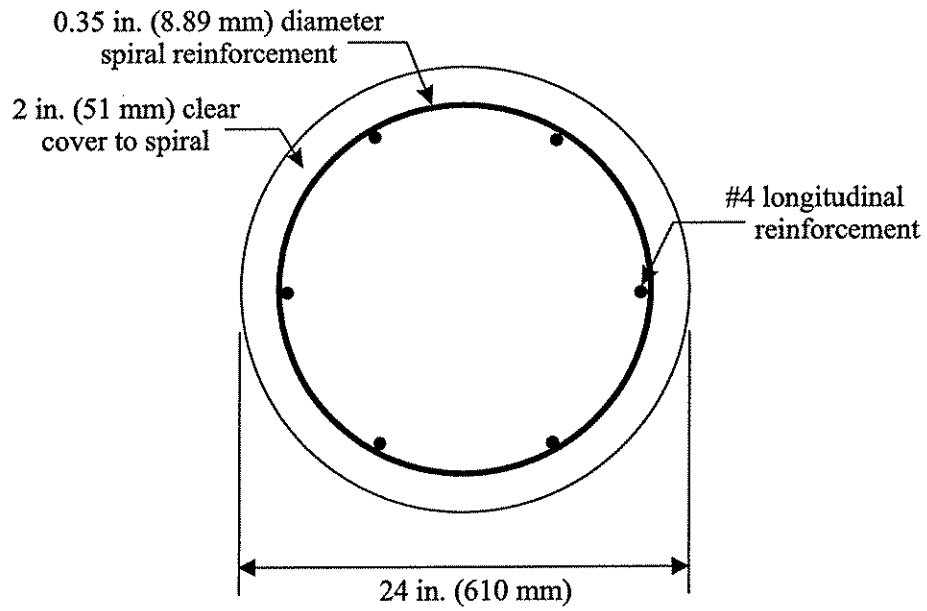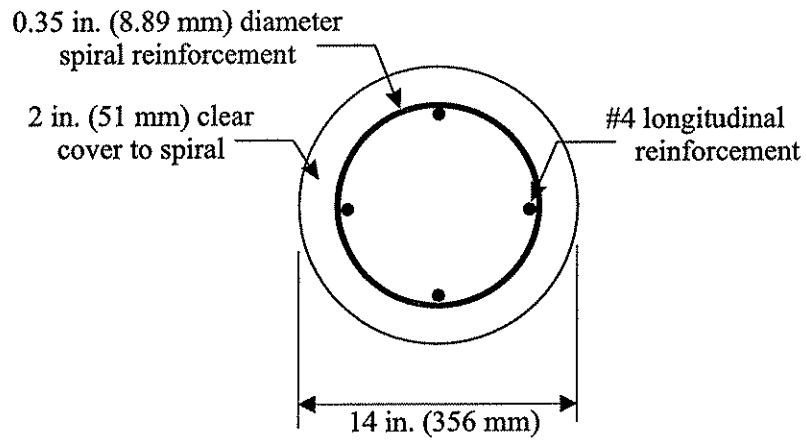
Figure 3.1   14 in. and 24 in. diameter pile cross-sections.
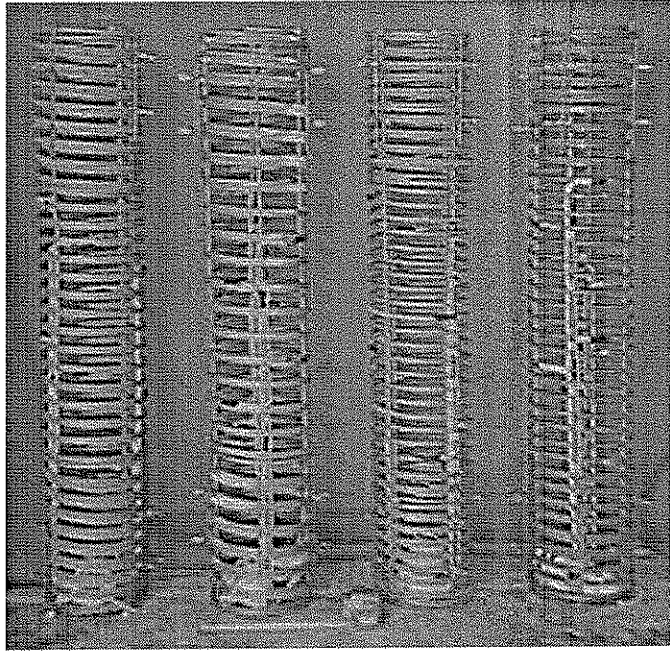
(a)
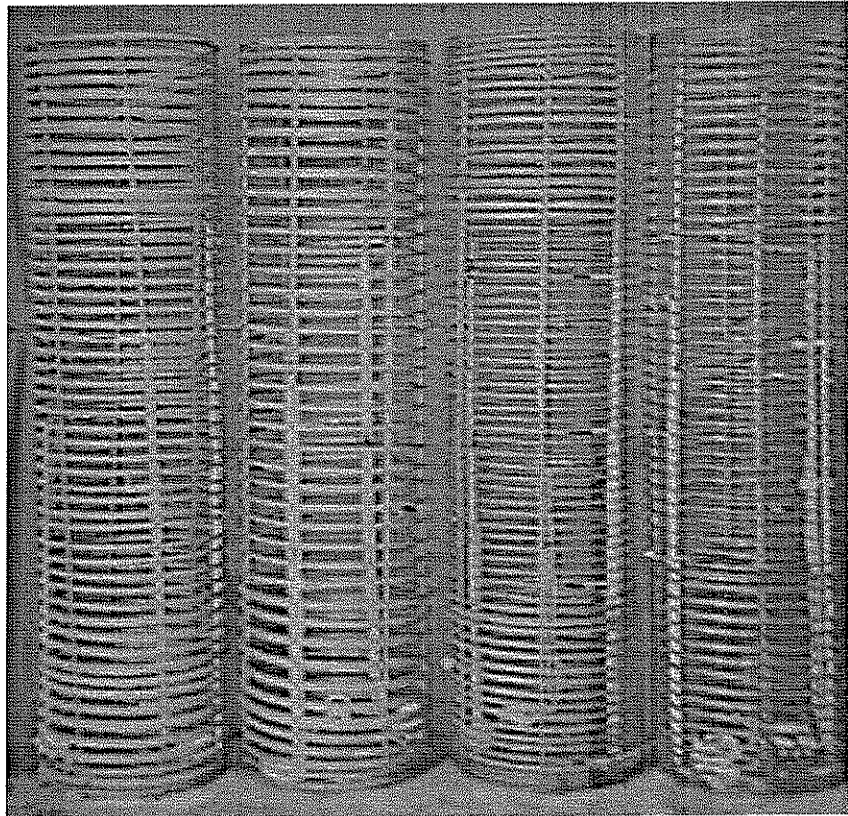
(b)

Figure 3.2   Reinforcing cages: (a) 10 in. diameter cage (spiral strengths A-D from left to right); (b) 20 in. diameter cage (spiral strengths A-D from left to right).
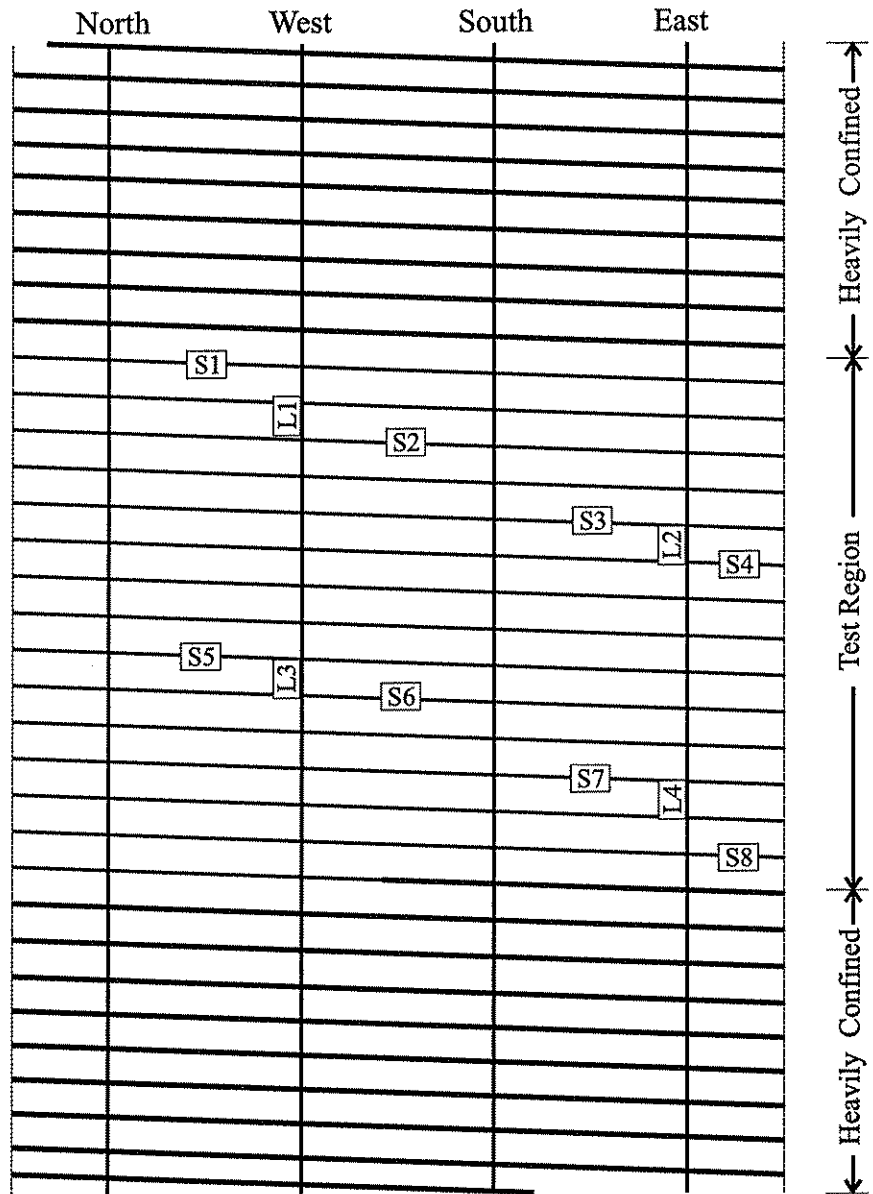
Figure 3.3   Typical 14 in. diameter pile reinforcing cage showing general layout of strain gages.
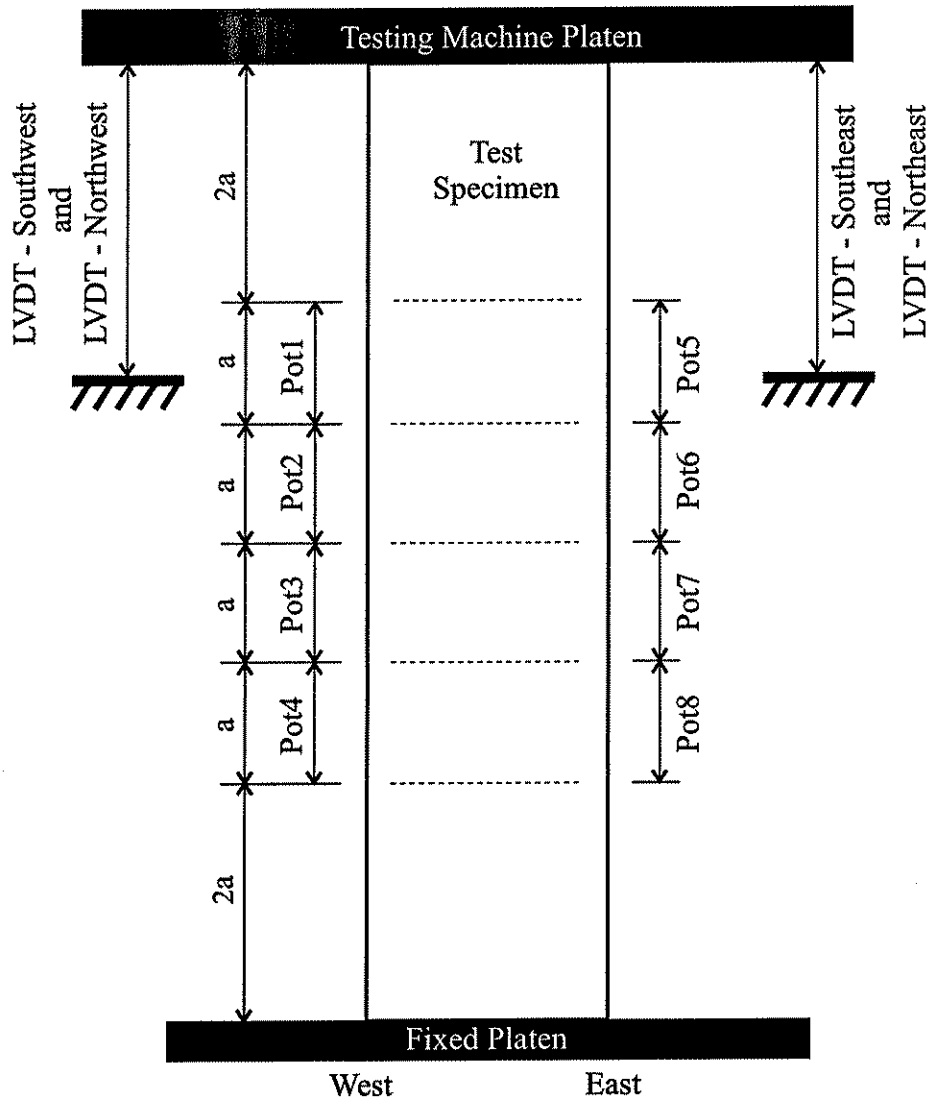
Figure 3.4 Instrumentation plan - layout of displacement transducers.

32

24 in. diameter piles

unreinforced piles

14 in. diameter piles
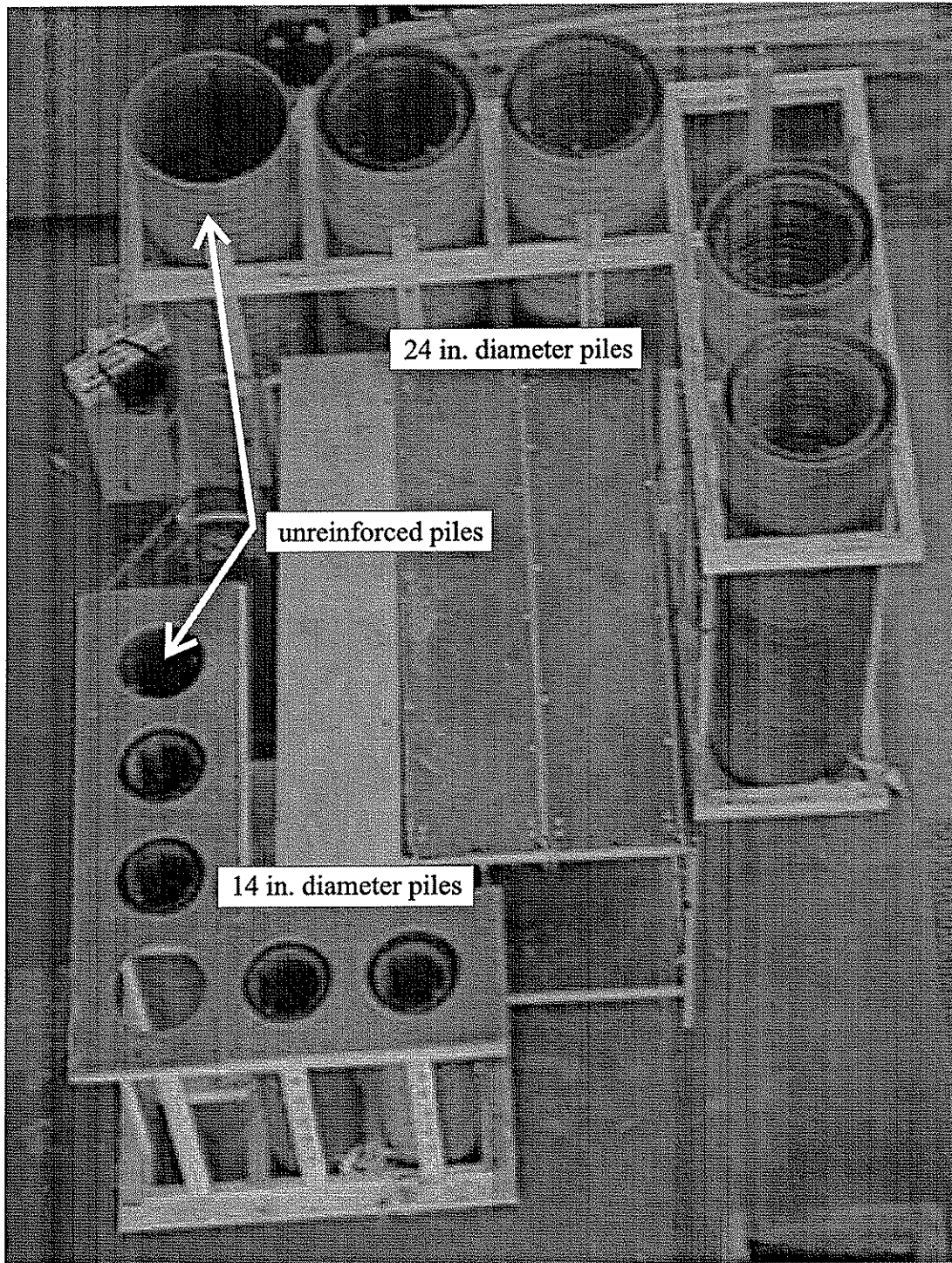
Figure 3.5   Formwork for pile specimens.
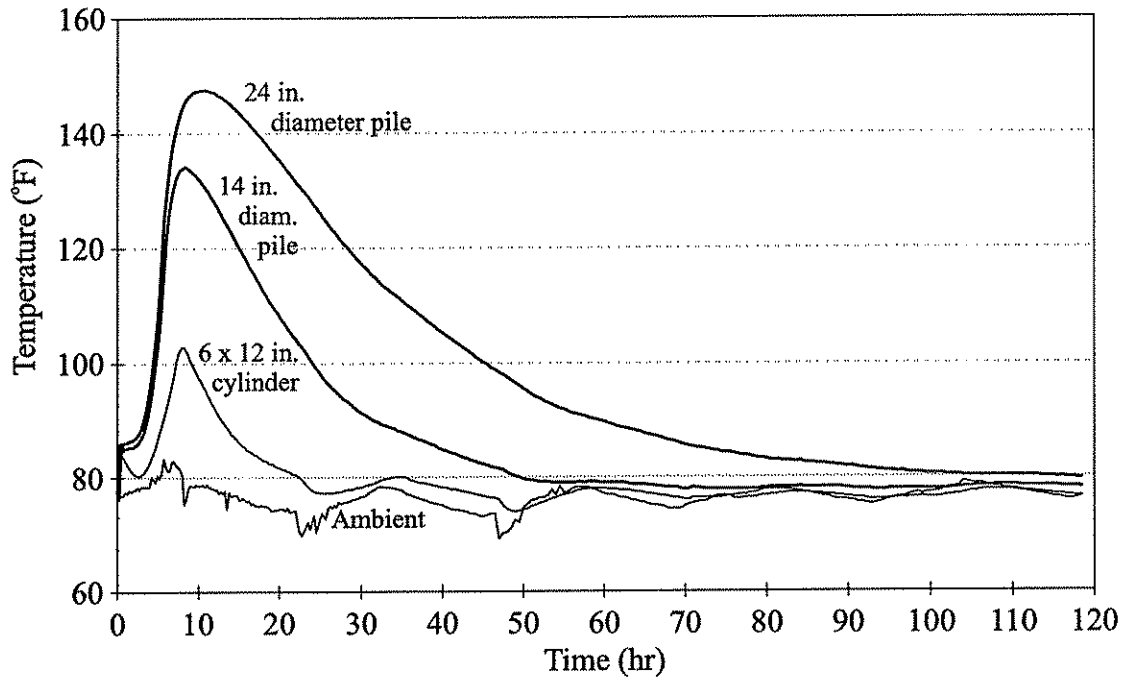
Figure 3.6   Time-temperature history of concrete during first 120 hours after concrete
placement.
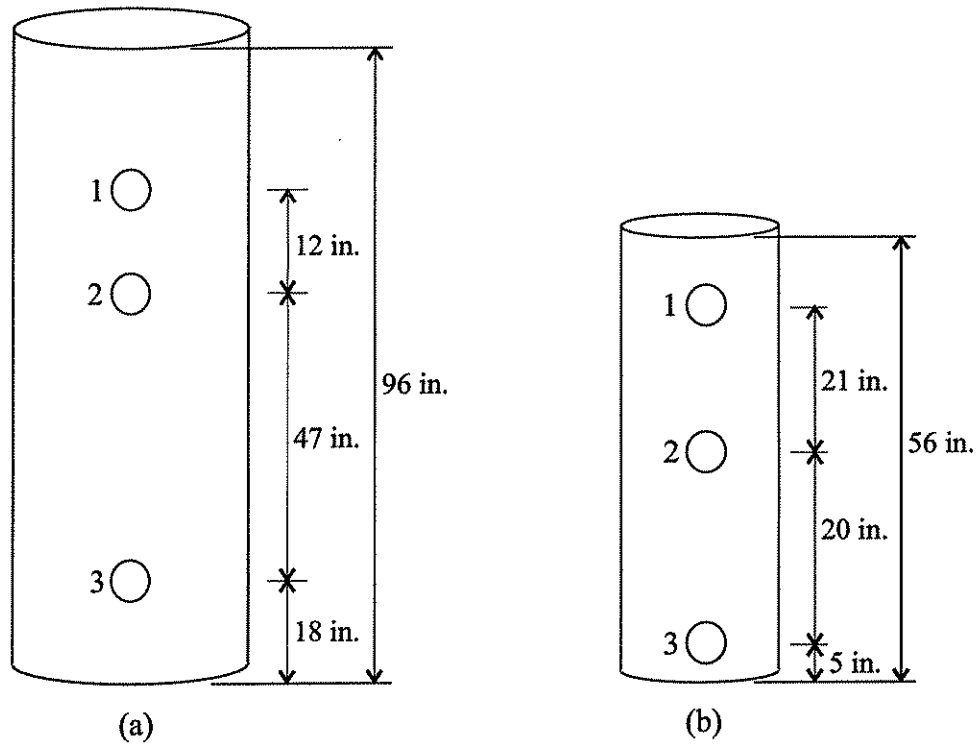
Figure 3.7   Locations at which cores were extracted: (a) 24 in. diameter unreinforced
pile; (b) 14 in. diameter unreinforced pile.
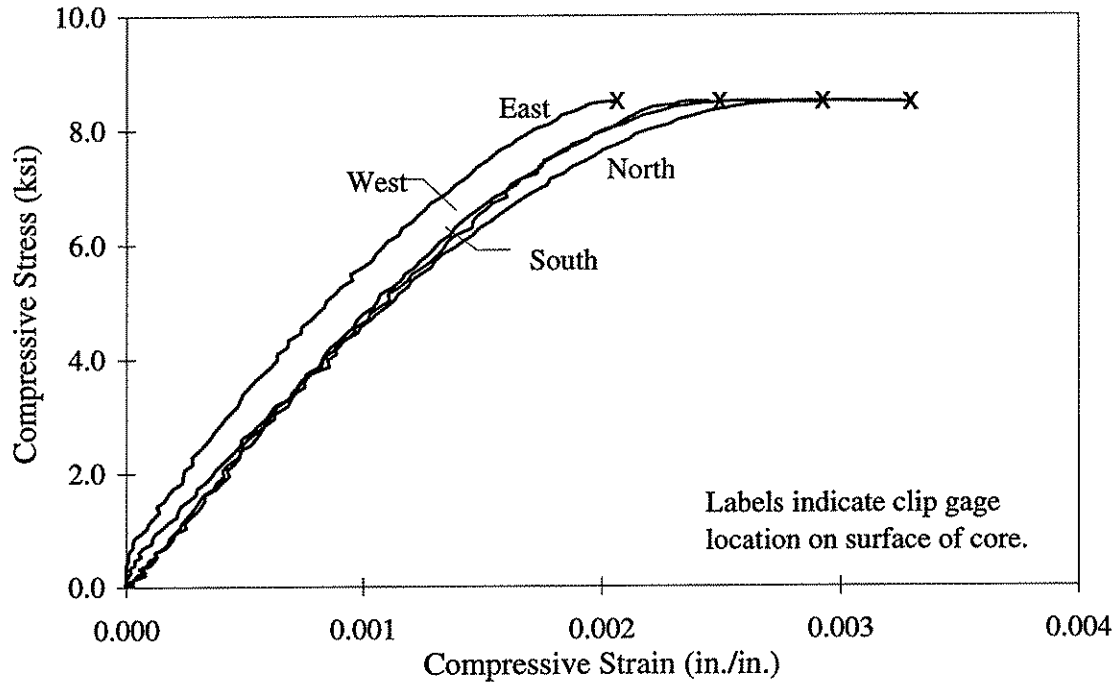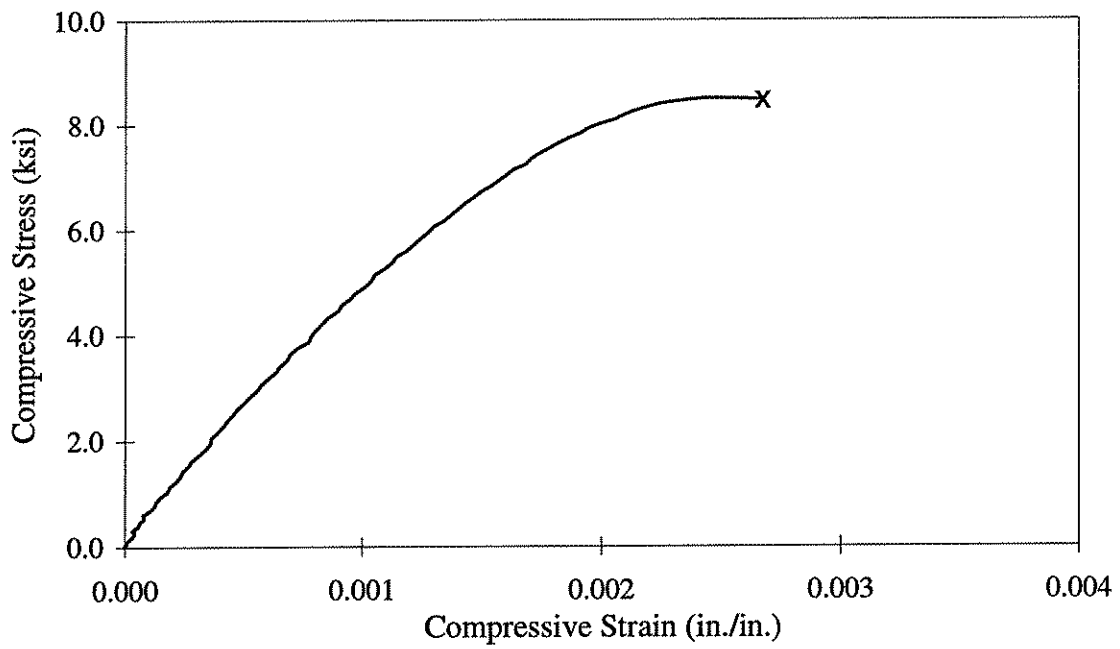
Figure 3.8   Unconfined concrete stress-strain behavior results from cored cylinder
              24-2 for: (a) all clip gages; and (b) average of clip gages.

35

CHAPTER 4
EXPERIMENTAL RESULTS

4.1 INTRODUCTION
This chapter presents a detailed description of the results of the experimental program. The individual test summaries for the eight pile specimens are all presented using the same general format as described in Section 4.2. Section 4.3 describes the loading procedure and presents the individual test summaries for the 24 in. (610 mm) diameter specimens. Similarly, Section 4.4 describes the loading procedure and presents the individual test summaries for the 14 in. (356 mm) diameter specimens.

4.2 FORMAT OF SUMMARIES
The individual test summary for each specimen is presented using the same general format as follows:

1. A summary of material properties present in specimen.
2. A description of the behavior of the pile during the test. Included are remarks about the axial load, axial shortening, and axial strain at key stages of the response including first peak, cover spalling, second peak, and pile failure. The axial strain reported is the average longitudinal strain gage strain computed for that point in the response.
3. A plot of axial load versus axial shortening. The axial shortening value is the average of the displacement readings which were taken at the corners of the machine head. Axial load values are noted on this figure at key stages in the response. P_1, P_{spall}, P_2, and $P_{failure}$ indicate the load at the first peak, after cover spalling, at the second peak, and at pile failure, respectively.
4. A plot of strain in the spiral reinforcement versus the axial shortening. The spiral strain values are the strains in the spiral reinforcement as recorded by the strain gages which were applied to the spiral during reinforcement cage fabrication.
5. A plot of strain in the longitudinal steel versus the axial shortening. The longitudinal strain values are the strains in the longitudinal reinforcement as recorded by the strain gages which were applied to the reinforcement during reinforcement cage fabrication. Also shown on this plot is the value of the average longitudinal strain computed at each increment of axial shortening. The average curve is truncated as soon as the average value is significantly disturbed due to failure of gages.
6. A plot of the axial strain, computed from the potentiometer axial shortening measurements, versus the axial shortening.
7. A schematic drawing which shows the post-test appearance of the pile. Noted in this sketch are locations of spiral fractures and other distinct features related to how the pile failed.
8. A series of photographs showing the pile immediately after cover spalling and at the completion of the test.

36

4.3 24 INCH DIAMETER PILE SPECIMENS
4.3.1 General Loading Procedure
Each 24 in. (610 mm) diameter pile specimen was tested under concentric axial compression in a 5000 kip (22.2 MN) capacity universal testing machine. Hydrostone was applied to both the top and bottom faces of each pile to provide uniform contact between the pile and the testing machine platens.

The load, load rate, and axial shortening rate were monitored throughout the test and the manner in which the specimen was tested was based upon these values. Through the initial portion of the test, the load rate was approximately 70 kips/min. (311 kN/min.), which corresponded to a stress rate of about 155 psi/min. (1069 kPa/min.) and an axial shortening rate of approximately 0.0040 in./min. (0.102 mm/min.).

The testing machine is hydraulically driven. Therefore, the actual rate of load or axial shortening is determined by the oil flow rate through the system. Once the desired load rate was achieved during the initial linear portion of the load-shortening behavior, no further adjustments were made to the oil flow rate of the machine. Thus, as each specimen neared the first peak in the load-axial shortening response, the load rate decreased due to the softening of the specimen. After the first peak and cover failure, testing of the specimen continued with the oil flow rate held constant through the second peak and until specimen failure.

4.3.2 Pile 24-A

Pile 24-A had an unconfined concrete compressive strength of 8.50 ksi (58.6 MPa). The spiral reinforcement had a design yield strength of 78 ksi (538 MPa). As noted in Chapter 3, this value of yield stress was reported by the spiral manufacturer. The longitudinal reinforcement had a yield strength of 71 ksi (490 MPa).

The spiral reinforcement was comprised of two 0.35 in. (8.89 mm) diameter smooth wires bundled together at a pitch of 1.875 in. (47.6 mm). The longitudinal reinforcement consisted of six 0.5 in. (12.7 mm) diameter deformed reinforcing bars spaced evenly around the perimeter of the confined concrete core.

The axial load versus axial shortening response of the pile is presented in Figure 4.1. The figure shows that the specimen exhibited a nearly linear load-shortening response from test initiation until the load reached approximately 2000 kips (8.90 MN). As the load increased beyond this point, the load-shortening plot shows that the specimen began to soften. The slope of the load-shortening plot continued to decrease as the load increased until the first peak load of $P_1 = 3910$ kips (17.39 MN) was reached. The overall axial shortening at this point was $\Delta_1 = 0.277$ in. (7.04 mm), and the corresponding axial strain was 0.0025 (average longitudinal strain gage strain). At this load, the cover concrete failed in a sudden manner.

Figure 4.6(a) is a photograph of the pile immediately after cover failure. Visible damage to the cover is apparent circumferentially around the specimen in the upper heavily confined region and upper test region. Longitudinal cracks also formed, extending from the top of the specimen down to the middle of the test region. No cracks were observed in the cover concrete prior to cover failure. The loss of the cover concrete caused the load to decrease to $P_{spall} = 2951$ kips (13.13 MN).

The pile exhibited considerably less axial stiffness after the loss of the concrete cover, as evidenced by the shallower slope of the axial load-axial shortening plot in Figure 4.1 after P_{spall}. The pile achieved its second peak at a load of $P_2 = 3826$ kips (17.02 MN) and an axial shortening of $\Delta_2 = 0.648$ in. (16.46 mm) (axial strain of approximately 0.0088). After this peak, the pile continued to shorten while the load decreased slightly until pile failure occurred at a load of $P_{failure} = 3678$ kips (16.36 MN) and an axial shortening of $\Delta_{failure} = 0.722$ in. (18.34 mm) (axial strain of approximately 0.0106). At failure, the axial load dropped to 42 kips (0.19 MN).

Figure 4.6(b) is a photograph of the pile immediately after pile failure. The spiral fractures occurred along an inclined failure plane which developed during the failure. This inclined plane formed at an angle of approximately 66 degrees from the horizontal and extended from the top of the test region on the north side of the pile to 19 in. (483 mm) from the bottom of the test region on the south side. Figure 4.7(a) shows a post-test photograph of the entire failed specimen from the west side. Figure 4.7(b) shows a post-test photograph of the inclined failure plane on the west side of the specimen.

38

The post test examination of this and other piles indicated that pile failure was precipitated by failure of the concrete core along an inclined failure plane. Movement of the core along this failure plane caused the spirals to fracture. This is discussed further in Chapter 6.

Figure 4.2 shows the strain in the spiral reinforcement plotted versus the axial shortening. Each channel is plotted to the point in the test where the strain gage failed. Indicated on Figure 4.2 are the displacements Δ_1 and Δ_2 which correspond, respectively, to the first and second peak in the load-shortening response.

Figures 4.3 and 4.4 show the strain in the longitudinal reinforcement and the axial strains computed from the potentiometer measurements, respectively, plotted versus the axial shortening. Indicated on Figure 4.3 are the following: (1) the yield strain in the longitudinal reinforcement, computed as the yield stress divided by 29×10^3 ksi (2×10^5 MPa); (2) the displacement Δ_1 which corresponds to the first peak in the load-shortening response; and (3) the displacement Δ_2 which corresponds to the second peak in the load-shortening response. Figure 4.3 shows that, on average, the longitudinal reinforcement was at its yield stress when Δ_1 was reached.

In many instances the potentiometers were disturbed by cover spalling, however, the point in the test at which this occurred is not clear. Therefore, axial strains from the potentiometer measurements are shown only up to the point of cover loss. Comparison between Figures 4.3 and 4.4 shows that axial strain results collected from the two sources correlates well up to cover loss. Thus, for behavior occurring after the first peak, the longitudinal strain gages are assumed to provide an accurate representation of the axial strain. This is the case for all piles treated in this study.

Finally, a schematic drawing of the failed pile is presented in Figure 4.5. The intersection of the inclined failure plane that formed in the specimen with the perimeter of the core is noted. Locations of fractured and necked spirals are also noted, as are the location of buckled longitudinal reinforcing bars. The spiral wire fractured 30 times in 15 locations (two bundled wires at each location) along the failure plane. The spiral reinforcement also exhibited necking at many locations on the opposite side of the failure plane from the spiral fractures. The locations of buckled longitudinal reinforcement coincide approximately with the intersection of this reinforcement with the inclined failure plane. Relative movement along the inclined failure plane may have caused the reinforcement to buckle. This is further supported by the appearance of the buckled bars in Figure 4.7(b).

39

Figure 4.1   Plot of axial load versus axial shortening for Pile 24-A.

Figure 4.2   Plot of spiral strain versus axial shortening for Pile 24-A.

40

Figure 4.3   Plot of longitudinal strain versus axial shortening for Pile 24-A.

Figure 4.4   Plot of potentiometer axial strain versus axial shortening for Pile 24-A.

41

East North West South East

buckled bar (typ.)

S1

L1

S2

S3

L2

S4

S5

S6 L3

S7

L4

Two bundled wires

S8

Heavily Confined

Test Region

Heavily Confined

- - - - - - - Concrete failure
—×— ×— Spiral fracture
▶····◀— Spiral necking
S# Spiral strain gage
L# Longitudinal strain gage

Figure 4.5   Schematic drawing of post-test appearance of Pile 24-A.

42

(b)

(a)

Figure 4.6   Pile 24-A: (a) northeast face after cover failure; (b) northeast face at end of test.

43

(b)

(a)
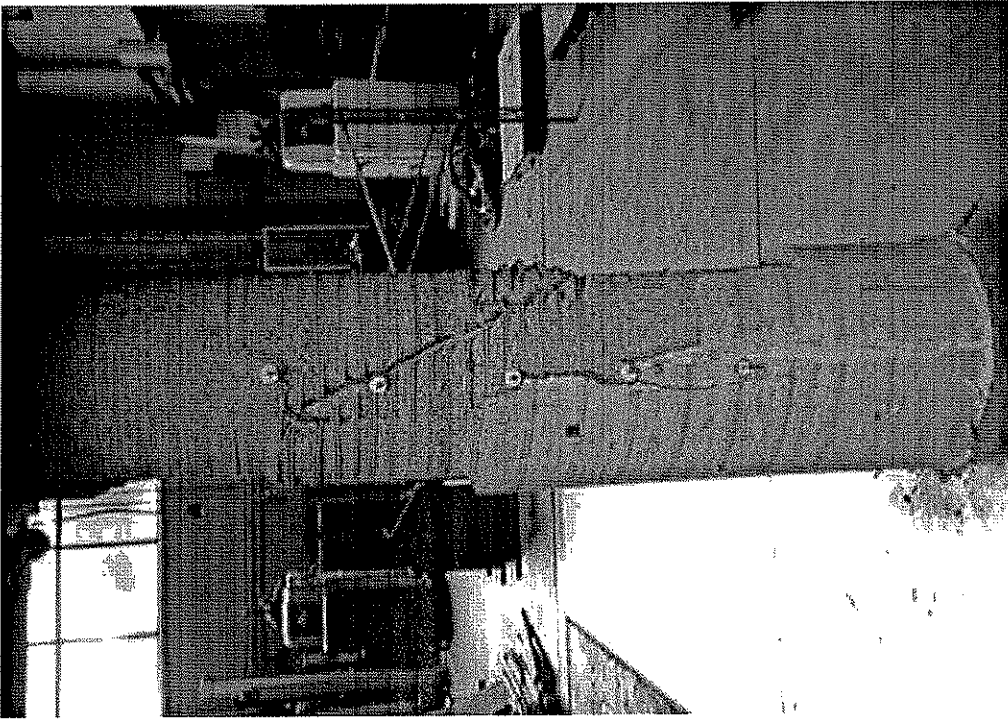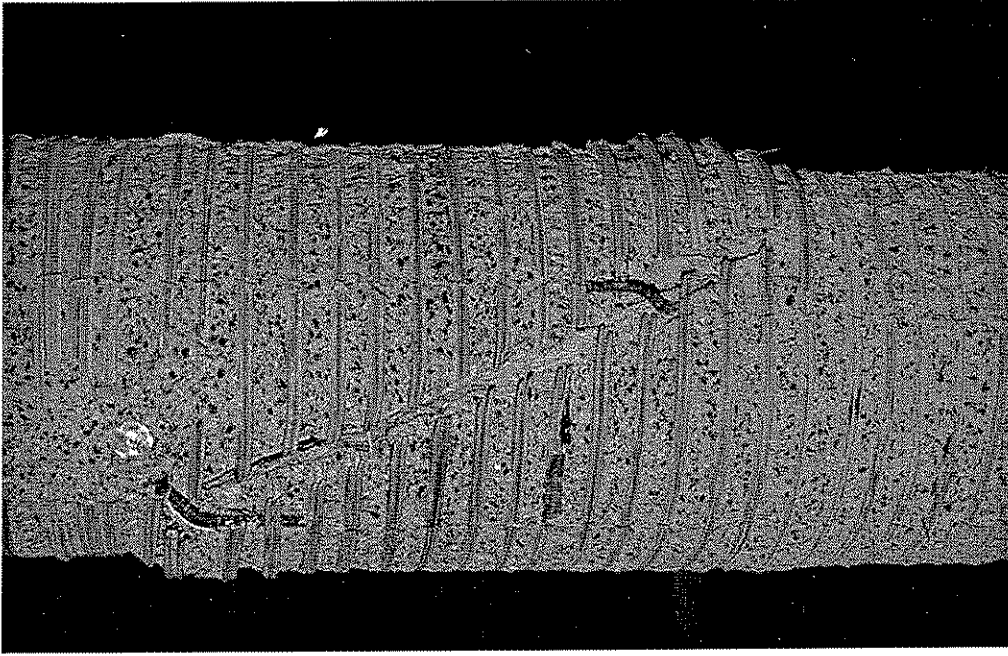
Figure 4.7   Pile 24-A: (a) west face of failed pile; (b) inclined failure plane on west face.

4.3.3 Pile 24-B

Pile 24-B had an unconfined concrete compressive strength of 8.50 ksi (58.6 MPa), a spiral reinforcement design yield strength of 107 ksi (738 MPa), and a longitudinal reinforcement yield strength of 71 ksi (490 MPa). The spiral reinforcement was comprised of two 0.35 in. (8.89 mm) diameter smooth wires bundled together at a pitch of 2.5 in. (63.5 mm). The longitudinal reinforcement consisted of six 0.5 in. (12.7 mm) diameter deformed reinforcing bars spaced evenly around the perimeter of the confined concrete core.

The axial load versus axial shortening response of the pile is presented in Figure 4.8. Similar to Pile 24-A, this specimen exhibited a nearly linear load-shortening response from test initiation until the load reached approximately 2000 kips (8.90 MN). As the load increased beyond this point, the load-shortening plot shows that the specimen began to soften until the first peak load of $P_1 = 3950$ kips (17.57 MN) was reached. The overall axial shortening at this point was $\Delta_1 = 0.292$ in. (7.42 mm), and the corresponding axial strain was 0.0034. At this load, the cover concrete failed in a sudden manner.

Figure 4.13(a) is a photograph of the pile immediately after cover failure. Visible damage to the cover is apparent circumferentially around the specimen in the upper heavily confined region and upper test region. Longitudinal cracks also formed within the test region. No cracks were observed in the cover concrete prior to cover failure. The loss of the cover concrete caused the load to decrease to $P_{spall} = 3173$ kips (14.11 MN).

After the loss of the concrete cover, the pile exhibited considerably less axial stiffness, as evidenced by the shallower slope of the load-shortening plot in Figure 4.8 after P_{spall}. The pile achieved its second peak at a load of $P_2 = 3691$ kips (16.42 MN) and an axial shortening of $\Delta_2 = 0.665$ in. (16.89 mm) (axial strain of approximately 0.0081). After this peak, the pile continued to shorten while the load decreased until pile failure occurred at a load of $P_{failure} = 2547$ kips (11.33 MN) and an axial shortening of $\Delta_{failure} = 0.965$ in. (24.51 mm) (axial strain of approximately 0.0093). At failure, the axial load dropped to 232 kips (1.03 MN).

Figure 4.13(b) is a photograph of the pile immediately after the failure. The spiral fractures occurred along an inclined failure plane which developed during the failure. This inclined plane formed at an angle of approximately 68 degrees from the horizontal and extended from the top of the test region on the southeast side of the pile to 20 in. (508 mm) from the bottom of the test region on the northwest side. Figure 4.14(a) shows a post-test photograph of the entire failed specimen from the north side. Figure 4.14(b) shows a post-test photograph of the inclined failure plane on the north side of the specimen.

Figure 4.9 shows the strain in the spiral reinforcement plotted versus the axial shortening. Just as for Pile 24-A, each channel is plotted to the point in the test where the strain gage failed. Δ_1 and Δ_2 are also indicated on this figure.

45

Figures 4.10 and 4.11 show the strain in the longitudinal reinforcement and the axial strains computed from the potentiometer measurements, respectively, plotted versus the axial shortening. Indicated on Figure 4.10 are the same key points in the axial shortening and longitudinal strain response as were indicated for Pile 24-A. Figure 4.10 shows that the longitudinal reinforcement was above or near its yield stress when Δ_1 was reached. Once again, the spalling of the concrete cover disturbed the potentiometers. For behavior occurring after the first peak, the longitudinal strain gages are assumed to provide an accurate representation of the axial strain.

Finally, a schematic drawing of the failed pile is presented in Figure 4.12. The intersection of the inclined failure plane that formed in the specimen with the perimeter of the core is noted, as are the locations of fractured spirals, necked spirals, and buckled longitudinal reinforcing bars. The spiral wire fractured 16 times in 8 locations along the failure plane. The spiral reinforcement also exhibited necking at many locations on the opposite side of the failure plane from the spiral fractures. The locations of buckled longitudinal reinforcement coincide approximately with the intersections of this reinforcement with the inclined failure plane. As was the case for Pile 24-A, it appears as though relative movement along the failure plane may have caused the longitudinal bars to buckle.
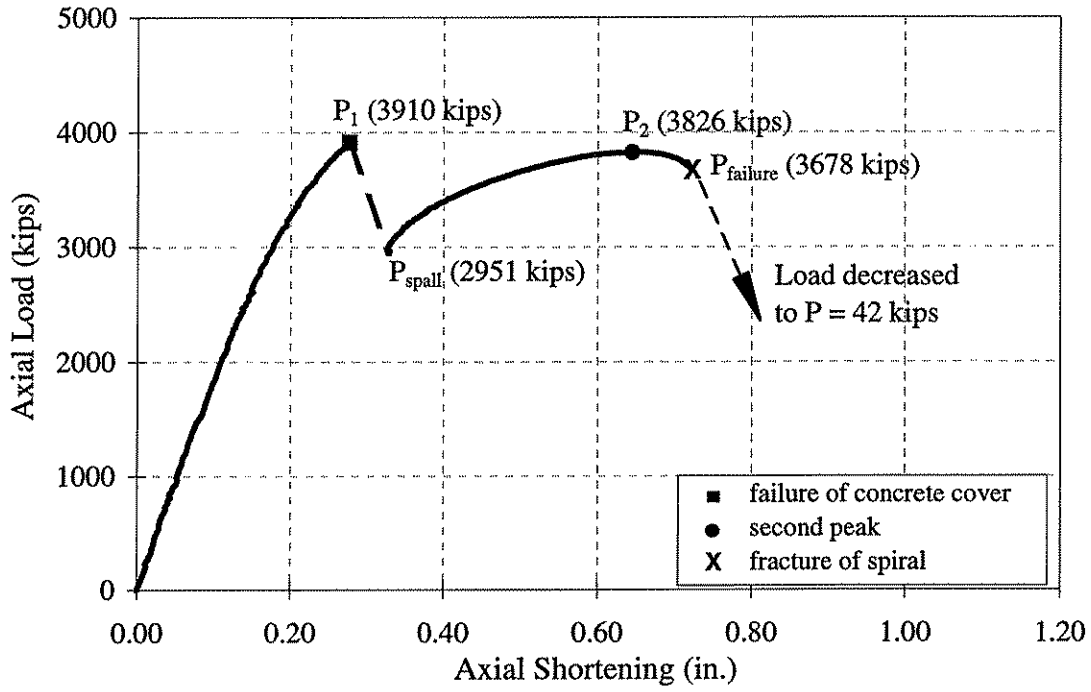
Figure 4.8   Plot of axial load versus axial shortening for Pile 24-B.
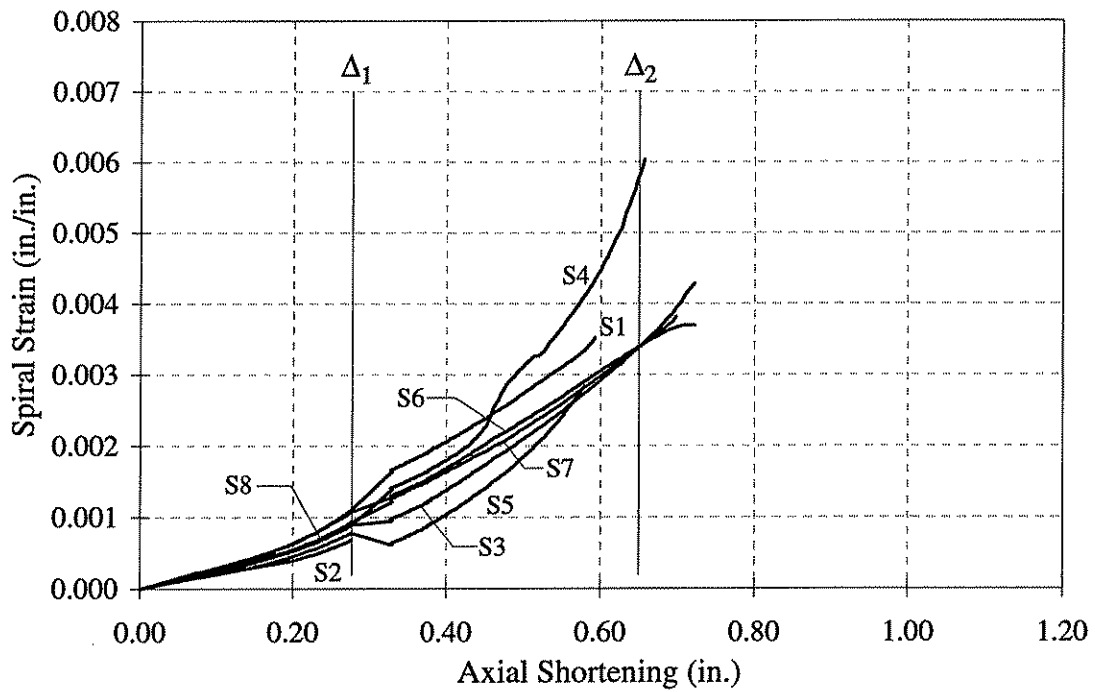

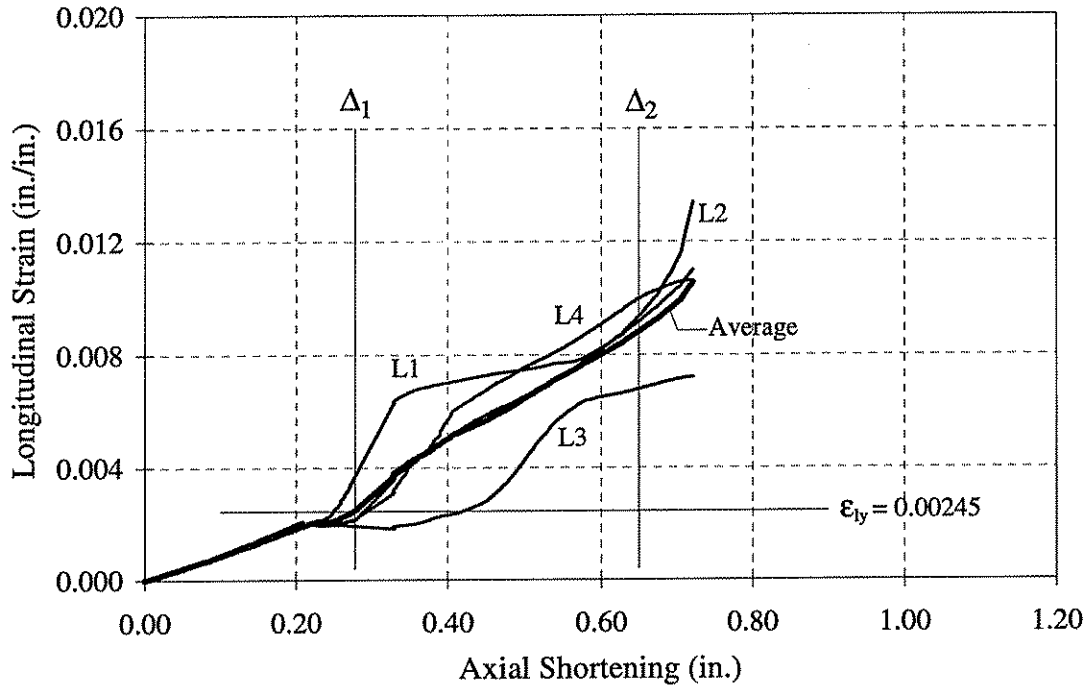Figure 4.9   Plot of spiral strain versus axial shortening for Pile 24-B.

47
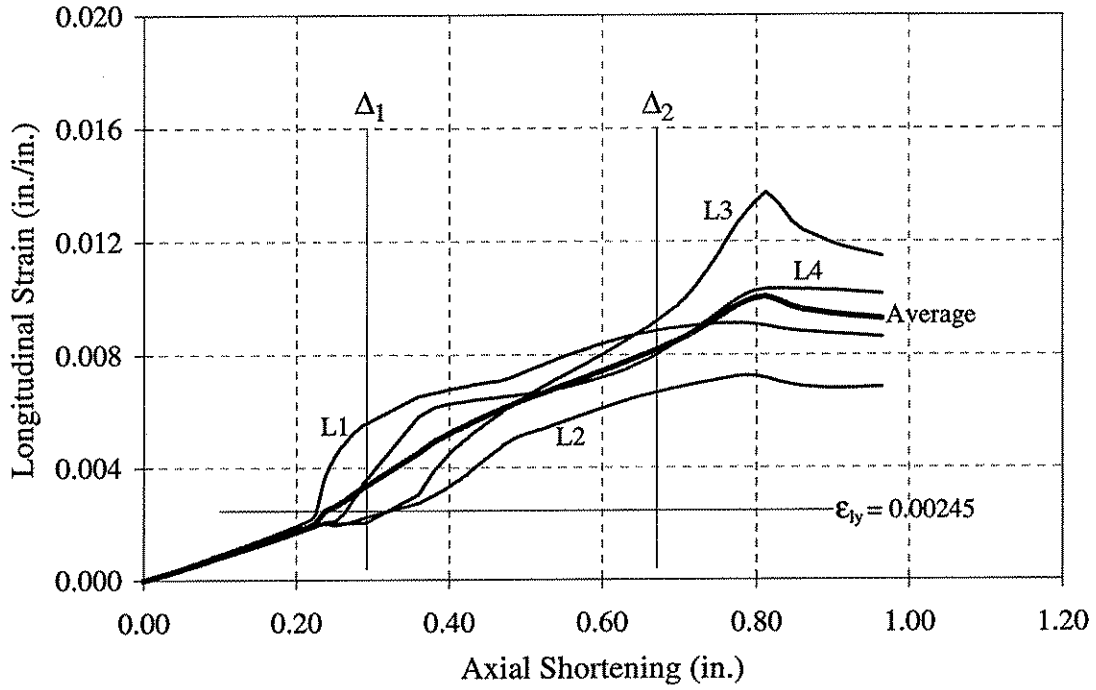
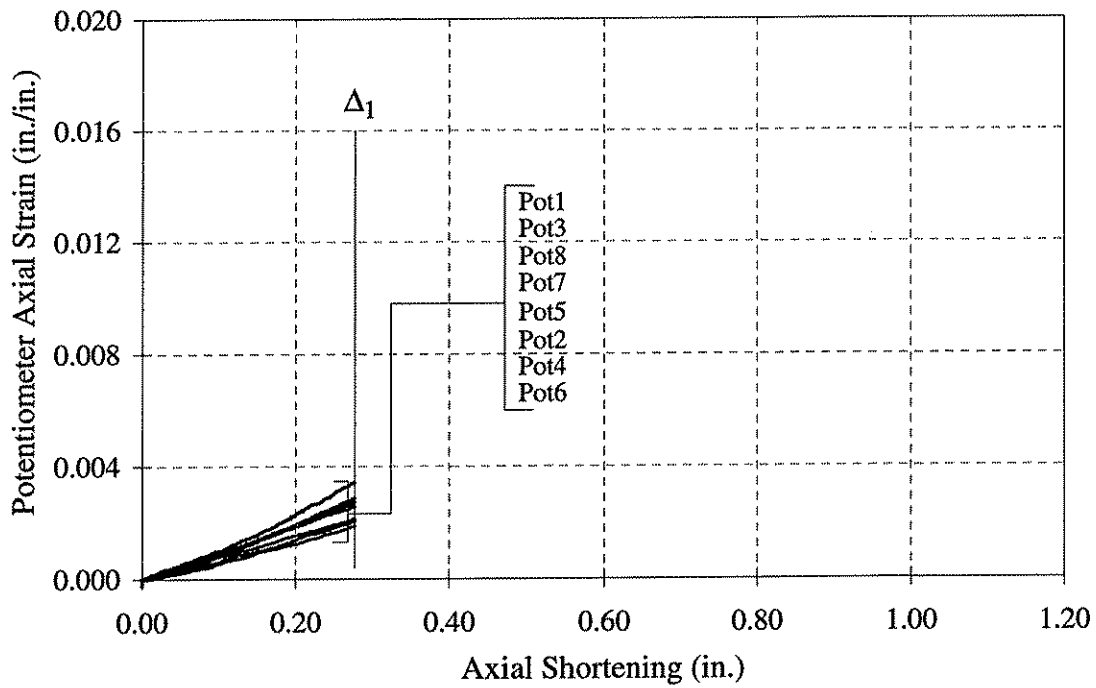Figure 4.10   Plot of longitudinal strain versus axial shortening for Pile 24-B.

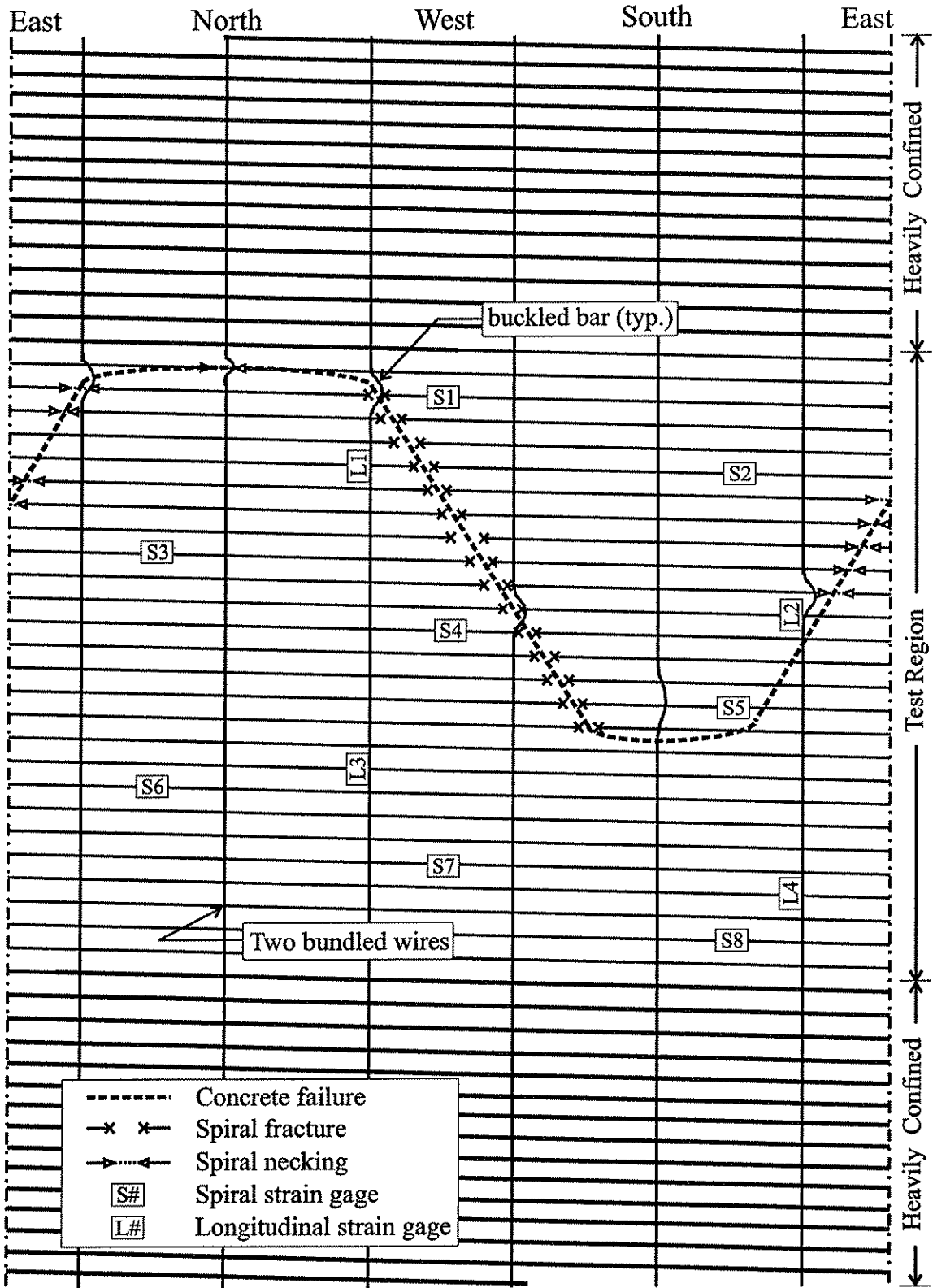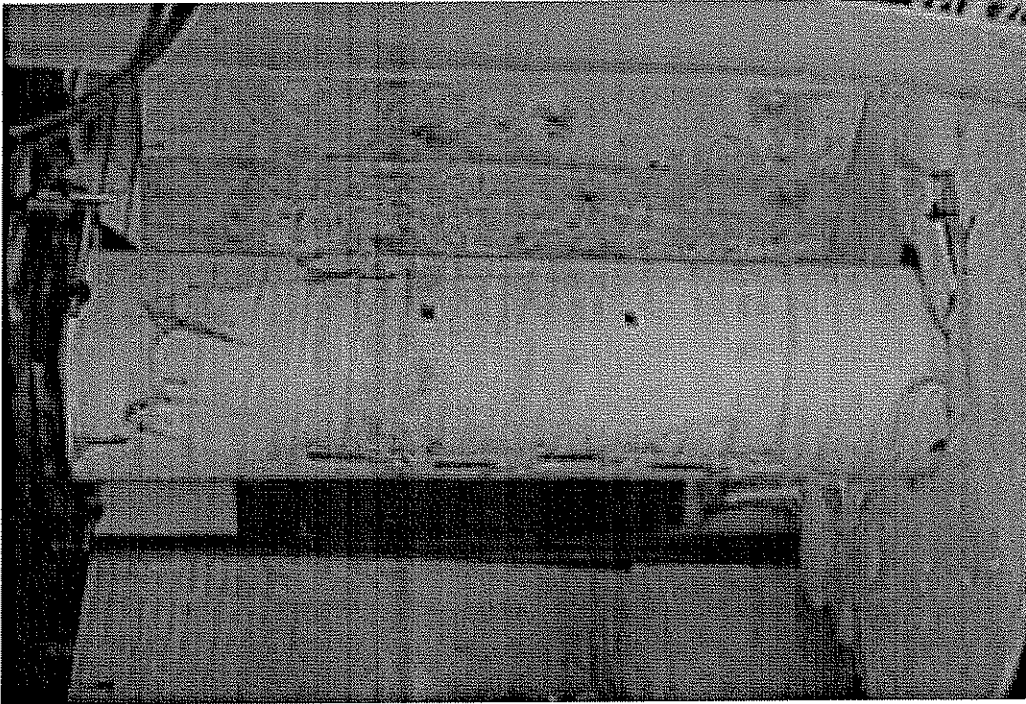Figure 4.11   Plot of potentiometer axial strain versus axial shortening for Pile 24-B.
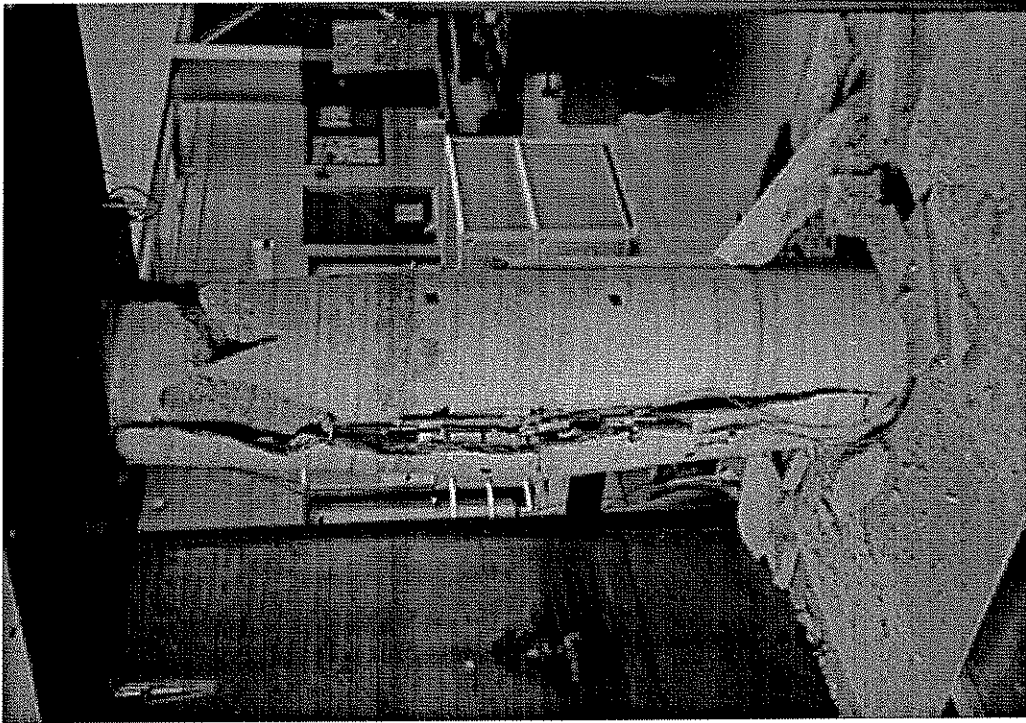
48
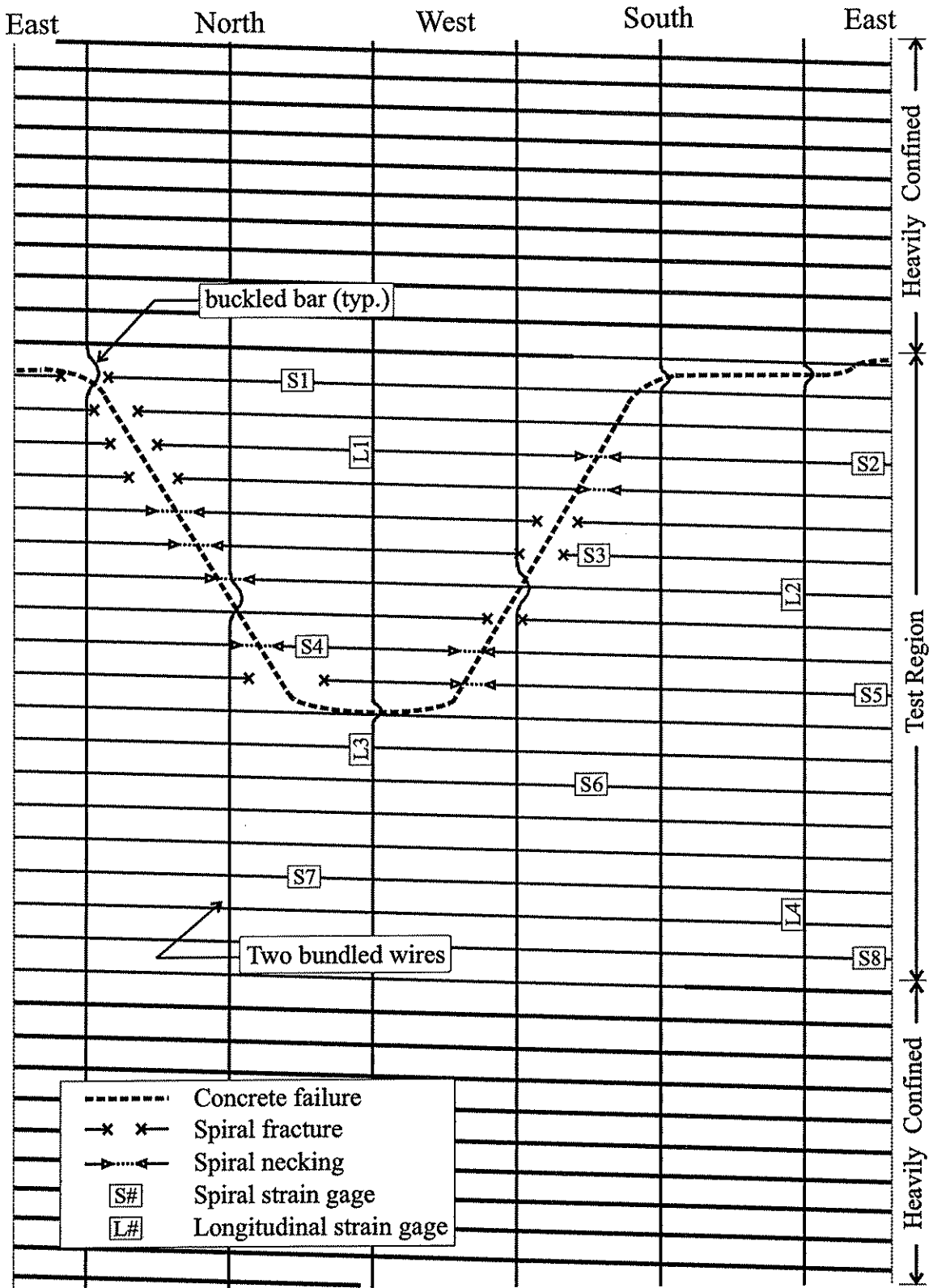
Figure 4.12   Schematic drawing of post-test appearance of Pile 24-B.

49

(b)

(a)
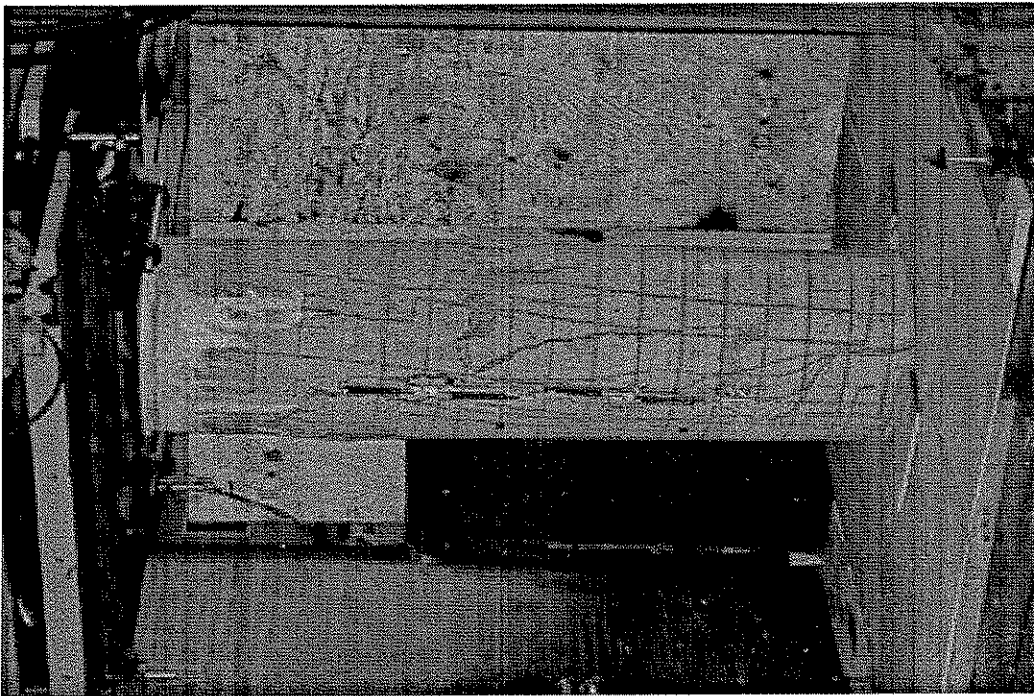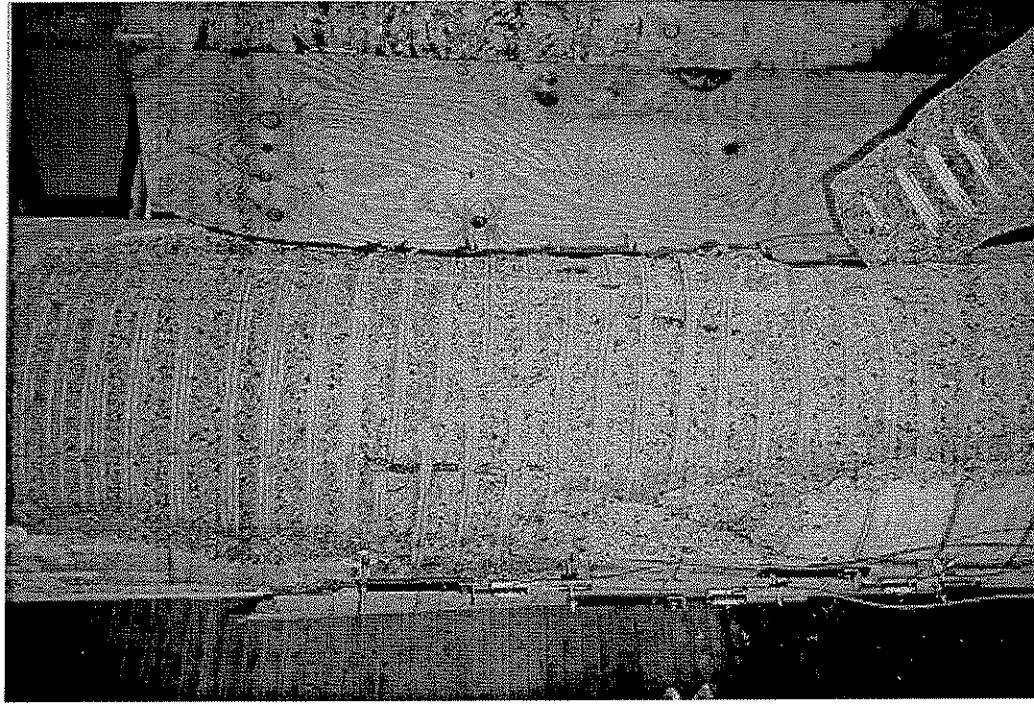
Figure 4.13   Pile 24-B: (a) northeast face after cover failure; (b) north face at end of test.

50

(b)

(a)
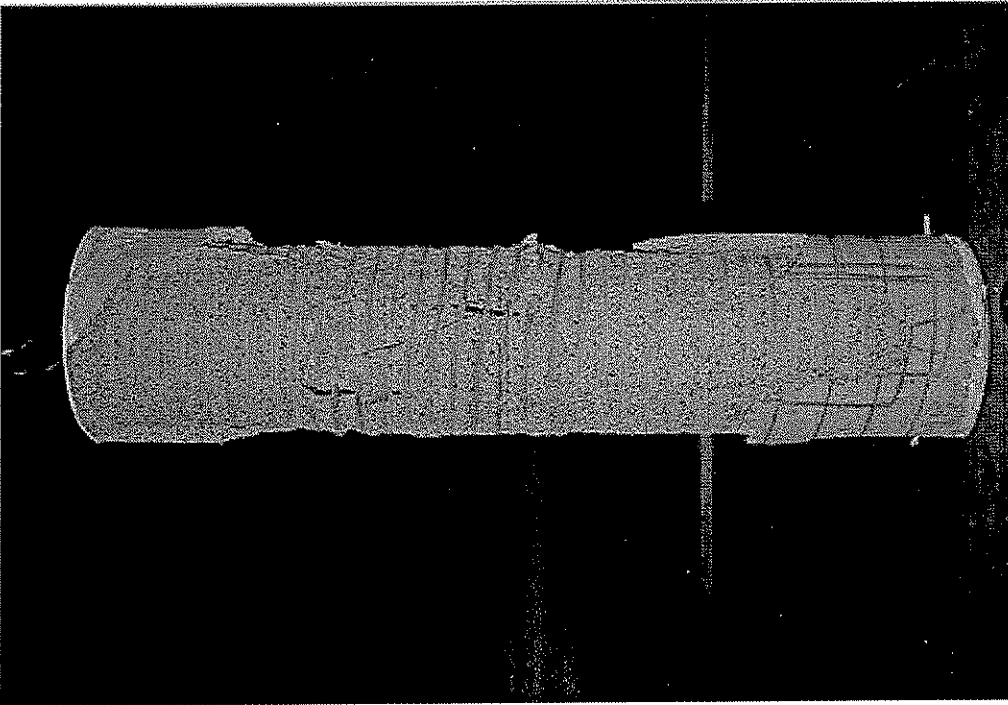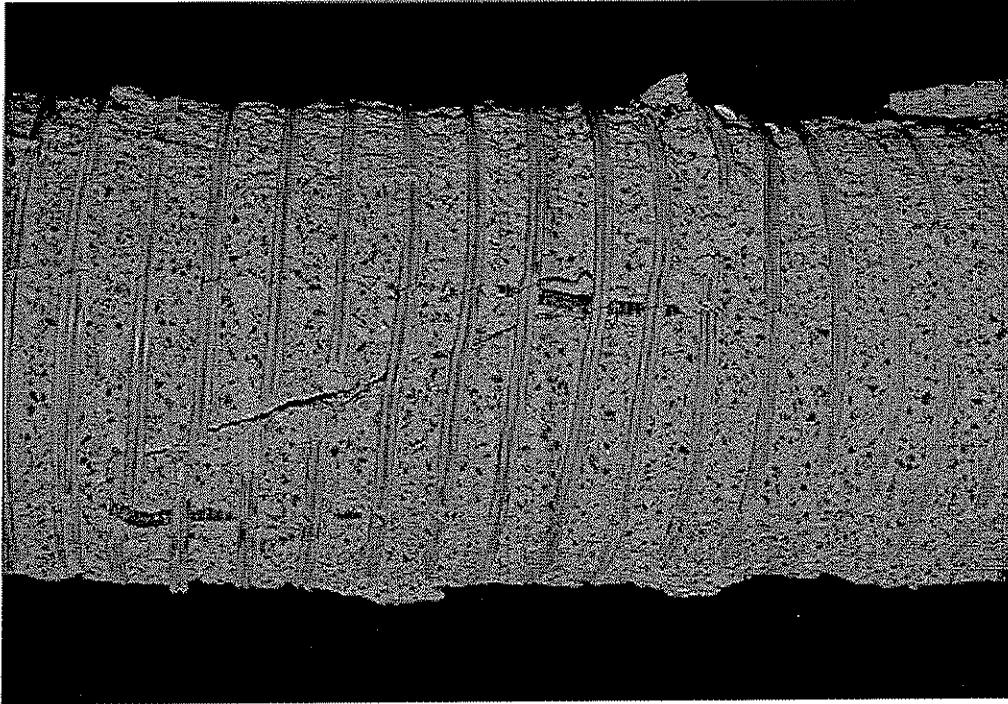
Figure 4.14   Pile 24-B: (a) north face of failed pile; (b) inclined failure plane on north face.

4.3.4 Pile 24-C

Pile 24-C had an unconfined concrete compressive strength of 8.50 ksi (58.6 MPa), a spiral reinforcement design yield strength of 121 ksi (834 MPa), and a longitudinal reinforcement yield strength of 71 ksi (490 MPa). The spiral reinforcement was comprised of one 0.35 in. (8.89 mm) diameter smooth wire at a pitch of 1.5 in. (38.1 mm). The longitudinal reinforcement consisted of six 0.5 in. (12.7 mm) diameter deformed reinforcing bars.

The axial load versus axial shortening response of the pile is presented in Figure 4.15. The figure shows that the specimen exhibited a nearly linear load-shortening response from test initiation until the load reached approximately 2000 kips (8.90 MN). As the load increased beyond this point, the load-shortening plot shows that the specimen began to soften until the first peak load of $P_1 = 3926$ kips (17.46 MN) was reached. The overall axial shortening at this point was $\Delta_1 = 0.299$ in. (7.59 mm), and the corresponding axial strain was 0.0030. At this load, the cover concrete failed in a sudden manner.

Figure 4.20(a) is a photograph of the pile immediately after cover failure. Visible damage to the cover is apparent longitudinally from the top of the pile down to the bottom of the test region. Some circumferential cracks also formed around the specimen in the upper heavily confined region and upper test region. No cracks were observed in the cover concrete prior to cover failure. The loss of the cover concrete caused the load to decrease to $P_{spall} = 3202$ kips (14.24 MN).

The pile exhibited considerably less axial stiffness after the loss of the concrete cover, as can be seen in Figure 4.15 after P_{spall}. The pile achieved its second peak at a load of $P_2 = 3579$ kips (15.92 MN) and an axial shortening of $\Delta_2 = 0.594$ in. (15.09 mm) (axial strain of approximately 0.0076). After this peak, the pile continued to shorten while the load decreased slightly until pile failure occurred at a load of $P_{failure} = 3551$ kips (15.79 MN) and an axial shortening of $\Delta_{failure} = 0.625$ in. (15.88 mm) (axial strain of approximately 0.0079). At failure, the axial load dropped to 94 kips (0.42 MN).

Figure 4.20(b) is a photograph of the pile immediately after failure. The spiral fractures occurred along an inclined failure plane which developed during the failure. This inclined plane formed at an angle of approximately 64 degrees from the horizontal and extended from the top of the test region on the southwest side of the pile to 7 in. (178 mm) from the bottom of the test region on the north side. Figure 4.21(a) shows a post-test photograph of the entire failed specimen from the southeast side. Figure 4.21(b) shows a post-test photograph of the inclined failure plane on the southeast side of the specimen.

Figure 4.16 shows the strain in the spiral reinforcement plotted versus the axial shortening. Figures 4.17 and 4.18 show the strain in the longitudinal reinforcement and the axial strains computed from the potentiometer measurements, respectively, plotted versus the axial shortening. The key values noted on these plots are the same as were described in the previous test summaries. Note that the longitudinal reinforcement was above or near its yield stress when Δ_1 was reached. Once again, the potentiometers were disturbed by cover spalling, thus for axial strain behavior occurring

after the first peak, the longitudinal strain gages are assumed to provide an accurate representation of the axial strain.

Finally, a schematic diagram of the failed pile is presented in Figure 4.19. The intersection of the inclined failure plane with the perimeter of the core is noted, as are the locations of necked and fractured reinforcement. In this pile, the spiral wire fractured 23 times along the failure plane. The spiral reinforcement also exhibited necking at many locations on the opposite side of the failure plane from the spiral fractures. The locations of buckled longitudinal reinforcement coincide approximately with the intersections of this reinforcement and the inclined failure plane, again suggesting that relative movement along this plane caused the bars to buckle.
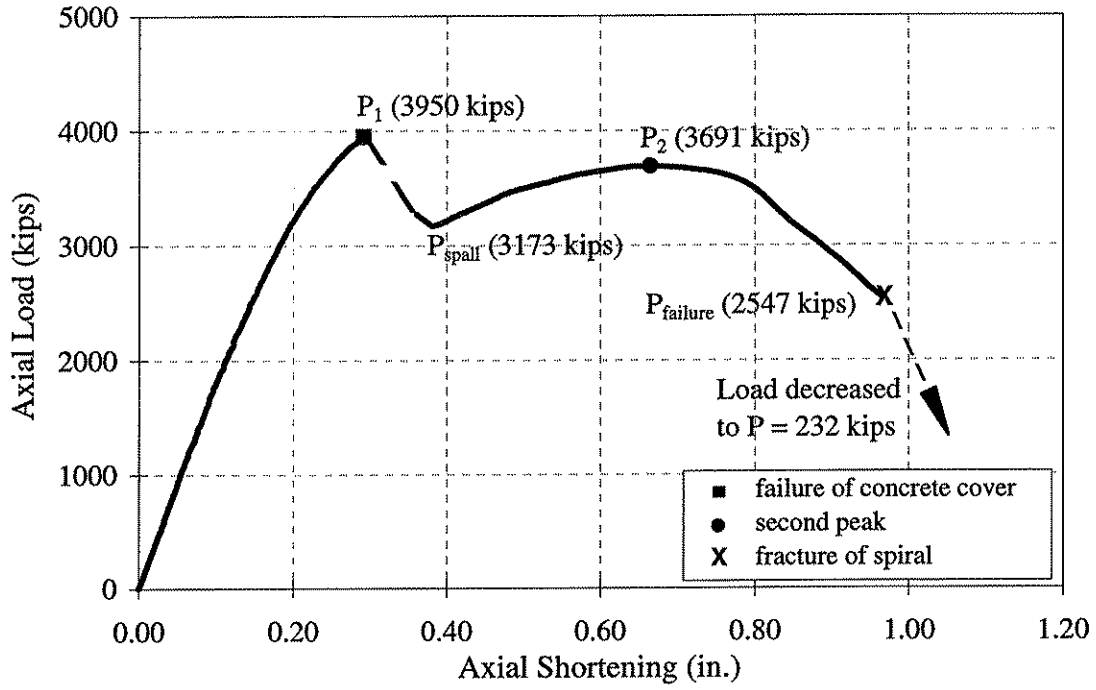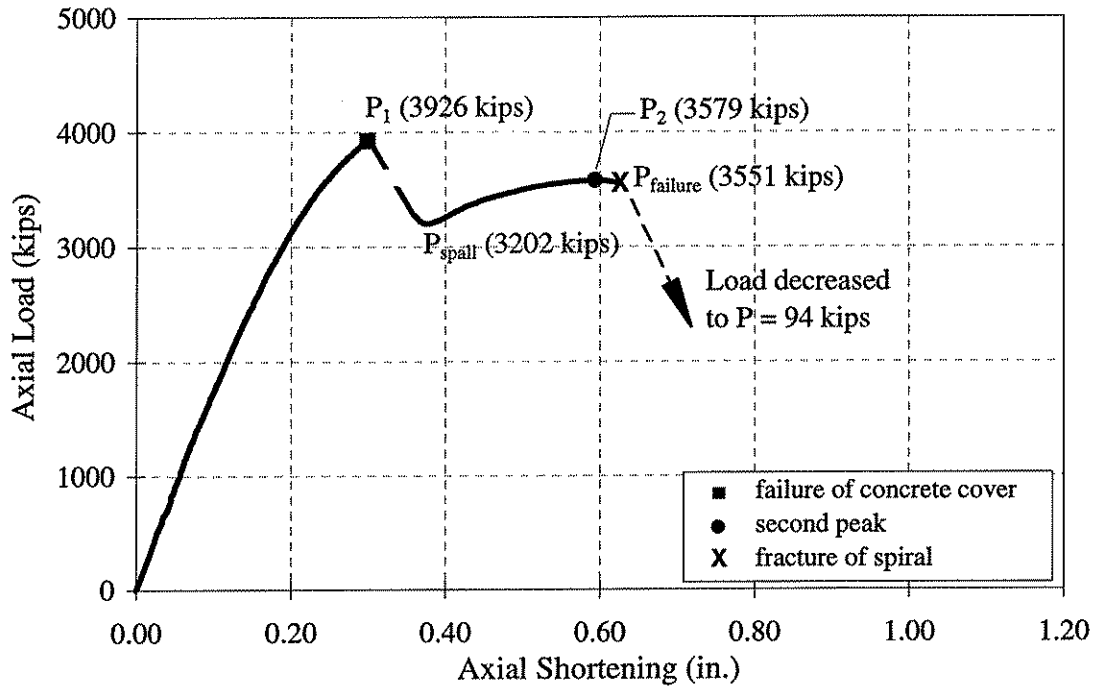
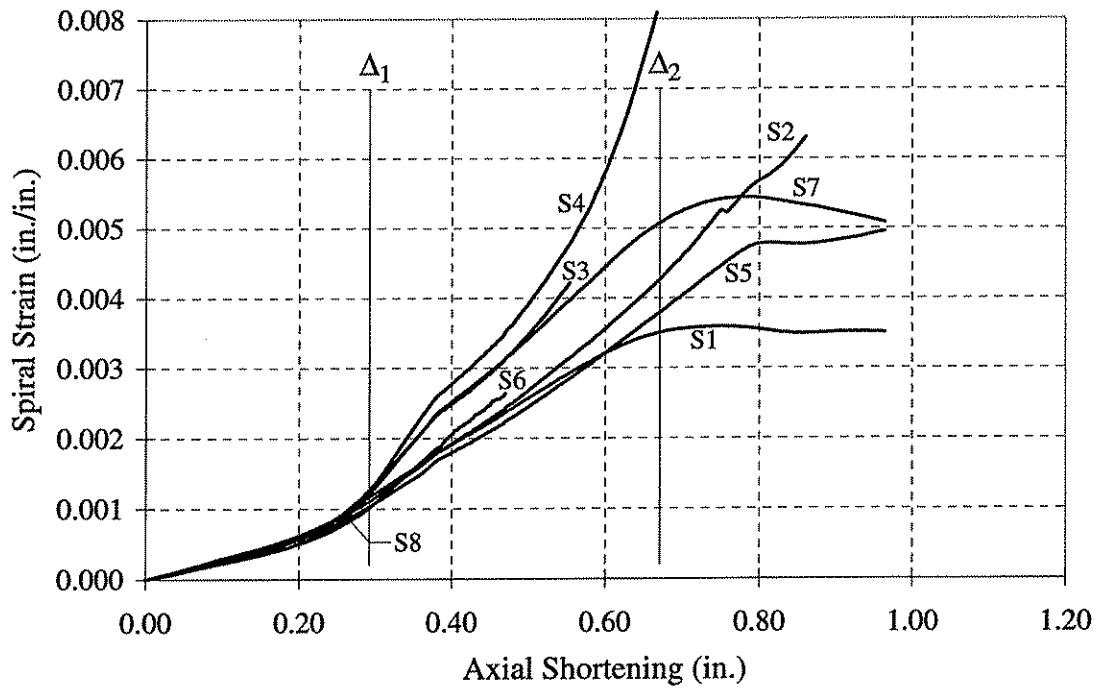Figure 4.15   Plot of axial load versus axial shortening for Pile 24-C.
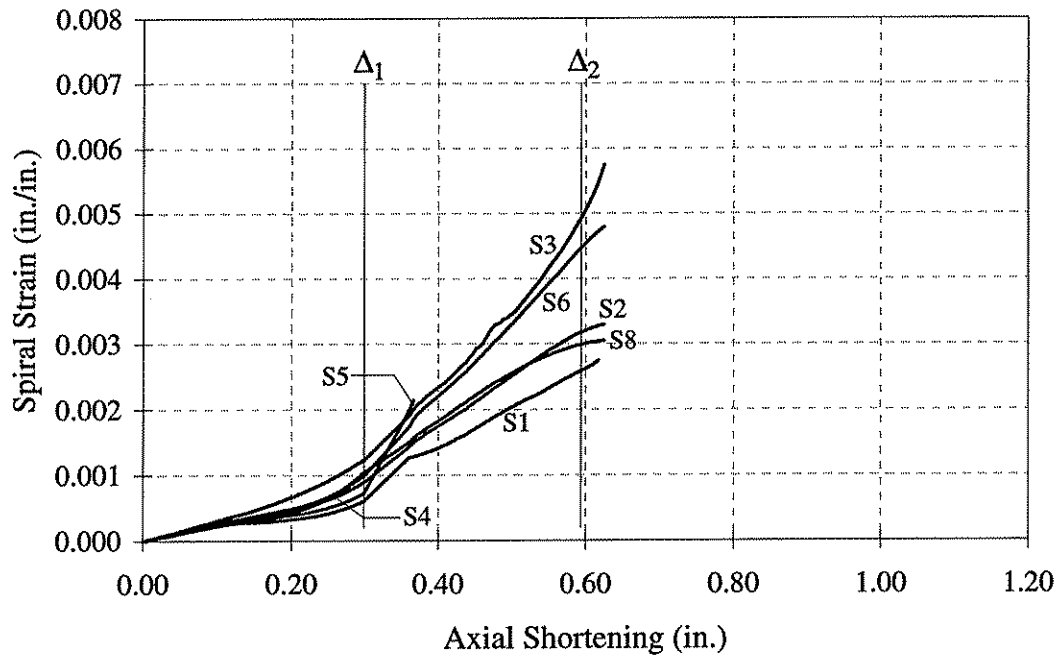
Figure 4.16   Plot of spiral strain versus axial shortening for Pile 24-C.

54
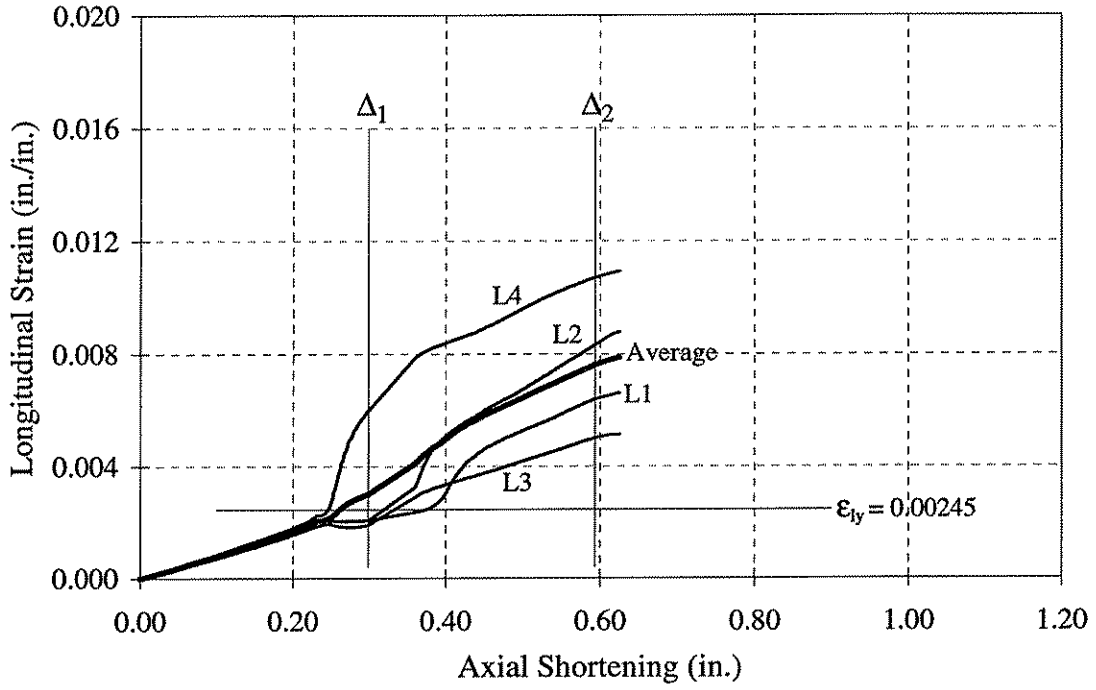
Figure 4.18   Plot of longitudinal strain versus axial shortening for Pile 24-C.
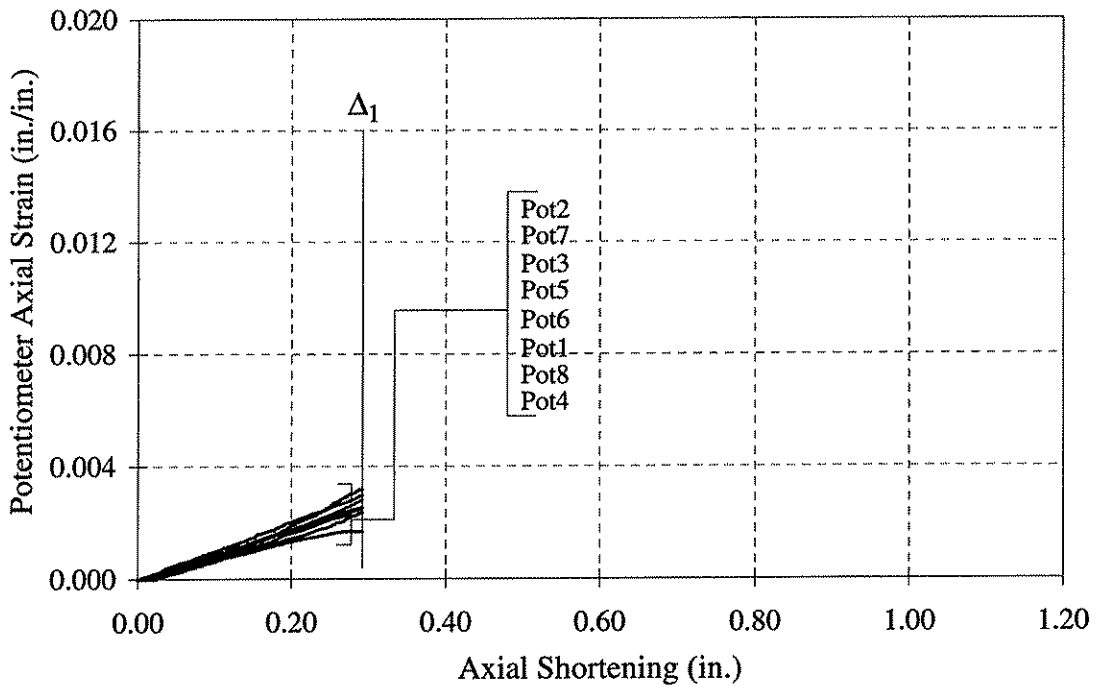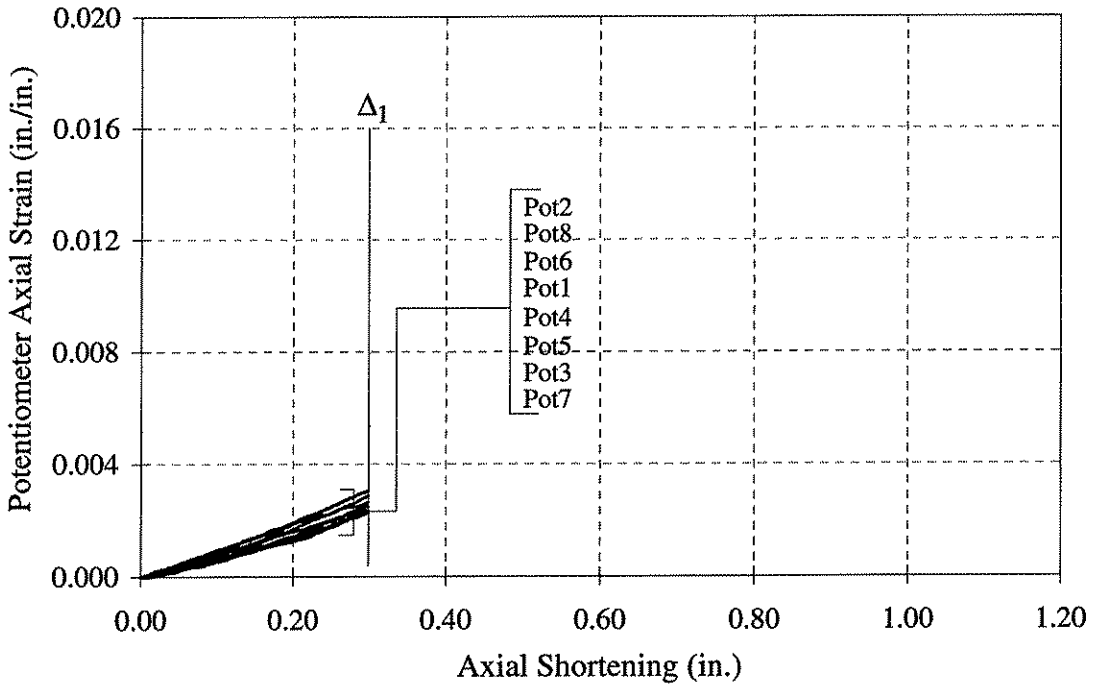

Figure 4.19   Plot of potentiometer axial strain versus axial shortening for Pile 24-C.
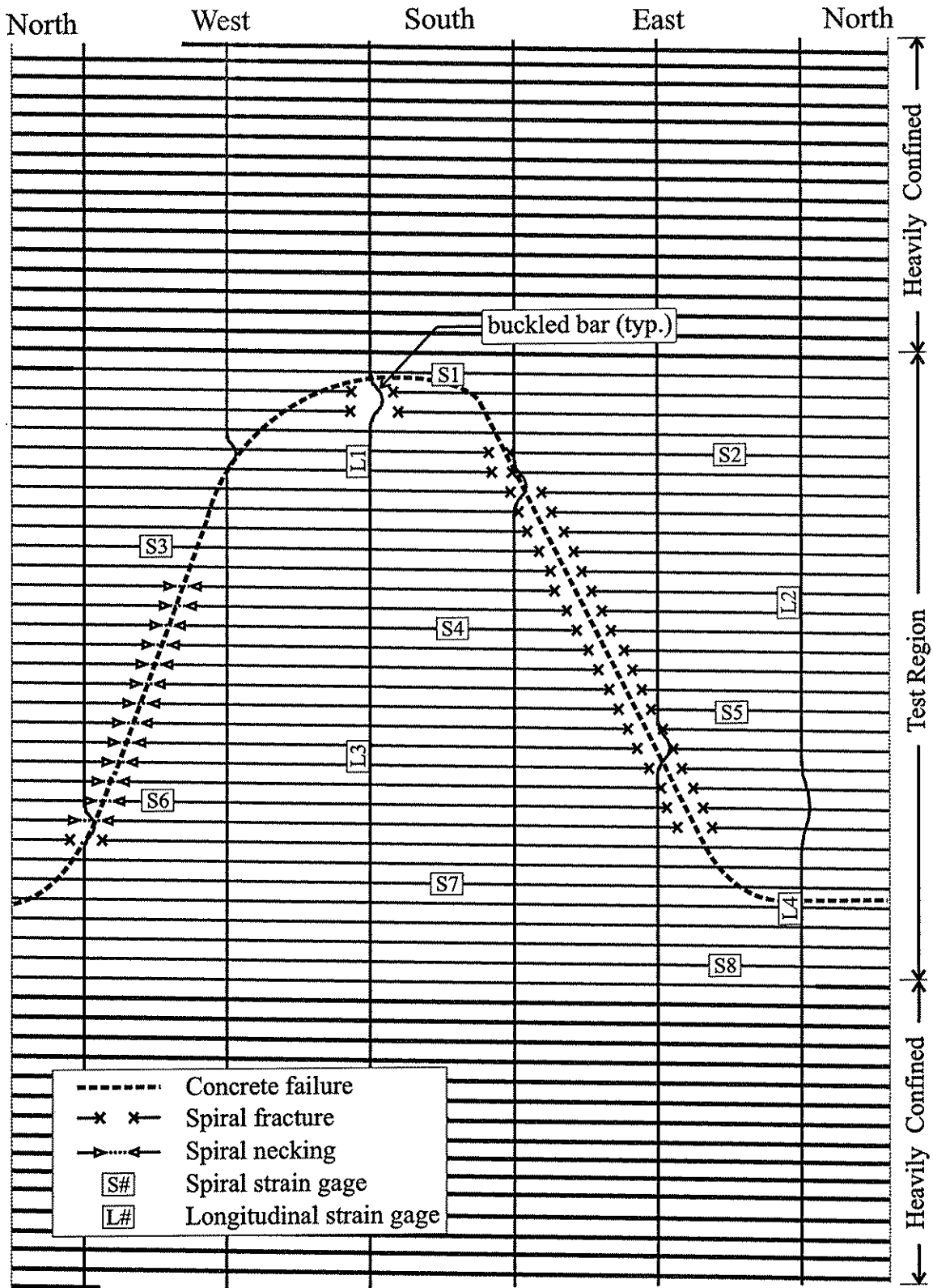
Figure 4.19   Schematic drawing of post-test appearance of Pile 24-C.
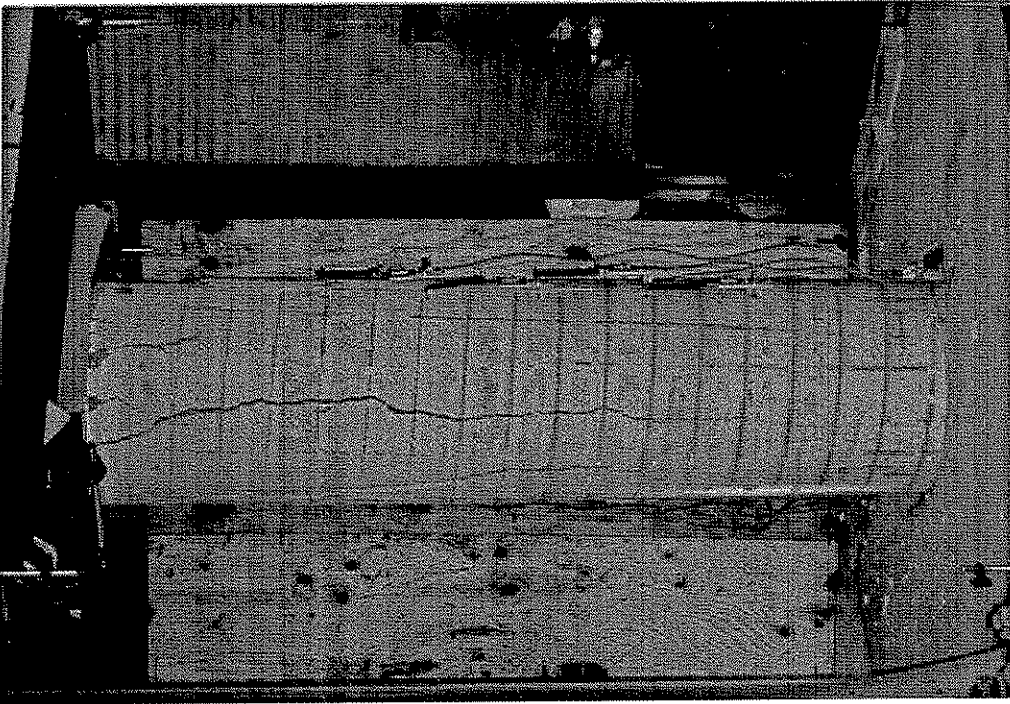
(a)
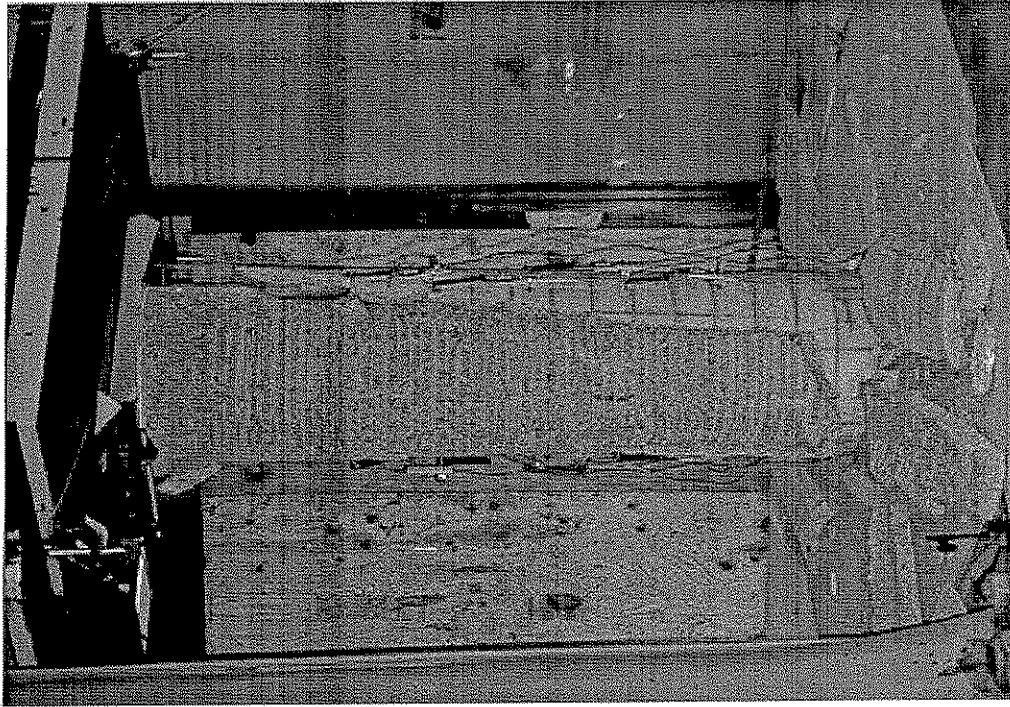
(b)

Figure 4.20   Pile 24-C: (a) northwest face after cover failure; (b) northwest face at end of test.

(b)

(a)
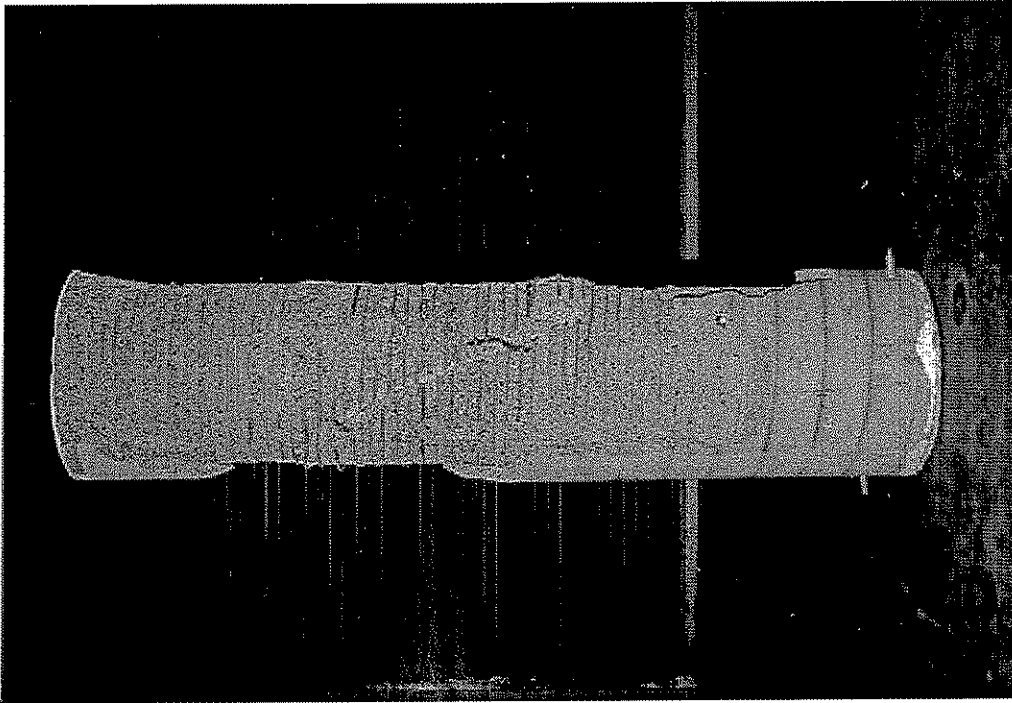
Figure 4.21   Pile 24-C: (a) southeast face of failed pile; (b) inclined failure plane on southeast face.

4.3.5 Pile 24-D

Pile 24-D had an unconfined concrete compressive strength of 8.50 ksi (58.6 MPa), a spiral reinforcement design yield strength of 140 ksi (965 MPa), and a longitudinal reinforcement yield strength of 71 ksi (490 MPa). The spiral reinforcement was comprised of one 0.35 in. (8.89 mm) diameter smooth wire at a pitch of 1.75 in. (44.5 mm). The longitudinal reinforcement consisted of six 0.5 in. (12.7 mm) diameter deformed reinforcing bars.

The axial load versus axial shortening response of the pile is presented in Figure 4.22. The figure shows that the specimen exhibited a nearly linear load-shortening response from test initiation until the load reached approximately 2000 kips (8.90 MN). As the load increased beyond this point, the load-shortening plot shows that the specimen began to soften until the first peak load of $P_1 = 3985$ kips (17.73 MN) was reached. The overall axial shortening at this point was $\Delta_1 = 0.312$ in. (7.92 mm), and the corresponding axial strain was 0.0048. At this load, the cover concrete failed in a sudden manner.

Figure 4.27(a) is a photograph of the pile immediately after cover failure. Visible damage to the cover is apparent circumferentially around the top north and around the bottom south side of the test region. Longitudinal cracks also formed, starting from the circumferential splitting and running toward the center of the test region. No cracks were observed in the cover concrete prior to cover failure. The loss of the cover concrete caused the load to decrease to $P_{spall} = 3092$ kips (13.75 MN).

After the loss of the concrete cover, the pile exhibited considerably less axial stiffness, as can be seen in Figure 4.22 after P_{spall}. The pile achieved its second peak at a load of $P_2 = 3337$ kips (14.84 MN) and an axial shortening of $\Delta_2 = 0.567$ in. (14.40 mm) (axial strain of approximately 0.0093). After this peak, the pile continued to shorten while the load decreased significantly until one spiral fracture occurred at a load of $P_{failure} = 2128$ kips (9.47 MN) and an axial shortening of $\Delta_{failure} = 0.973$ in. (24.71 mm). The average longitudinal strain recorded at this point is not reported due to failure of some longitudinal strain gages. This spiral fracture resulted in a load decrease of just over 100 kips (0.44 MN). Shortly thereafter, at a slightly increased axial shortening, a series of spiral fractures occurred. At this failure, the axial load dropped to 618 kips (2.75 MN).

Figure 4.27(b) is a photograph of the pile immediately after failure. The spiral fractures occurred along an inclined failure plane which developed during the failure. This inclined plane formed at an angle of approximately 68 degrees from the horizontal and extended from the top of the test region on the south side of the pile to the bottom of the test region on the north side. Figure 4.28(a) shows a post-test photograph of the entire failed specimen from the east side. Figure 4.28(b) shows a post-test photograph of the inclined failure plane on the east side of the specimen.

Figure 4.23 shows the strain in the spiral reinforcement plotted versus the axial shortening. Figures 4.24 and 4.25 show the strain in the longitudinal reinforcement and the axial strains computed from the potentiometer measurements, respectively, plotted versus the axial shortening. The key

values noted on these plots are the same as was described in previous test summaries. Note that the longitudinal reinforcement was above or near its yield stress when Δ_1 was reached. Once again, for behavior occurring after the first peak, the longitudinal strain gages are assumed to provide an accurate representation of the axial strain.

Finally, a schematic diagram of the failed pile is presented in Figure 4.26. The intersection of the inclined failure plane with the perimeter of the core is noted as are the locations of necked and fractured reinforcement. In this pile, the spiral wire fractured at 19 locations along the failure plane. The spiral reinforcement also necked at many locations on the opposite side of the failure plane from the spiral fractures. The locations of buckled longitudinal reinforcement coincide approximately with the intersection of this reinforcement and the inclined failure plane. Again, it appears as though relative movement along the inclined failure plane may have caused these bars to buckle.

Figure 4.22   Plot of axial load versus axial shortening for Pile 24-D.

Figure 4.23   Plot of spiral strain versus axial shortening for Pile 24-D.

Figure 4.24   Plot of longitudinal strain versus axial shortening for Pile 24-D.

Figure 4.25   Plot of potentiometer axial strain versus axial shortening for Pile 24-D.

62
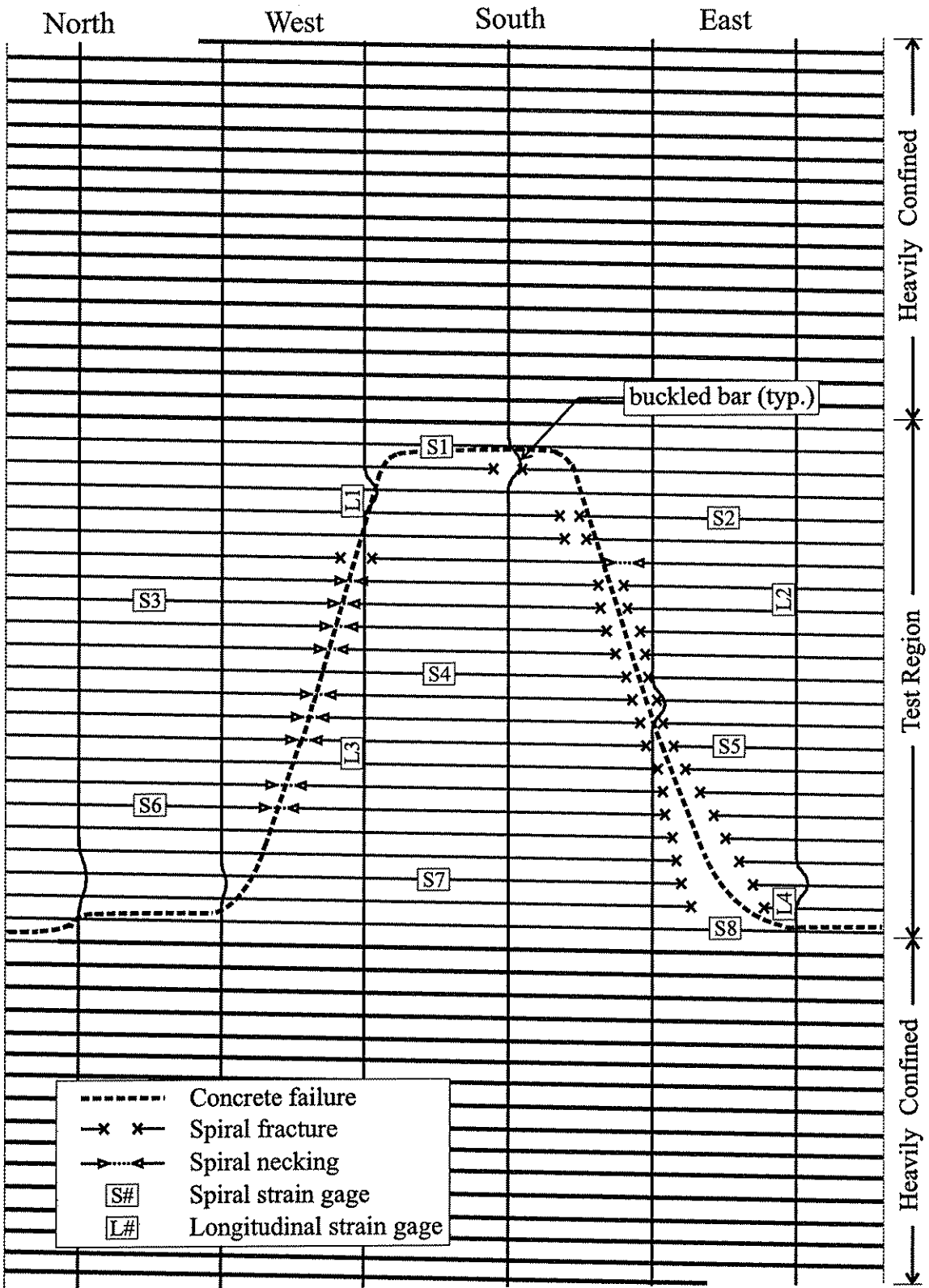
Figure 4.26   Schematic drawing of post-test appearance of Pile 24-D.
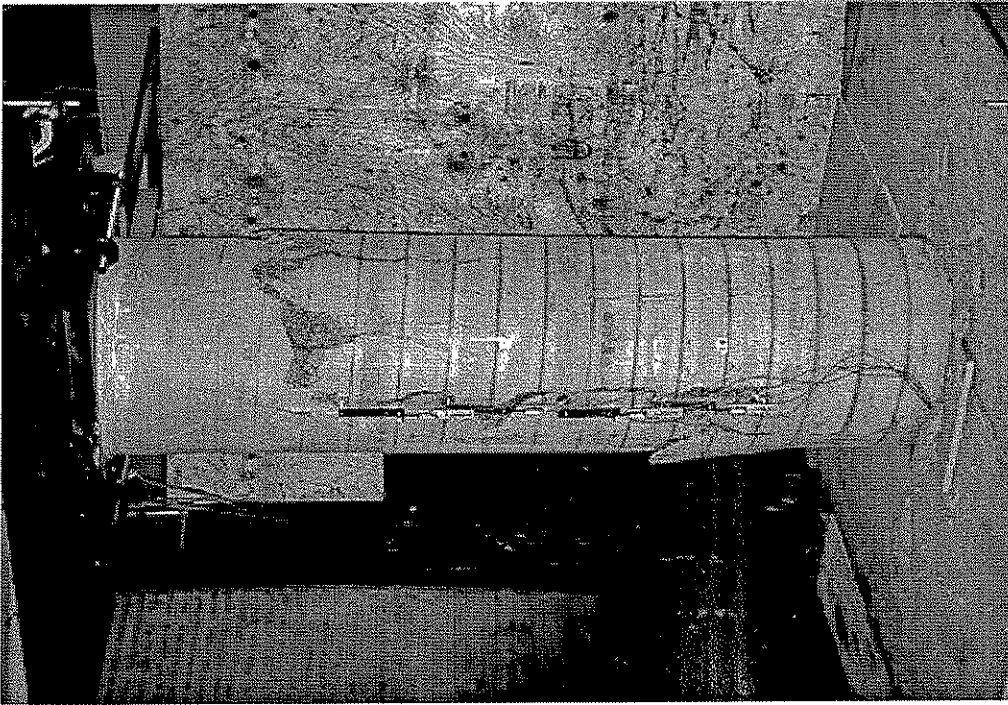
(a)
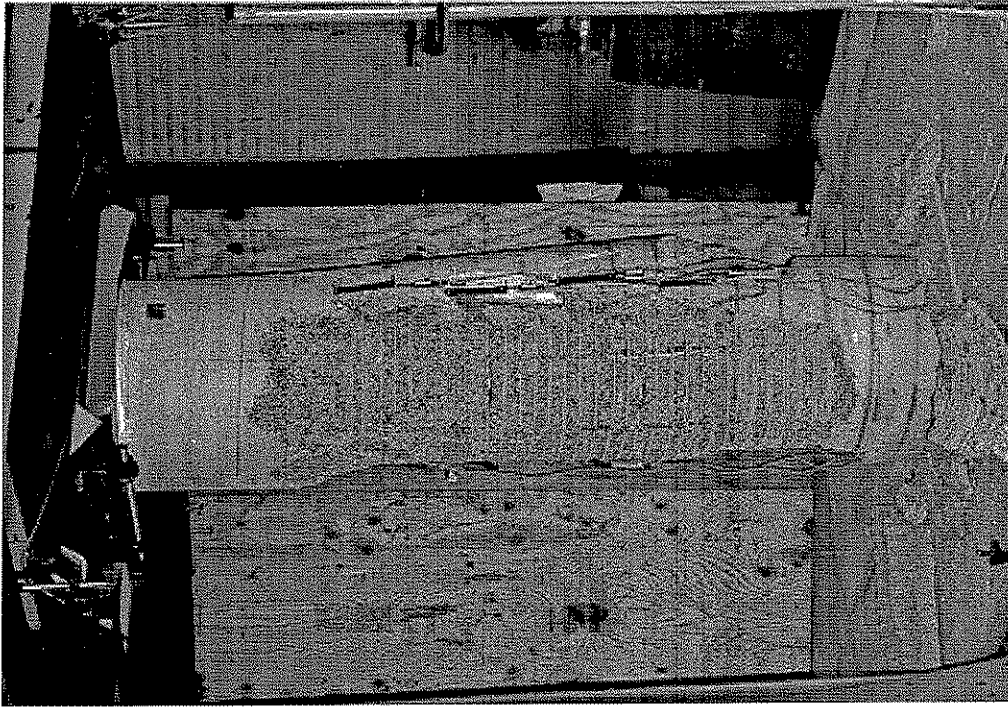
(b)

Figure 4.27   Pile 24-D: (a) northeast face after cover failure; (b) northwest face at end of test.
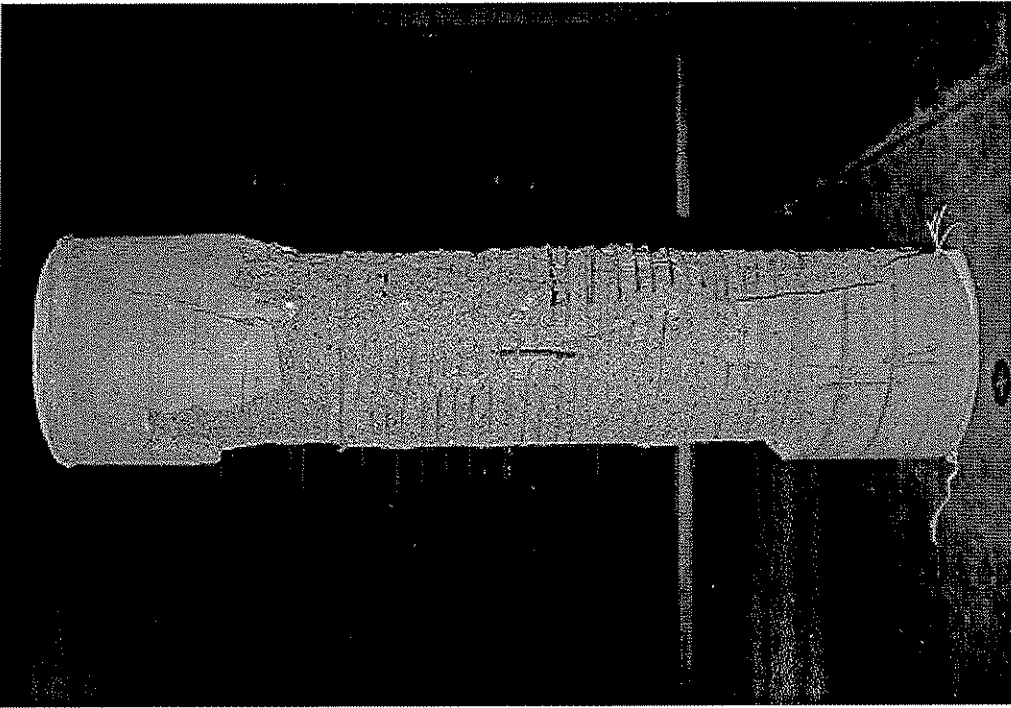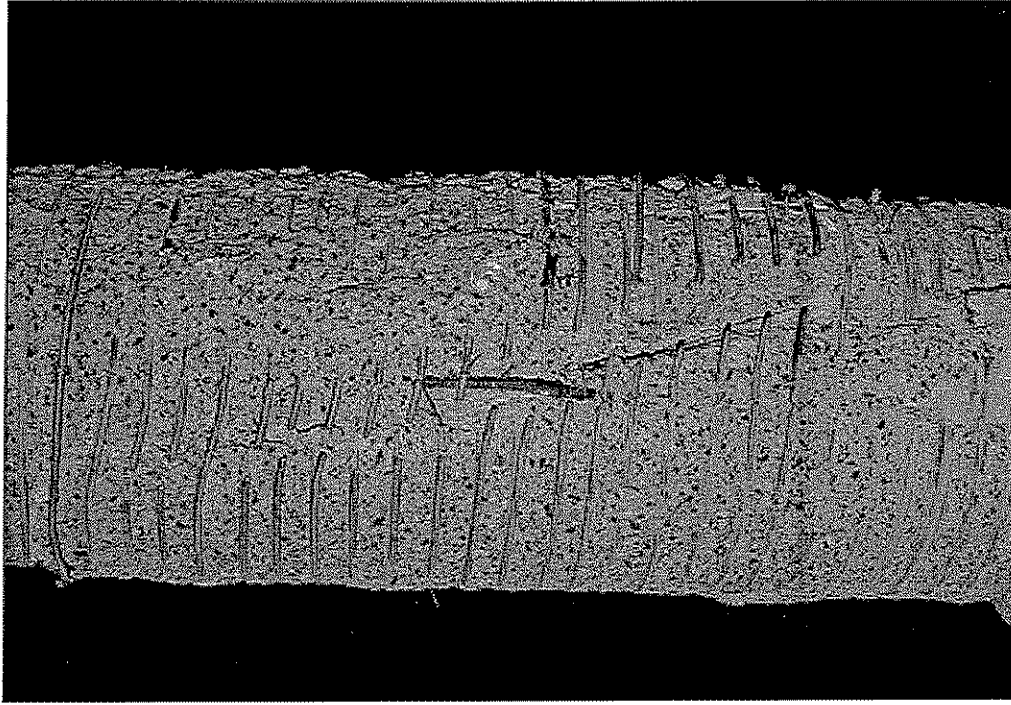
Figure 4.28   Pile 24-D: (a) east face of failed pile; (b) inclined failure plane on east face.

4.4   14 INCH DIAMETER PILE SPECIMENS

4.4.1   General Loading Procedure

The 14 in. (356 mm) diameter pile specimens were tested in the same manner as the 24 in. (610 mm) diameter piles. Each 14 in. (356 mm) diameter pile was tested under concentric axial compression in a 5000 kip (22.2 MN) capacity universal testing machine. Hydrostone was used to provide uniform contact between the ends of the specimen and the testing machine platens.

The load, load rate, and axial shortening rate were monitored throughout the test and the manner in which each specimen was tested was based upon these values. Through the initial portion of the test, the load rate was about 24 kips/min. (107 kN/min.), which corresponded to a stress rate of about 155 psi/min. (1069 kPa/min.) and an axial shortening rate of approximately 0.0023 in./min. (0.058 mm/min.). Once the load rate was obtained during the initial linear portion of the load-shortening behavior, no further adjustments were made to the oil flow rate of the machine until spiral fracture and subsequent specimen failure.

4.4.2 Pile 14-A

Pile 14-A had an unconfined concrete compressive strength of 8.50 ksi (58.6 MPa). The spiral reinforcement had a design yield strength of 78 ksi (538 MPa). As noted in Chapter 3, this is the value of yield stress reported by the spiral manufacturer. The longitudinal reinforcement had a yield strength of 71 ksi (490 MPa).

The spiral reinforcement was comprised of two 0.35 in. (8.89 mm) diameter smooth wires bundled together at a pitch of 1.75 in. (44.5 mm). The longitudinal reinforcement consisted of four 0.5 in. (12.7 mm) diameter deformed reinforcing bars spaced evenly around the perimeter of the confined concrete core.

The axial load versus axial shortening response of the pile is presented in Figure 4.29. The figure shows that the specimen exhibited a nearly linear load-shortening response from test initiation until the load reached approximately 800 kips (3.56 MN). As the load increased beyond this point, the specimen began to soften. The slope of the load-shortening plot continued to decrease as the load increased until the first peak load of $P_1 = 1359$ kips (6.04 MN) was reached. The overall axial shortening at this point was $\Delta_1 = 0.179$ in. (4.55 mm), and the corresponding axial strain was 0.0035. At this load, the cover concrete failed in a sudden manner.

Figure 4.34(a) is a photograph of the pile immediately after cover failure. Visible damage to the cover is apparent circumferentially around the test region. Longitudinal cracks also formed, extending from the circumferential splitting toward the top and bottom of the specimen. No cracks were observed in the cover concrete prior to cover failure. The loss of the cover concrete caused the load to decrease to $P_{spall} = 957$ kips (4.26 MN).

The pile exhibited considerably less axial stiffness after the loss of the concrete cover, as evidenced by the shallower slope of the axial load-axial shortening plot in Figure 4.29 after P_{spall}. The pile achieved its second peak at a load of $P_2 = 1337$ kips (5.95 MN) and an axial shortening of $\Delta_2 = 0.684$ in. (17.37 mm) (axial strain of approximately 0.0113). After this peak, the pile continued to shorten while the load decreased until a failure occurred at a load of $P_{failure} = 992$ kips (4.41 MN) and an axial shortening of $\Delta_{failure} = 1.043$ in. (26.49 mm) (axial strain of approximately 0.0172). At failure, the axial load dropped to 214 kips (0.95 MN).

Figure 4.34(b) shows a photograph of the pile immediately after failure. A diagram of the failed pile is presented in Figure 4.33. In this figure, locations of fractured and necked spirals are noted, as are the locations of buckled longitudinal reinforcing bars. The pattern of fractured and necked spirals suggests that a poorly defined inclined failure plane developed along the fractures. The angle of the inclined plane was approximately 41 degrees. The plane extended from the center of the test region on the west face to 4 in. (102 mm) from the bottom of the test region on the northeast face. Unlike the 24 in. (610 mm) diameter specimens, this failure plane was defined only by necking and fracture of the spirals, and no clearly defined concrete failure plane could be seen. Figure 4.35(a) shows a post-test photograph of the entire failed specimen from the north side. Figure 4.35(b) shows a post-test photograph of the failure region on the north side of the specimen.

Figure 4.30 shows the strain in the spiral reinforcement plotted versus the axial shortening. Each channel is plotted to the point in the test where the strain gage failed. Figures 4.31 and 4.32 show the strain in the longitudinal reinforcement and the axial strains computed from the potentiometer measurements, respectively, plotted versus the axial shortening. Note that the stress in the longitudinal reinforcement was above or near its yield stress when Δ_1 was reached. Once again, the potentiometer measurements are only shown up to the point of cover failure, and the longitudinal strain gage measurements are assumed to provide an accurate representation of the axial strain after cover failure. In all three figures, the key values plotted are similar to the values plotted in previous test summaries.

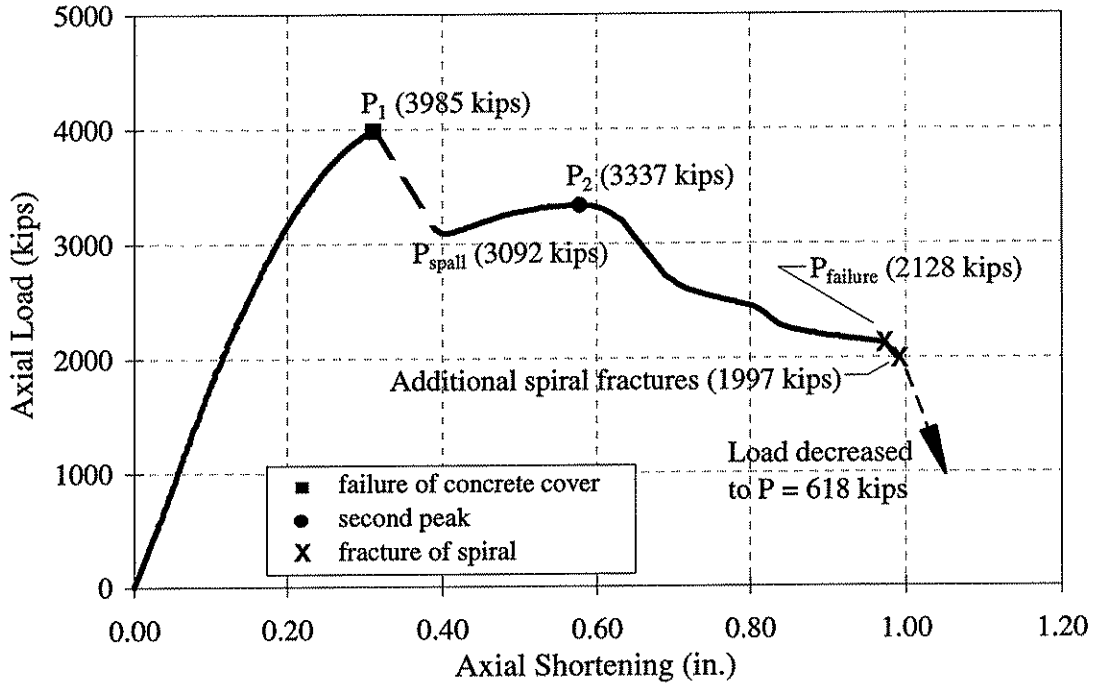Figure 4.29   Plot of axial load versus axial shortening for Pile 14-A.

Figure 4.30   Plot of spiral strain versus axial shortening for Pile 14-A.

69

Figure 4.31   Plot of longitudinal strain versus axial shortening for Pile 14-A.

Figure 4.32   Plot of potentiometer axial strain versus axial shortening for Pile 14-A.
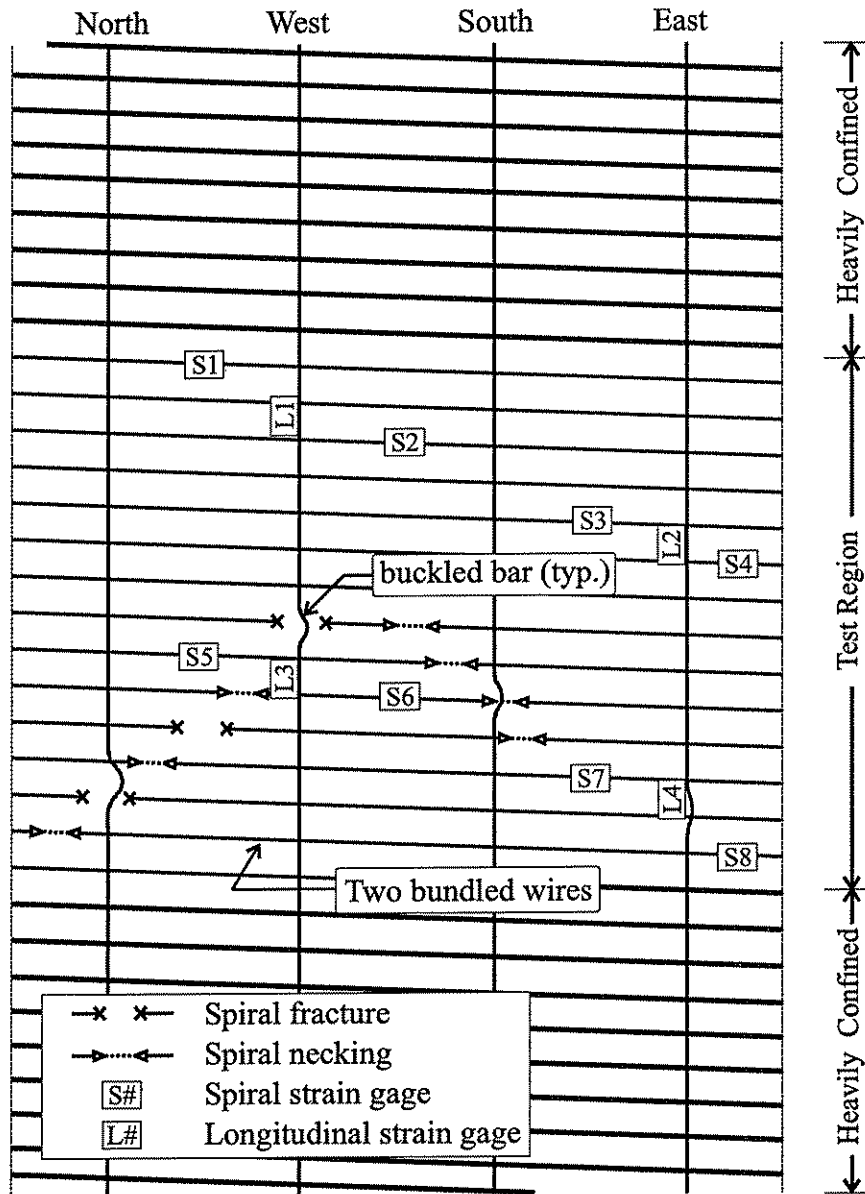
Figure 4.33   Schematic drawing of post-test appearance of Pile 14-A.
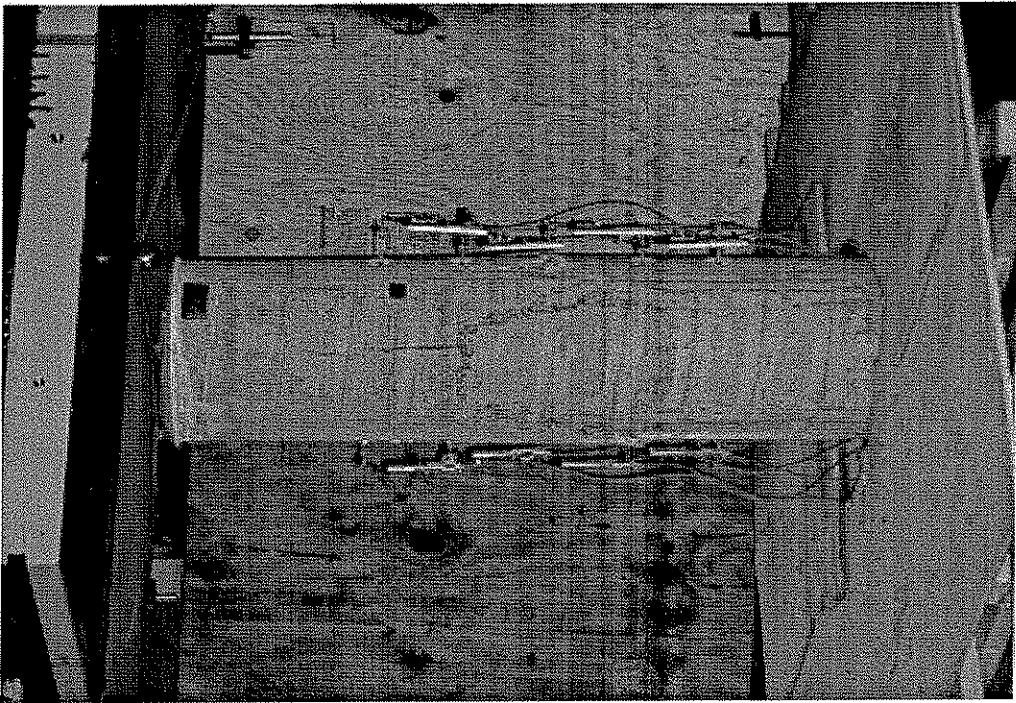
(a)

(b)

Figure 4.34   Pile 14-A: (a) northwest face after cover failure; (b) northeast face after spiral fracture.

(b)

(a)
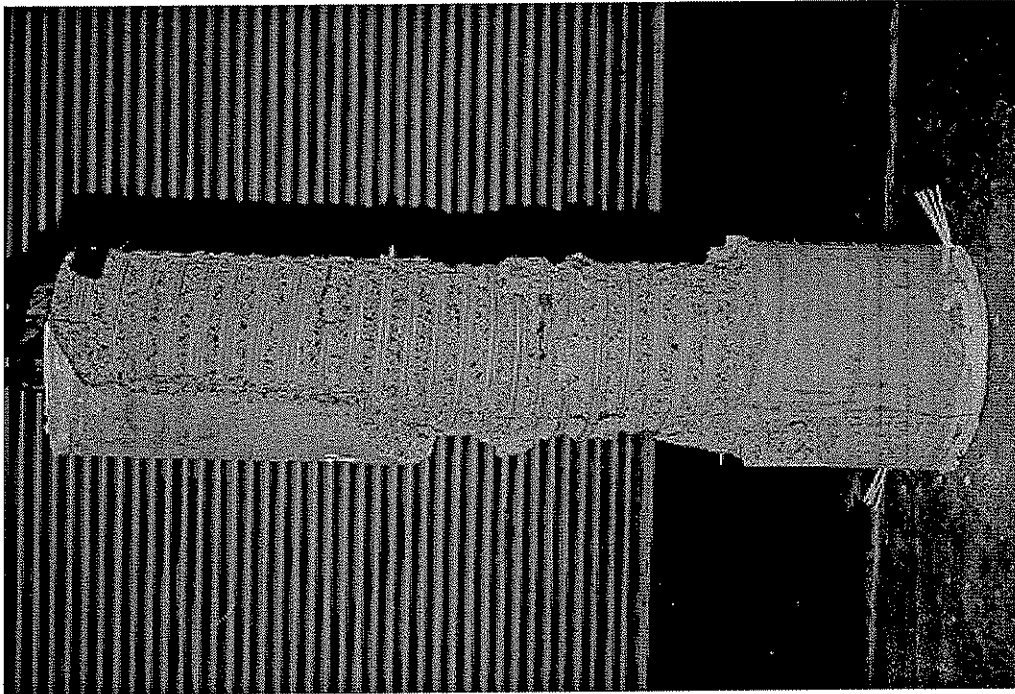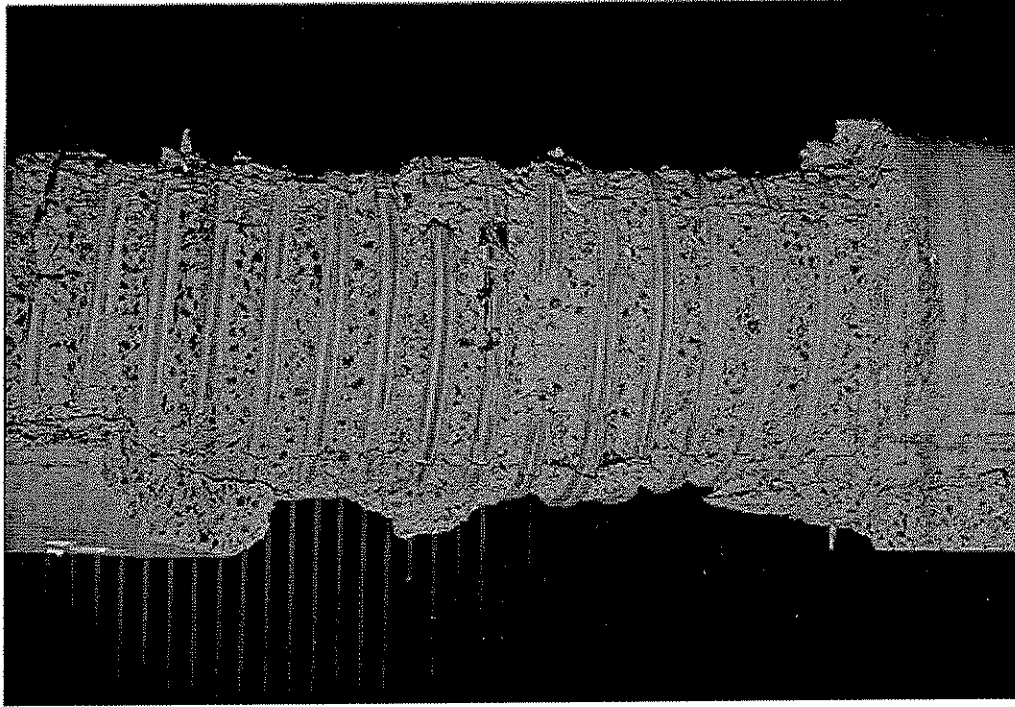
Figure 4.35   Pile 14-A: (a) north face of failed pile; (b) inclined failure plane on north face.

4.4.3 Pile 14-B

Pile 14-B had an unconfined concrete compressive strength of 8.50 ksi (58.6 MPa), a spiral rein-
forcement design yield strength of 107 ksi (738 MPa), and a longitudinal reinforcement yield
strength of 71 ksi (490 MPa). The spiral reinforcement was comprised of two 0.35 in. (8.89 mm)
diameter smooth wires bundled together at a pitch of 2.375 in. (60.3 mm). The longitudinal rein-
forcement consisted of four 0.5 in. (12.7 mm) diameter deformed reinforcing bars.

The axial load versus axial shortening response of the pile is presented in Figure 4.36. Similar to
previously discussed piles, this specimen exhibited a nearly linear load-shortening response from
test initiation until the load reached approximately 800 kips (3.56 MN). As the load increased
beyond this point, the load-shortening plot shows that the specimen began to soften until the first
peak load of P_1 = 1366 kips (6.08 MN) was reached. The overall axial shortening at this point was
Δ_1 = 0.181 in. (4.60 mm), and the corresponding axial strain was 0.0047. At this load, the cover
concrete failed in a sudden manner.

Figure 4.41(a) is a photograph of the pile immediately after cover failure. Visible damage to the
cover is apparent circumferentially around the test region. Longitudinal cracks also formed, ex-
tending from the circumferential splitting toward the top and bottom of the specimen. No cracks
were observed in the cover concrete prior to cover failure. The loss of the cover concrete caused
the load to decrease to P_{spall} = 959 kips (4.27 MN).

The pile exhibited considerably less axial stiffness after the loss of the concrete cover, as can be
seen in Figure 4.36 after P_{spall}. The pile achieved its second peak at a load of P_2 = 1276 kips (5.68
MN) and an axial shortening of Δ_2 = 0.659 in. (16.74 mm) (axial strain of approximately 0.0159).
After this peak, the pile continued to shorten while the load decreased until failure occurred at a
load of $P_{failure}$ = 1050 kips (4.67 MN) and an axial shortening of $\Delta_{failure}$ = 1.033 in. (26.24 mm)
(axial strain of approximately 0.0146). At failure, the axial load dropped to 112 kips (0.50 MN).

Figure 4.41(b) is a photograph of the pile immediately after failure. A schematic diagram of the
failed pile is presented in Figure 4.40. The spiral fractures occurred in two bundles of bars just
below the center of the test region on the south side of the pile. No inclined failure plane could be
seen either in the concrete or in the pattern of the fractured and necked spiral steel. Figure 4.42(a)
shows a post-test photograph of the entire failed pile from the south side. Figure 4.42(b) shows a
post-test photograph of the failure region on the south side of the pile.

Figure 4.37 shows the strain in the spiral reinforcement plotted versus the axial shortening. Fig-
ures 4.38 and 4.39 show the strain in the longitudinal reinforcement and the axial strains computed
from the potentiometer measurements, respectively, plotted versus the axial shortening. Note that
the longitudinal reinforcement was above or near its yield stress when Δ_1 was reached. Once
again, the potentiometers were disturbed by cover spalling. Thus for behavior occurring after the
first peak, the longitudinal strain gages are assumed to provide an accurate representation of the
axial strain.

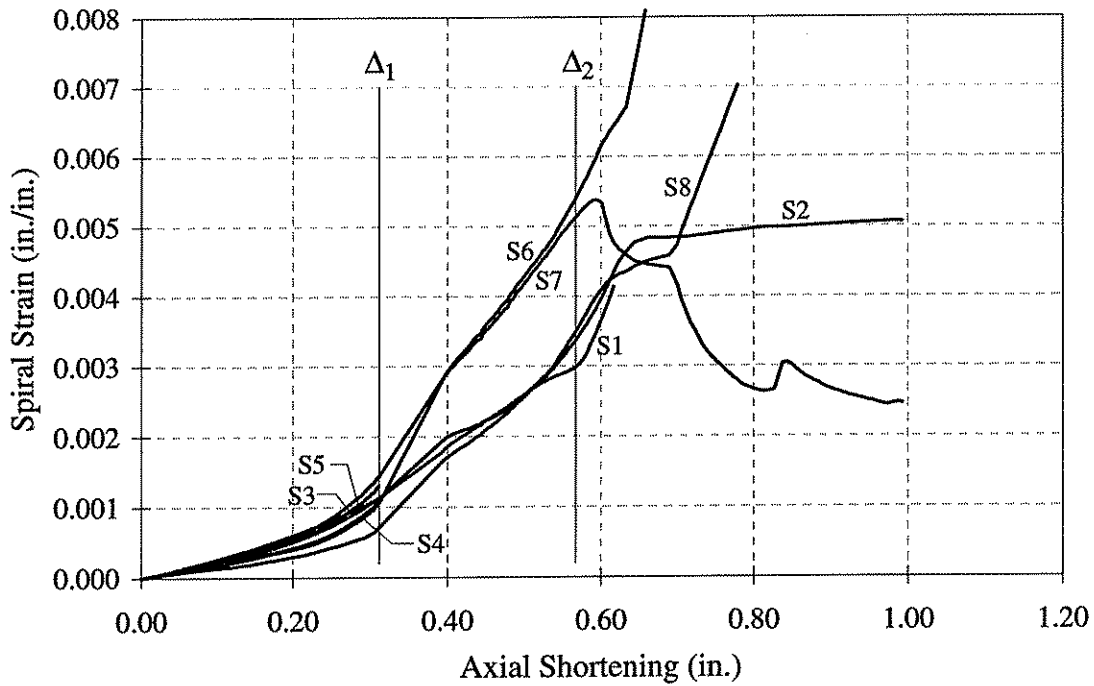Figure 4.36   Plot of axial load versus axial shortening for Pile 14-B.

Figure 4.37   Plot of spiral strain versus axial shortening for Pile 14-B.
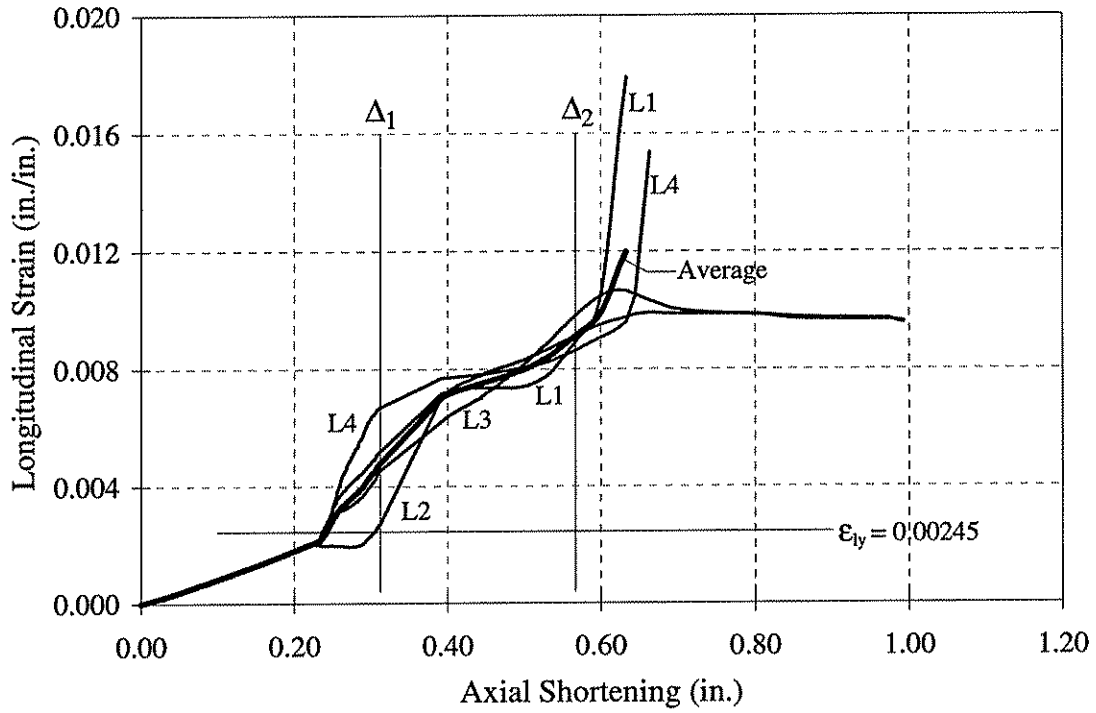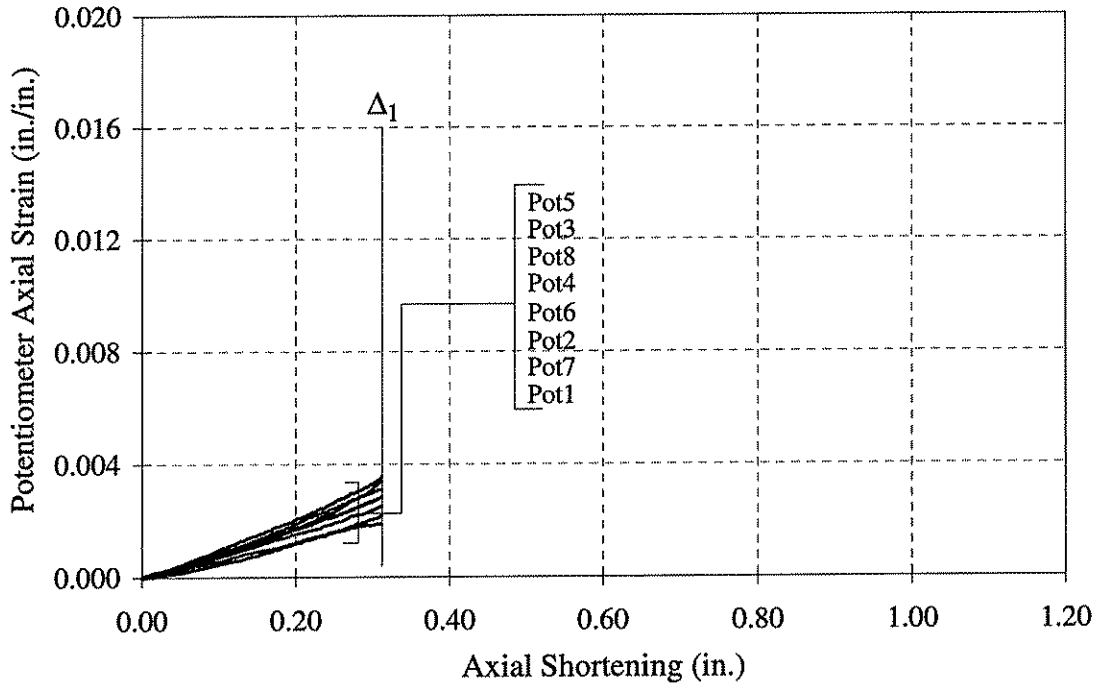
Figure 4.38   Plot of longitudinal strain versus axial shortening for Pile 14-B.

Figure 4.39   Plot of potentiometer axial strain versus axial shortening for Pile 14-B.

Figure 4.40   Schematic drawing of post-test appearance of Pile 14-B.

(a)

(b)

Figure 4.41 Pile 14-B: (a) northwest face after cover failure; (b) northwest face at end of test.

78
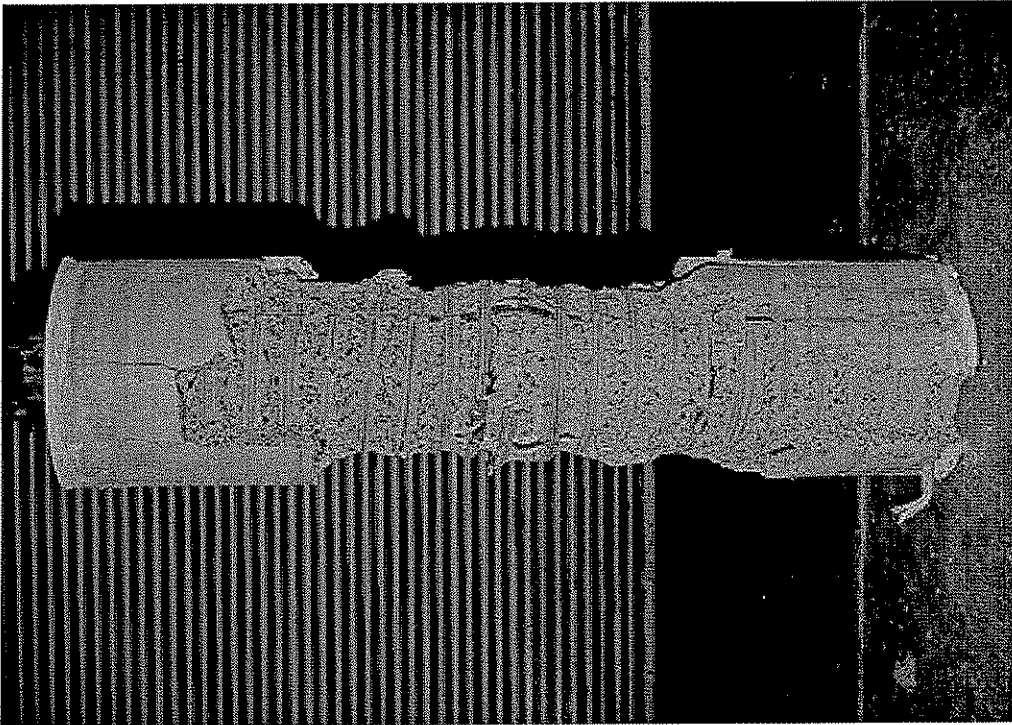
(a)
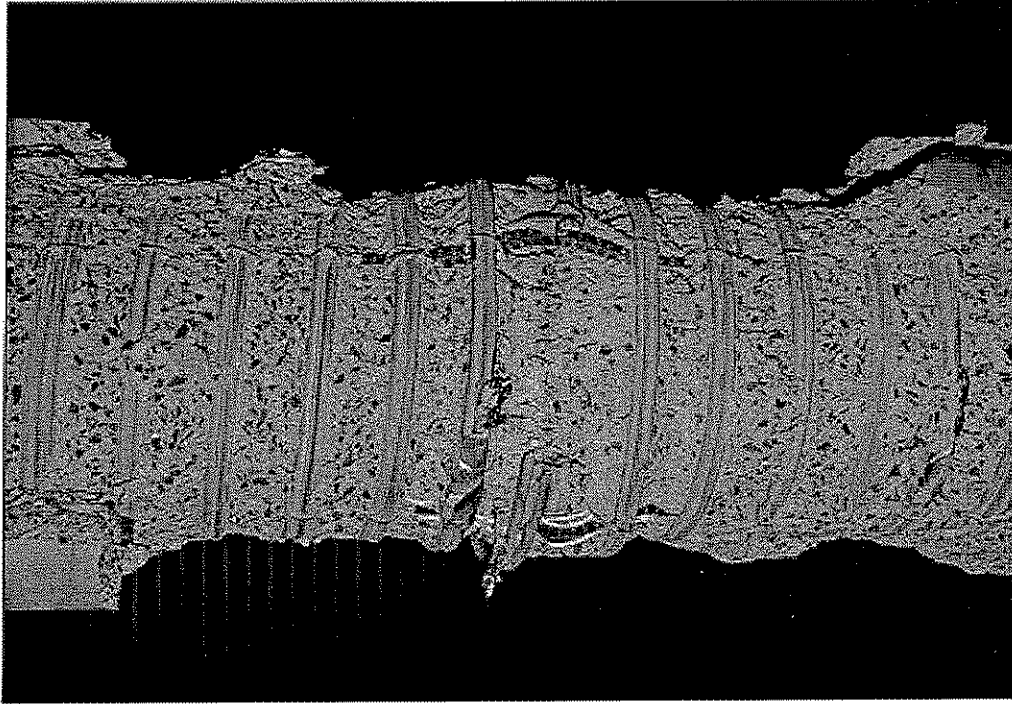
(b)

Figure 4.42   Pile 14-B: (a) south face of failed pile; (b) failure region on south face.

4.4.4 Pile 14-C

Pile 14-C had a concrete compressive strength of 8.50 ksi (58.6 MPa), a spiral reinforcement design yield strength of 121 ksi (834 MPa), and a longitudinal reinforcement yield strength of 71 ksi (490 MPa). The spiral reinforcement was comprised of one 0.35 in. (8.89 mm) diameter smooth wire at a pitch of 1.375 in. (34.9 mm). The longitudinal reinforcement consisted of four 0.5 in. (12.7 mm) diameter deformed reinforcing bars.

The axial load versus axial shortening response of the pile is presented in Figure 4.43. The figure shows that the specimen exhibited a nearly linear load-shortening response from test initiation until the load reached approximately 800 kips (3.56 MN). As the load increased beyond this point, the load-shortening plot shows that the specimen began to soften until the peak load of $P_1 = 1367$ kips (6.08 MN) was reached. The overall axial shortening at this point was $\Delta_1 = 0.183$ in. (4.65 mm), and the corresponding axial strain was 0.0049. At this load, the cover concrete failed in a sudden manner.

Figure 4.48(a) is a photograph of the pile immediately after cover failure. Visible damage to the cover is apparent circumferentially around the test region. Longitudinal cracks also extended from the circumferential splitting toward the top and bottom of the specimen. No cracks were observed in the cover concrete prior to cover failure. The loss of the cover concrete caused the load to decrease to $P_{spall} = 921$ kips (4.10 MN).

The pile exhibited considerably less axial stiffness after the loss of the concrete cover, as evidenced by the shallower slope of the axial load-axial shortening plot in Figure 4.43 after P_{spall}. The pile achieved its second peak at a load of $P_2 = 1248$ kips (5.55 MN) and an axial shortening of $\Delta_2 = 0.700$ in. (17.78 mm) (axial strain of approximately 0.0183). After this peak, the pile continued to shorten while the load decreased until what appeared to be a single spiral fracture occurred at a load of $P_{failure} = 962$ kips (4.28 MN) and an axial shortening of $\Delta_{failure} = 1.076$ in. (27.33 mm) (axial strain of approximately 0.0136). This fracture caused the load to decrease by almost 250 kips (1.11 MN). A short time after this fracture, at a slightly increased load and axial shortening, multiple spiral fractures occurred. At failure, the axial load dropped to 108 kips (0.48 MN).

Figure 4.48(b) shows a photograph of the pile immediately after the multiple spiral fractures. A schematic diagram of the failed pile is presented in Figure 4.47. Observations from the reinforcement failures are inconclusive as to the existence of an inclined failure plane. However, if one did form, it was very poorly defined on the southwest face of the pile at an angle of approximately 36 degrees from the horizontal. Figure 4.49(a) shows a post-test photograph of the entire failed specimen from the west side. Figure 4.49(b) shows a post-test photograph of the failure region plane on the west side of the specimen.

Figure 4.44 shows the strain in the spiral reinforcement plotted versus the axial shortening. Figures 4.45 and 4.46 show the strain in the longitudinal reinforcement and the axial strains computed from the potentiometer measurements, respectively, plotted versus the axial shortening. Note that the longitudinal reinforcement was above or near its yield stress when Δ_1 was reached. Once

80

again, the potentiometers were disturbed by cover spalling. For behavior occurring after the first peak, the longitudinal strain gages are assumed to provide an accurate representation of the axial strain.
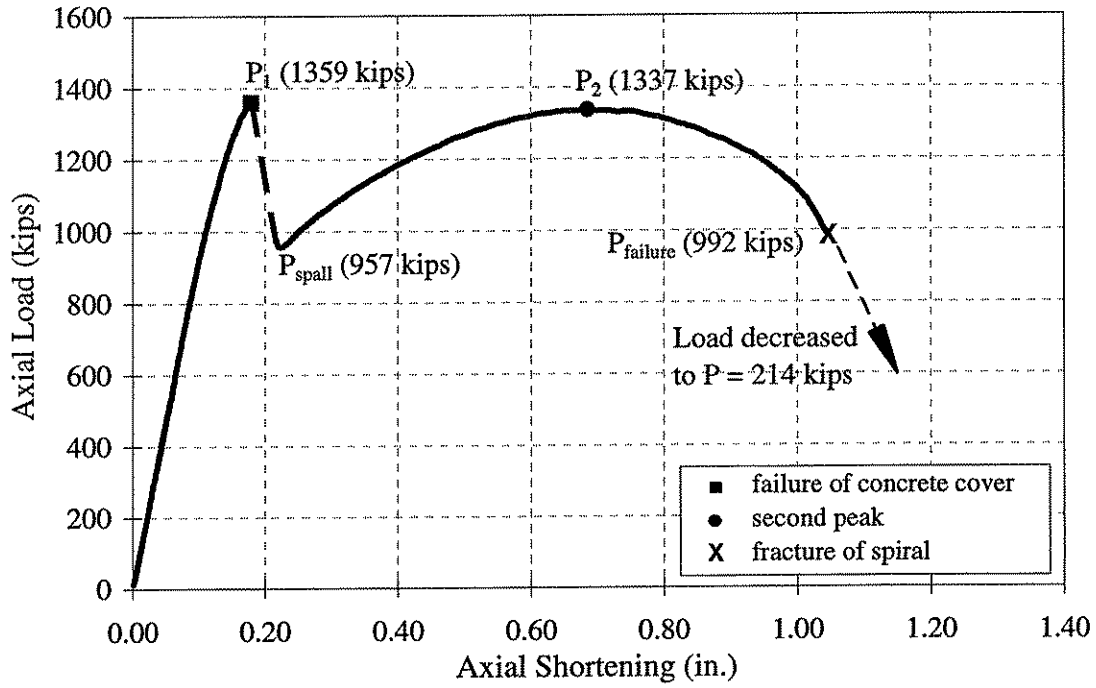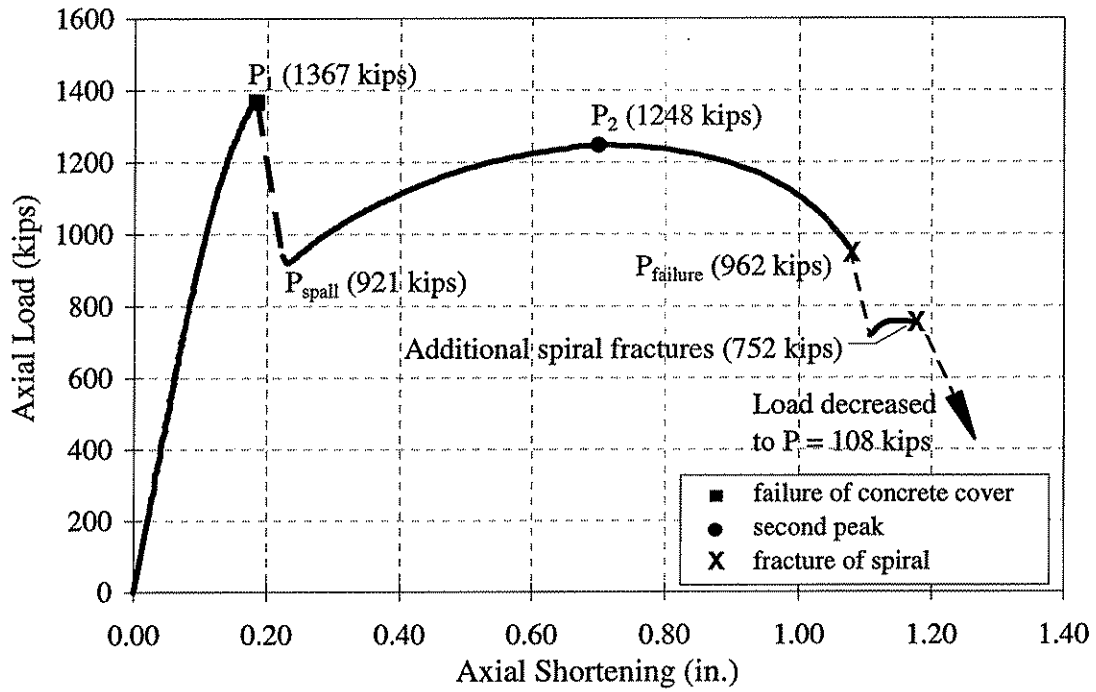
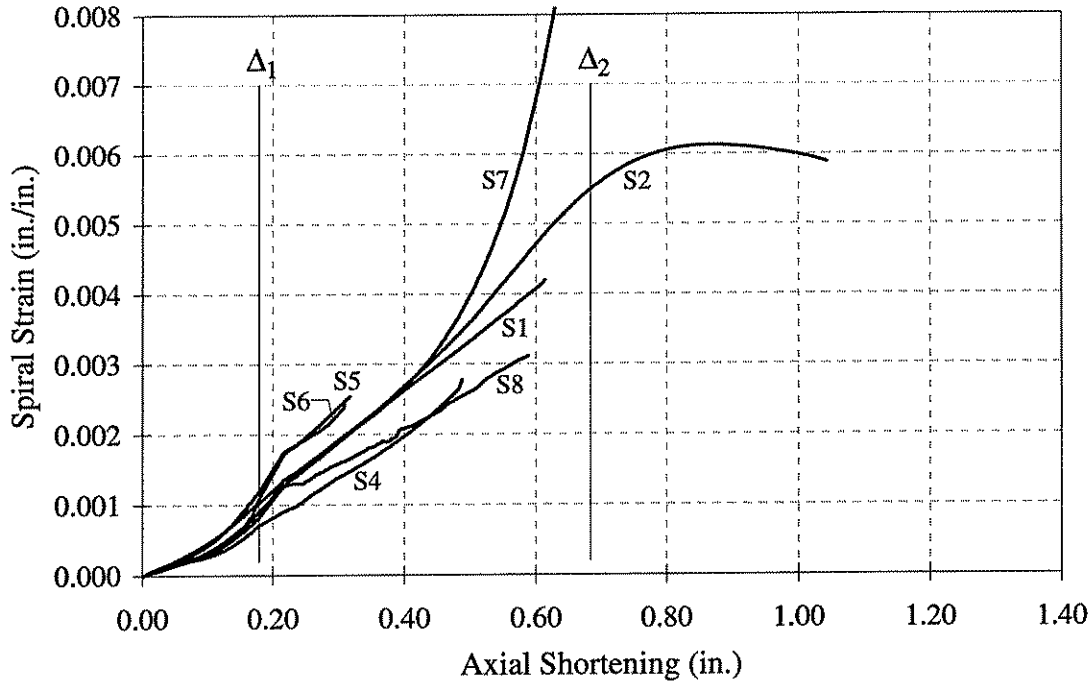Figure 4.43   Plot of axial load versus axial shortening for Pile 14-C.
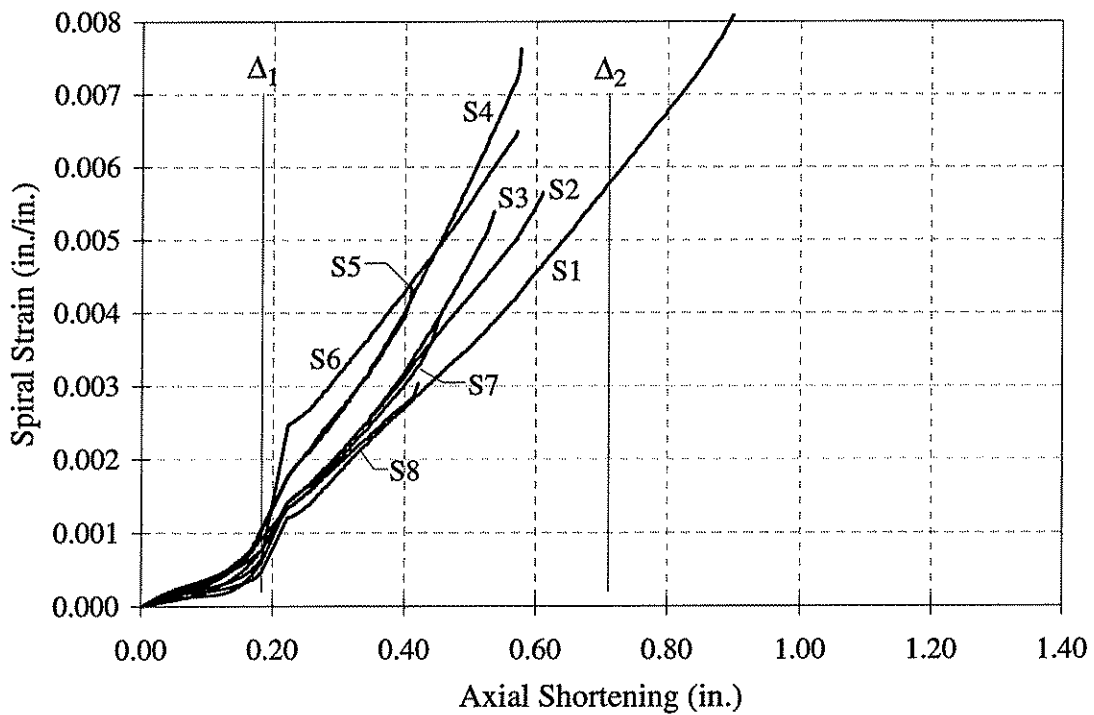
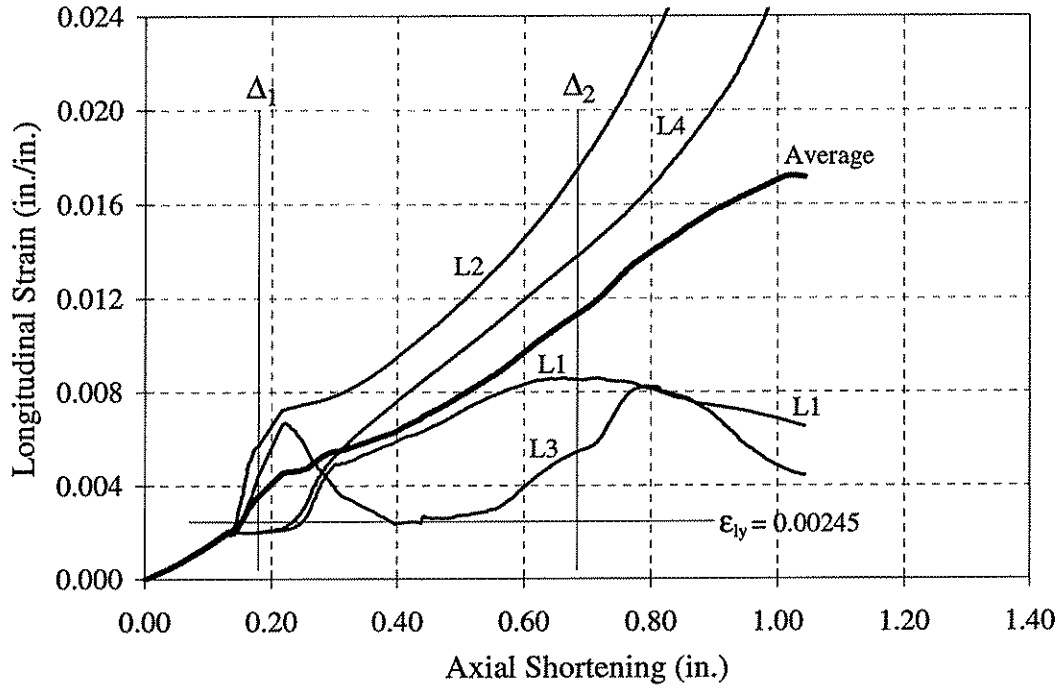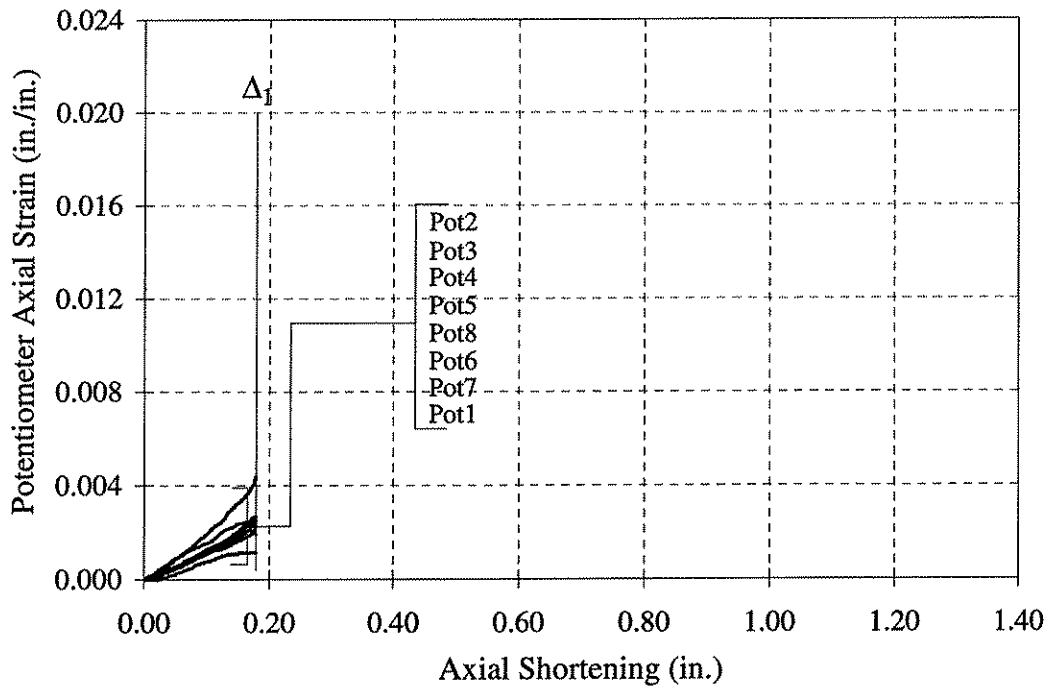Figure 4.44   Plot of spiral strain versus axial shortening for Pile 14-C.

82
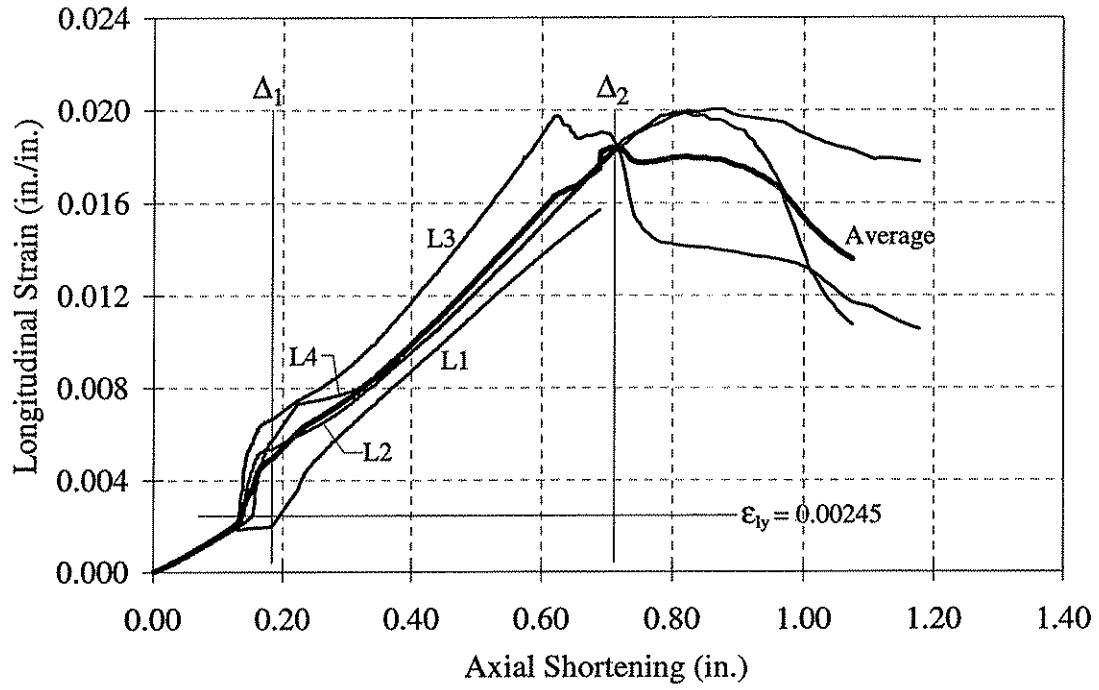
Figure 4.45   Plot of longitudinal strain versus axial shortening for Pile 14-C.
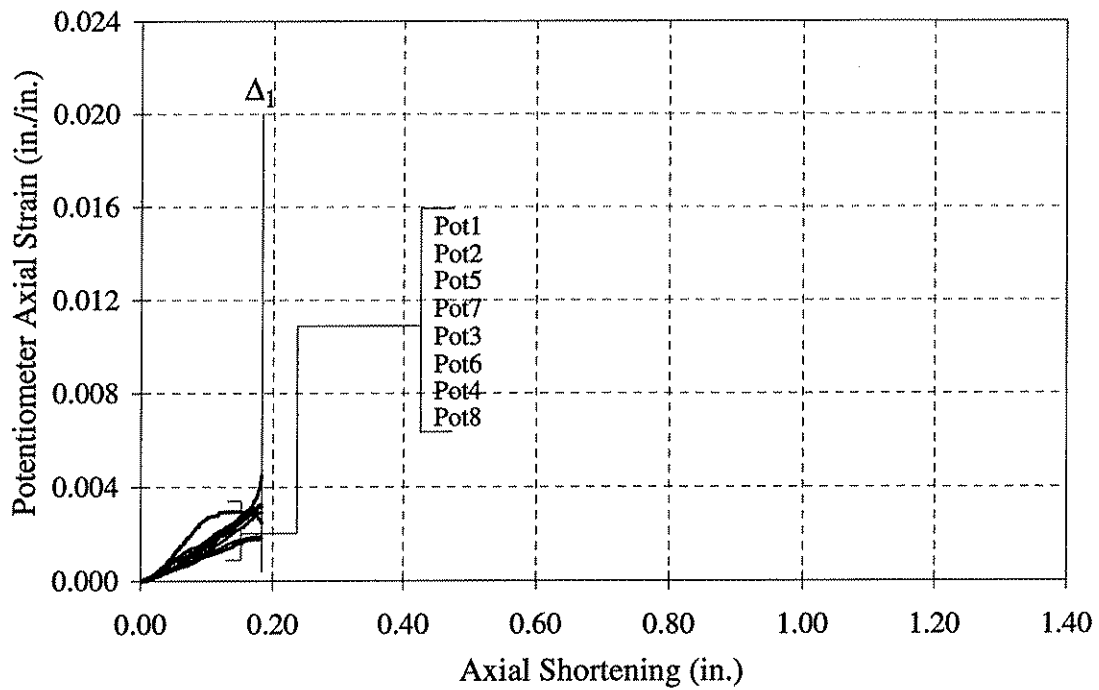
Figure 4.46   Plot of potentiometer axial strain versus axial shortening for Pile 14-C.

83
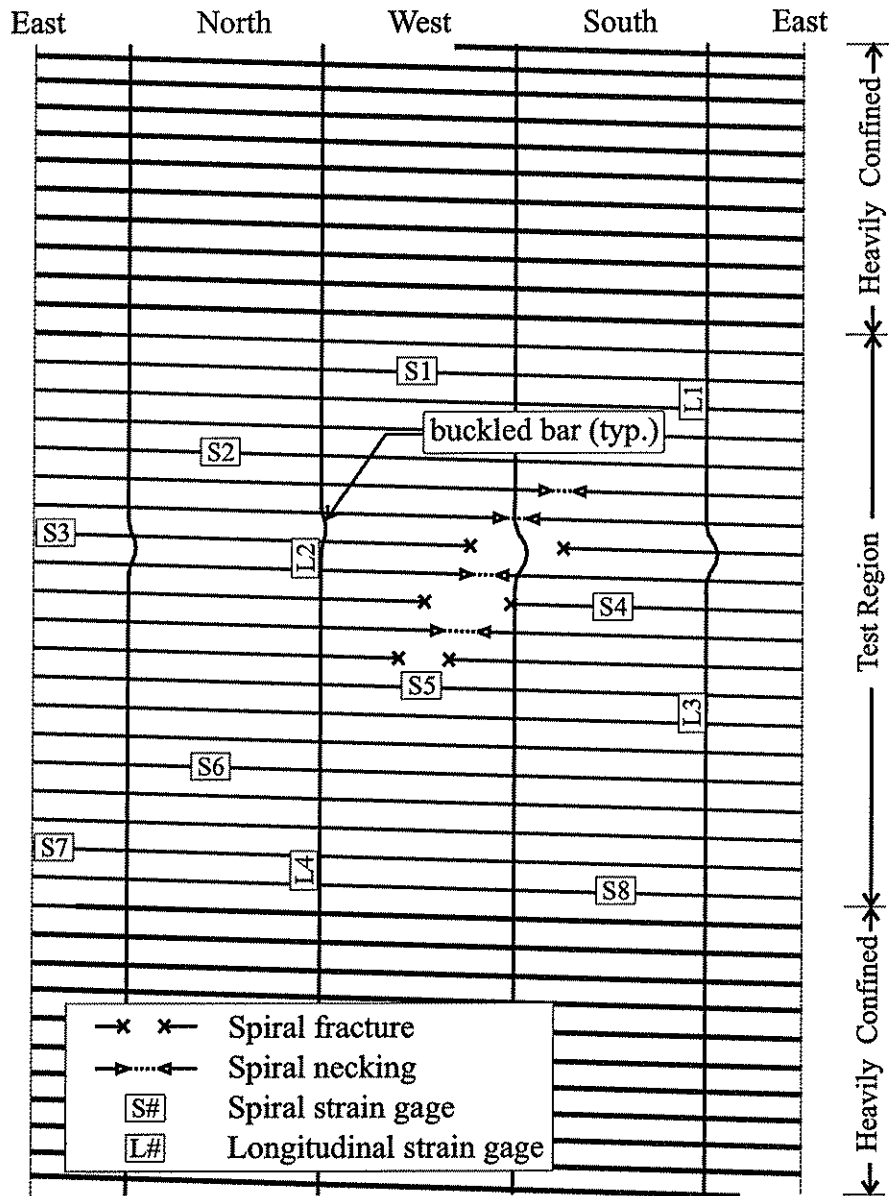
Figure 4.47   Schematic drawing of post-test appearance of Pile 14-C.

(b)

(a)
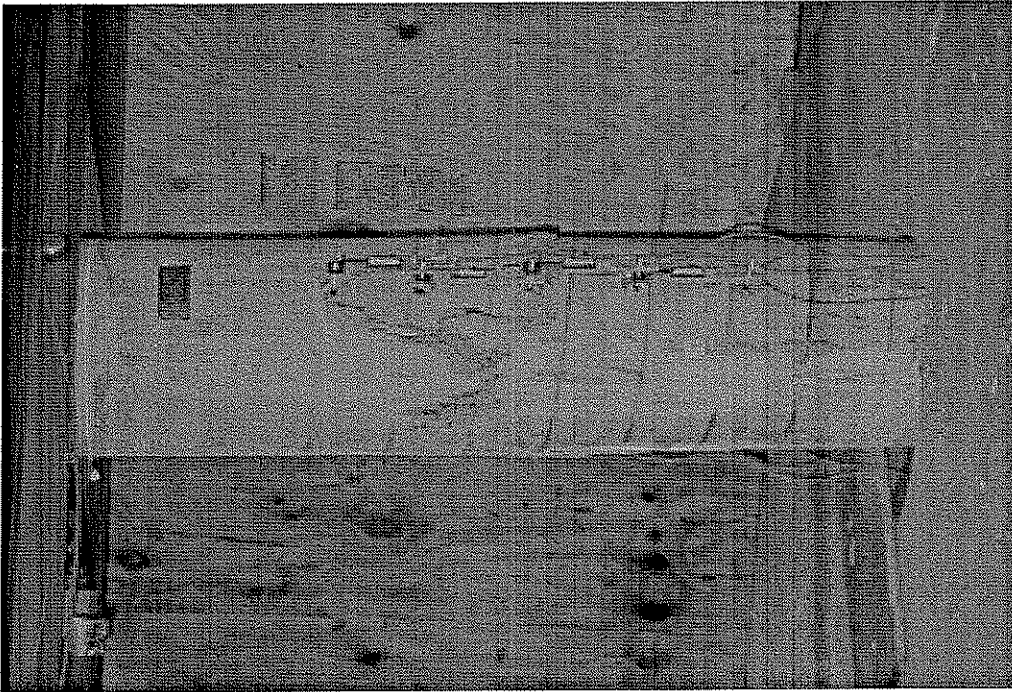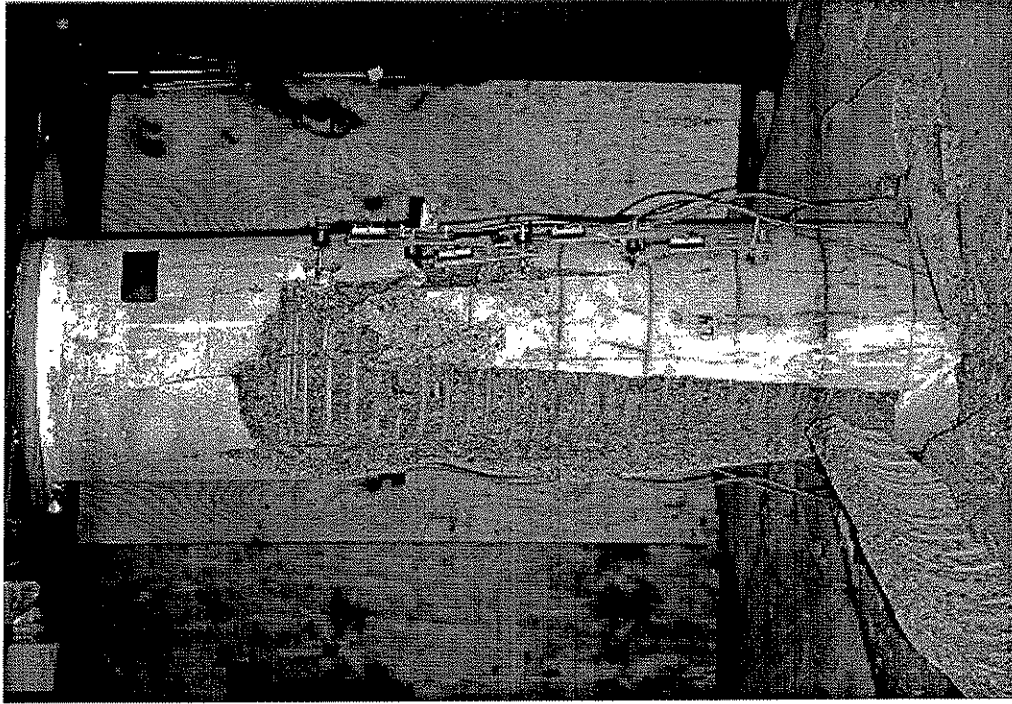
Figure 4.48   Pile 14-C: (a) northwest face after cover failure; (b) northwest face at end of test.

(b)

(a)
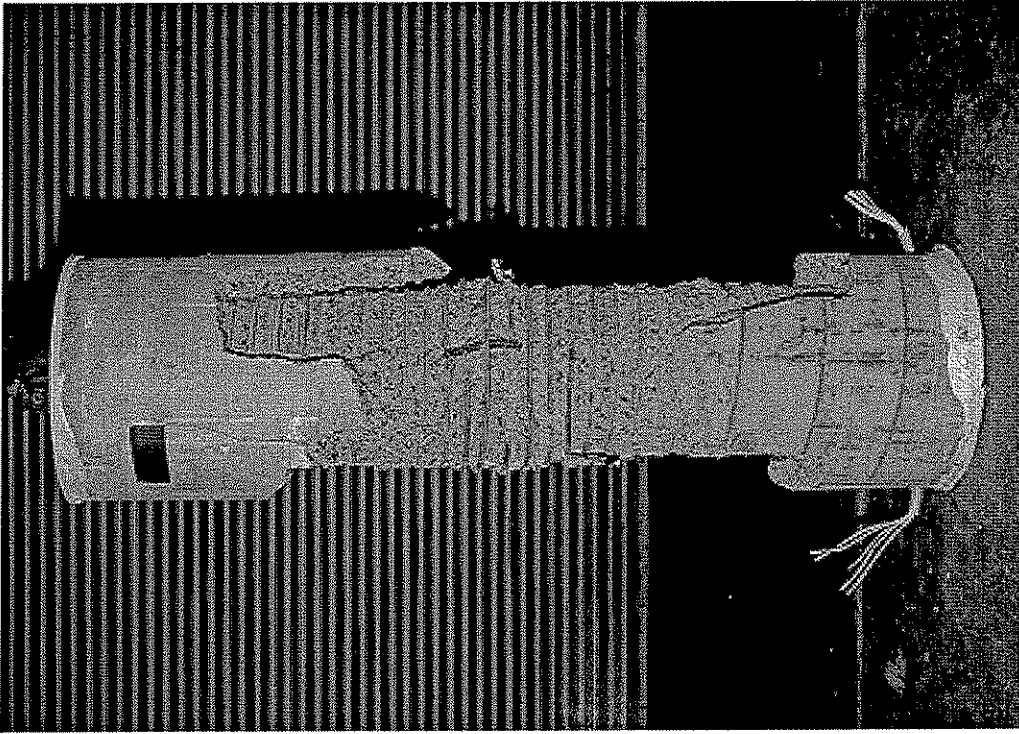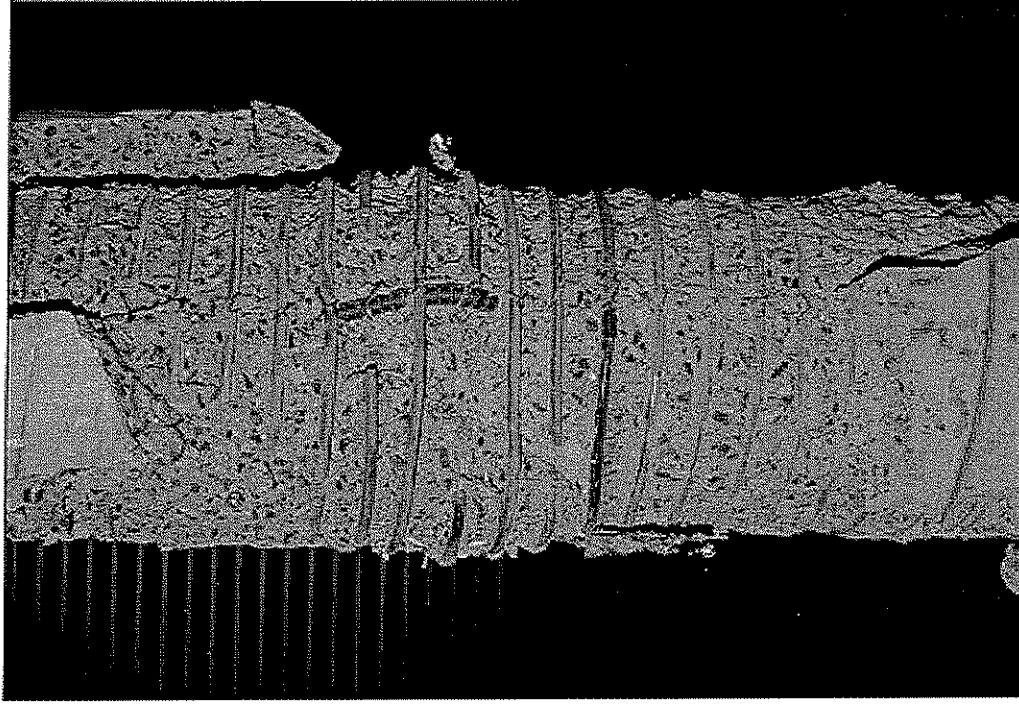
Figure 4.49   Pile 14-C: (a) west face of failed pile; (b) failure region on west face.

4.4.5 Pile 14-D

Pile 14-D had an unconfined concrete compressive strength of 8.50 ksi (58.6 MPa), a spiral reinforcement design yield strength of 140 ksi (965 MPa), and a longitudinal reinforcement yield strength of 71 ksi (490 MPa). The spiral reinforcement was comprised of one 0.35 in. (8.89 mm) diameter smooth wire at a pitch of 1.5 in. (38.1 mm). The longitudinal reinforcement consisted of four 0.5 in. (12.7 mm) diameter deformed reinforcing bars.

The axial load versus axial shortening response of the pile is presented in Figure 4.50. The figure shows that the specimen exhibited a nearly linear load-shortening response from test initiation until the load reached approximately 800 kips (3.56 MN). As the load increased beyond this point, the load-shortening plot shows that the specimen began to soften until the first peak load of $P_1 = 1355$ kips (6.03 MN) was reached. The overall axial shortening at this point was $\Delta_1 = 0.179$ in. (4.55 mm), and the corresponding axial strain was 0.0051 (average longitudinal strain gage strain). At this load, the cover concrete failed in a sudden manner.

Figure 4.55(a) is a photograph of the pile immediately after cover failure. Visible damage to the cover is apparent circumferentially around the test region. Longitudinal cracks also formed, extending from the circumferential splitting toward the top and bottom of the specimen. No cracks were observed in the cover concrete prior to cover failure. The loss of the cover concrete caused the load to decrease to $P_{spall} = 924$ kips (4.11 MN).

The pile exhibited considerably less axial stiffness after the loss of the concrete cover, as can be seen in Figure 4.50 after P_{spall}. The pile achieved its second peak at a load of $P_2 = 1228$ kips (5.46 MN) and an axial shortening of $\Delta_2 = 0.710$ in. (18.03 mm) (axial strain of approximately 0.0194). After this peak, the pile continued to shorten while the load decreased until failure occurred at a load of $P_{failure} = 932$ kips (4.15 MN) and an axial shortening of $\Delta_{failure} = 1.000$ in. (25.40 mm) (axial strain of approximately 0.0176). At failure, the axial load dropped to 295 kips (1.31 MN).

Figure 4.55(b) shows a photograph of the pile immediately after failure. A schematic diagram of the failed pile is presented in Figure 4.54. Observations indicate the possible existence of an inclined failure plane. The fractured and necked spirals as well as the failed concrete indicate that a failure plane may have formed just above the center of the test region on the northwest face of the pile. The angle of this inclined plane was approximately 61 degrees from the horizontal. No indications of a failure plane were observed anywhere else on the specimen within the concrete. However, the buckling of the southeast and northeast longitudinal bars indicates that a failure plane may have formed on this face of the specimen at a shallower angle than occurred on the northwest face. Figure 4.56(a) shows a post-test photograph of the entire failed specimen from the north side. Figure 4.56(b) shows a post-test photograph of the failure region on the north side of the specimen.

Figure 4.51 shows the strain in the spiral reinforcement plotted versus the axial shortening. Figures 4.52 and 4.53 show the strain in the longitudinal reinforcement and the axial strains computed from the potentiometer measurements, respectively, plotted versus the axial shortening. Note that

87

the longitudinal reinforcement was above its yield stress when Δ_1 was reached. Once again, the potentiometers were disturbed by cover spalling. For behavior occurring after the first peak, the longitudinal strain gages are assumed to provide an accurate representation of the axial strain.
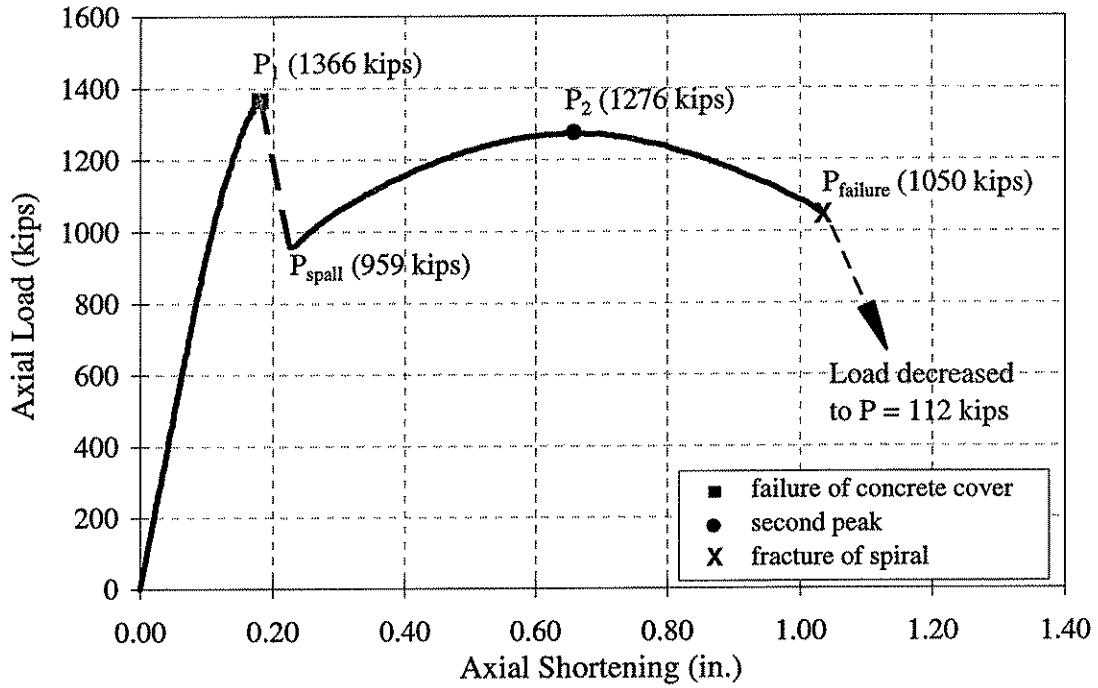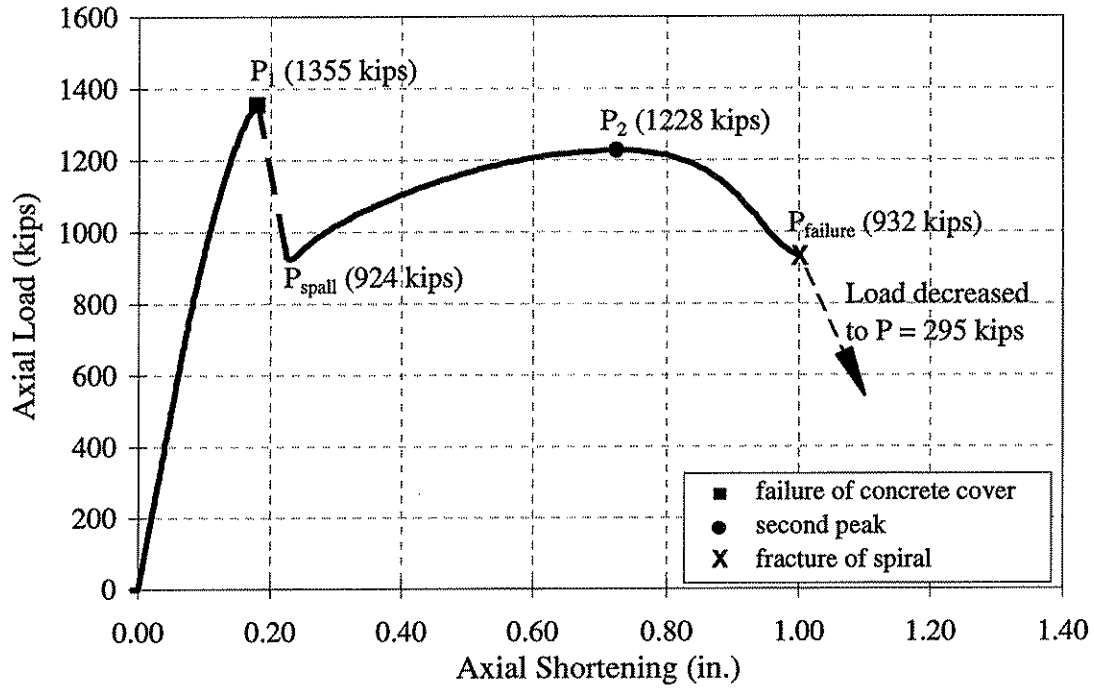
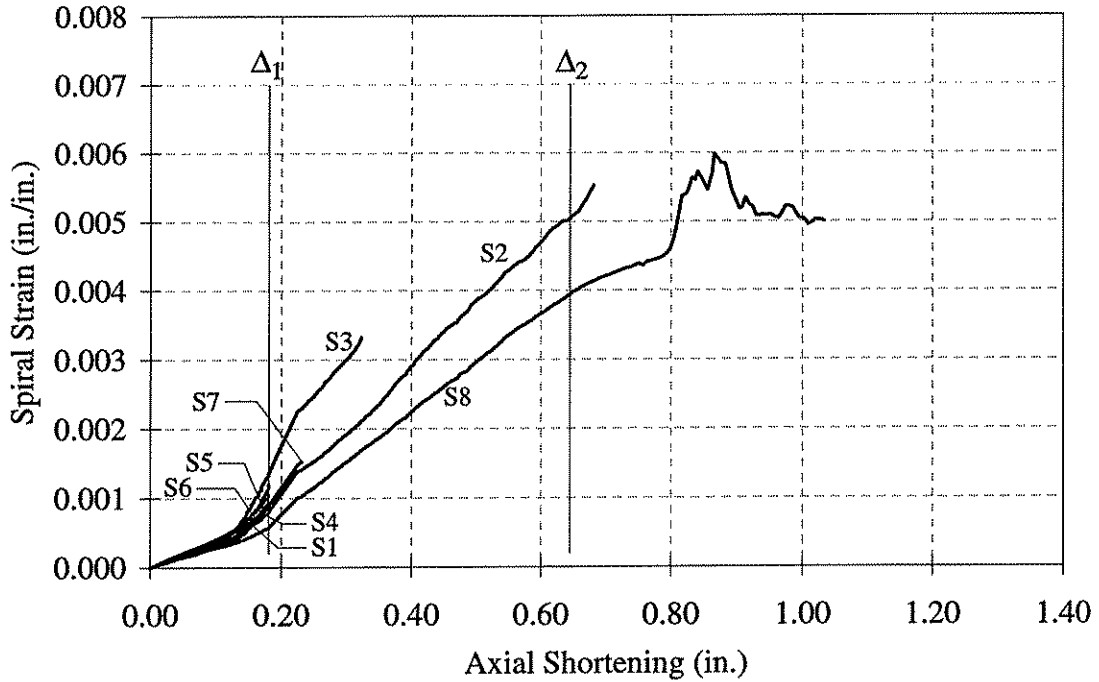Figure 4.50   Plot of axial load versus axial shortening for Pile 14-D.
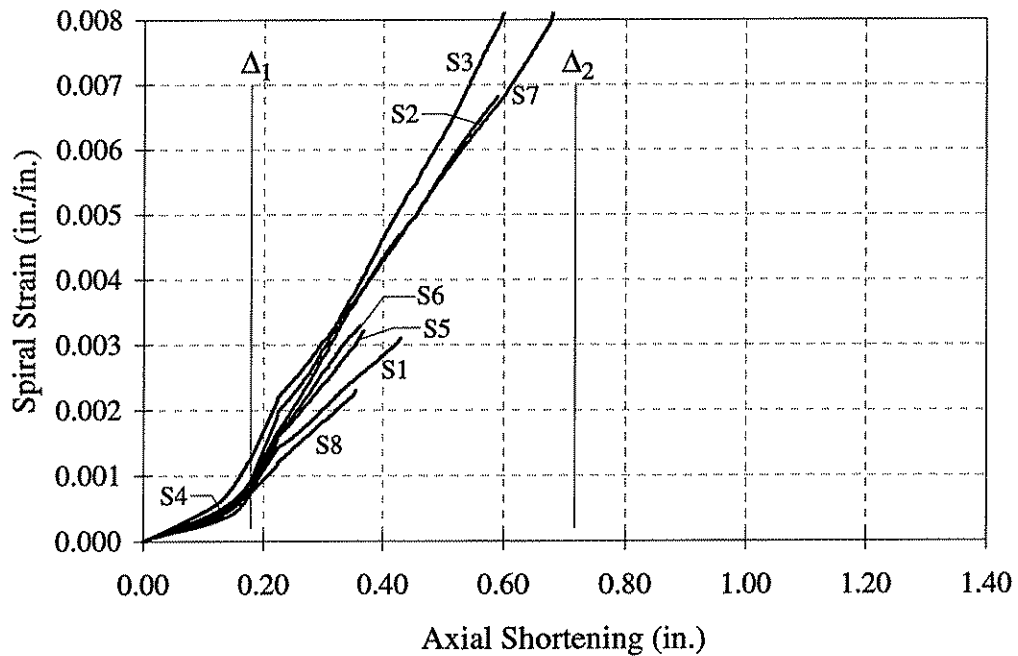
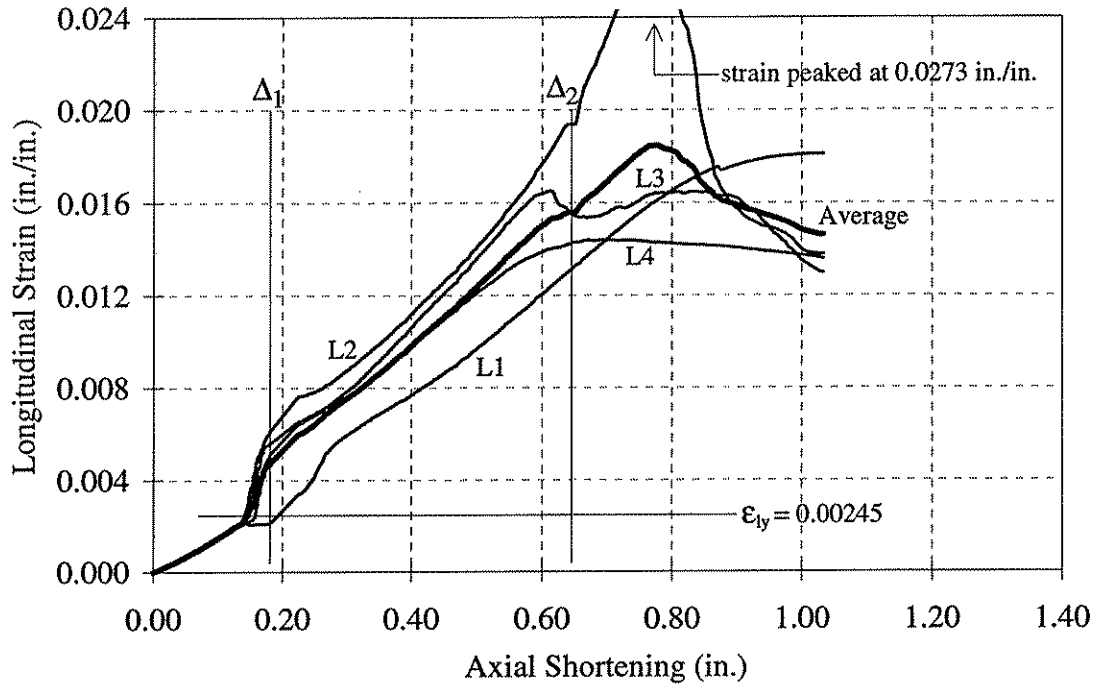Figure 4.51   Plot of spiral strain versus axial shortening for Pile 14-D.
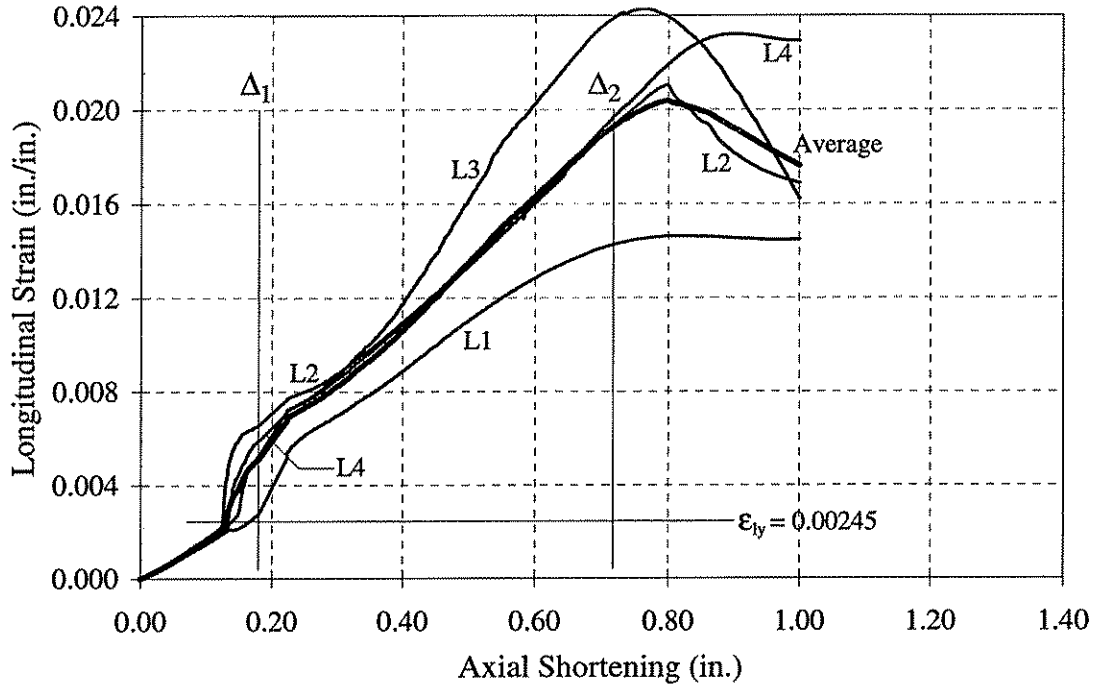
Figure 4.52   Plot of longitudinal strain versus axial shortening for Pile 14-D.
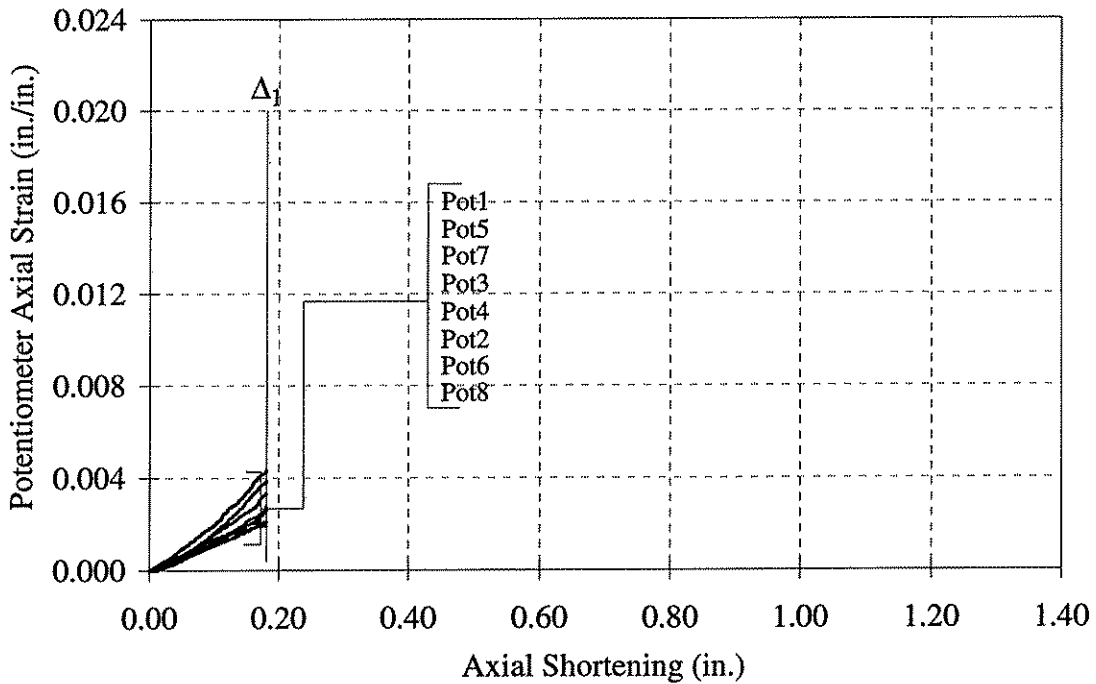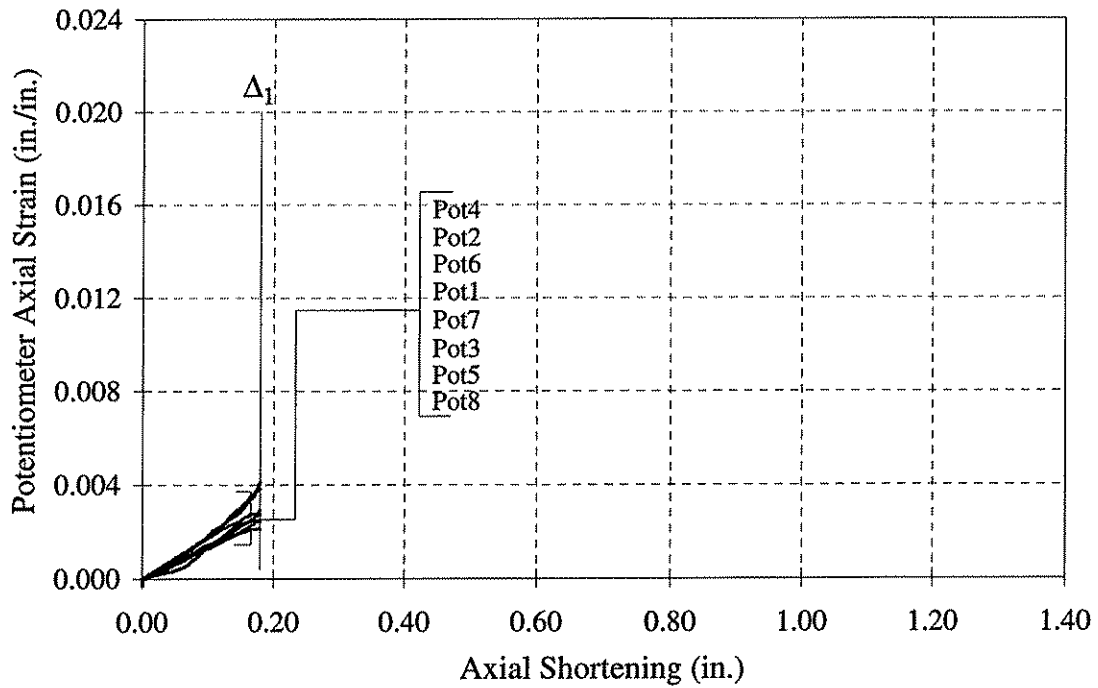

Figure 4.53   Plot of potentiometer axial strain versus axial shortening for Pile 14-D.
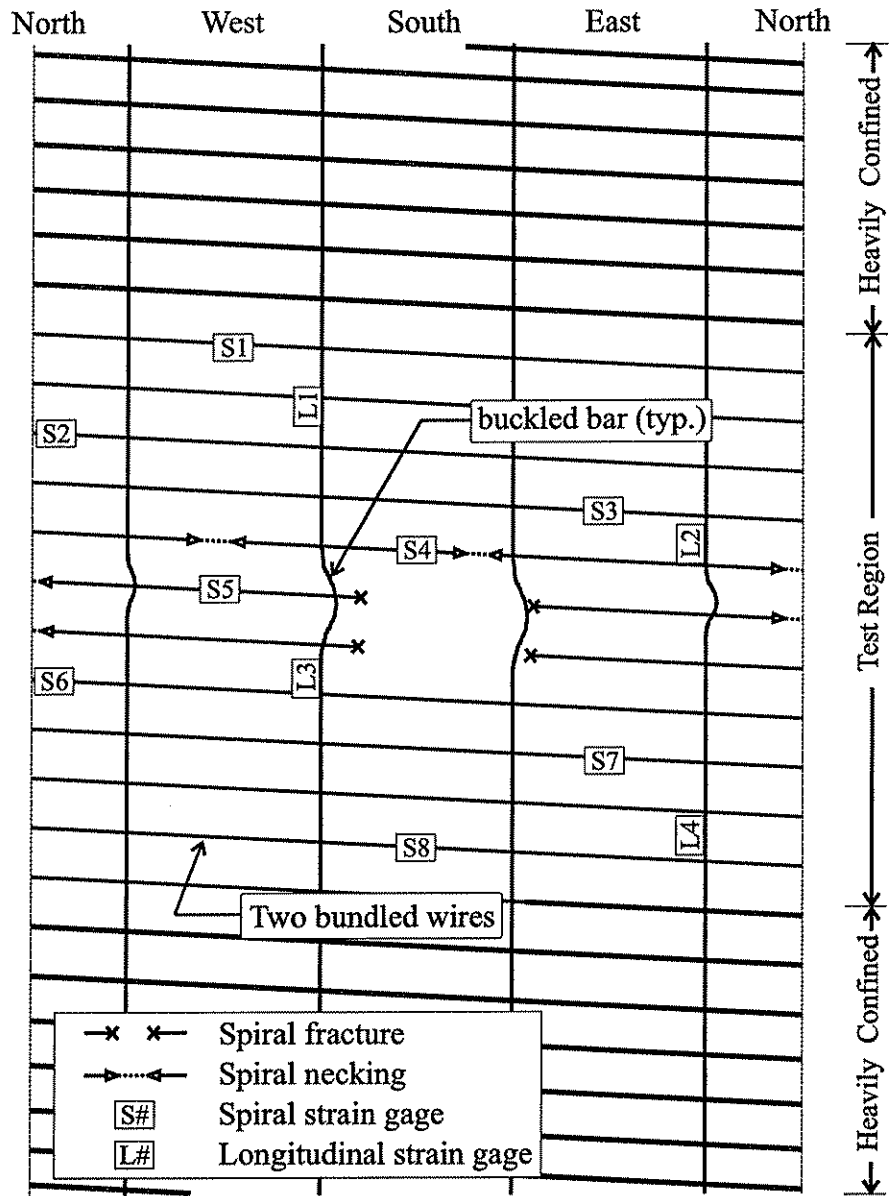
90
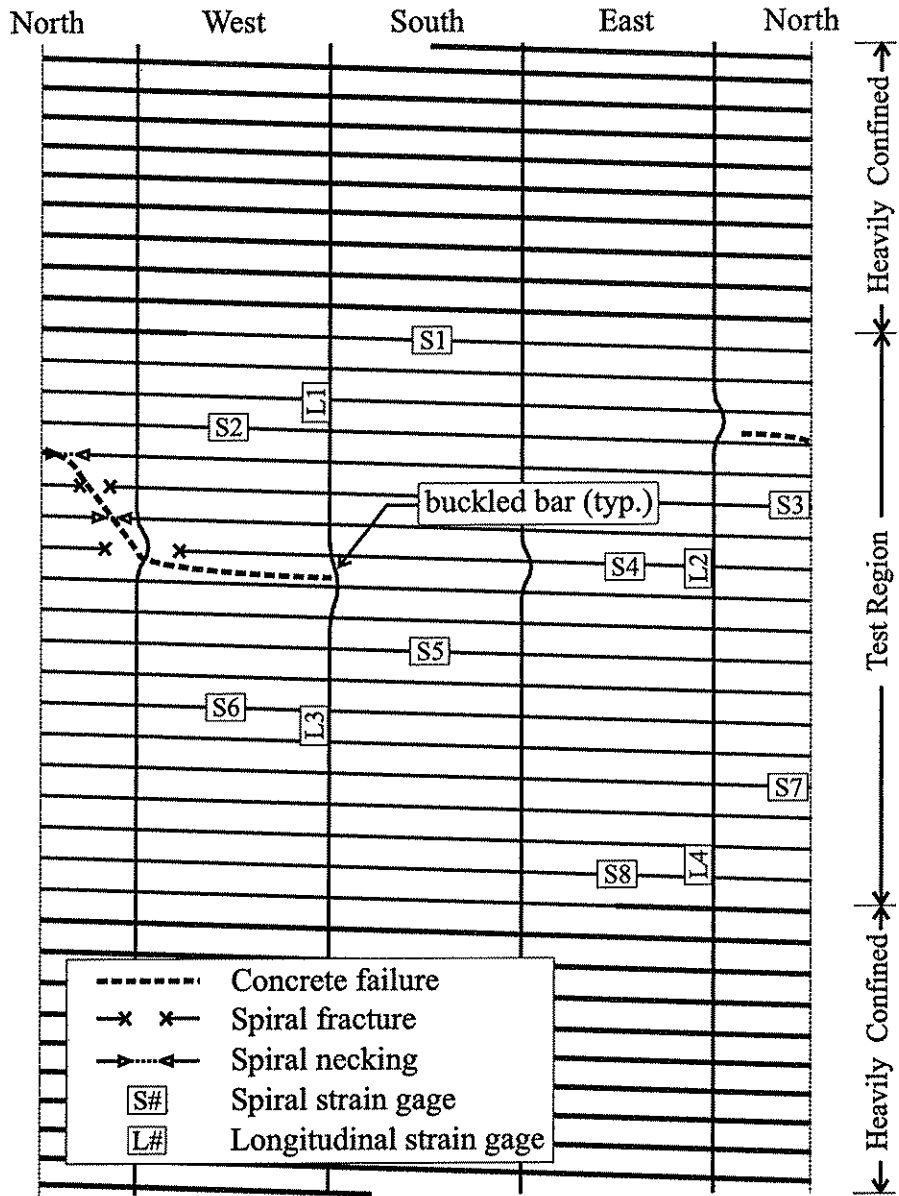
Figure 4.54   Schematic drawing of post-test appearance of Pile 14-D.

(b)

(a)
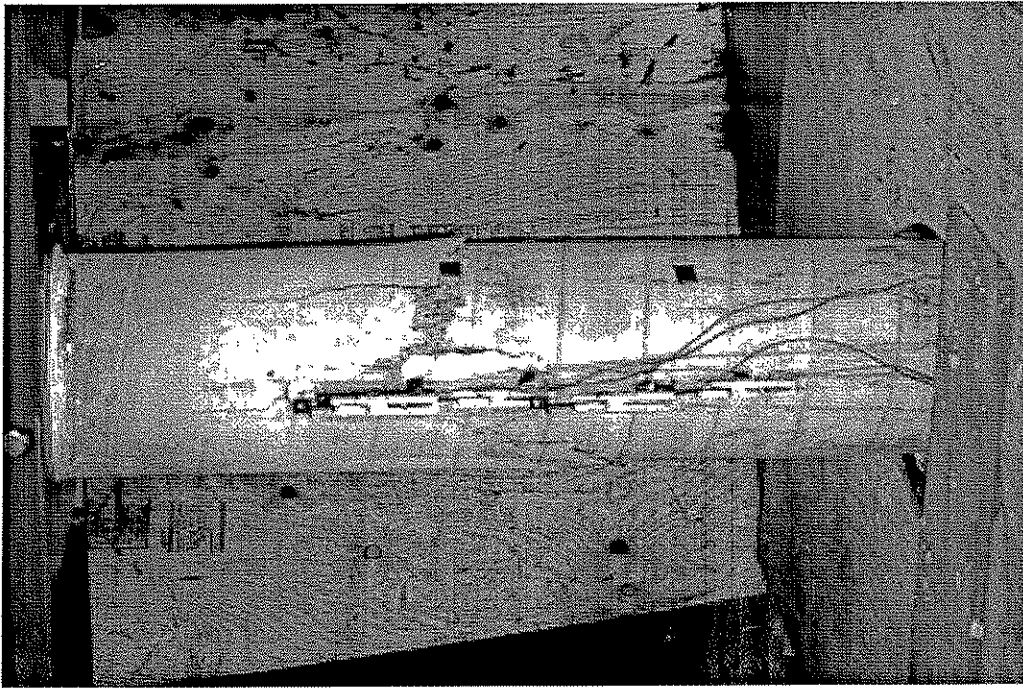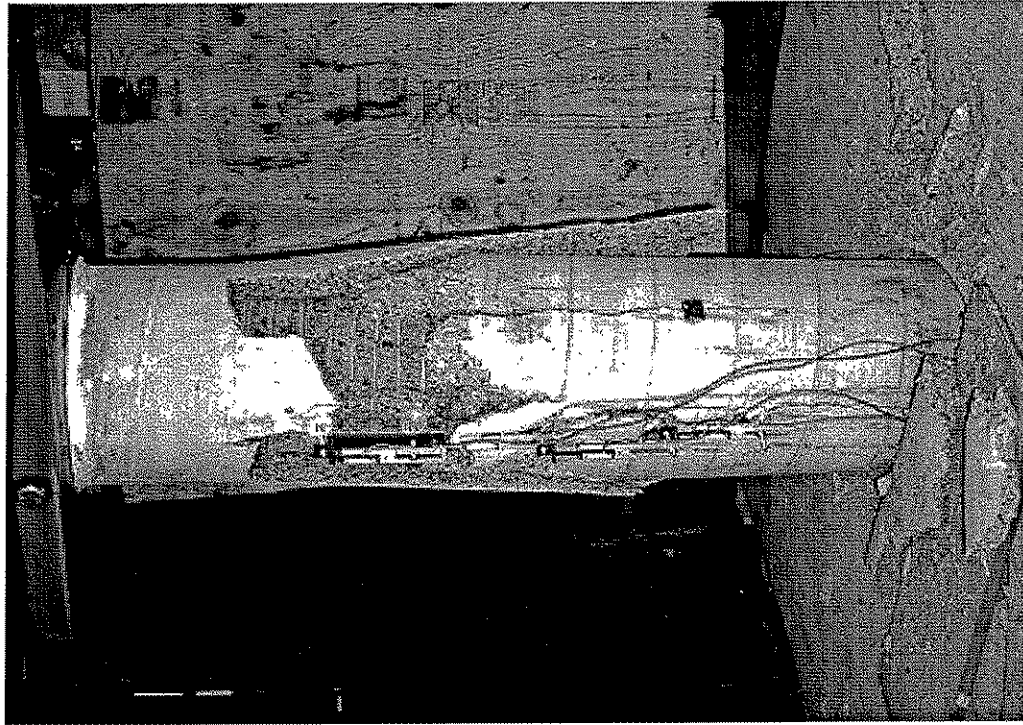
Figure 4.55   Pile 14-D: (a) northeast face after cover failure; (b) northeast face at end of test.

92

(b)

(a)
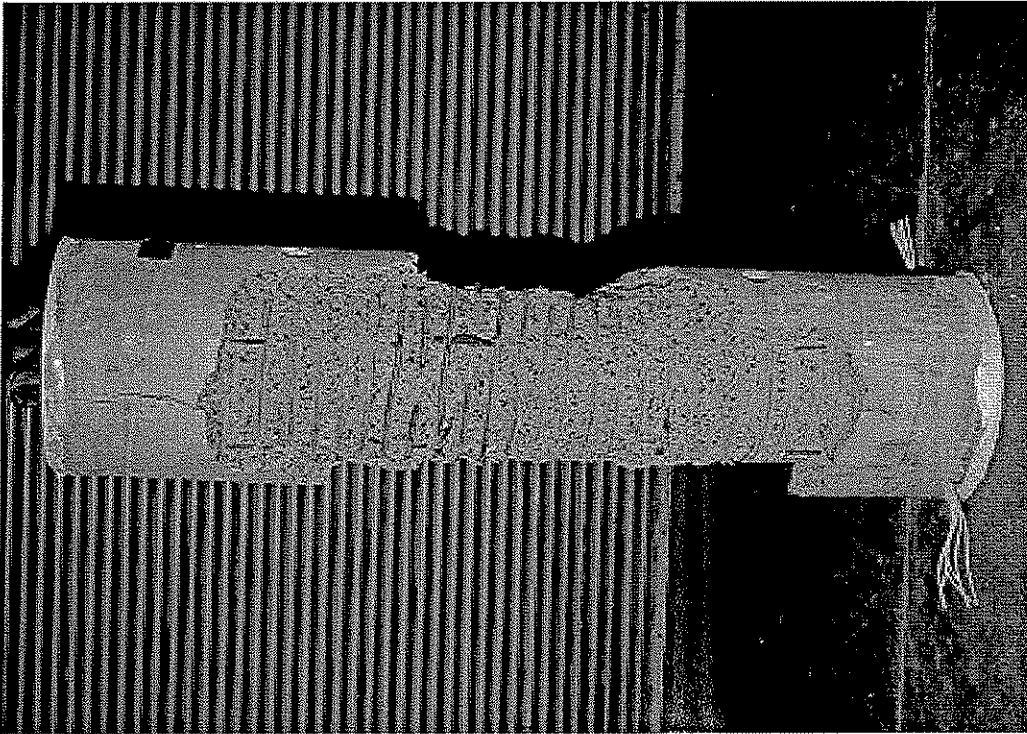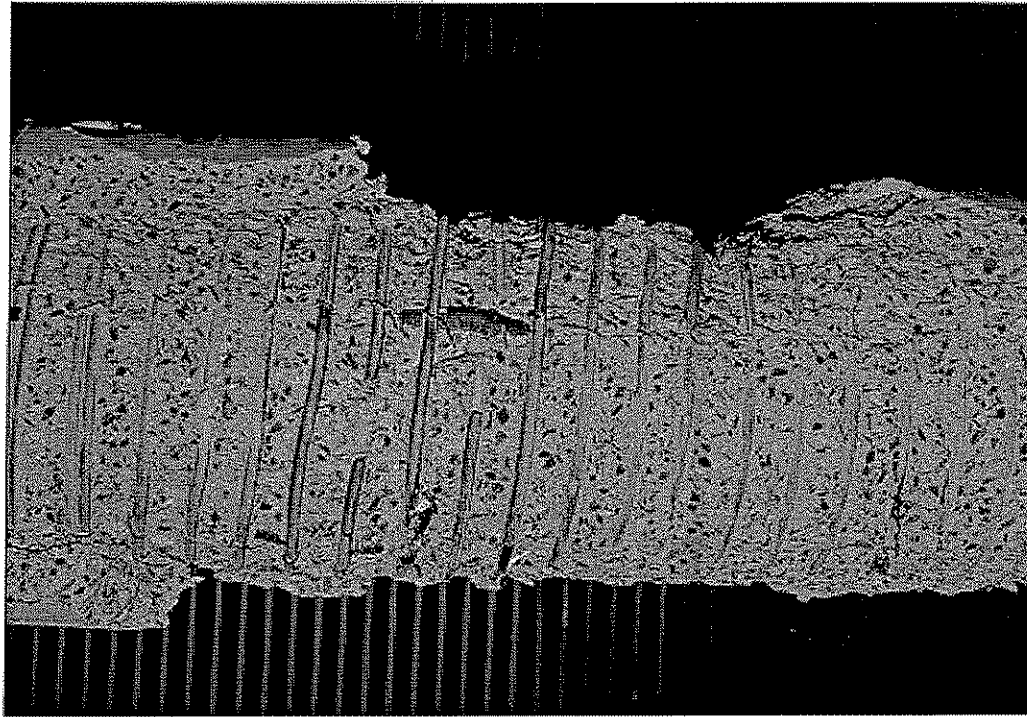
Figure 4.56   Pile 14-D: (a) north face of failed pile; (b) inclined failure plane on north face.

CHAPTER 5
SPIRAL REINFORCEMENT PROPERTIES

5.1 INTRODUCTION

The material properties of the spiral reinforcement, as provided by the spiral manufacturer, were presented in Chapter 3. As discussed earlier, these manufacturer supplied values were used to design the pile specimens. However, for reasons explained in Chapter 3, the properties obtained from the spiral manufacturer may not be sufficiently accurate representations of the actual properties of the spirals. This chapter examines in greater detail the properties of the spiral reinforcement, and the importance of these properties on the behavior of the spiral as it acts in tension as confinement to the core concrete.

A general description of the material properties inherent to high strength steel used as spiral reinforcement is described first in Section 5.2. Coiling a straight length of wire into a permanent spiral configuration introduces residual stresses that alter the mechanical properties of the wire. Section 5.3 presents a qualitative description of the effect that this coiling or "spiraling" has on the mechanical properties of the reinforcement. The effect that spiraling has on the mechanical properties of the reinforcement is studied further in Section 5.4. Numerical analyses are performed to further evaluate the residual stresses on the cross-section created by spiraling. The DRAIN-2DX computer program is used for these analyses. Results from tension tests of the spiral reinforcement which were performed at Lehigh University are presented in Section 5.5. Finally, Section 5.6 presents an approximation of the stress-strain properties of the spiral reinforcement treated in this study.

5.2 GENERAL PROPERTIES OF HIGH STRENGTH SPIRAL STEEL

Figure 5.1 shows sketches of the stress-strain curves of both mild steel and high strength steel. As shown in this figure, the stress-strain behavior of high strength steel differs from that of mild steel. Mild steel exhibits a stress-strain relationship with an effectively constant initial modulus of elasticity, a well-defined yield point, a yield plateau, a strain hardening region, and finally necking and fracture at a relatively large strain. In contrast, high strength steel exhibits few if any of these characteristics. In Figure 5.1, the high strength steel exhibits a decrease in its modulus early on in its stress-strain behavior. This decrease continues throughout the stress-strain curve and no well defined yield point occurs. Eventually, necking occurs, followed by fracture at a strain less than the fracture strain of mild steel.

5.3 EFFECT OF SPIRALING ON THE MECHANICAL PROPERTIES OF REINFORCEMENT

The spiraling of a steel wire into a circular configuration is a physical process which changes the shape of the material. This process also changes the mechanical properties of the steel. Specifically, spiraling causes permanent plastic deformations and residual stresses within the cross-section of the wire. Therefore, a spiraled length of wire will not exhibit the same tensile stress-strain properties as a similar length of wire which was never spiraled (hereafter called unspiraled).

94

The explanation of the effect of spiraling on the mechanical properties of reinforcement requires knowledge of the stress-strain relationship of the reinforcement. For the purposes of the qualitative discussion presented here, an idealized elastic-plastic stress-strain curve will be used. The monotonic uniaxial stress-strain curve for an elastic-plastic material is shown in Figure 5.2(a). Figure 5.2(b) shows the idealized cyclic stress-strain relationship.

Figure 5.3 shows a schematic diagram of the processes which a reinforcement cross-section undergoes during the spiraling process between its unspiraled and its spiraled states. In this figure, the spiraling is caused by the application and subsequent removal of a constant bending moment along the length of the wire. As noted above, the strain and stress distributions shown in this figure are based upon the idealized elastic-plastic stress-strain relationships for mild steel which are shown in Figure 5.2.

Figure 5.3 is arranged in four parts, each of which has five columns. Part (a) describes either the state that exists in the wire or the process that is applied to the wire between two successive states. States are enclosed in boxes and are numbered with Roman numerals (I, II, and III). Processes are enclosed in ovals. Part (b) of the figure shows the moment applied to the length of wire as well as the deformed shape of the wire. Part (c) shows the strain on the cross-section, while part (d) shows the corresponding stresses which occur in the cross-section.

The first column shows the moment, deformed shape, cross-section strain, and cross-section stress for the length of wire in its unspiraled state (I). The second column shows the first process which is performed on the wire. This is the application of the spiraling moment, 'M'. The moment, deformed shape, cross-section strain, and cross-section stress are shown. The third column, intermediate spiraled (II), shows the result of applying the spiraling moment to the unspiraled length of wire. Continuing in the same manner, the fourth column shows the effects of the restoring moment, 'M', which is applied to the wire. The application of this moment can be thought of as a process which removes the spiraling moment which was applied between stages I and II. Note that due to the cyclic stress-strain relationship, a compressive stress of up to two times the yield stress can be applied to portions of the cross-section that at stage II exhibited the tensile yield stress. Similarly, portions of the cross-section that exhibited the compressive yield stress can accept a tensile stress increment equal to up to times the yield stress. The fifth column, spiraled (III), shows the result of applying the restoring moment to the intermediate spiraled length of wire. In the spiraled state, no external moment is applied to the wire, and the original straight length of wire has been turned into a spiral.

Figure 5.5 shows the stress and strain at two depths within the cross-section from the unspiraled (I) through the spiraled (III) state. Figure 5.5(a) shows the stress and strain in the most distant fiber on the portion of the section which initially receives tensile stresses while Figure 5.5(b) shows the stress and strain at the depth indicated in Figure 5.3(c). Additional figures of this type which correspond to the stress and strain diagrams shown in Figure 5.3(c) and (d) could be drawn for any depth within the wire cross-section.

The last column of Figure 5.3(d) shows the residual stress distribution in the cross-section of the length of spiraled wire. These residual stresses exist within the cross-section even though there are no external loads applied to the section (i.e. they are self-equilibrating). Due to these residual stresses in the cross-section, a segment of spiraled reinforcement loaded in direct tension along its curved longitudinal axis (i.e. loaded in the manner in which it would be used in a pile to provide confinement) will not exhibit the same stress-strain properties as it would prior to the spiraling process. In other words, the spiraling process has changed the mechanical properties of the reinforcement. A uniaxial elastic-plastic stress-strain relationship, such as is idealized in Figure 5.2(a) for a piece of unspiraled wire, can no longer occur.

Figure 5.6 explains how the residual stresses in the cross-section of a spiraled wire change the tensile stress-strain properties of the wire. Pure axial tensile loading produces a uniform increase in strain in the cross-section. Initially, this increase in strain causes a uniform increase in stress throughout the cross-section. This continues until the tensile stress in any part of the cross-section reaches the yield stress. Once any part of the cross-section reaches the yield stress, that part of the cross-section no longer exhibits an increase in stress proportional to the continued increase in strain. Through this means, the effective area of the cross-section which can carry additional stress decreases as more of the cross-section reaches the yield stress. As a result of the decrease in effective area of the cross-section, the modulus of the wire decreases. This process continues until the entire cross-section has yielded and the modulus of the wire is zero (i.e. infinite additional strain without any additional stress).

The stresses in the cross-section of a spiraled wire at four points during the application of pure axial loading are shown in Figure 5.6. At point (a), no axial load has yet been applied to the wire. Therefore, point (a) shows only the residual stresses which exist in the cross-section due to the spiraling process. Point (b) shows the wire after the axial load has been increased such that the stress in a small portion of the cross-section has reached the yield stress. Any additional strain increase after this point causes additional portions of the cross-section to yield. This can be seen at point (c) where a significant portion of the cross-section has reached the yield stress. Note that the tensile strain at point (c) is the same strain as would be considered the yield strain for an unspiraled wire. Finally, point (d) shows the wire after the entire cross-section has reached the yield stress.

Section 5.5 presents the results of tension tests that were performed on lengths of the 20 in. (508 mm) diameter spiral wire. The tension specimens were made by straightening lengths of the spiraled wire. The following discussion addresses the influence of this straightening process on the residual stresses in the cross-section and the impact of these residual stresses on the stress-strain curve of the wire. Again, to simplify matters, the discussion is presented for a material that has the idealized stress-strain properties shown in Figure 5.2.

The process of straightening a spiraled wire is similar to the process of spiraling a straight length of wire. Figure 5.4 shows the states and processes which a spiraled wire undergoes as it is straightened. This figure is organized in the same manner as was Figure 5.3. The first column of

Figure 5.4 shows the spiraled state (III) as shown in the fifth column of Figure 5.3. The process of applying a straightening moment to the spiraled state (III) is shown in the second column. The third column shows the result of the application of this process and is labeled as intermediate straightened (IV). The straightening moment is then removed from the wire through the process shown in the fourth column. The fifth column shows the straightened state (V). The residual stress on the cross-section of a spiraled/straightened wire is shown in the fifth column of Figure 5.4(d). Once again, Figure 5.5 shows the stresses and strains at two cross-sectional depths for the spiraled (III) through the straightened state (V).

Similar to Figure 5.6, Figure 5.7 shows the stresses in the cross-section of a spiraled/straightened wire at four points during the application of tensile axial load. Once again, point (a) shows the unloaded cross-section with residual stresses. Point (b) shows the cross-section at the limit of elastic behavior. Point (c) shows the point when a significant portion of the cross-section has reached the yield stress, and point (d) shows the wire when the entire cross-section has reached the yield stress.

In addition to the unspiraled stress-strain properties of the reinforcement, there are three factors which influence the magnitude and pattern of residual stresses which exist in the cross-section after the spiraling and/or straightening processes. These factors are: (1) the shape of the reinforcement cross-section; (2) the dimensions of the reinforcement cross-section; and, (3) the diameter of the spiral. A detailed evaluation of these three additional factors is beyond the scope of the present study.

5.4 NUMERICAL EVALUATION OF THE EFFECT OF SPIRALING ON THE MECHANICAL PROPERTIES OF REINFORCEMENT

The analysis program DRAIN-2DX (Prakash and Powell 1993) was used to study the effect of spiraling on the mechanical properties of reinforcement. The study focused on two issues: (1) the strains and stresses that exist on the cross-section of a wire during the various states as the wire is spiraled; and (2) the effect that spiraling and straightening have on the tensile stress-strain relationship of an unspiraled wire. A brief description of the fiber modeling procedure in the DRAIN-2DX program, and the use of the fiber model in the current study to model the wire in the spiraling process, is presented first in Section 5.4.1. Section 5.4.2 explains the strains and stresses that exist on the wire cross-section during spiraling, and Section 5.4.3 explains the effect that spiraling and straightening have on the stress-strain curve.

5.4.1 DRAIN-2DX Fiber Modeling

The analyses described in this section use the fiber element in the DRAIN-2DX analysis program. This fiber element is a nonlinear inelastic element. Among other things, the fiber element can be used to model the axial and/or flexural behavior of a steel member into the inelastic range. Modeling of inelastic behavior is achieved by discretizing the cross-section of the member into a number of fibers. Each fiber is characterized by a uniaxial stress-strain relationship, an area, and a distance from a reference axis along the length of the member. The monotonic uniaxial stress-strain relationship for each fiber is user defined and applies to the fiber loaded under uniaxial

97

loading. This stress-strain relationship can be defined by up to five linear segments. The cyclic stress-strain relationship of the fiber is computed by the program based on the monotonic uniaxial curve and hysteretic rules that are predefined for a steel member. Sample cyclic stress-strain curves are shown in Figure 5.8(b) and 5.8(c). Figure 5.8(b) shows the cyclic stress-strain relationship for idealized elastic-plastic steel. Figure 5.8(c) shows the cyclic stress-strain relationship for a four linear segment idealization of a high strength steel uniaxial stress-strain curve. As shown in Figure 5.8(c), the strains in the uniaxial stress-strain curve are doubled in order to determine the shape of the cyclic curve.

The response of the fiber element assumes linear strain compatibility of the cross-section. Using a plane section analysis, an assumed curvature leads to the strain that exists in each fiber. The stress-strain curve is then used to compute the stress in each fiber. These stresses are integrated over the cross-section and equilibrium is checked with the applied forces (moments in this case). Successive values of curvature are assumed until equilibrium is satisfied.

The modeling of the wire in DRAIN-2DX requires that the cross-section and length of the wire be defined. The DRAIN-2DX model of the wire was composed of a segment of wire whose length was equal to 10 percent of the circumference of the spiraled configuration of the same wire. This length of wire can be seen in Figure 5.8(a). The shape of the cross-section is circular with a diameter of 0.35 in. (8.89 mm). However, note that the dimensions of the cross-section are entirely defined through the definition of the fibers which comprise the cross-section. Figure 5.8(a) shows a circular cross-section divided into 14 fibers, each of the same height.

The number and location of fibers within the cross-section of the wire has a large influence on the accuracy of the model results. In general, an increase in the number of fibers will increase the accuracy of the results. However, an increase in the number of fibers also increases the computational time required to complete an analysis. Beyond a certain number of fibers, adding additional fibers to the cross-section will only increase the computational time but will not greatly alter the results of the analysis. A study was performed to determine the number of fibers with uniform height and oriented parallel to the bending axis of the member that were required to provide convergence. The solution was considered to have converged when the curvature caused by an applied load did not change by more than 0.5 percent. The division of the cross-section into 140 fibers was found to provide the required convergence.

The spiraling and straightening of a steel wire was modeled through the application of a constant moment over the length of the wire. In this way, throughout all processes, every cross-section of the wire exhibited the same response. Specifically, the modeling of the spiraling and straightening processes was performed as follows. The spiraling process was initiated with the application of a constant moment to the ends of the wire. This moment was of such a magnitude that the radius of curvature of the deformed shape of the wire would be smaller than the desired spiral radius of curvature. The next step was to release the spiraling moment. This was done through the application of an equal and opposite moment to the original spiraling moment. In a trial and error man-

ner, this process was repeated from the beginning with the unspiraled wire until the radius of the wire in the spiraled configuration was equivalent to the desired spiral radius.

The modeling of the straightening process is similar to the spiraling process described above. First, a moment was applied to the spiraled wire. This moment was slightly smaller in magnitude than the original spiraling moment and was oriented so as to straighten the wire. Next the equal and opposite moment was applied (i.e. the straightening moment was released). This set of moment applications was repeated through a trial and error manner, each time beginning with the spiraled wire, until the correct straightening moment was determined. The correct straightening moment caused all strains in the cross-section to equal zero after all applied moments were removed.

DRAIN-2DX was also used to model the application of an axial tensile load to the wire in its unspiraled, spiraled, and spiraled/straightened states. The application of load was displacement controlled. Through this load application, a monotonic uniaxial stress-strain curve for the wire in each state was obtained.

5.4.2   Residual Stresses in the Cross-Section of Spiraled and Straightened Wire

DRAIN-2DX was used determine the stresses which remain in the cross-section of the steel wire after the spiraling and the straightening processes. At each state in the spiraling and straightening processes, the strains in the cross-section of the wire were obtained. Through the use of these strains and the unspiraled stress-strain relationship which was defined in the model, the stresses in the cross-section at each state were determined.

Figures 5.9 and 5.10 show the residual stresses which remain in a wire cross-section after the spiraling process and the straightening process. These figures treat the case of an elastic-plastic steel wire (with the cyclic stress-strain properties shown in Figure 5.8(b)). Figures 5.9 and 5.10 are drawn to scale.

Figure 5.9 presents the residual stresses on the wire cross-section after spiraling. Part (a) of the figure is for a 20 in. (508 mm) diameter spiral, and part (b) of the figure is for a 10 in. (254 mm) diameter spiral. Figures 5.9(a) and (b) agree well with the sketch of the distribution of residual stresses shown in the last column of Figure 5.3(d). Finally, a comparison of Figures 5.9(a) and (b) shows that the magnitude of residual stresses increases as the diameter of the spiraled steel decreases.

Figure 5.10 show the residual stresses on the cross-section after straightening as obtained from DRAIN-2DX. Just as for Figure 5.9, part (a) of this figure is for a 20 in. (508 mm) diameter spiral, and part (b) is for a 10 in. (254 mm) diameter spiral. These figures show good agreement with the qualitative description of residual stresses presented in the last column of Figure 5.4(d). Comparison of Figures 5.10(a) and (b) shows that the area of the portion of the cross-section nearest the neutral axis which remains elastic throughout the entire spiraling and straightening process (and

99

thus has no residual stresses in the straightened configuration) decreases as the spiraled diameter decreases.

5.4.3 Effect of Spiraling on the Tensile Stress-Strain Relationship

The DRAIN-2DX analysis program was used to study the tensile stress-strain relationships of spiraled and spiraled/straightened wires. Figure 5.11 shows the DRAIN-2DX results of the tensile load application to the unspiraled, spiraled, and spiraled/straightened states of a 60 ksi (414 MPa) elastic-plastic wire. This figure shows results of applying an axial tensile load to a wire that was spiraled into a 20 in. (508 mm) diameter spiral. It also shows the results of applying an axial tensile load to a 20 in. (508 mm) diameter spiraled/straightened wire. The curves shown on this figure can be directly related back to Figures 5.6 and 5.7. As described earlier, the residual stresses which are present in the spiraled and spiraled/straightened wire as shown in Figures 5.9 and 5.10, respectively, cause the stress-strain relationship to become more rounded as compared to the stress-strain relationship for the unspiraled wire.

The DRAIN-2DX model was also used to study the effect that spiraling and straightening had on the Grade D steel which was used in the experimental portion of the study. First, the unspiraled stress-strain curve was obtained through tensile testing performed at Lehigh University. This testing is explained in Section 5.5. The stress-strain curve obtained is shown in Figure 5.12. A 5 segment linear approximation of this stress-strain curve was then computed and entered into the DRAIN-2DX model. This multi-linear approximated curve is also shown in Figure 5.12.

Using the multi-linear stress-strain curve shown in Figure 5.12 and the DRAIN-2DX model, the same processes as described above were applied to this Grade D wire to form it into a spiraled then into a spiraled/straightened configuration. Two different spiral diameters were analyzed, 20 in. (508 mm) and 10 in. (254 mm). The results are shown in Figure 5.12. Once again, the same changes in behavior as occurred in the idealized elastic-plastic steel are observed. Specifically, the spiraled/straightened steel exhibits a more rounded stress-strain curve than the unspiraled steel. In turn, the spiraled steel exhibits a more rounded curve than the spiraled/straightened steel. This applies to both spiral diameters. Finally, this figure shows that different tensile stress-strain relationships are exhibited by a wire which is spiraled to different diameters. Specifically, this figure shows that the smaller diameter spiral exhibits a more rounded curve than does the larger diameter spiral. Thus, the in situ stress-strain properties also depend in part on the spiral diameter.

5.4.4 Summary of Findings from Numerical Modeling of Influence of Spiraling on Mechanical Properties of Reinforcement

The results obtained from the numerical modeling of the spiraling and straightening of reinforcement compare well with the qualitative discussions presented in Section 5.3. This can be seen by comparing the residual stresses presented in Figures 5.3 and 5.4 with the DRAIN-2DX results presented in Figures 5.9 and 5.10, respectively. Also, the results presented in Figures 5.6 and 5.7 correlate well to the DRAIN-2DX results presented in Figure 5.11. Clearly, residual stresses in the cross-section, introduced by spiraling, or by spiraling/straightening, cause a rounding of the stress-strain curve.

100

5.5 LEHIGH UNIVERSITY TENSION TESTS OF SPIRAL REINFORCEMENT

As was noted earlier, tension testing was performed at Lehigh University on the spiral reinforcement. Tension tests were performed on unspiraled pieces of the Grade D spiral obtained from the spiral manufacturer. Tension tests were also performed on lengths of spiral that were cut from the 20 in. (508 mm) diameter spirals for all four grades of steel. These lengths were first straightened as much as possible by bending prior to the tension tests. All tensile tests were performed in a 60 kip (267 kN) capacity universal testing machine. Strain gages were placed along the longitudinal axis of the wire to obtain axial strain readings. In the initial tests performed, four gages were positioned around the perimeter of one cross-section of the wire. These gages showed that one gage was sufficient to determine the cross-sectional strain. In subsequent tests, only one gage was used. This gage was placed arbitrarily on the unspiraled steel and on the neutral axis of the cross-section in the spiraled/straightened steel. Note that the neutral axis of the wire is defined as the axis about which the wire was bent to form the spiral.

Figure 5.14 shows the tensile stress-strain curves which were obtained from the sections of straightened spiral. Each curve is either the average reading of the four strain gages or the reading from the one strain gage, depending on the gage configuration used. All four grades of steel are shown in the figure. Note that these stress-strain relations come from 20 in. (508 mm) diameter straightened spirals and, based on Figure 5.13, are expected to differ from those obtained from a straightened 10 in. (254 mm) diameter spiral. For the three higher strength steel grades, just prior to fracture, both the stress and strain are observed to decrease. This is due to necking which occurs along the wire at a location away from where the strain gages were located. For the Grade A spiral, necking occurred directly under the strain gages. Therefore, no necking or fracture data was obtained as the gages debonded from the wire as the wire necked.

Figure 5.15 shows a close-up of the stress-strain curves for the four grades of straightened 20 in. (508 mm) spiral up to a strain of 0.01. This range is of particular importance in this study because the strain in the spiral reinforcement generally did not exceed 0.01 prior to reaching Δ_2 in the pile tests. In this figure, the rounded nature of the stress-strain curves is clearly visible. This is especially evident for the three higher grades of reinforcement.

Table 5.1 provides material properties for the four grades of spiral reinforcement. The yield strength is given both as reported by the spiral manufacturer and as determined from the experimental testing performed at Lehigh University. The EUL Method is the Elongation Under Load Method and is the method used by the spiral manufacturer to determine the yield strength of the spirals. The 0.2% offset method was used in the experimental testing performed at Lehigh University to determine the yield strength. In this method, the initial modulus of the steel is calculated using stresses from approximately 0 to 25 ksi (0 to 172 MPa). Then a line with this modulus is drawn on the spiral stress-strain plot beginning at an offset strain of 0.002. The point of intersection between the offset modulus line and the stress-strain curve defines the yield stress and strain.

101

Table 5.1 shows that the yield strengths determined from the spiraled/straightened steel tests performed at Lehigh are below the yield strengths determined by the spiral manufacturer. This can be attributed to both the effects of spiraling and straightening on the steel as well as the different methods used to determine yield. The table also provides the ultimate strength of the spiral steel, f_{su}, as well as the corresponding strain, ε_{su}. Note that, as expected, the ultimate strengths of all specimens of each grade are similar.

As stated previously and shown in Table 5.1, experimental stress-strain curves were obtained for both unspiraled and spiraled/straightened wires for the Grade D steel. Through the comparison of the curves from these tests, the effect of the spiraling/straightening process on this steel can be observed. The stress-strain curve for unspiraled Grade D steel is shown in Figure 5.16. Also shown in this figure is the stress-strain curve for the spiraled/straightened piece of Grade D steel.

As can be seen on the figure, the ultimate strength of these two wires differs by approximately 5 ksi (34.5 MPa). In order to allow for direct comparison between the two stress-strain curves, the stress values in these curves were normalized by the ultimate stress that each wire reached. A plot of the normalized stress stress-strain relationships can be seen in Figure 5.17. This figure clearly shows that the spiraled/straightened steel does exhibit an earlier reduction in its modulus and thus a more rounded stress-strain curve than the unspiraled steel.

5.6 APPROXIMATION OF SPIRAL STRESS-STRAIN PROPERTIES

In order to accurately study the behavior of spiral reinforcement in a spirally reinforced member, it is important to understand the mechanical properties of spiral reinforcement. However, as a practical matter, it is difficult to obtain the stress-strain properties of spiral reinforcement while it is in its spiraled configuration. This section presents an approximation of the spiral properties of each grade of spiral reinforcement treated in this research. These approximations are based on the experimental testing performed at Lehigh University on spiraled/straightened pieces of wire. Additionally, a discussion is presented which notes the changes which could be made to the spiraled/straightened stress-strain curves to make them more closely resemble the actual in situ properties of the spiral reinforcement.

For practical reasons, experimental tensile testing of spiral reinforcement is generally performed on a straight piece of reinforcement. This reinforcement could be in either the unspiraled or spiraled/straightened state. As was explained in Section 5.5, the four grades of steel treated in this study were tested in their spiraled/straightened configuration after they were cut from the 20 in. (508 mm) diameter spirals. These stress-strain relationships are shown in Figure 5.14. These are the only experimentally obtained stress-strain relationships obtained for all four grades of steel.

The stress-strain relationships shown in Figure 5.14 do not represent the actual in situ stress-strain properties of the spiral. The components required to understand the in situ spiraled steel stress-strain relationship have been presented throughout this chapter. It was shown that the stress-strain properties of the spiraled reinforcement are not solely a function of the grade of the steel. Instead,

102

the properties are also a function of the residual stresses in the cross-section, which in turn are a function of the mechanical processes applied to the spiral as it is formed.

Two deviations are admitted, both of which will cause a more rounded appearance (i.e. larger strain at any given stress) to the stress-strain relation. First, the curves shown in Figure 5.14 do not represent steel from the 10 in. (254 mm) diameter spiral. Curves for a 10 in. (254 mm) diameter spiral would fall slightly inside the curve for the 20 in. (508 mm) diameter spiral. Second, the curves shown in Figure 5.14 represent the spiraled/straightened state, not the spiraled state. The curve for the spiraled state would also fall slightly inside the curve for the spiraled/straightened state.

Correction factors which would adjust the spiraled/straightened stress-strain curve to better represent the in situ spiraled stress-strain curve are not known. For this reason, the spiraled/straightened stress-strain curve is used as an approximation of the spiraled stress-strain curve. A best-fit equation was determined for each of the curves shown in Figure 5.14. The best-fit equation curves are plotted as dashed lines on Figure 5.14 and were fitted for strains between 0.000 and 0.030. The strain value of 0.030 was chosen because the strains measured in the pile tests were always below this value and the ultimate strain of each piece of steel as determined from the Lehigh University spiral steel tests was above this value. The figure also shows the equations for the best-fit curves, along with their R^2 value to denote the accuracy of the approximation. These best-fit curves are used in the analysis of results presented in Chapter 6.

Spiral Steel Type	State at Testing	EUL Method Yield Stress (ksi)	0.2% Offset Yield Strain	0.2% Offset Yield Stress (ksi)	f_{su} (ksi)	ε_{su}	Data Source
A	Unspiraled	78	-	-	84	-	Manufacturer
A	Straightened	-	0.0048	76	85	> 0.0030	Lehigh
B	Unspiraled	107	-	-	116	-	Manufacturer
B	Straightened	-	0.0058	102	119	0.0029	Lehigh
C	Unspiraled	121	-	-	143	-	Manufacturer
C	Straightened	-	0.0065	109	140	0.0033	Lehigh
D	Unspiraled	140	-	-	174	-	Manufacturer
D	Unspiraled	-	0.0071	132	173	0.0033	Lehigh
D	Straightened	-	0.0065	111	168	0.0032	Lehigh

1 ksi = 6.895 MPa

Table 5.1   Spiral reinforcing steel material properties.
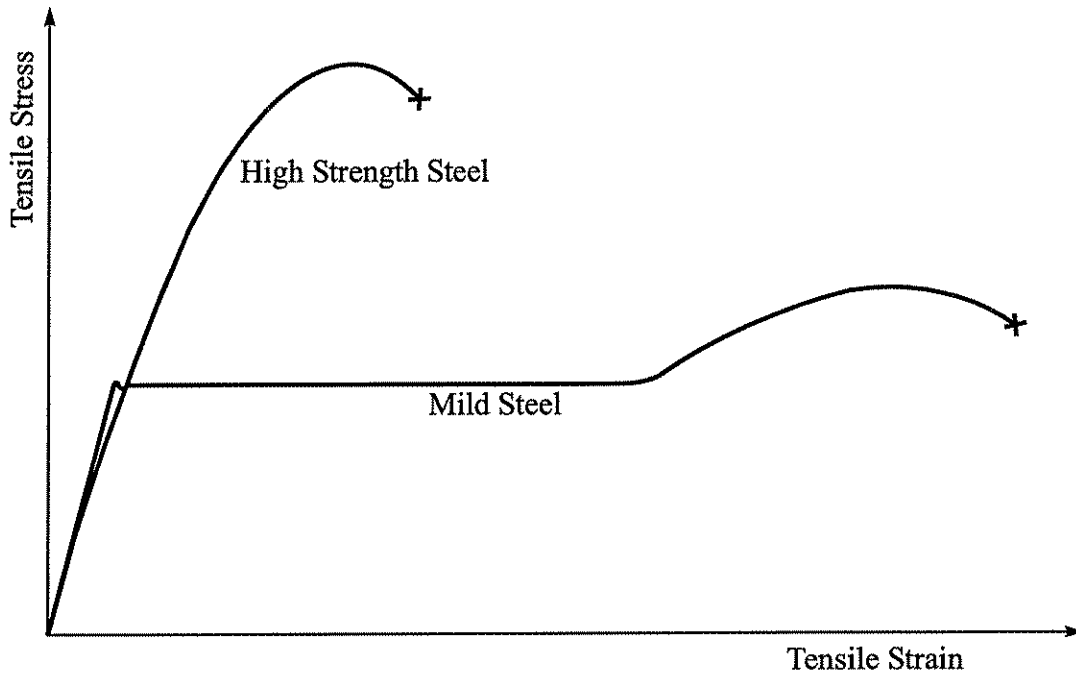
Figure 5.1   Comparison of stress-strain relationships of mild and high strength steel.
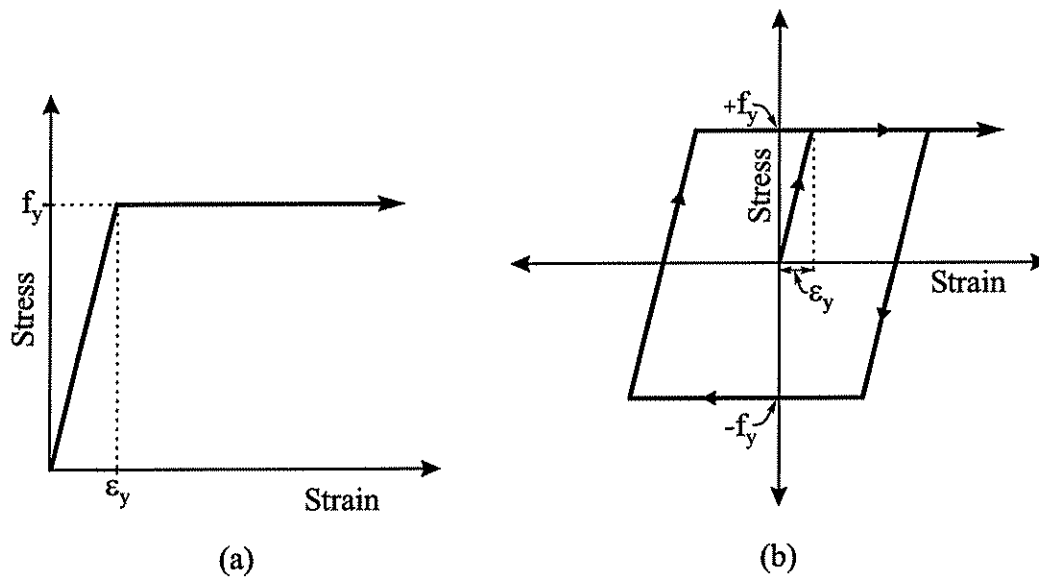
Figure 5.2   Idealized stress-strain relationships for mild steel: (a) monotonic; and
(b) cyclic.

105

(a) State or Process

(b) Loading and Deformed Shape

(c) Strain on Cross-Section

— (depth on cross-section treated in Figure 5.5(b))
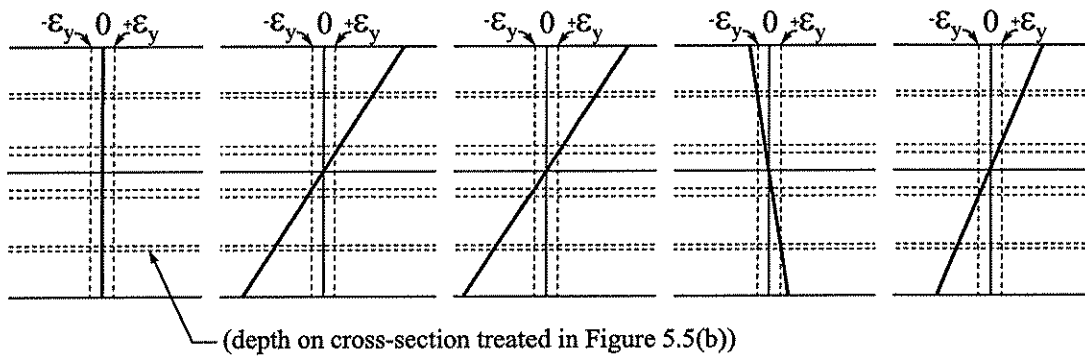
(d) Stress on Cross-Section

Figure 5.3   Effect of spiraling on the strains and stresses in the cross-section of an unspiraled wire.

(a) State or Process
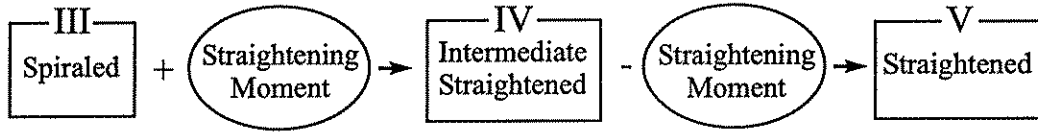
(b) Loading and Deformed Shape
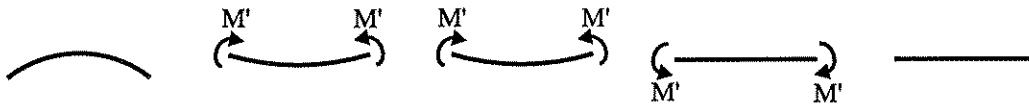
(c) Strain on Cross-Section
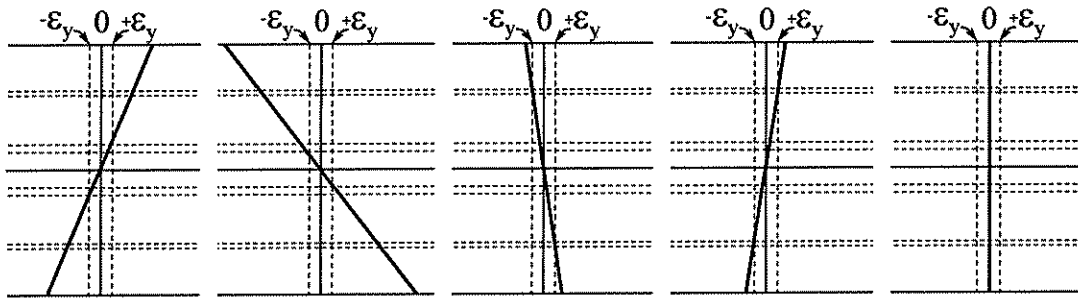
(d) Stress on Cross-Section
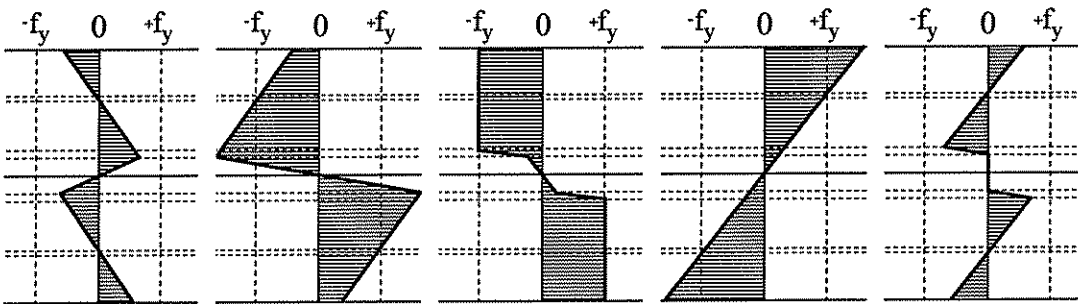
Figure 5.4   Effect of straightening on the strains and stresses in the cross-section of a spiraled wire.

107

(a)

(b)
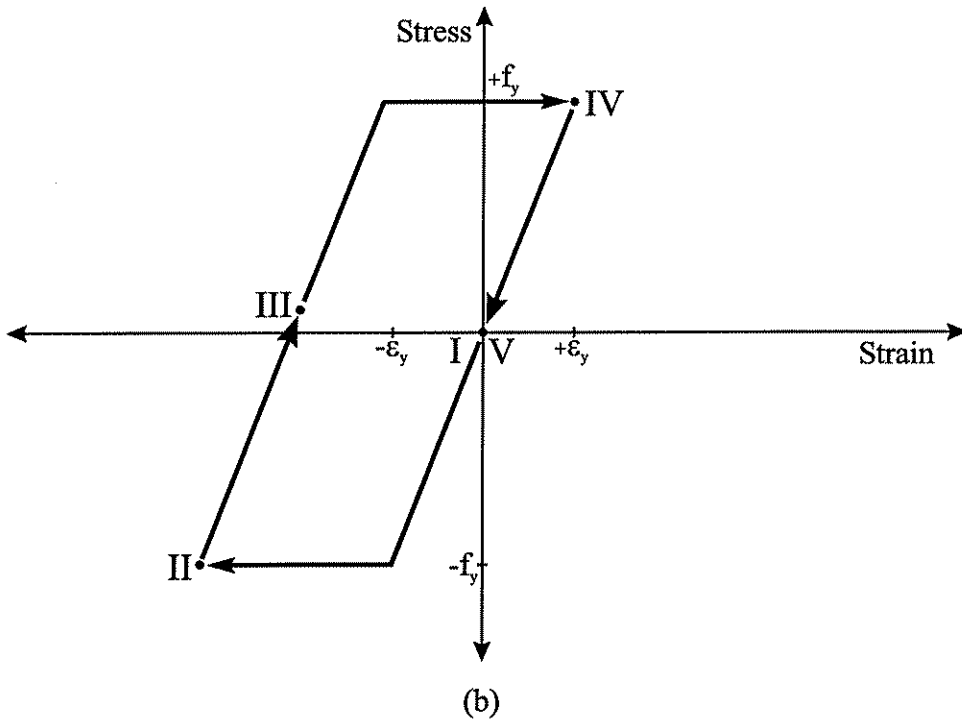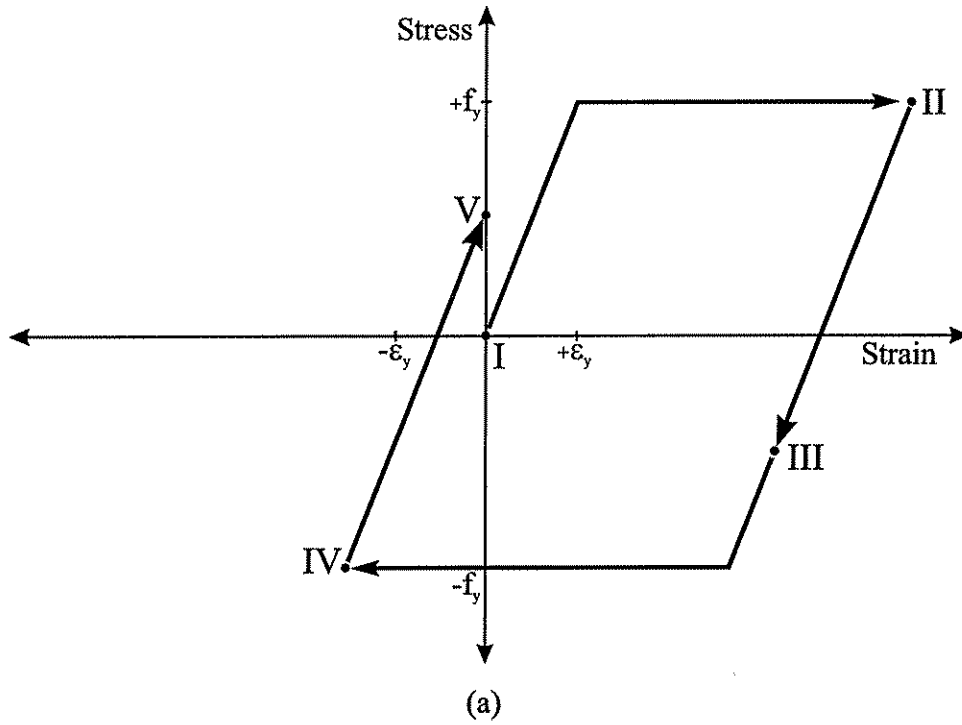
Figure 5.5   Stress and strain during the spiraling and straightening processes at: (a) the most distant initial tensile fiber; and (b) the location noted in Figure 5.3(c).

108
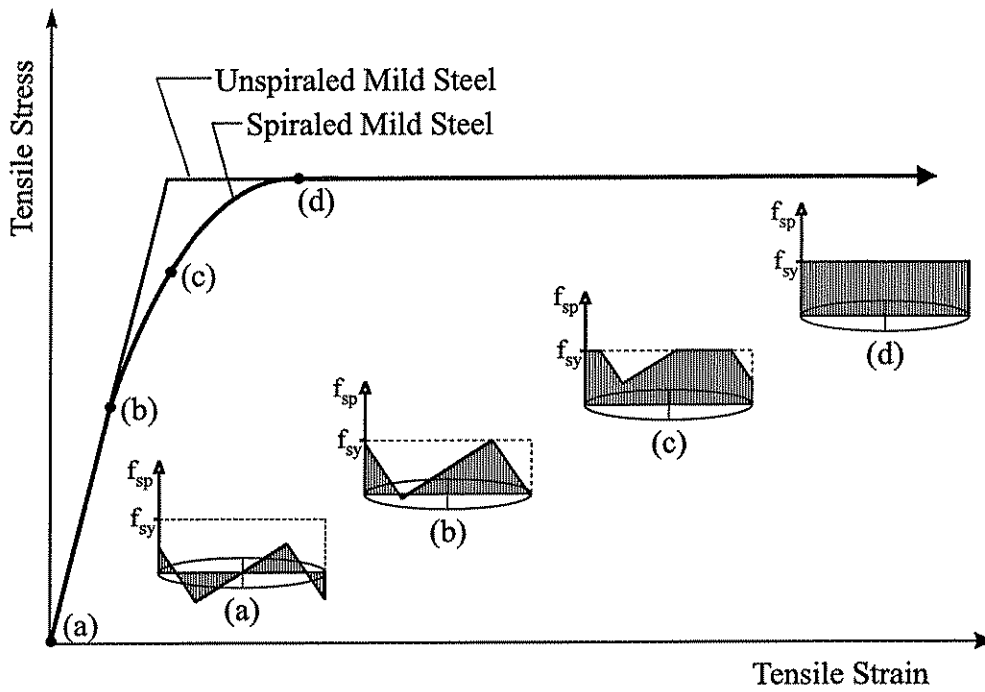
Figure 5.6   Stresses in the cross-section of a spiraled wire throughout the application of a tensile load.
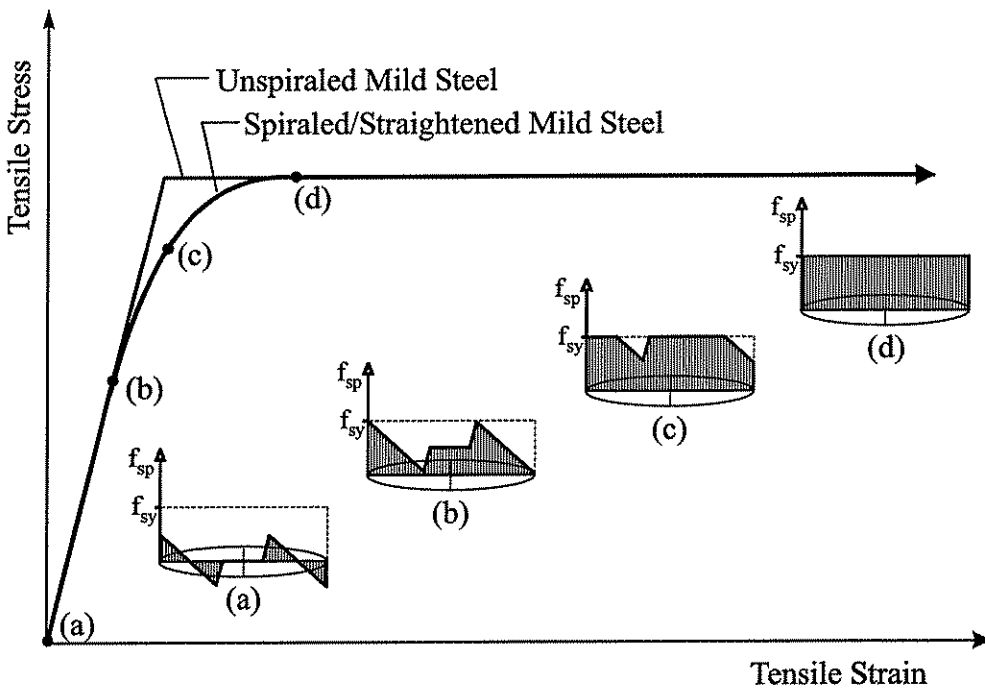
Figure 5.7   Stresses in the cross-section of a spiraled/straightened wire throughout the application of a tensile load.

109
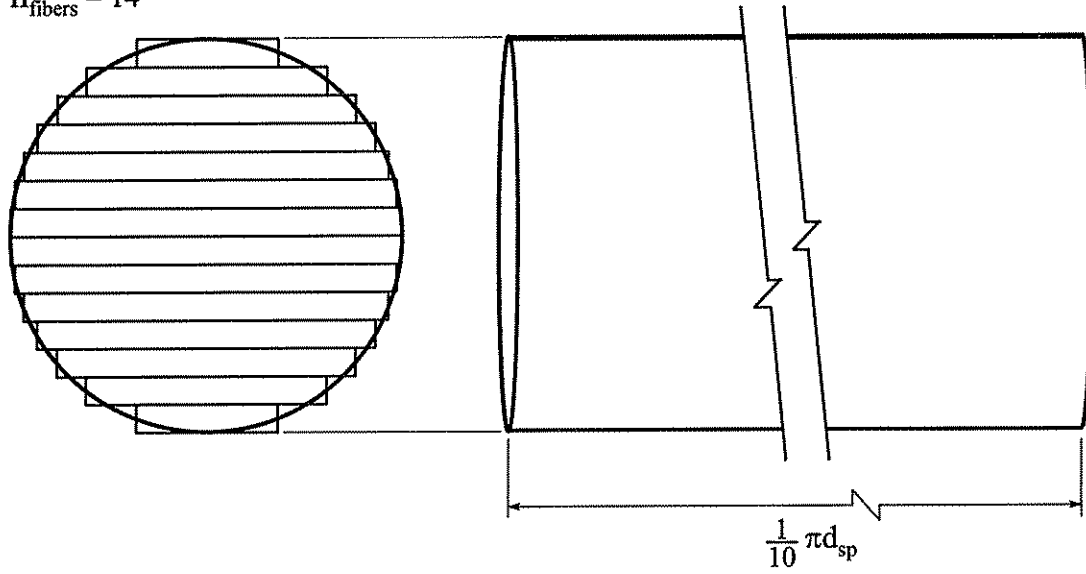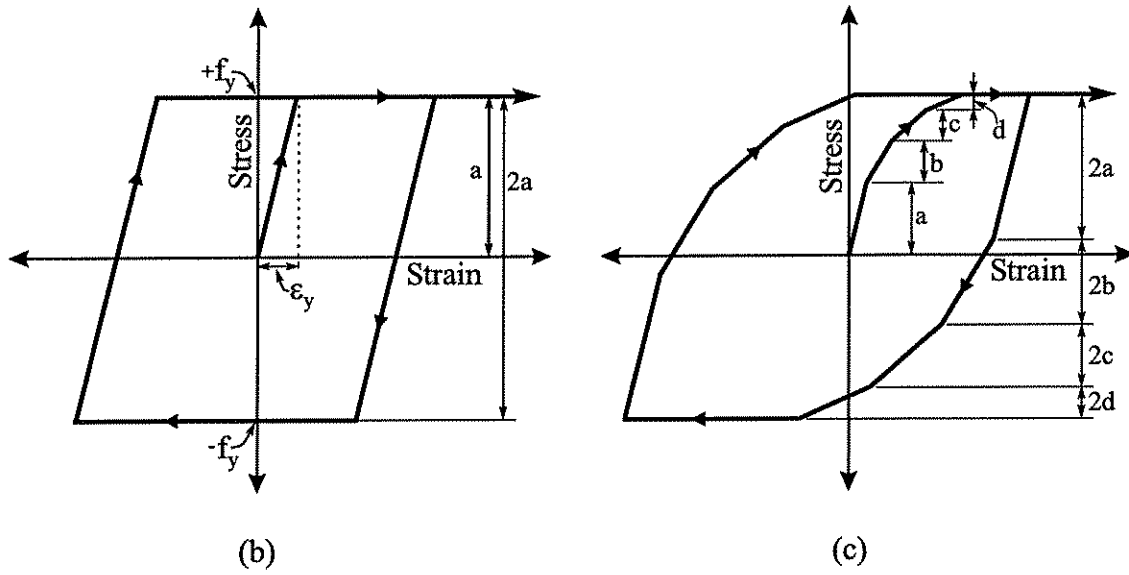
Figure 5.8   DRAIN-2DX model of: (a) wire cross-section and length; (b) cyclic
stress-strain relationship of idealized elastic-plastic stress-strain curve; and
(c) cyclic stress-strain relationship of multi-linear stress-strain curve.

110
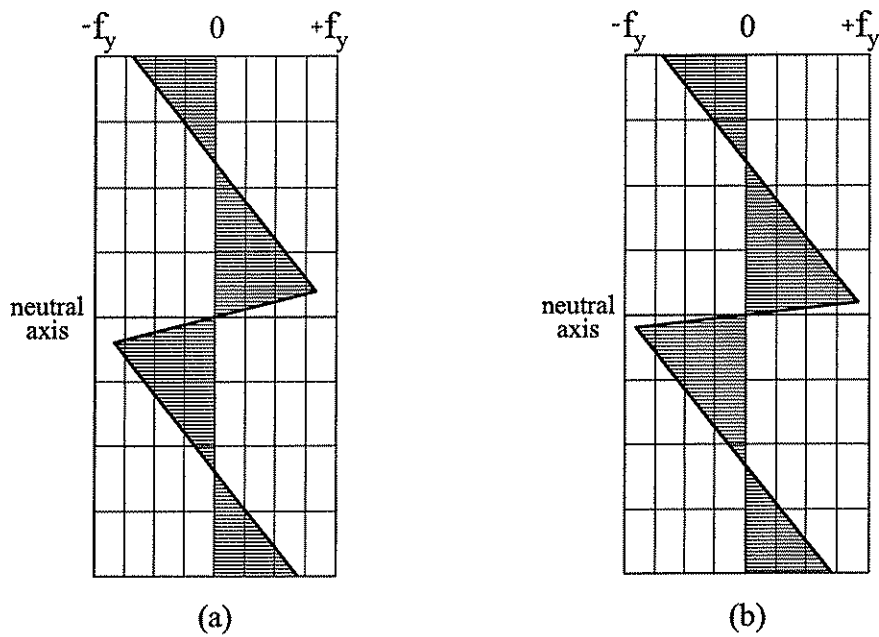
Figure 5.9   Residual stresses on the cross-section of a spiraled wire from DRAIN-2DX
results for 60 ksi elastic-plastic steel, 0.35 in. diameter wire: (a) 20 in.
spiral diameter; (b) 10 in. spiral diameter.
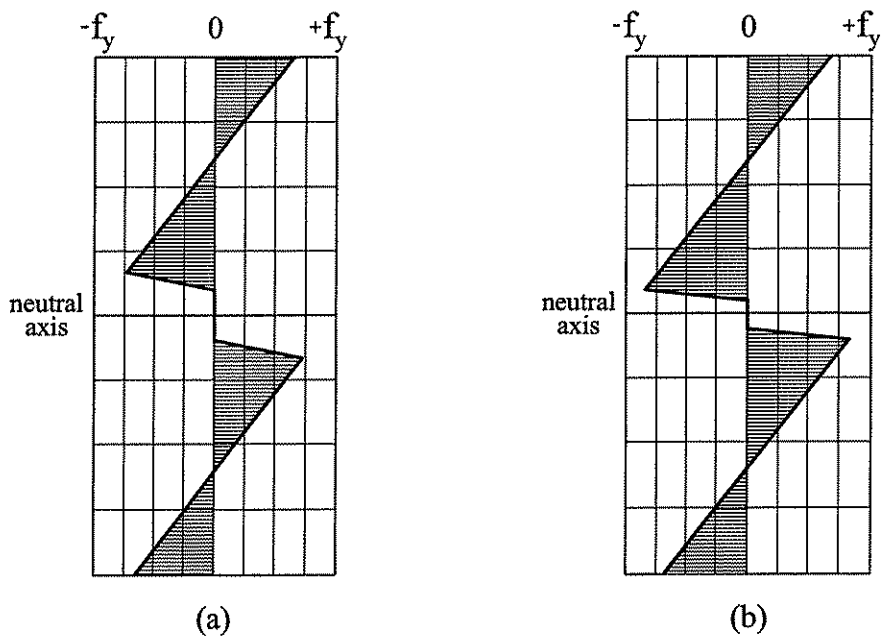
Figure 5.10   Residual stresses on the cross-section of a spiraled/straightened wire from
DRAIN-2DX results for 60 ksi elastic-plastic steel, 0.35 in. diameter wire:
(a) 20 in. spiral diameter; (b) 10 in. spiral diameter.
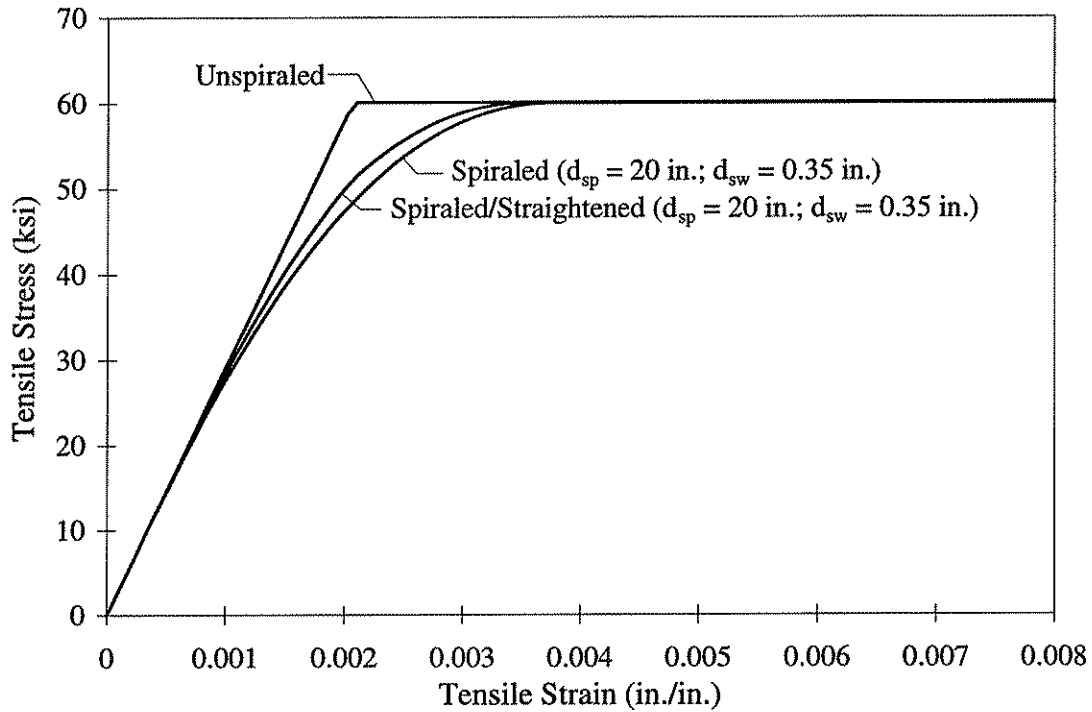
Figure 5.11   DRAIN-2DX analysis results showing effect of spiraling on 60 ksi
elastic-plastic steel.
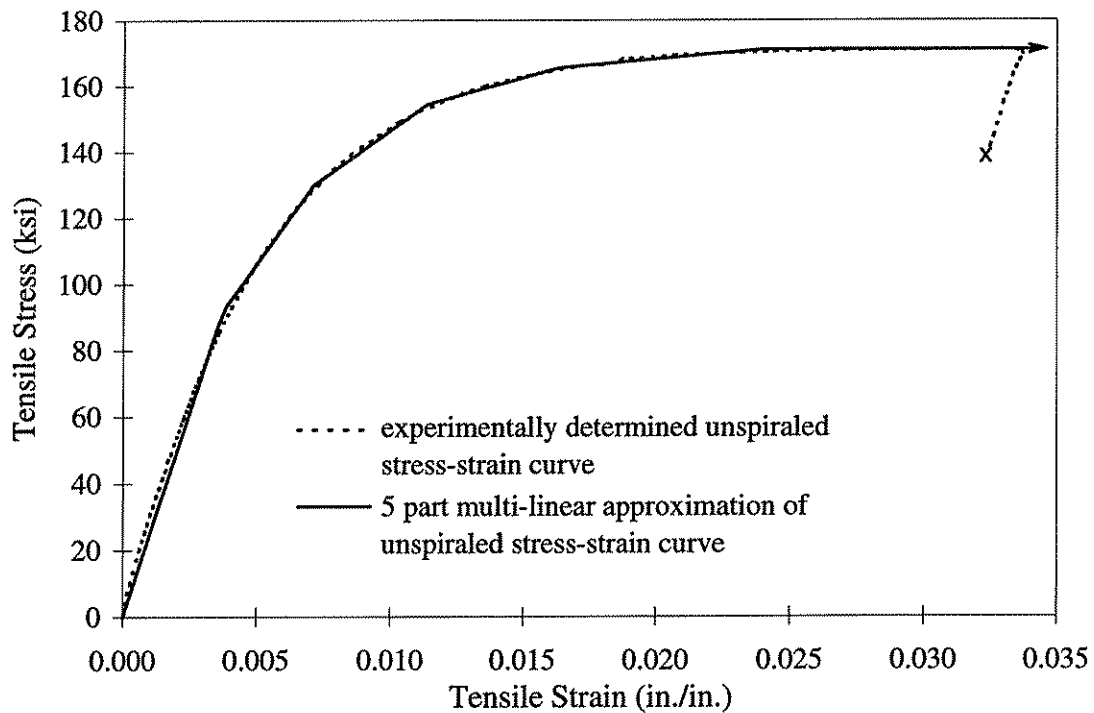
Figure 5.12   Approximation of Grade D unspiraled stress-strain curve used in
DRAIN-2DX.

112
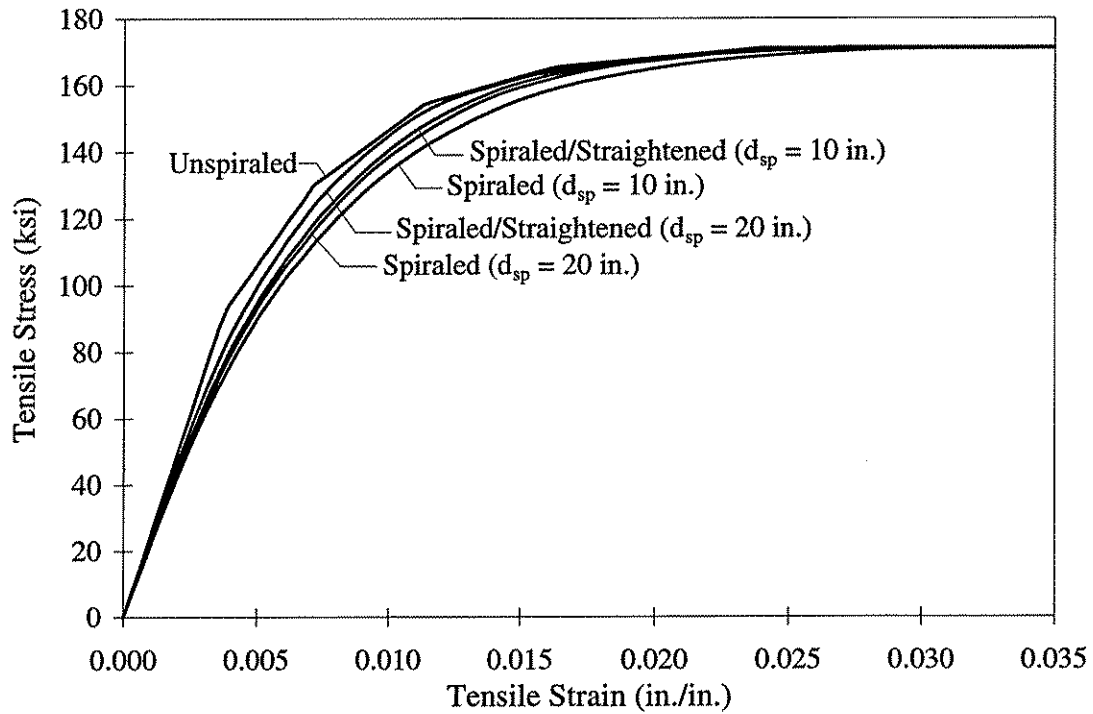
Figure 5.13   DRAIN-2DX analysis results showing effect of spiraling on Grade D
spiral reinforcement.

113
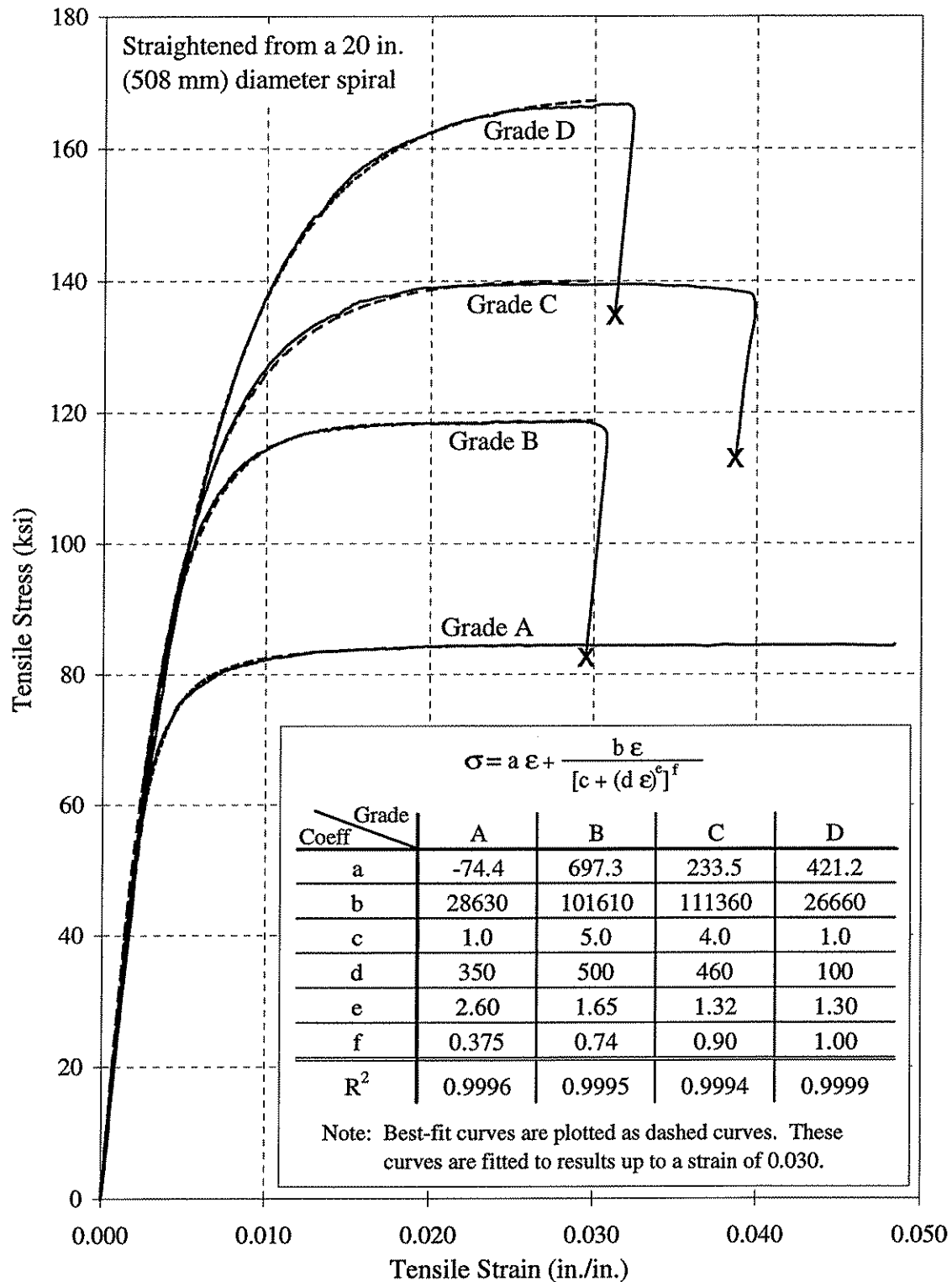
Figure 5.14   Stress-strain behavior of spiraled/straightened steel tested at Lehigh
University.

114
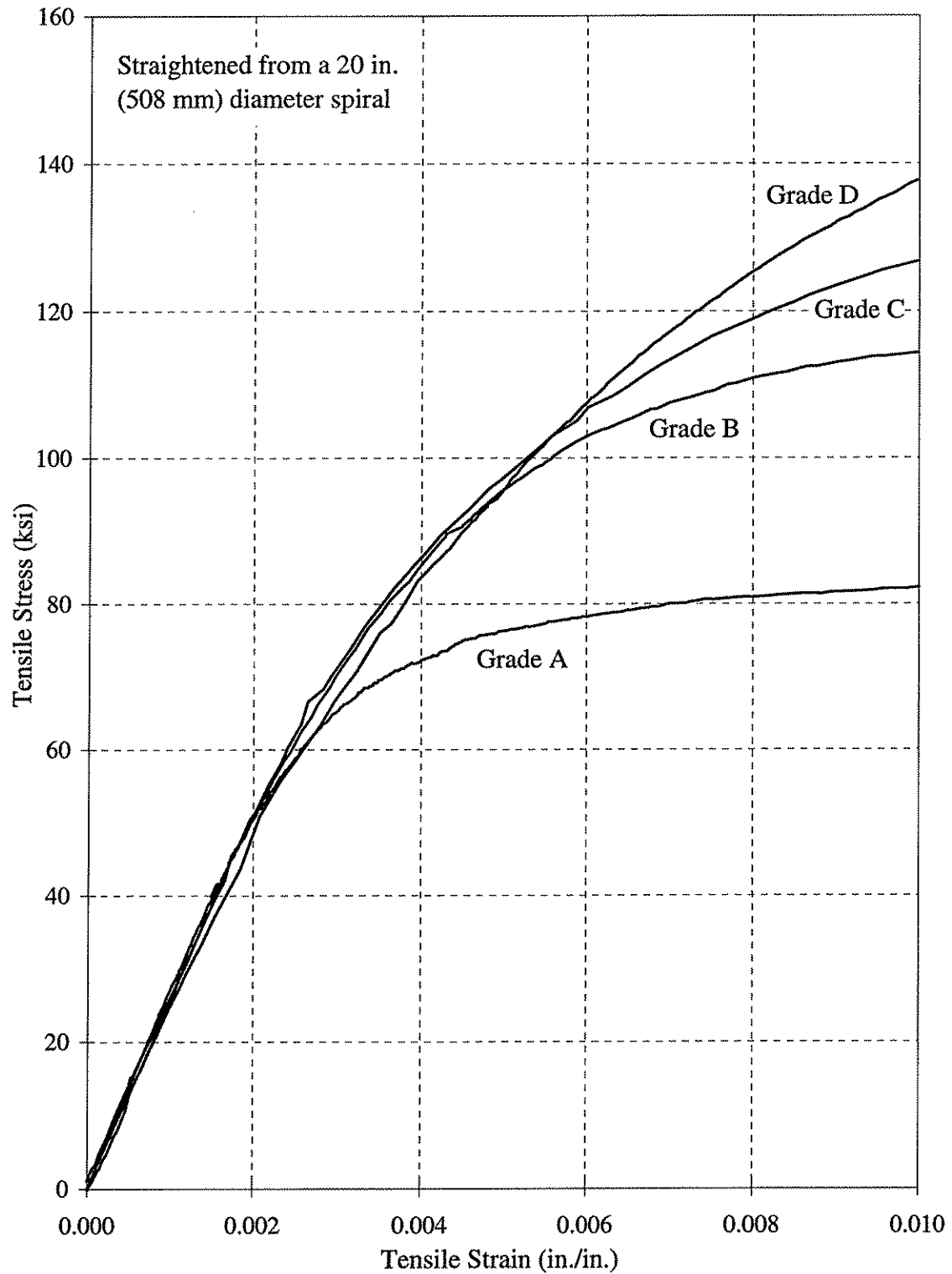
Figure 5.15   Stress-strain behavior of spiraled/straightened steel tested at Lehigh
University.

115
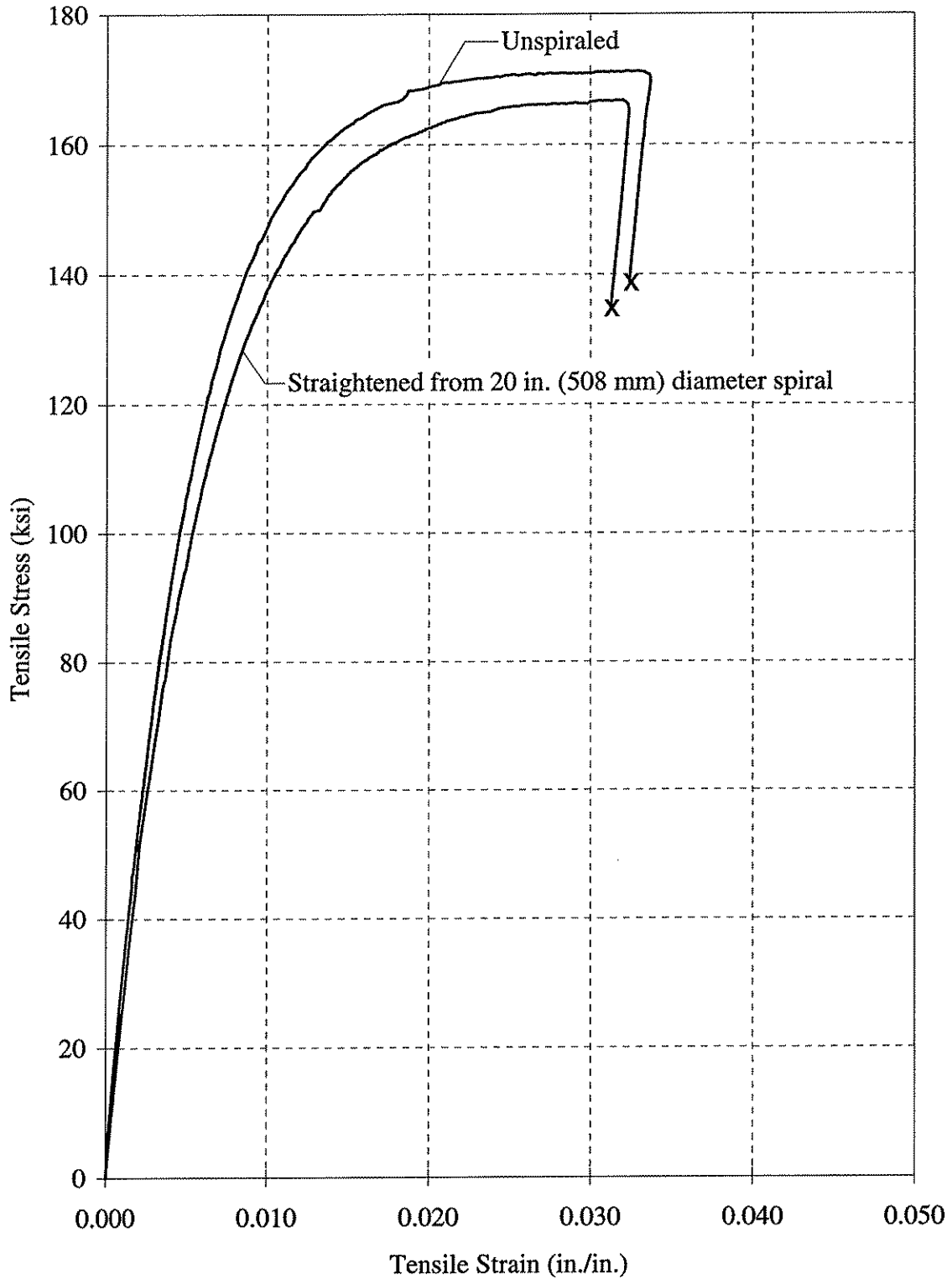
Figure 5.16   Experimental test results for stress-strain behavior of Grade D steel for
both unspiraled and spiraled/straightened configurations.
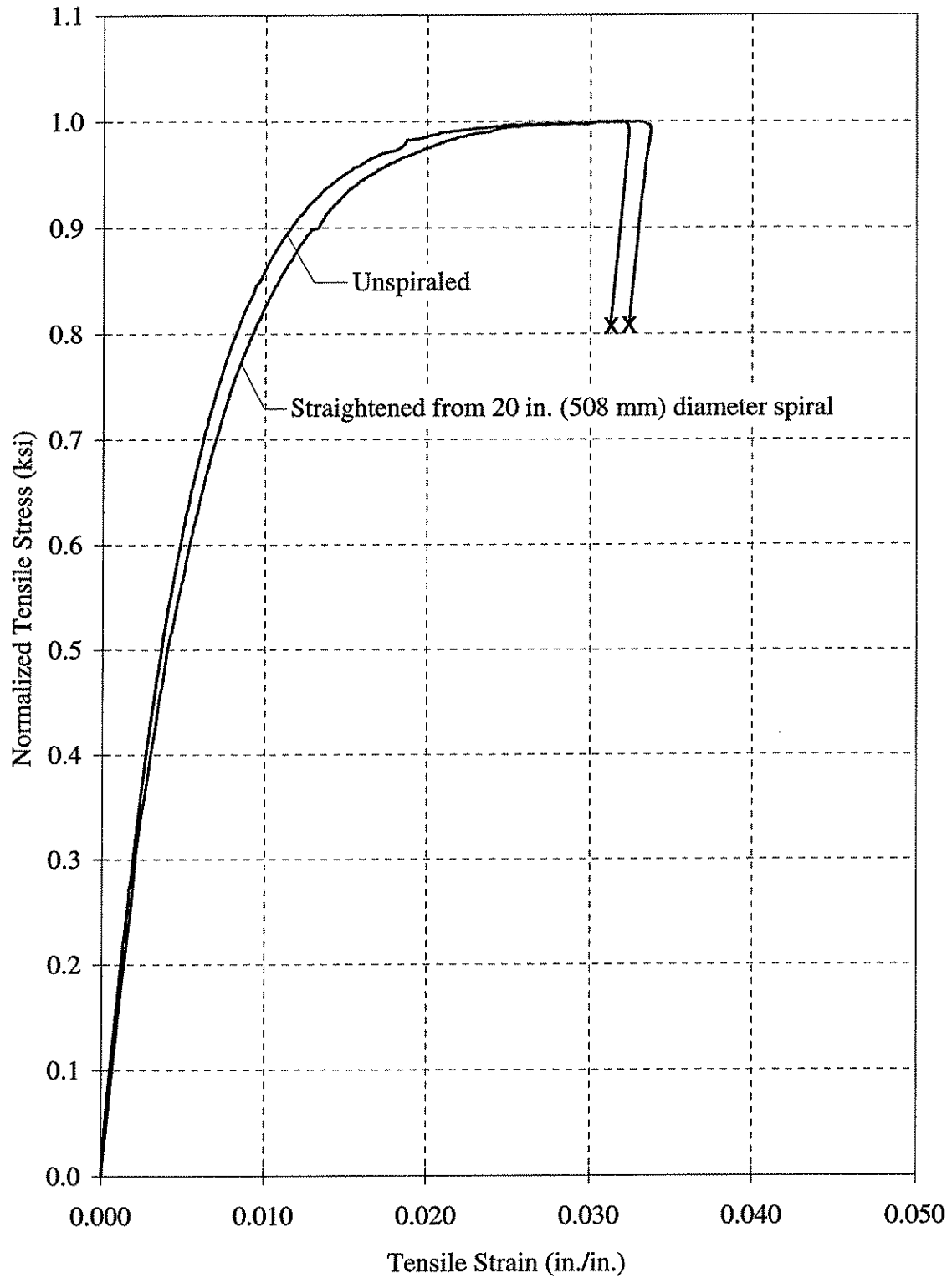
Figure 5.17   Normalized experimental results for stress-strain behavior of Grade D steel for both unspiraled and spiraled/straightened configurations.

117

CHAPTER 6
ANALYSIS OF RESULTS

6.1 INTRODUCTION

This chapter presents an analysis and discussion of the results obtained from the experimental program. The topics covered in this chapter include spiral behavior, cover behavior, pile failure mechanisms, and concrete dilation ratio behavior. Additionally, comparisons between experimental results and a number of empirical equations are performed.

Section 6.2 examines the behavior of the spiral reinforcement. The stress in the spiral reinforcement was determined at key stages in the response of the pile. These stresses were then compared to values of stresses which were expected to be observed.

The cover behavior is discussed in Section 6.3. The observations relating to cover behavior are presented, along with numerical results from the pile tests.

The pile failure mechanisms observed in the pile tests are presented in Section 6.4. This section primarily focuses on the inclined failure plane which developed in many of the specimens.

Section 6.5 presents a comparison between the experimental increase in confined concrete strength and the increase which would be predicted by the Richart et al. confined concrete strength equation, Equation 2.3. This comparison is done in two ways. First, the experimental increase in confined concrete strength between Δ_1 and Δ_2 is compared to the strength enhancement which was expected due to the amount of spiral reinforcement provided in each pile. Second, the experimental strength increase is compared to the strength increase which would be predicted based on the stress which was recorded in the spiral reinforcement.

Section 6.6 provides a comparison between the experimentally recorded longitudinal strain at Δ_2 and the strain which would be predicted through two different empirical equations. First, the experimental results are compared to the Richart et al. equation, (Equation 2.4), then the experimental results are compared to the Cusson and Paultre (1995) equation (Equation 6.6).

Finally, Section 6.7 provides a discussion of dilation ratio behavior. First, Section 6.7.1 provides a conceptual explanation of the secant and tangent dilation ratios. The next section presents the results from the pile tests. Section 6.7.3 then provides a comparison between the experimentally determined value of the transverse strain at Δ_2, ε_{ct2} and the values of ε_{ct2} which would be predicted by the secant and tangent dilation ratios. Section 6.7.4 then proposes an average tangent dilation ratio and Section 6.7.5 compares this proposed dilation ratio curve to the experimental results.

6.2 SPIRAL BEHAVIOR

Included in each individual test summary in Chapter 4 was a plot of spiral strain versus axial shortening for each pile specimen. Those results, replotted in terms of stress in the spiral reinforcement, are shown in Figures 6.1 through 6.8 for Piles 24-A through 14-D, respectively. The

118

stresses were obtained from the strain measurements using the best-fit curves which were developed in Section 5.6 (Figure 5.14) to represent the tensile stress-strain relationship of the spiral reinforcement. The ultimate spiral strength, f_{su}, shown on each figure is based on the spiraled/straightened tension test results presented in Table 5.1.

As was noted in Chapter 4, the spiral strain gages failed at various points throughout the tests. In general, the gages failed earlier in the 14 in. (356 mm) diameter piles than in the 24 in. (610 mm) diameter piles. However, clear trends can be observed from the data collected. In some cases, these trends are used to indicate an approximate range over which the spiral stress most likely lies at key stages in the pile behavior.

Table 6.1 presents the minimum and maximum stresses in the spiral reinforcement at three values of axial shortening, Δ_1, Δ_{spall}, and Δ_2. Also presented in this table are single value approximations for the spiral stresses at these three key stages in the pile response. Two of these single value approximations of the spiral stress, f_{sp1} and f_{sp2}, are also noted on Figures 6.1 through 6.8 for each individual pile specimen.

Table 6.2 presents the single value approximations of f_{sp} at the same three key stages, along with the volumetric ratio of spiral steel present in each specimen. Through the use of Equation 2.7, the values of the confining pressure, f_2, at each of the key stages is also calculated.

The spiral behavior of the 24 in. (610 mm) and 14 in. (356 mm) diameter specimens was consistent throughout the specimens at Δ_1. The minimum and maximum spiral stress values reported in Table 6.1 at cover failure (Δ_1) range from approximately 25 to 32 ksi (172 to 221 MPa). The small scatter between the f_{sp1} values shows that the transverse strain in the core concrete was similar in all specimens of a given diameter. Due to the different ρ_{sp} values, the similarity in f_{sp1} leads to a difference in f_{2-1}. However, this difference in confining pressure at the first peak is not though to have affected the behavior between specimens as the confining stress values are all still relatively low. Additionally, note that Figures 6.1 through 6.8 show that just prior to Δ_1 the stress in the spiral reinforcement begins to increase more rapidly. This is due to the increased dilation which is beginning to occur in the concrete core. The topic of dilation of the concrete core was discussed in Section 2.4 and is further discussed in Section 6.7.1.

The stress in the spiral reinforcement, and therefore the confining pressure on the concrete core, increased significantly between Δ_1 and Δ_{spall}. This increase can be attributed to a large portion of the load carried by the concrete cover being transferred into the core. This increase in core stress results in increased transverse dilation of the core. At this point in the behavior the spiral is clearly providing enough confining pressure to keep the core intact.

The spiral stress values reported for Δ_2 are based on fewer strain gage readings than were available for the values at Δ_1. At Δ_2, fewer strain gages remained functioning and the gages that remained functioning showed more variability than the values obtained at Δ_1. As shown in Table 6.1, for a

119

given pile the range of spiral stress at Δ_2 is as large as 35 ksi (240 MPa). However, based on the trends shown in Figures 6.1 through 6.8, an approximation of the spiral stress, f_{sp2}, was made.

The values of f_{sp2} show that the higher yield strength specimens did reach a high steel stress, but not the design yield stress. As a result, Table 6.2 shows that the lower yield strength specimens exhibited a larger value of f_{2-2}. Recall that in the design of these specimens, the ρ_{sp} and $f_{sy,nom}$ values are proportioned such that the f_{2-2} values within each diameter pile will be the same. The final column of Table 6.1 shows the ratio of the approximate average spiral stress at Δ_2 to the nominal design value of the spiral yield stress. This ratio is also plotted in Figure 6.9 versus the nominal spiral yield stress. The ratio of f_{sp2} to $f_{sy,nom}$ ranges from 0.68 to 1.03. In only one case, Pile 14-A, was f_{sp2} above $f_{sy,nom}$.

Two observations are made from Table 6.1 and Figure 6.9. First, in general, the spirals in the smaller diameter piles reach a greater fraction of the design yield stress as compared to the spirals in the larger diameter piles. The second observation is that, in general, the stress in the spiral reinforcement is closer to the design yield stress in the lower nominal spiral yield strength specimens. In the higher yield strength specimens, especially for the larger diameter piles, the stress in the spiral is significantly below the nominal yield value.

6.3 COVER BEHAVIOR

As was described in Chapter 4, the concrete cover behaved in a similar manner in all eight pile specimens. In general, the cover failed in a sudden brittle manner when P_1 was reached. No visible damage was observed prior to P_1. The damage which appeared during cover failure included cracks that formed longitudinally as well as circumferentially in the cover concrete. The circumferential cracks were primarily located within the test region of the pile.

The events which immediately precede and result from cover failure are as follows. First, with the cover intact at a load which corresponds to a concrete stress of approximately $0.8f_{co}$, the pile load-shortening response begins to show appreciable softening. This stress corresponds to a value of approximately 6.8 ksi (46.9 MPa). The softening is likely due to increased microcracking which occurs within concrete at this stress level. In the core concrete, the increased microcracking is likely reduced by the confining pressure beginning to be applied by the spiral reinforcement. When the pile load reaches P_1, the cover concrete fails in a sudden, brittle fashion. The portion of the total load carried by the cover no longer has a load path, so the total load on the specimen decreases. During this decrease in load, the confined core picks up a sizable percentage of the load released by the cover. In this way, the load decrease is always less than the unconfined concrete strength multiplied by the area of the cover.

Following the rapid load decrease caused by cover spalling, it was observed that the load carried by the pile may decrease slightly further before beginning to increase again toward the confined peak load, P_2. Observations during the test show that the cover failure was particularly more sudden for some piles than for others. In the less dramatic cases, only cracks developed in the cover, but very little cover concrete fell from the specimen. In the more dramatic cases, large

120

pieces of cover concrete fell from the pile. It seems that just after the less dramatic failures, a small portion of the load was still carried in the cover. P_{spall} is defined as the lowest load level between P_1 and P_2. Once P_{spall} is reached, the cover is considered to be completely ineffective.

Table 6.3 summarizes several key load values for each pile which are related to cover loss. Included in this table are the loads immediately before coverloss (P_1), after cover loss (P_{drop}), and after the small additional load decrease which occurred in some piles (P_{spall}).

6.4 PILE FAILURE MECHANISMS

Failure of all eight piles was defined by rupture of one or more turns of wire of the spiral reinforcement and a subsequent loss of confining pressure on the concrete core. This resulted in a significant decrease in the load carrying capacity of the pile. However, two observations indicate that the failures were not due to the spiral reinforcement reaching its ultimate strain as caused by lateral expansion of the core. First, for all specimens, the strain in the spiral reinforcement just before failure was less than 33 percent of the spiral strain at ultimate stress, ε_{su}. Typically, the maximum strains were less than 0.01. Second, for most of the piles, multiple spiral fractures occurred simultaneously along a well defined inclined plane throughout the test region. These two observations suggest that the failures were a function of the properties of the concrete and not of the spiral steel.

Numerous reports have been published which indicate that high strength concrete (defined here as concrete with a strength above 8 ksi (55 MPa)) fails in confined compression through the formation of an inclined failure plane. Additional information on this topic is presented in Section 2.4. As a point of reference beyond the information presented in Section 2.4, Martinez, Nilson, and Slate (1984) and Pessiki and Pieroni (1997) both have presented findings which pertain specifically to spirally reinforced high strength concrete compression members. Both studies found clearly defined inclined failure planes in the members which contained moderate levels of confinement and high strength concrete. Martinez et al. reported that the planes that formed in their test specimens were oriented at an angle of approximately 62 degrees from the horizontal.

The test summaries in Chapter 4 indicate the location of spiral fractures as well as any inclined concrete failure plane. For the larger diameter specimens, the failure plane was clearly defined by both the spiral fractures and the failed concrete. The angle of the plane with the horizontal ranged from 64 to 68 degrees. For the smaller diameter specimens, the failure plane was only clearly evident in 2 of the 4 piles. The angles of these failure planes were 36 and 41 degrees in Piles 14-A and 14-C, respectively. It was not clear whether the inclined plane failure mechanism developed in Piles 14-B or 14-D.

The decreased failure plane angle in conjunction with the confinement increases in the small piles seems to be consistent with the findings presented in Section 2.4. Also, it seems that the in the smaller piles, the failure occurred through either the formation of a poorly defined inclined failure plane or a sudden bulging failure mechanism. This type of failure may have been forced by the high level of confinement in the small diameter piles. In any event, it is clear that since the spiral

121

reinforcement strain was not near rupture at pile failure, the concrete failure is what caused spiral fracture and pile failure.

6.5 COMPARISON OF EXPERIMENTAL AND PREDICTED INCREASES IN CONFINED CONCRETE STRENGTH

The axial stress level in the confined concrete is determined from the axial force carried by the pile. First, throughout the entire behavior, the force carried by the longitudinal reinforcement is subtracted from the total force carried by the pile. The force in the longitudinal reinforcement is calculated from the average longitudinal strain gage strain in conjunction with the material properties given in Section 3.7.1. In this way, only the force carried by the concrete remains. Then, through the initial portion of the pile behavior from load initiation to P_1, the confined concrete stress, f_c, is determined by dividing the force carried by the concrete by the net concrete cross-sectional area of the pile, $A_{c,total}$. This is shown in Equation 6.1.

$$f_c = \frac{P - A_{lg}f_{lg}}{A_{c,total}} \quad \text{for } 0 \le P \le P_1 \tag{6.1}$$

After P_1 and until failure, f_c is determined by dividing the force carried by the concrete by the area of the core concrete, $A_{c,o-o}$. This core area is computed using the out-to-out diameter of the spiral, which is the same definition used by Richart et al. Equation 6.2 shows this calculation.

$$f_c = \frac{P - A_{lg}f_{lg}}{A_{c,o-o}} \quad \text{for } P_{drop} \le P \le P_{fracture} \tag{6.2}$$

This method of calculating the core concrete stress assumes that the cover concrete is equally as effective as the core concrete prior to cover failure, and that the cover carries no axial force after cover failure has occurred. As discussed in Section 6.3, in some instances the cover concrete did not completely unload at cover failure, but instead continued to unload from P_{drop} to P_{spall}. Thus, a small error may be introduced in the computed stress on the core concrete at this stage. This does not affect the discussions or conclusions that follow.

The experimentally determined increase in the strength of the confined concrete core, $\Delta f_{c12,exp}$, is computed as the stress in the confined core at the second peak, f_{c2}, minus the unconfined compressive strength, f_{co}. This is shown in Equation 6.3.

$$\Delta f_{c12,exp} = f_{c2} - f_{co} \tag{6.3}$$

In the following paragraphs, the experimental increase in strength of the confined core is compared to the design value of the increase in strength of the confined core, $\Delta f_{c12,dsgn}$, and to the value of the increase in strength of the confined core calculated from the stress in the spiral reinforcement,

$\Delta f_{c12,rich}$. The value of $\Delta f_{c12,dsgn}$ is calculated from Equation 6.4, which is a combination of Equations 2.3 and 2.7.

$$\Delta f_{c12,dsgn} = 2.05 \rho_{sp} f_{sy,nom} \tag{6.4}$$

The value of $\Delta f_{c12,rich}$ is calculated from Equation 6.5, which is a combination of Equations 2.3 and 2.7 as well as the stress in the spiral steel at Δ_2, f_{sp2}, as shown in Table 6.1.

$$\Delta f_{c12,rich} = 2.05 \rho_{sp} f_{sp2} \tag{6.5}$$

Table 6.4 shows the experimental and design values for Δf_{c12}. The final column of Table 6.4 shows the ratio of $\Delta f_{c12,exp}$ to $\Delta f_{c12,dsgn}$. In Figure 6.10, this ratio is plotted versus the nominal spiral yield strength of each pile. Table 6.4 and Figure 6.10 show that six of the eight piles did not achieve the level of strength enhancement which was expected based on the spiral design yield strength. For the 14 in. (356 mm) diameter piles, $R(\Delta f_{c12})_{exp/dsgn}$ ranged from 0.86 to 1.09, with Piles 14-A, 14-B, and 14-C all achieving at least 95 percent of the design strength enhancement. For the 24 in. (610 mm) diameter piles, the ratio ranged from 0.59 to 1.03, with only Pile 24-A achieving at least 95 percent of the design strength enhancement. For both diameter piles, the strength increase achieved was greater for the specimens with lower yield strength spirals than it was for the specimens with higher yield strength spirals. Based on the results of Table 6.4 and Figure 6.10, it is concluded that there is a limit on the strength of spiral reinforcing steel which can be assumed to reach yield for a given pile size and volumetric quantity of spiral reinforcement. This limit depends in part upon spiral diameter. Using a smaller volumetric quantity of a higher yield strength spiral will not provide the same confining pressure when Δ_2 is reached.

Table 6.5 shows the experimental and Richart et al. predicted values of Δf_{c12}. The final column of Table 6.5 shows the ratio of $\Delta f_{c12,exp}$ to $\Delta f_{c12,rich}$. In Figure 6.11 this ratio is also plotted versus the nominal spiral yield strength of each specimen. These ratios range from 0.87 to 1.17 with seven of the eight values above 0.95. These ratios show that all eight piles exhibited experimental strength increases consistent with the stresses observed in the spiral steel. Therefore, for the piles treated in this study, Equation 2.3 adequately represents the relationship between confining pressure and the strength enhancement of the core concrete.

To summarize in generalized terms, for the pile geometries and material properties treated in this study, Equation 2.1 provides an accurate means of estimating the confined concrete compressive strength, f_{cc}, from the unconfined concrete compressive strength, f_{co}, and the actual confining stress, f_{2-c}. It is emphasized that the equation is accurate only if the actual confining pressure is used. The equation may not provide accurate results if a confining pressure is used which is based on an assumed yield stress in the spiral reinforcement. Equation 2.1 is used in the proposed method for the design of high strength spiral reinforcement in piles.

6.6 COMPARISON OF EXPERIMENTAL AND PREDICTED LONGITUDINAL STRAINS

An experimental value of longitudinal strain at Δ_2 was obtained for each pile specimen from the measurements of strain in the longitudinal steel reinforcement. This value, $\varepsilon_{c2,exp}$, was calculated as the average strain in the longitudinal reinforcement at Δ_2. Equation 2.4, repeated here, was proposed by Richart et al. to predict the strain at peak confined compressive strength.

$$\varepsilon_{c2,rich} = \varepsilon_{co}\left(5\frac{f_{c2}}{f_{co}} - 4\right) \tag{2.4}$$

The applicability of Equation 2.4 was examined by substituting into it the experimentally determined values for ε_{co}, f_{c2}, and f_{co}. The strain computed by this equation is referred to as the derived longitudinal strain, $\varepsilon_{c2,rich}$. ε_{co} and f_{co} were taken as 0.0027 and 8.50 ksi (58.6 MPa), respectively. The value of f_{c2} was determined from Equation 6.2.

Table 6.6 shows the experimentally obtained values and Richart values of ε_{c2}. This table also shows the ratio of the two values, $R(\varepsilon_{c2})_{exp/rich}$. These ratios are also plotted in Figure 6.12. In seven of the eight cases, the experimentally observed longitudinal strain is greater than the predicted value. Additionally, the trend shows that as the value of f_{c2} decreases for a given pile size (i.e. lower confining pressure), the Richart et al. prediction becomes more conservative.

Cusson and Paultre (1995) also derived an equation to predict ε_{c2}. Equation 6.6 provides this relationship.

$$\varepsilon_{c2,cus} = \varepsilon_{co} + 0.21\left(\frac{f_{2-2}}{f_{co}}\right)^{1.7} \tag{6.6}$$

The applicability of this equation was examined by substituting into it the experimentally determined values for ε_{co}, f_{2-2}, and f_{co}. The strain computed by this equation is referred to as $\varepsilon_{c2,cus}$. ε_{co} and f_{co} were taken as 0.0027 and 8.50 ksi (58.6 MPa), respectively. The value of f_{2-2} was calculated from Equation 2.7 using the value of f_{sp2} approximated in Section 6.2.

Table 6.6 shows the experimentally obtained values and Cusson et al. values of ε_{c2}. Once again, the ratio of the two values, $R(\varepsilon_{c2})_{exp/cus}$, is also shown. These ratios are plotted in Figure 6.13. As before, in seven of the eight cases, the experimentally observed longitudinal strain is greater than the predicted value. Also, the trend shows that as the value of f_{c2} decreases for a given pile size, the Cusson et al. prediction becomes more conservative.

Based on these results, it is concluded that both Equation 2.4 and Equation 6.6, in general, provide conservative estimates of ε_{c2}. Overall, it seems that the Richart et al. equation provides a slightly

124

more accurate prediction than the Cusson et al. equation. For this reason, Equation 2.4 is used in the proposed design procedure discussed in Chapter 7.

6.7 DILATION RATIO RELATIONSHIPS

As part of the proposed procedure for the design of high strength spiral reinforcement (presented in Chapter 7), Equation 2.4 is used to estimate the longitudinal strain in the concrete core at Δ_2. Also needed in the proposed design procedure is a means to estimate the transverse strain from the longitudinal strain. The dilation ratio is used for this purpose.

6.7.1 Definitions

The dilation ratio is a quantity which describes the relationship between transverse strain and longitudinal strain of the concrete core. In this research, the relationship between the transverse and longitudinal strains is defined in two ways. Figure 6.14(a) shows an idealized plot of transverse strain versus longitudinal strain for a pile. Figures 6.14(b) and 6.14(c) are plots of the secant and tangent dilation ratios, respectively, both of which are obtained from Figure 6.14(a).

The secant dilation ratio, η_{sec}, is defined as the ratio between transverse and longitudinal strain at any point in the response of the core. This is represented by Equation 6.7.

$$\eta_{sec} = \frac{\varepsilon_{ct}}{\varepsilon_c} \tag{6.7}$$

If known, the secant dilation ratio can be used to compute the transverse strain at any point based on the value of the longitudinal strain. Basically, Figure 6.14(b) represents the slope of a line drawn from the origin of Figure 6.14(a) to any point on the curve. This line is a secant to the curve, hence the slope of this line is called the secant dilation ratio. Note that when estimating the transverse strain using the secant dilation ratio, the path which the concrete transverse to axial strain plot followed to reach the longitudinal strain of interest is irrelevant. If η_{sec} and the longitudinal strain are known at a point, the transverse strain is calculated directly.

The tangent dilation ratio, η_{tan}, is defined as the slope of the curve of transverse strain versus longitudinal strain at any point along the curve. Equation 6.8 defines the tangent dilation ratio at any point.

$$\eta_{tan} = \frac{d\varepsilon_{ct}}{d\varepsilon_c} \tag{6.8}$$

In order to calculate the transverse strain in the concrete which corresponds to any longitudinal strain, the tangent dilation ratio relationship is needed for all values of longitudinal strain prior to that point. Equation 6.9 defines the total transverse strain as a function of the total longitudinal strain and η_{tan}.

125

$$\varepsilon_{ct} = \int\limits_{\varepsilon_c=0}^{\varepsilon_c} \eta_{tan} d\varepsilon_c \qquad (6.9)$$

Equation 6.9 shows that the area under the η_{tan} curve between $\varepsilon_c = 0$ and ε_c is ε_{ct}.

6.7.2 Experimentally Determined Dilation Ratios

Figure 6.15(a) shows the experimentally determined strain in the spiral reinforcement in all eight strain gages versus average longitudinal strains in the concrete for Pile 14-C. Note that the strains in the spiral reinforcement are equal to the transverse strains in the concrete. Also, the average strain in the longitudinal reinforcement is assumed to equal the longitudinal strain in the concrete. The response is shown from $\varepsilon_c = 0$ to ε_{c2}, therefore, any behavior occurring after ε_{c2} is ignored. Also, the average longitudinal strains at two key points, ε_{c1} and ε_{c2}, are noted on the figures.

Figure 6.15(b) shows the experimentally determined secant dilation ratio for each of the eight spiral strain gages throughout the test for Pile 14-C. The secant dilation ratio for each spiral gage is calculated as the spiral strain divided by the average longitudinal strain gage strain. The approximated secant dilation ratio at the second peak, η_{sec2}, is also noted on this plot. This value is approximated based on the trends observed in the eight η_{sec} curves. This is the value which directly relates ε_{c2} to ε_{ct2} as is shown in Equation 6.10.

$$\varepsilon_{ct2} = \eta_{sec2}\, \varepsilon_{c2} \qquad (6.10)$$

Figure 6.15(c) shows the experimentally determined average tangent dilation ratio for Pile 14-C. This curve (the darker line curve in Figure 6.15(c)) was determined as follows. First, the increment of increased transverse strain was calculated for each increment of increased longitudinal strain throughout the response of the pile. This calculation was performed for each of the eight spiral strain gages for each increment of longitudinal strain. The eight resulting curves are the tangent dilation ratio relationship for the eight spiral gages. These eight curves were then averaged to generate the lighter curve shown on Figure 6.15(c). The somewhat erratic oscillations of the curve are attributed to the incremental approach used to determine the curve. Finally, to reduce these erratic oscillations, this average curve was smoothed by taking a moving average of the ten values of η_{tan} closest to each value of η_{tan} for each longitudinal strain increment. This smoothed average curve is the darker curve shown on Figure 6.15(c). As was described in Section 6.7.1, the area under the η_{tan} curve up to any longitudinal strain is equal to the transverse dilation at that longitudinal strain. Thus, the area under smoothed η_{tan} curve between $\varepsilon_c = 0$ and ε_{c2} was calculated using Equation 6.9 and is shown on the figure, denoted as $A_{\eta tan2}$. This area is equal to the transverse strain ε_{ct2}. This is shown in equation form in Equation 6.11.

$$\varepsilon_{ct2} = A_{\eta tan2} \qquad (6.11)$$

Through the same manner described above for Pile 14-C, the dilation ratio plots of interest are plotted for all eight specimens in Figure 6.16 through 6.21. Figure 6.16 shows the spiral strain versus average longitudinal strain for the 24 in. (610 mm) diameter piles, while Figure 6.17 shows the same plots for the 14 in. (356 mm) diameter piles. Figures 6.18 and 6.19 show the secant dilation ratio plots for the 24 in. (610 mm) and 14 in. (356 mm) piles, respectively. Figures 6.20 and 6.21 show the tangent dilation ratio plots for the 24 in. (610 mm) and 14 in. (356 mm) piles, respectively.

The secant dilation ratio at any point in the behavior can be obtained from Figures 6.18 and 6.19. In general, these plots show that the secant dilation behavior of the pile was constant or decreasing until ε_{c1} was neared. This is to be expected as the concrete under low axial compressive stresses exhibits a nearly constant relationship between axial and transverse strain. Between ε_{c1} and ε_{c2}, the plots show that the general trend was for a slight increase in η_{sec}. This is also expected as confined concrete under higher axial compressive loads generally exhibits larger transverse strains per axial strain than it did under lower loads. Additionally, noted on these figures are the approximated values of η_{sec2}. In the 24 in. (610 mm) diameter piles, the approximated values of η_{sec2} range from 0.45 to 0.5 while in the 14 in. (356 mm) diameter piles, the approximated values range from 0.35 to 0.45.

The tangent dilation ratios for each pile are shown in Figures 6.20 and 6.21. The area under smoothed η_{tan} curve is shown on each figure, denoted as $A_{\eta tan2}$. The general behavior shown on these plots corresponds well to the discussion of the dilation behavior of concrete presented in Section 2.4. The plots show that η_{tan} is approximately constant from $\varepsilon_c = 0$ to nearly ε_{c1}. This is expected as the concrete in this portion of the response is behaving as if it is unconfined with a constant Poisson's ratio. The plots also show that the concrete exhibits a higher dilation ratio after cover spalling. This is also expected as confined concrete under high axial compressive stresses will exhibit increased dilation due to the microcracking and macrocracking. Finally, in the 24 in. (610 mm) specimens, η_{tan} increases as ε_{c2} is neared. This is in contrast to the behavior exhibited by the 14 in. (356 mm) diameter piles where the tangent dilation ratio is constant near ε_{c2}. It may be that the higher confining stresses on the smaller diameter piles did not allow the dilation to continue increasing above a certain limit.

6.7.3 Evaluation of Secant and Tangent Dilation Ratios

Table 6.7 compares the experimentally determined values of transverse strain at Δ_2 with the values of transverse strain obtained using the experimentally determined secant and tangent dilation ratios. In Table 6.7, the experimental value of ε_{ct2} was determined from the stress in the spiral at Δ_2, f_{sp2}, as discussed in Section 6.2, and the stress-strain curves presented in Section 5.6.

The secant dilation ratio approximation of ε_{ct2} is computed from Equation 6.10 and the experimental value of ε_{c2} (listed in Table 6.7). The approximated values of η_{sec2} for each pile are shown on Figures 6.18 and 6.19 as well as in Table 6.7. The predicted values of ε_{ct2} are also shown in

127

Table 6.7. The table shows that in every case the prediction of the transverse strain is within 25 percent of the experimentally obtained value.

The tangent dilation ratio approximation of ε_{ct2} is computed from Equation 6.11. The area under the η_{tan} curve at ε_{c2}, $A_{\eta tan2}$, is shown on Figures 6.20 and 6.21 as well as in Table 6.7. The table shows that in every case, the predicted values of the transverse strain is within 12 percent of the experimentally obtained value.

6.7.4 Proposed Tangent Dilation Ratio Relationship

This section presents a proposed tangent dilation ratio relationship for spirally confined concrete. The proposed relationship is based on the behavior observed in the experimental testing program as well as the understanding of the dilation behavior of concrete presented in Section 2.4. In Chapter 7, this proposed tangent dilation ratio relationship is used to estimate the value of ε_{ct2} from the value of ε_{c2} as part of the procedure for the design of high strength spirals.

The basic shape of the proposed tangent dilation ratio relationship between $\varepsilon_c = 0$ and ε_{c2} is shown in Figure 6.22(a). This figure shows that the tangent dilation ratio has an initial constant value, $\eta_{tan,ini}$, up to a longitudinal strain of $\alpha\varepsilon_{co}$. At this point the tangent dilation ratio increases in a linear manner to a second constant value of $\eta_{tan,lim}$. This limiting value is reached at a longitudinal strain of $\beta\varepsilon_{c2}$.

Figure 6.22(b) shows the same plot with the longitudinal strain normalized by the unconfined concrete strain, ε_{co}. Accordingly, the variable 'm' is defined as Equation 6.12.

$$m = \frac{\varepsilon_{c2}}{\varepsilon_{co}}$$
(6.12)

As was shown in Equation 6.11, the area under the tangent dilation ratio curve between $\varepsilon_c = 0$ and ε_{c2}, denoted as $A_{\eta tan2}$, is equivalent to ε_{ct2}. Calculating the area shown in Figure 6.22(a) provides the area $A_{\eta tan2}$ shown in Equation 6.13.

$$A_{\eta tan2} = \varepsilon_{co}\left(\frac{1}{2}\alpha\left(\eta_{tan,ini} - \eta_{tan,lim}\right) + m\left(\frac{1}{2}\eta_{tan,ini}\beta - \frac{1}{2}\eta_{tan,lim}\beta + \eta_{tan,lim}\right)\right)$$
(6.13)

Dividing Equation 6.13 by the normalizing factor, ε_{co}, provides the normalized value of the area, $\overline{A}_{\eta tan2}$. This is shown in Equation 6.14.

$$\overline{A}_{\eta tan2} = \frac{1}{2}\alpha\left(\eta_{tan,ini} - \eta_{tan,lim}\right) + m\left(\frac{1}{2}\eta_{tan,ini}\beta - \frac{1}{2}\eta_{tan,lim}\beta + \eta_{tan,lim}\right)$$
(6.14)

128

Based on the results of this study, values for the variables α, β, $\eta_{tan,ini}$, $\eta_{tan,lim}$ are proposed as follows: $\alpha = 0.7$; $\beta = 0.6$; $\eta_{tan,ini} = 0.2$; and $\eta_{tan,lim} = 0.5$. Inserting these proposed values into Equation 6.14 provides Equation 6.15.

$$A_{\eta\tan 2} = \varepsilon_{co}\left(m(0.41) - 0.105\right) \tag{6.15}$$

Again, noting that $A_{\eta tan2}$ equals ε_{ct2}, this equation can be rewritten as Equation 6.16.

$$\varepsilon_{ct2} = 0.41\varepsilon_{c2} - 0.105\varepsilon_{co} \tag{6.16}$$

Therefore, through the use of the proposed tangent dilation ratio, the value of ε_{ct2} at a value of ε_{c2} can be calculated directly from a value of ε_{c2} without explicit knowledge of the tangent dilation behavior between $\varepsilon_c = 0$ and ε_{c2}. This proposed tangent dilation ratio curve is used in the proposed procedure for the design of piles using high strength spiral reinforcement presented in Chapter 7.

6.7.5 Comparison of Proposed and Experimental Tangent Dilation Ratio Relationships

Figures 6.23 and 6.24 show the experimentally determined tangent dilation ratio curves for the pile specimens. The curves are the same as the smoothed curves shown in Figures 6.20 and 6.21, respectively. Note that the curves are shown with the longitudinal strains normalized by ε_{co}. Figures 6.23 and 6.24 also show the proposed tangent dilation ratio relationship for each specimen. The 'm' value for each specimen is given in Table 6.8.

A comparison of the proposed and experimental tangent dilation ratio curves reveals the following. First, the initial constant portion of the proposed curve models well the behavior observed in the 14 in. (356 mm) diameter piles. For the 24 in. (610 mm) piles, this portion of the proposed curve tends to underestimate the experimental behavior. Next, for both diameter piles, the increasing portion of the proposed curve tends to model the experimental findings relatively well. Finally, in general, for the 14 in. (356 mm) diameter piles, the constant portion of the proposed curve models well the tangent dilation ratio behavior near ε_{c2}. The 24 in. (610 mm) diameter piles tend to exhibit an increased η_{tan} near ε_{c2}. Therefore, the model provides a conservative estimate of the tangent dilation ratio for these piles.

Table 6.8 provides a numerical comparison between the proposed and experimental tangent dilation ratio relationships. The normalized area under the experimental tangent dilation ratio curve is shown as $\overline{A}_{\eta tan2}$. Also, the experimentally determined strain in the spiral reinforcement at Δ_2 is shown as ε_{ct2}. The normalized area under the proposed curve is shown as $\overline{A}_{\eta tan2,prpsd}$. Finally, the transverse strain in the core concrete at Δ_2 calculated from the proposed curve area, $A_{\eta tan2,prpsd}$, is shown as $\varepsilon_{ct2,prpsd}$. Comparison between the normalized areas shows that the proposed curve provides a conservative estimate with the ratio of experimental to proposed being approximately 1.2. A comparison between the transverse core strains at Δ_2 shows a similar result, with the proposed method generally providing a slight underprediction of the experimental value.

129

| Pile | Nominal Spiral Yield Stress (ksi) | Δ_1 | | | Δ_{spall} | | | Δ_2 | | | |
		Spiral Stress Min. (ksi)	Max. (ksi)	Approximate Spiral Stress, f_{sp1} (ksi)	Spiral Stress Min. (ksi)	Max. (ksi)	Approximate Spiral Stress, $f_{sp,spall}$ (ksi)	Spiral Stress Min. (ksi)	Max. (ksi)	Approximate Spiral Stress, f_{sp2} (ksi)	$R_{fsp2/fsy,nom}$
24-A	78	19.2	30.5	25	17.4	42.9	35	67.7	78.2	70	0.90
24-B	107	29.1	35.6	32	41.6	59.2	50	78.6	110.4	95	0.89
24-C	121	18.7	35.7	28	36.8	53.4	45	65.2	97.0	85	0.70
24-D	140	18.6	36.0	29	40.5	63.7	55	69.5	104.2	85	0.61
14-A	78	20.0	32.6	25	25.3	45.5	35	70 †	82 †	80	1.03
14-B	107	17.1	38.2	28	29.1	58.4	45	85.2	110 †	95	0.89
14-C	121	14.4	31.0	20	35.4	63.0	45	103.4	125 †	115	0.95
14-D	140	19.3	32.0	22	29.6	51.1	40	110 †	140 †	125	0.89

† indicates an approximation of the minimum or maximum value based on trends observed in Figures 6.1 through 6.8.

1 ksi = 6.895 MPa

Table 6.1   Minimum, maximum, and approximate stress in the spiral reinforcement at Δ_1, Δ_{spall}, and Δ_2.

Pile	ρ_{sp} %	Δ_1		Δ_{spall}		Δ_2	
		f_{sp1} (ksi)	f_{2-1} (ksi)	$f_{sp,spall}$ (ksi)	$f_{2-spall}$ (ksi)	f_{sp2} (ksi)	f_{2-2} (ksi)
24-A	2.09	25	0.26	35	0.37	70	0.73
24-B	1.57	32	0.25	50	0.39	95	0.75
24-C	1.31	28	0.18	45	0.29	85	0.56
24-D	1.12	29	0.16	55	0.31	85	0.48
14-A	4.56	25	0.57	35	0.80	80	1.82
14-B	3.36	28	0.47	45	0.76	95	1.60
14-C	2.90	20	0.29	45	0.65	115	1.67
14-D	2.66	22	0.29	40	0.53	125	1.66

1 ksi = 6.895 MPa

Table 6.2   Confining pressure on concrete core at Δ_1, Δ_{spall}, and Δ_2.

Pile	P_1 (kips)	P_{drop} (kips)	P_{spall} (kips)
24-A	3910	2951	2951
24-B	3950	3274	3173
24-C	3926	3274	3202
24-D	3985	3127	3092
14-A	1359	977	957
14-B	1366	959	959
14-C	1367	939	921
14-D	1355	956	924

1 kip = 4.448 kN

Table 6.3   Pile load values at stages just prior to, during, and after cover failure.

131

Pile	Experimental			Design			$R(\Delta f_{c12})_{exp/dsgn}$
	P_2 (kips)	f_{c2} (ksi)	Δf_{c12} (ksi)	$f_{sy,nom}$ (ksi)	f_{2-2} (ksi)	$\Delta f_{c12,dsgn}$ (ksi)	
24-A	3826	11.96	3.46	78	0.82	3.36	1.03
24-B	3691	11.52	3.02	107	0.84	3.44	0.88
24-C	3579	11.17	2.67	121	0.79	3.25	0.82
24-D	3337	10.39	1.89	140	0.78	3.21	0.59
14-A	1337	16.46	7.96	78	1.78	7.29	1.09
14-B	1276	15.68	7.18	107	1.80	7.37	0.97
14-C	1248	15.33	6.83	121	1.75	7.19	0.95
14-D	1228	15.07	6.57	140	1.86	7.63	0.86

1 kip = 4.448 kN
1 ksi = 6.895 MPa

Table 6.4   Comparison of experimental peak core concrete strength increase to design value of core concrete strength increase based on assumed yielding of spiral steel and Equation 6.3.

Pile	Experimental			Richart et al.			$R(\Delta f_{c12})_{exp/rich}$
	P_2 (kips)	f_{c2} (ksi)	Δf_{c12} (ksi)	f_{sp2} (ksi)	f_{2-2} (ksi)	$\Delta f_{c12,rich}$ (ksi)	
24-A	3826	11.96	3.46	70	0.73	3.00	1.15
24-B	3691	11.52	3.02	95	0.74	3.05	0.99
24-C	3579	11.17	2.67	85	0.55	2.28	1.17
24-D	3337	10.39	1.89	85	0.48	1.95	0.97
14-A	1337	16.46	7.96	80	1.82	7.47	1.06
14-B	1276	15.68	7.18	95	1.60	6.54	1.10
14-C	1248	15.33	6.83	110	1.60	6.54	1.04
14-D	1228	15.07	6.57	125	1.66	6.81	0.96

1 kip = 4.448 kN
1 ksi = 6.895 MPa

Table 6.5   Comparison of experimental peak core concrete strength increase to strength increase based on stress observed in spiral steel and Equation 6.4.

Pile	Experimental					Richart et al.		Cusson and Paultre	
	ε_{co}	f_{co} (ksi)	f_{c2} (ksi)	f_2 (ksi)	ε_{c2}	$\varepsilon_{c2,rich}$	$R(\varepsilon_{c2})_{exp/rich}$	$\varepsilon_{c2,cus}$	$R(\varepsilon_{c2})_{exp/cus}$
24-A	0.0027	8.50	11.96	0.73	0.0088	0.0082	1.07	0.0059	1.48
24-B	0.0027	8.50	11.52	0.75	0.0081	0.0075	1.08	0.0061	1.33
24-C	0.0027	8.50	11.17	0.56	0.0076	0.0069	1.10	0.0048	1.60
24-D	0.0027	8.50	10.39	0.48	0.0093	0.0057	1.64	0.0043	2.18
14-A	0.0027	8.50	16.46	1.82	0.0113	0.0153	0.74	0.0180	0.63
14-B	0.0027	8.50	15.68	1.60	0.0159	0.0141	1.13	0.0150	1.06
14-C	0.0027	8.50	15.33	1.67	0.0183	0.0135	1.35	0.0159	1.15
14-D	0.0027	8.50	15.07	1.66	0.0194	0.0131	1.48	0.0158	1.23

1 ksi = 6.895 MPa

Table 6.6   Comparison of experimental longitudinal strain at Δ_2 to value predicted by Richart et al. and Cusson and Paultre.

Pile	Experimental		Secant Dilation Ratio		Tangent Dilation Ratio
	ε_{c2}	ε_{ct2}	η_{sec2}	$\varepsilon_{ct2,sec}$	$\varepsilon_{ct2,tan} = A_{\eta tan2}$
24-A	0.0088	0.0035	0.45	0.0040	0.0039
24-B	0.0081	0.0050	0.50	0.0041	0.0049
24-C	0.0076	0.0039	0.45	0.0034	0.0036
24-D	0.0093	0.0040	0.45	0.0042	0.0044
14-A	0.0113	0.0070	0.45	0.0051	0.0072
14-B	0.0159	0.0050	0.35	0.0056	0.0056
14-C	0.0183	0.0068	0.40	0.0073	0.0077
14-D	0.0194	0.0078	0.45	0.0087	0.0079

Table 6.7   Comparison of experimentally determined values of transverse strain at Δ_2 with the values obtained using the secant and tangent dilation ratios.

Pile	Experimental			Proposed Tangent Dilation Ratio	
	m	$\overline{A}_{\eta tan2}$	ε_{ct2}	$\overline{A}_{\eta tan2,prpsd}$	$\varepsilon_{ct2,prpsd}$
24-A	3.26	1.46	0.0035	1.23	0.0033
24-B	3.00	1.82	0.0050	1.12	0.0030
24-C	2.81	1.34	0.0039	1.04	0.0028
24-D	3.44	1.64	0.0040	1.30	0.0035
14-A	4.19	2.68	0.0070	1.59	0.0043
14-B	5.89	2.07	0.0050	2.30	0.0062
14-C	6.78	2.84	0.0068	2.67	0.0072
14-D	7.19	2.94	0.0078	2.64	0.0071

Table 6.8   Comparison of experimental values of tangent dilation ratio relationship to values obtained from proposed relationship.

Figure 6.1   Plot of spiral stress versus axial shortening for Pile 24-A.

Figure 6.2   Plot of spiral stress versus axial shortening for Pile 24-B.

135
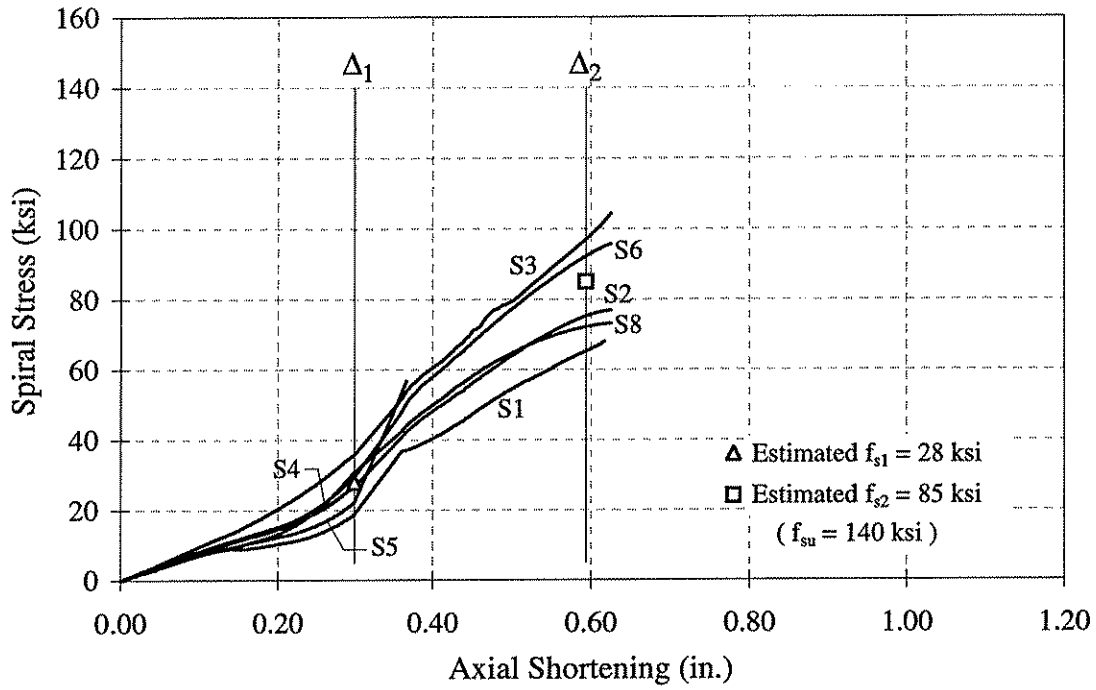
Figure 6.3   Plot of spiral stress versus axial shortening for Pile 24-C.
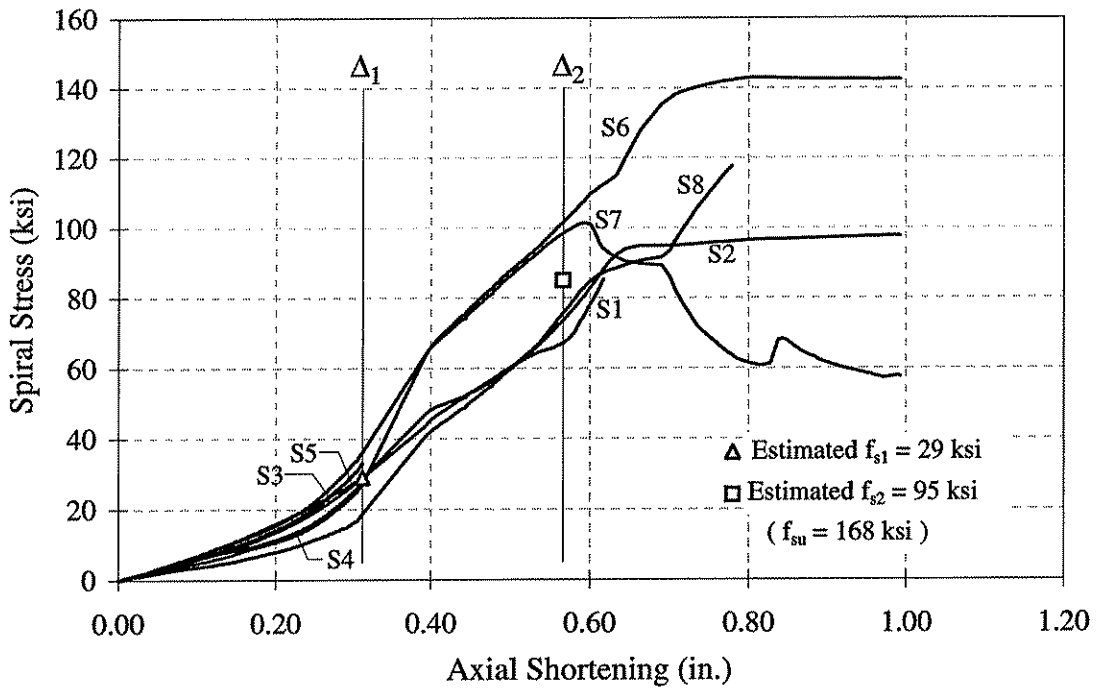
Figure 6.4   Plot of spiral stress versus axial shortening for Pile 24-D.

136
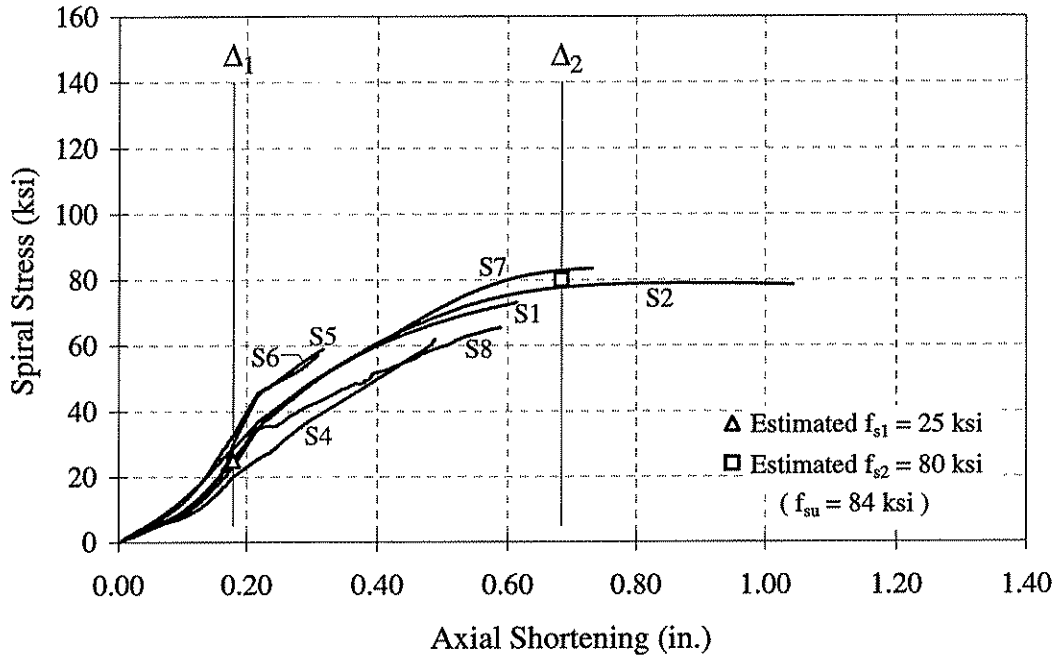
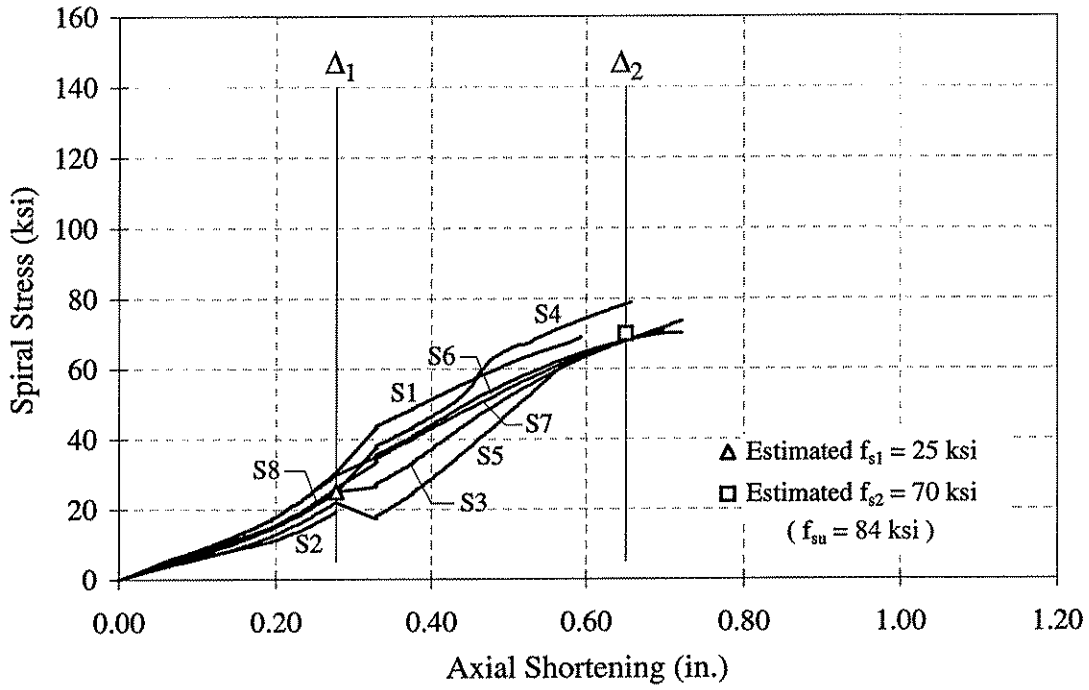Figure 6.5   Plot of spiral stress versus axial shortening for Pile 14-A.
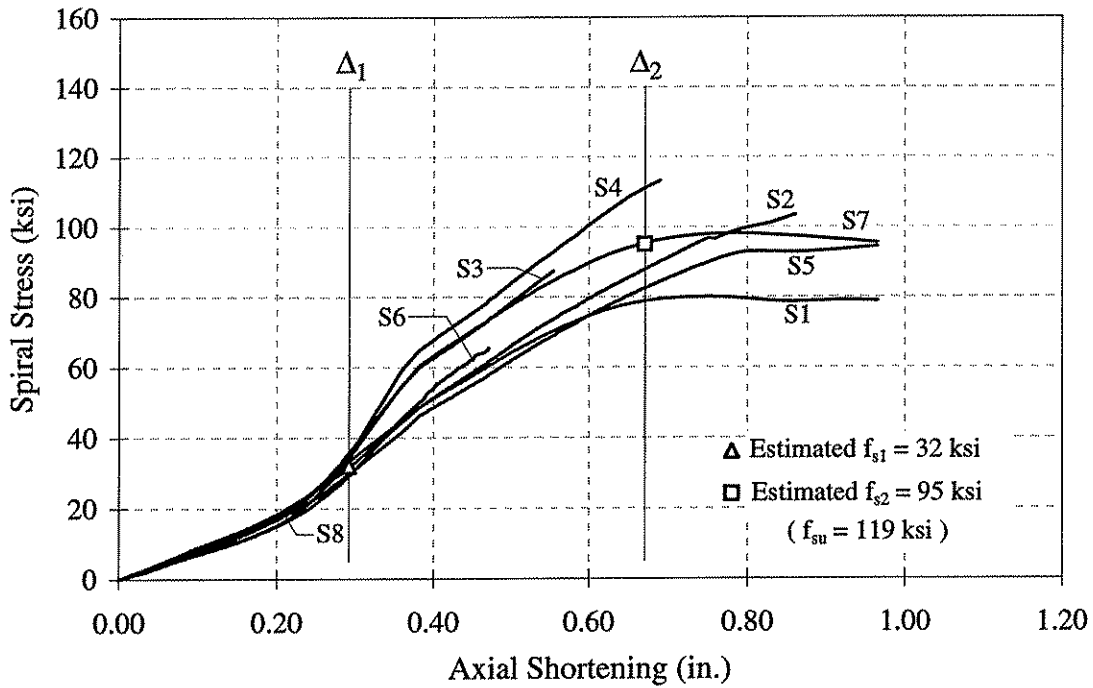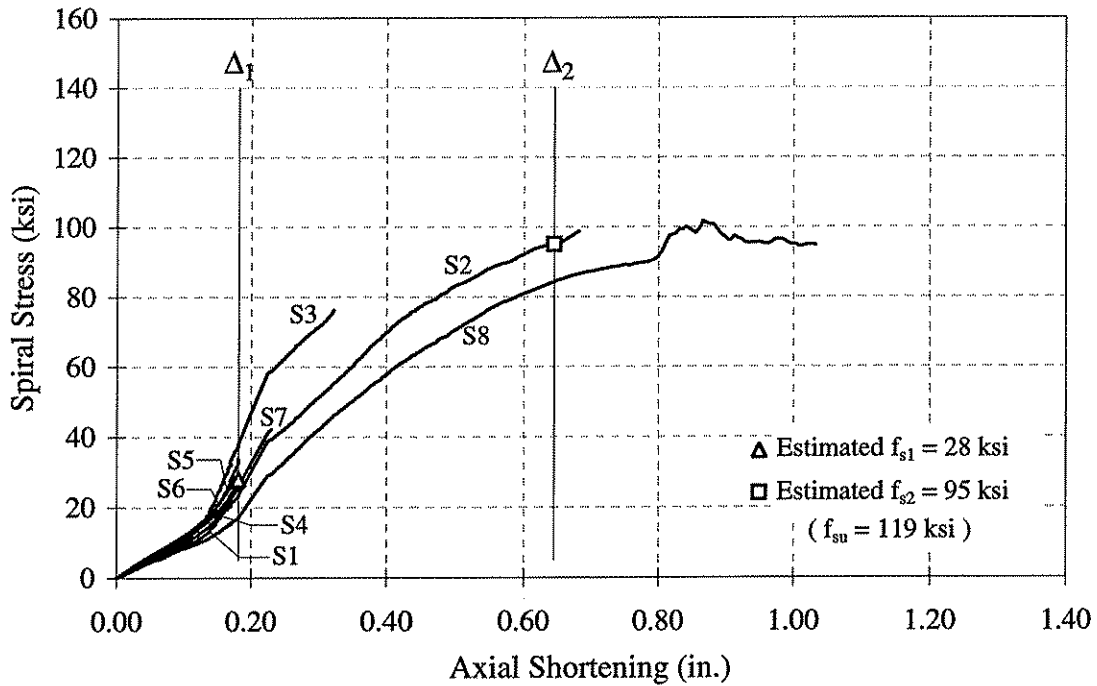

Figure 6.6   Plot of spiral stress versus axial shortening for Pile 14-B.

137
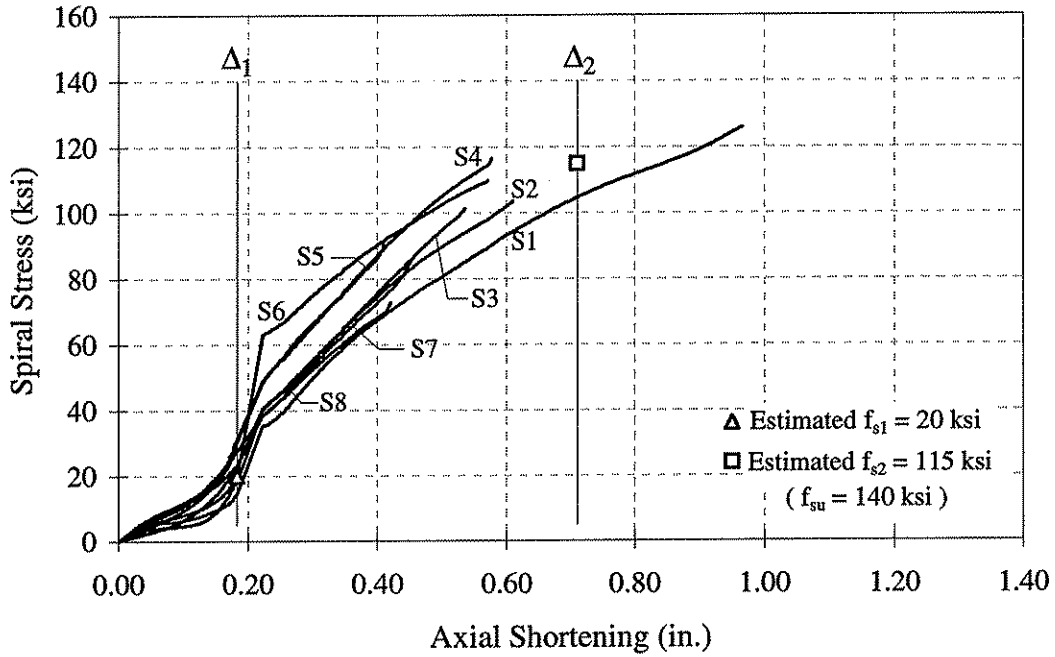
Figure 6.7   Plot of spiral stress versus axial shortening for Pile 14-C.
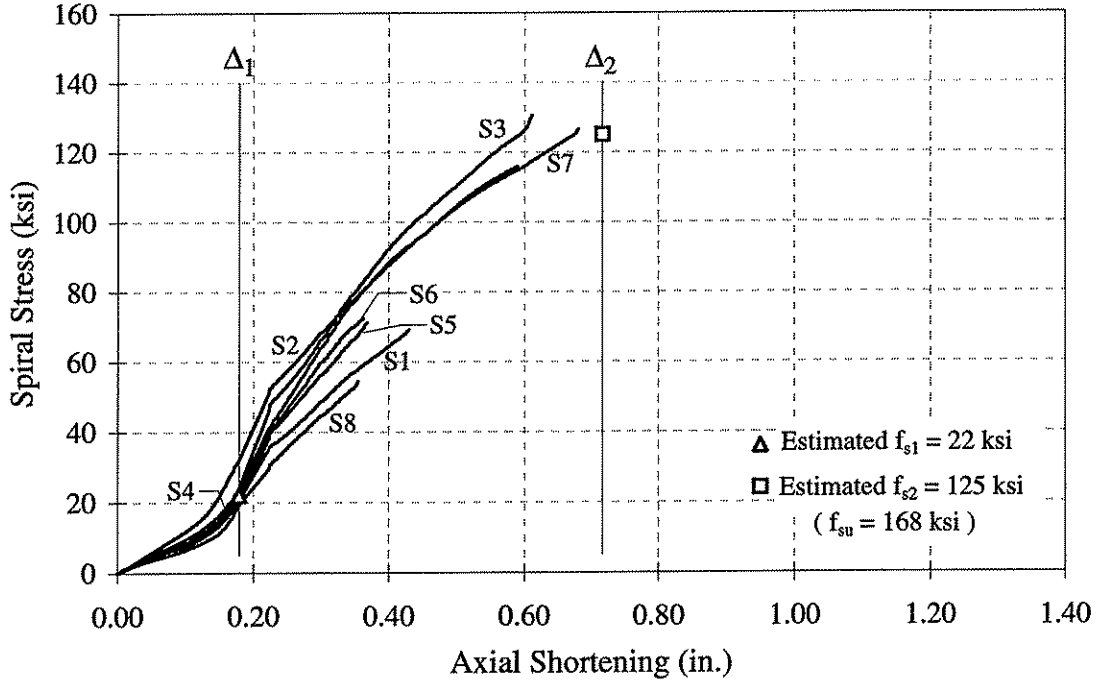
Figure 6.8   Plot of spiral stress versus axial shortening for Pile 14-D.

138
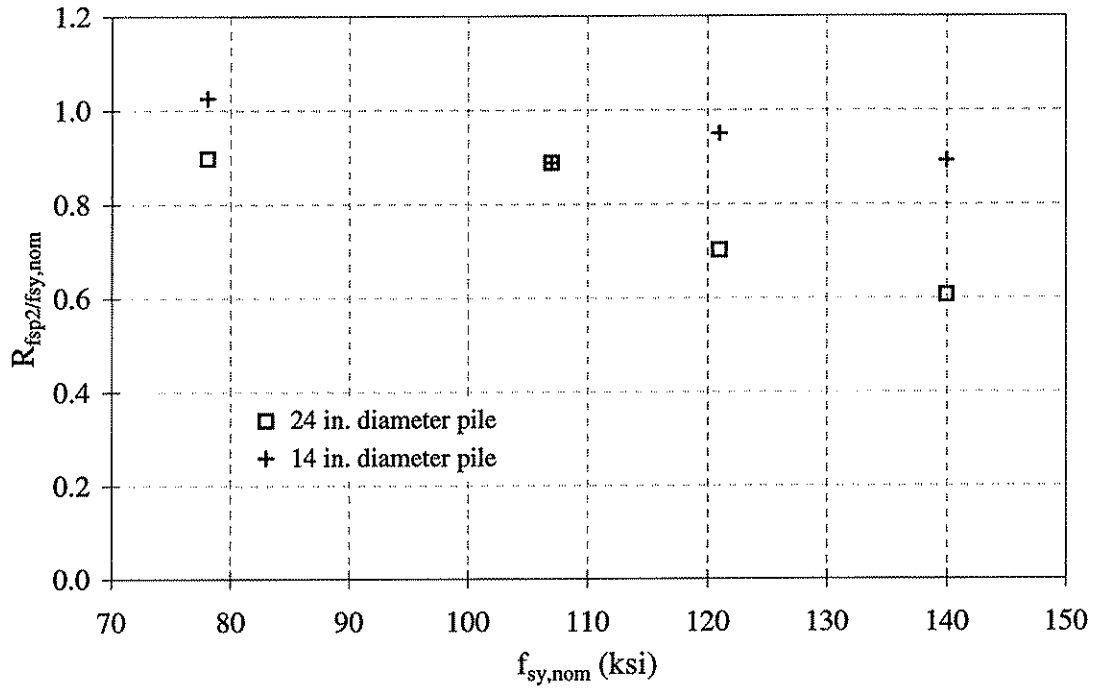
Figure 6.9   Ratio of experimentally determined spiral stress at Δ_2, f_{sp2}, to the nominal design spiral yield stress, $f_{sy,nom}$.
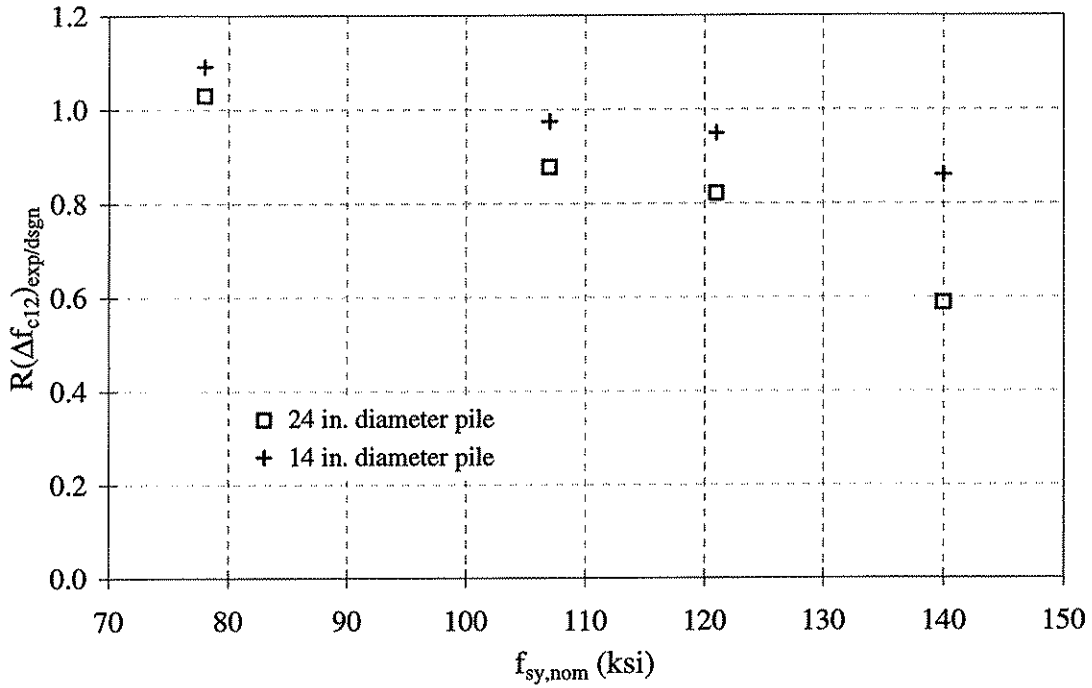
Figure 6.10   Ratio of experimental to design Δf_{c12}.
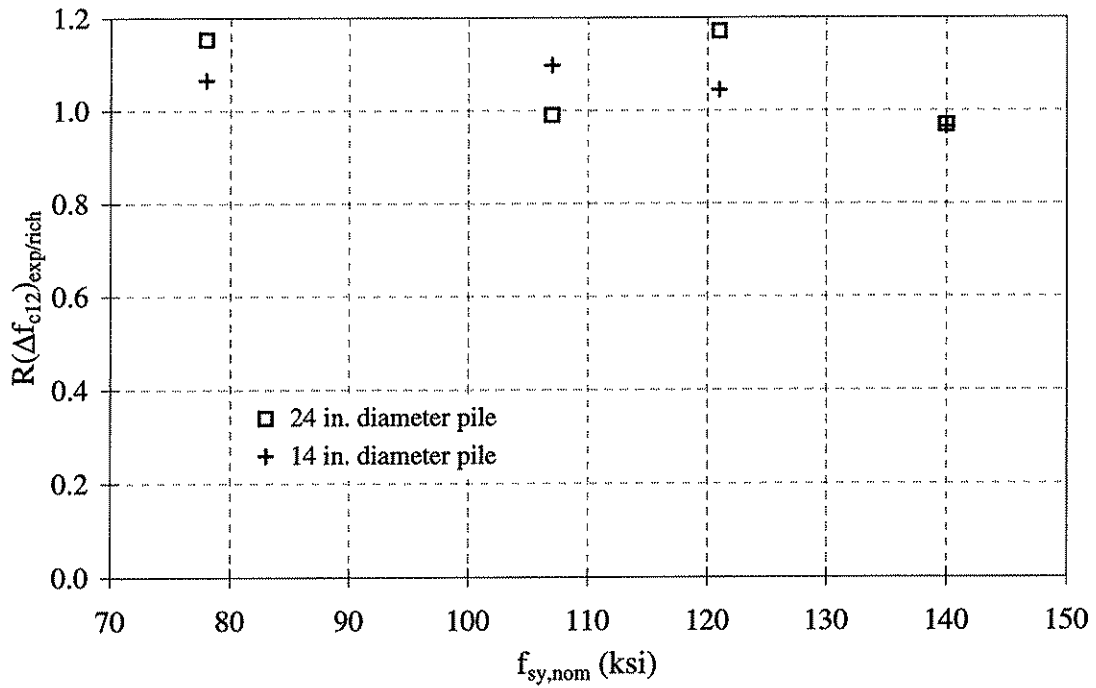
Figure 6.11   Ratio of experimental to Richart et al. Δf_{c12}.
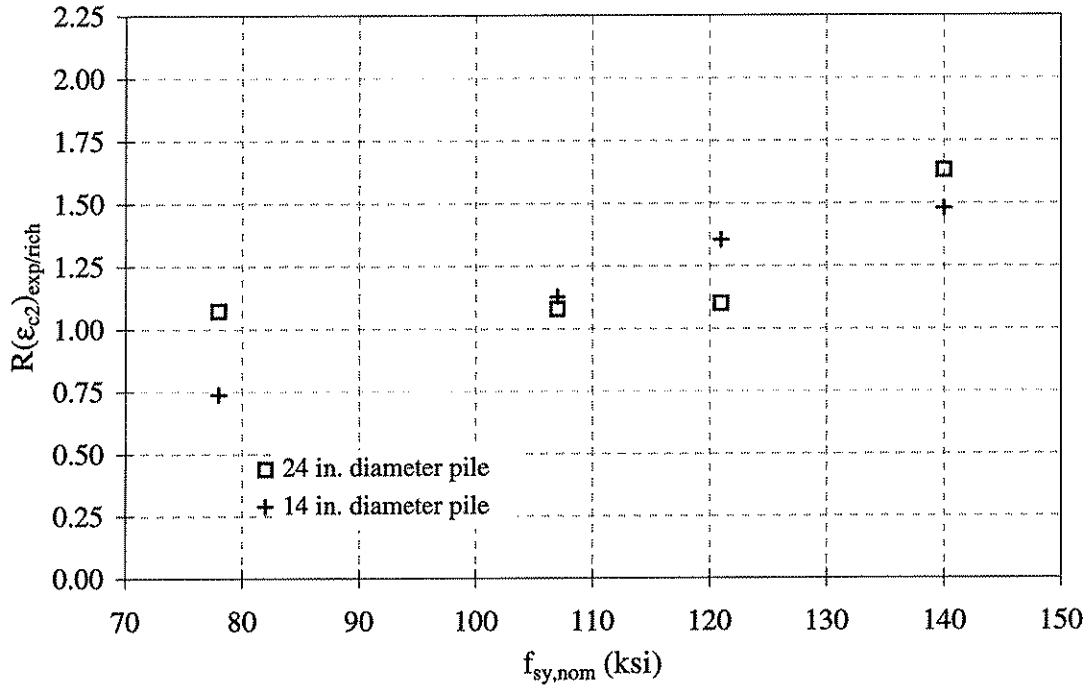
Figure 6.12   Ratio of experimental to Richart et al. ε_{c2}.
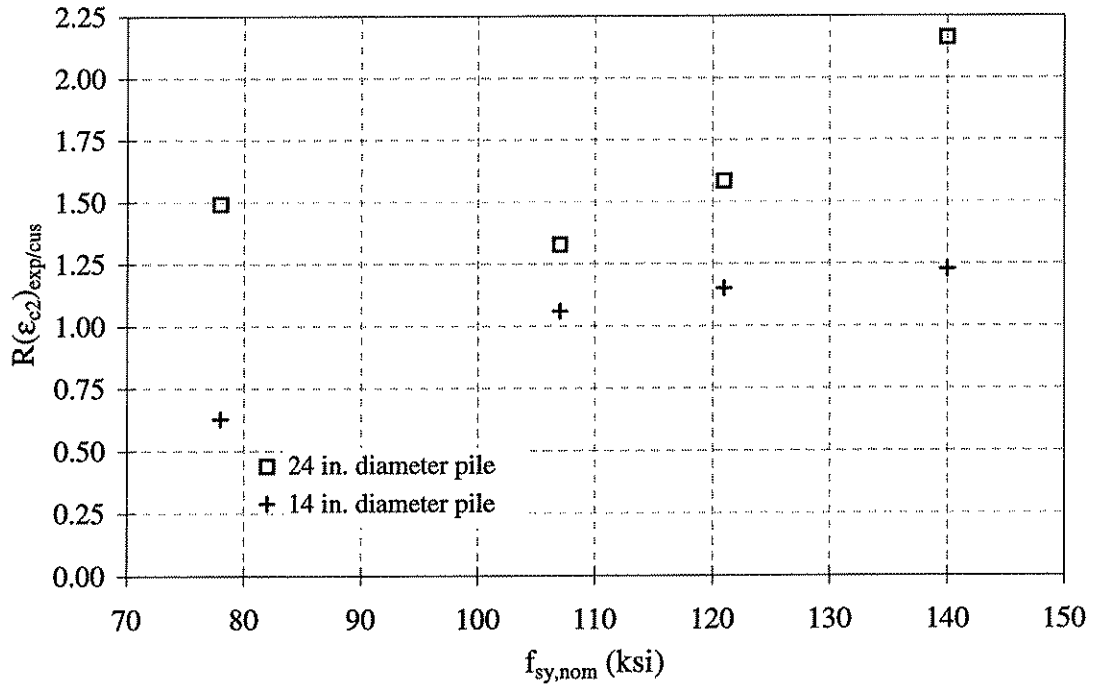
Figure 6.13   Ratio of experimental to Cusson et al. ε_{c2}.

141
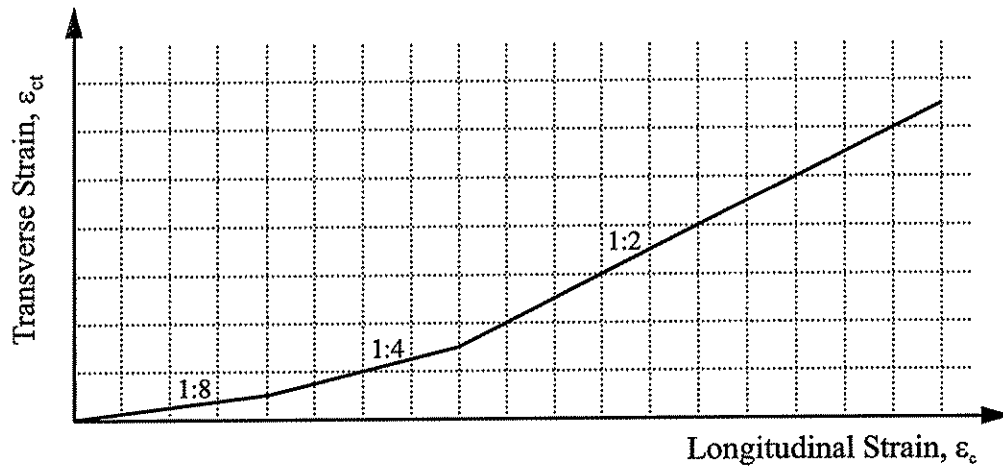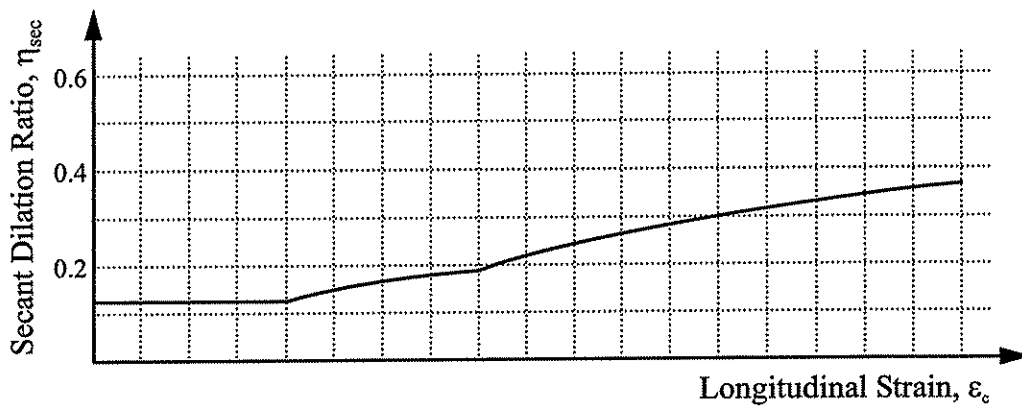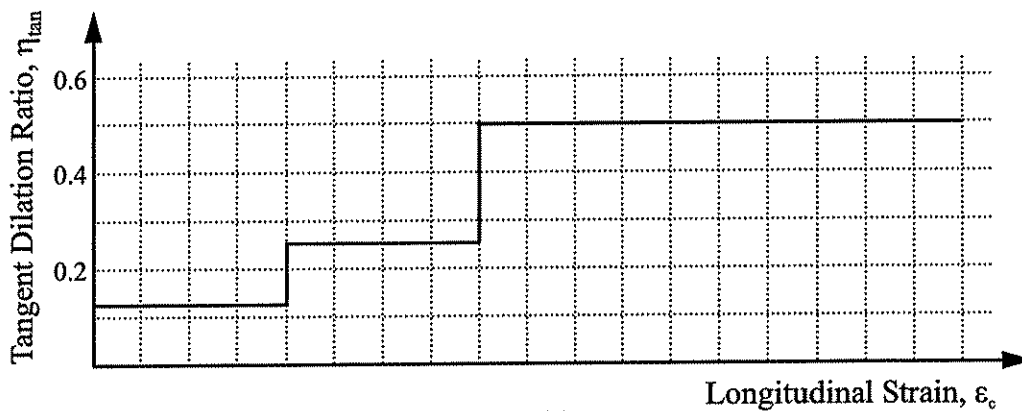
Figure 6.14   Definitions of dilation ratios: (a) idealized plot of transverse strain
versus longitudinal strain; (b) secant dilation ratio; and (c) tangent
dilation ratio.

142
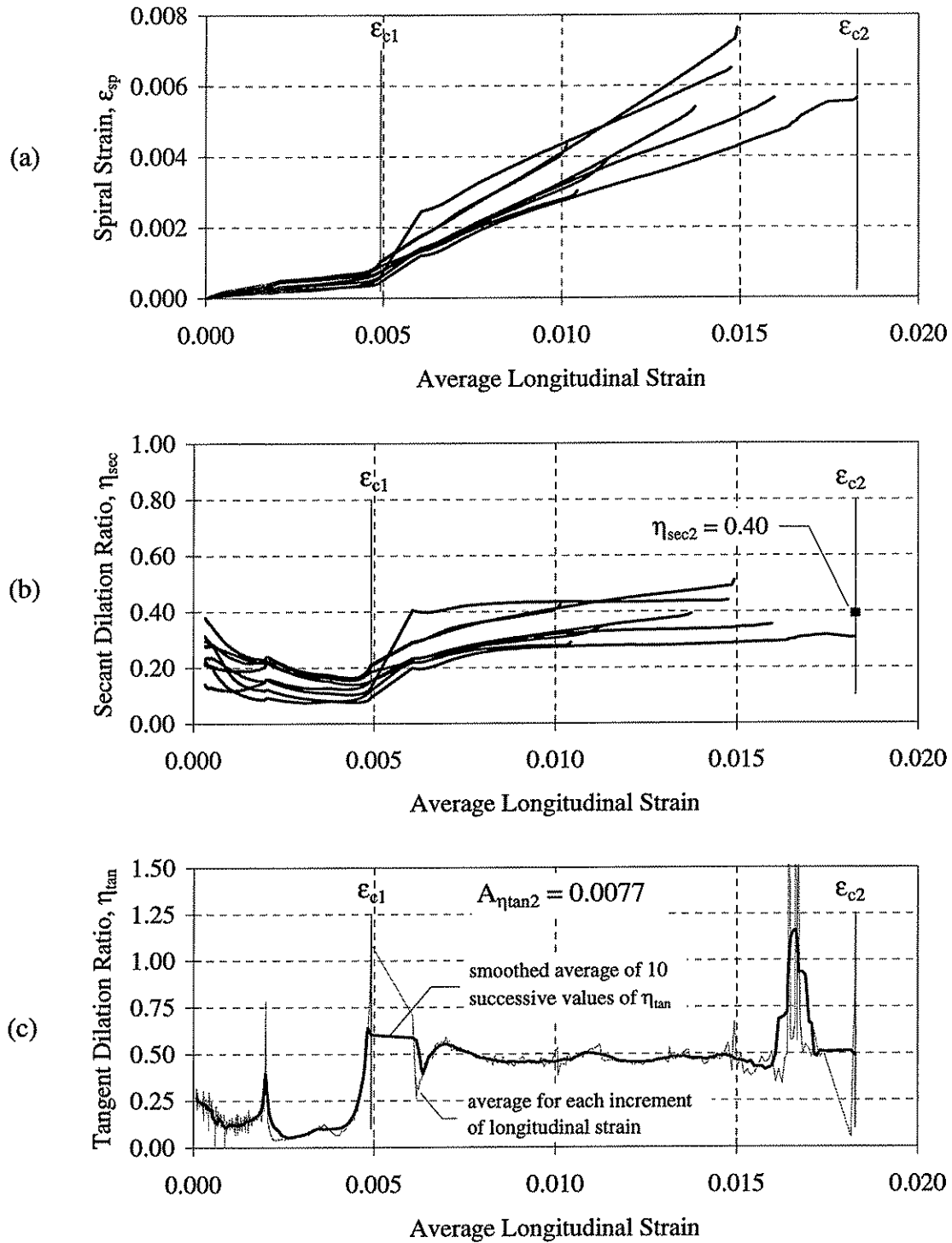
Figure 6.15   Pile 14-C experimentally determined dilation ratio parameters:
(a) spiral versus longitudinal strain; (b) secant dilation ratio; and
(c) tangent dilation ratio.
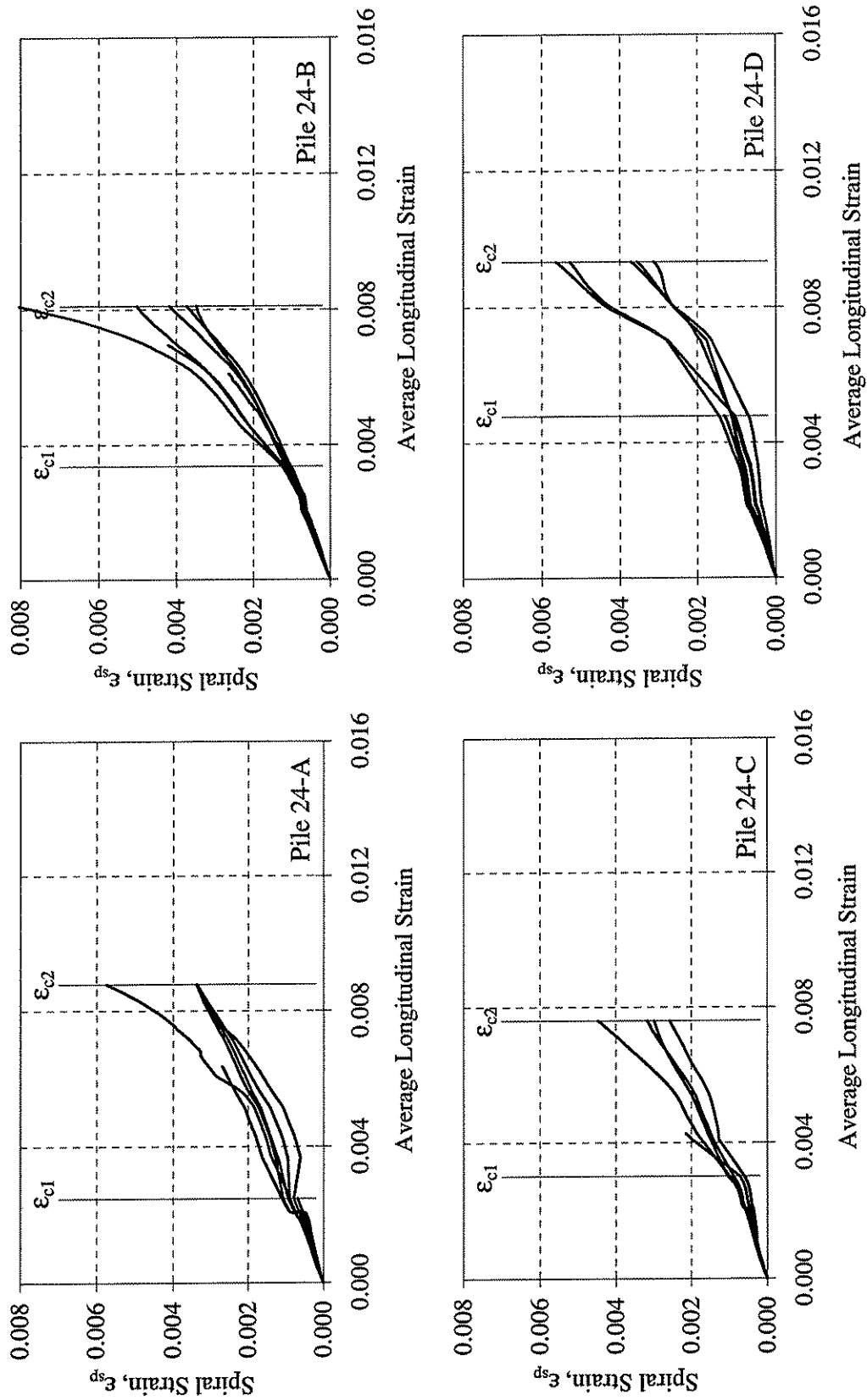
Figure 6.16   Spiral strains plotted versus average longitudinal strain for 24 in. diameter piles.

144
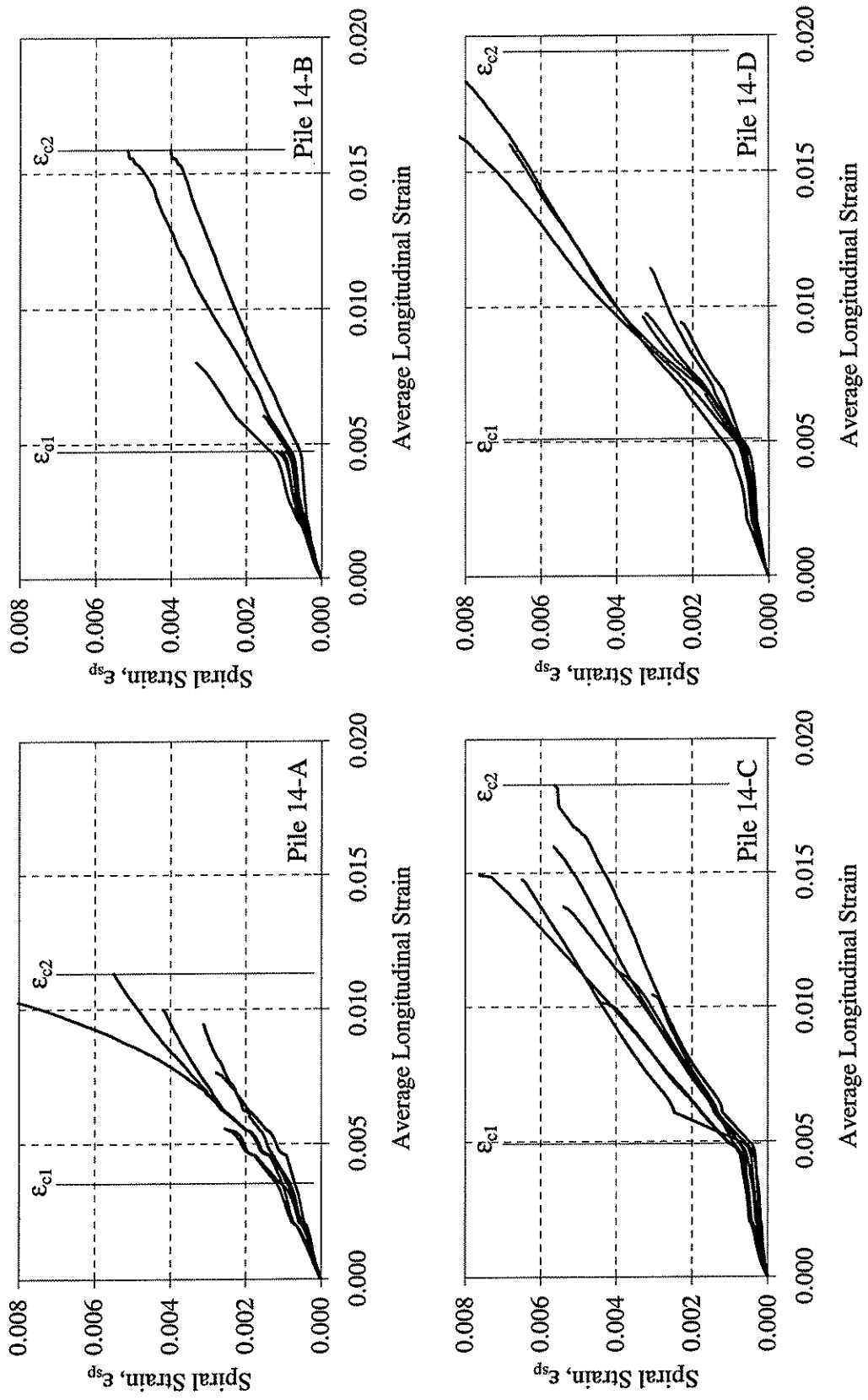
Figure 6.17 Spiral strains plotted versus average longitudinal strain for 14 in. diameter piles.

145
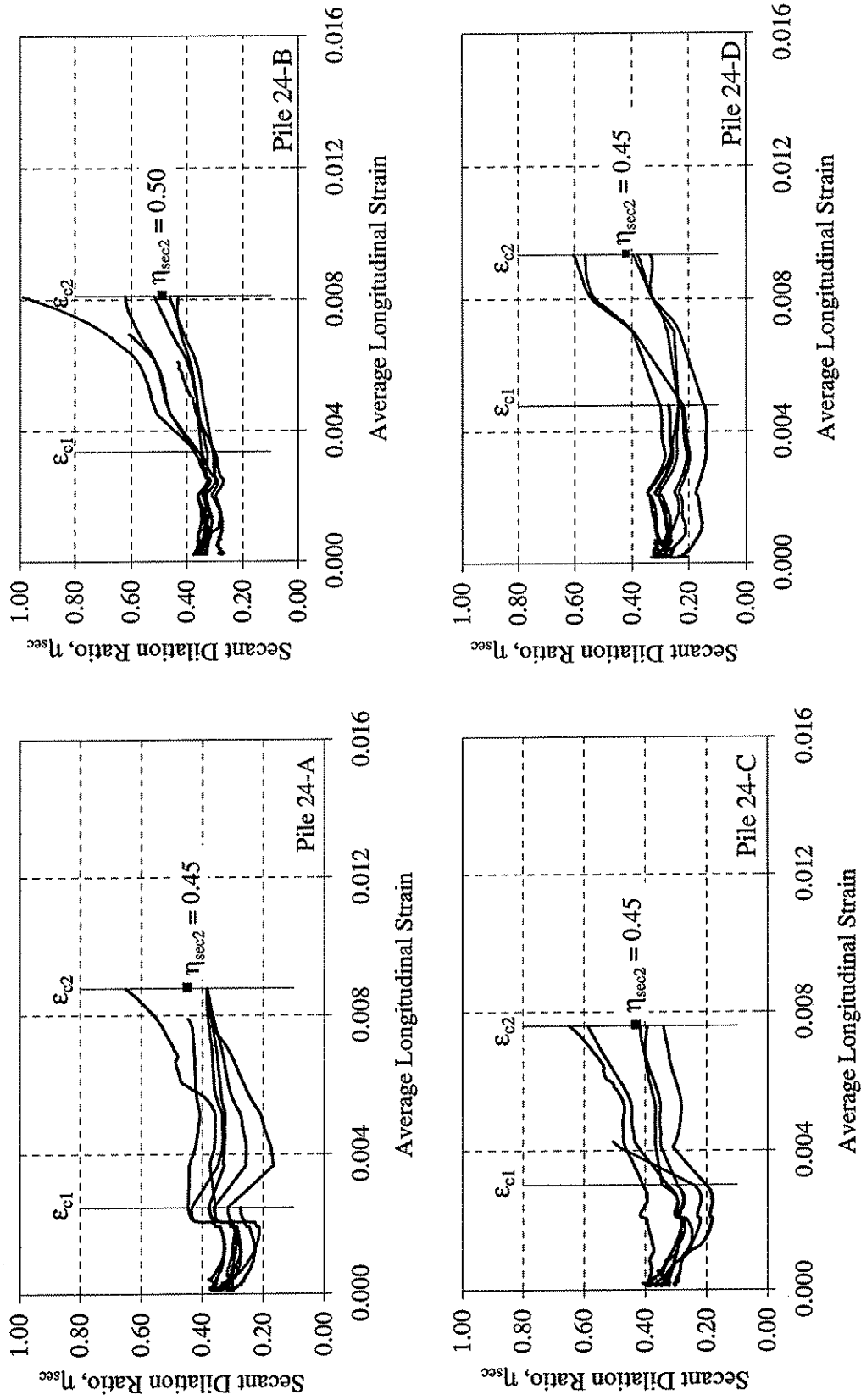
Figure 6.18   Plots of secant dilation ratios for 24 in. diameter piles.

146
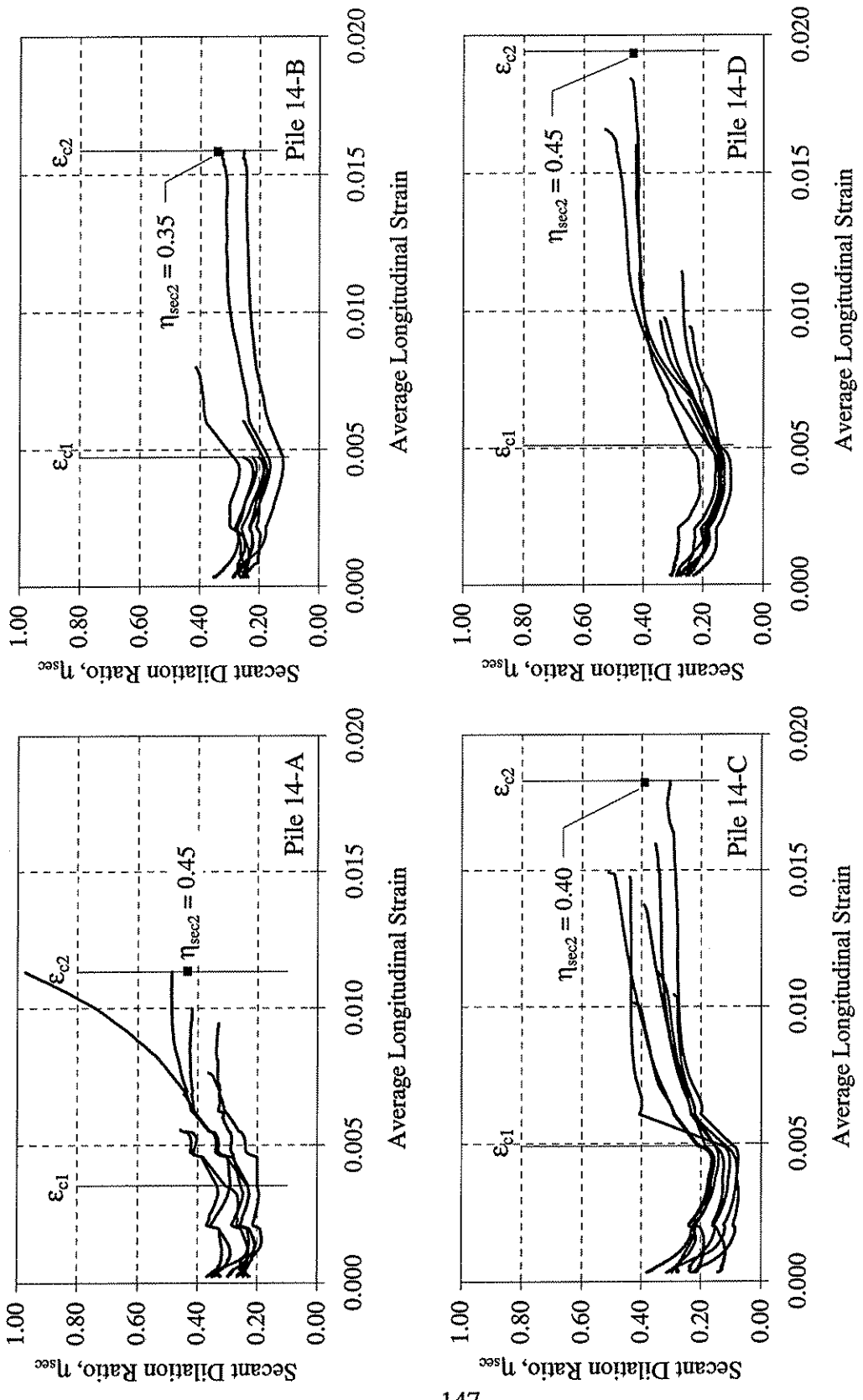
Figure 6.19   Plots of secant dilation ratios for 14 in. diameter piles.
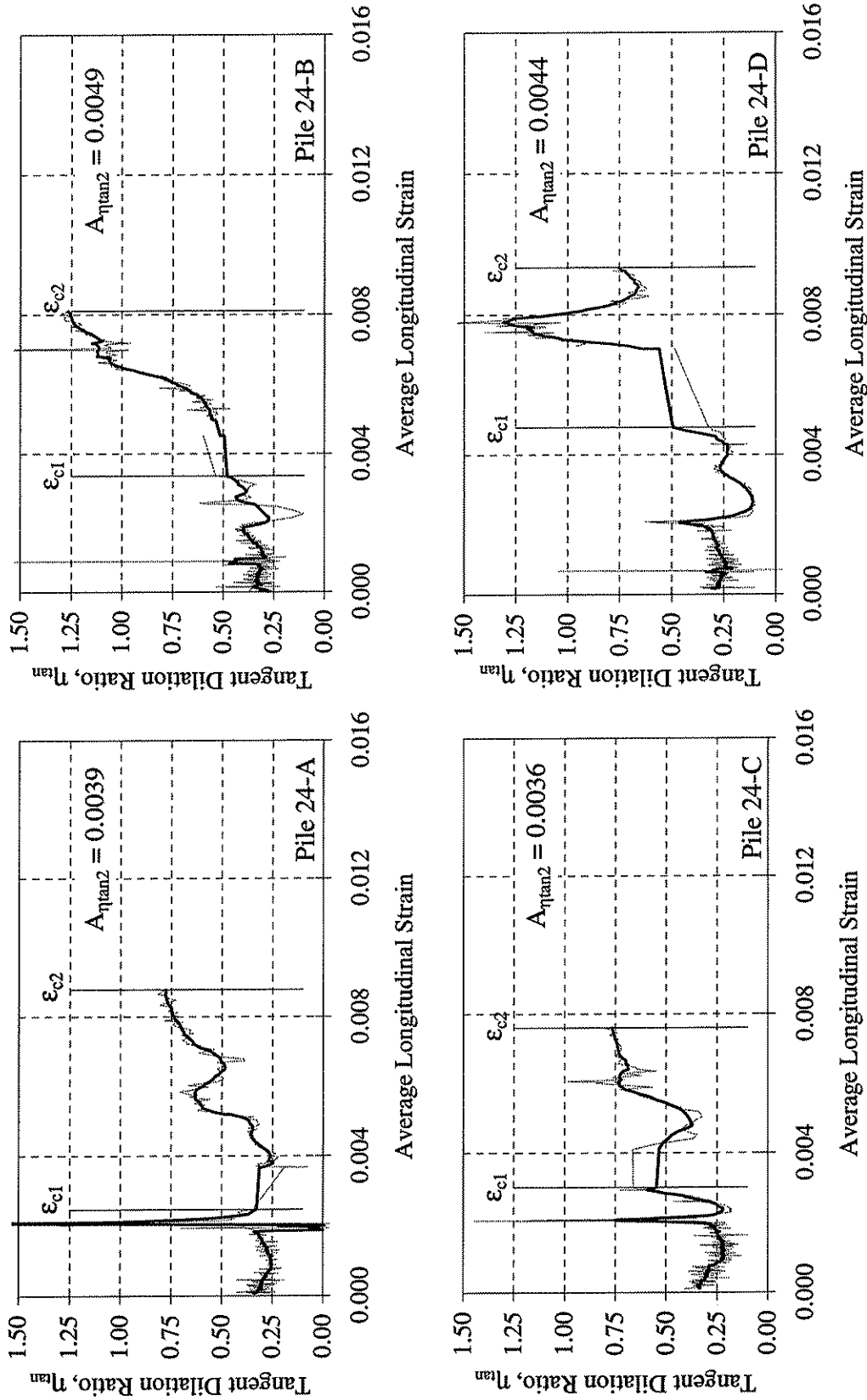
Figure 6.20   Plots of average tangent dilation ratios for 24 in. diameter piles.

148
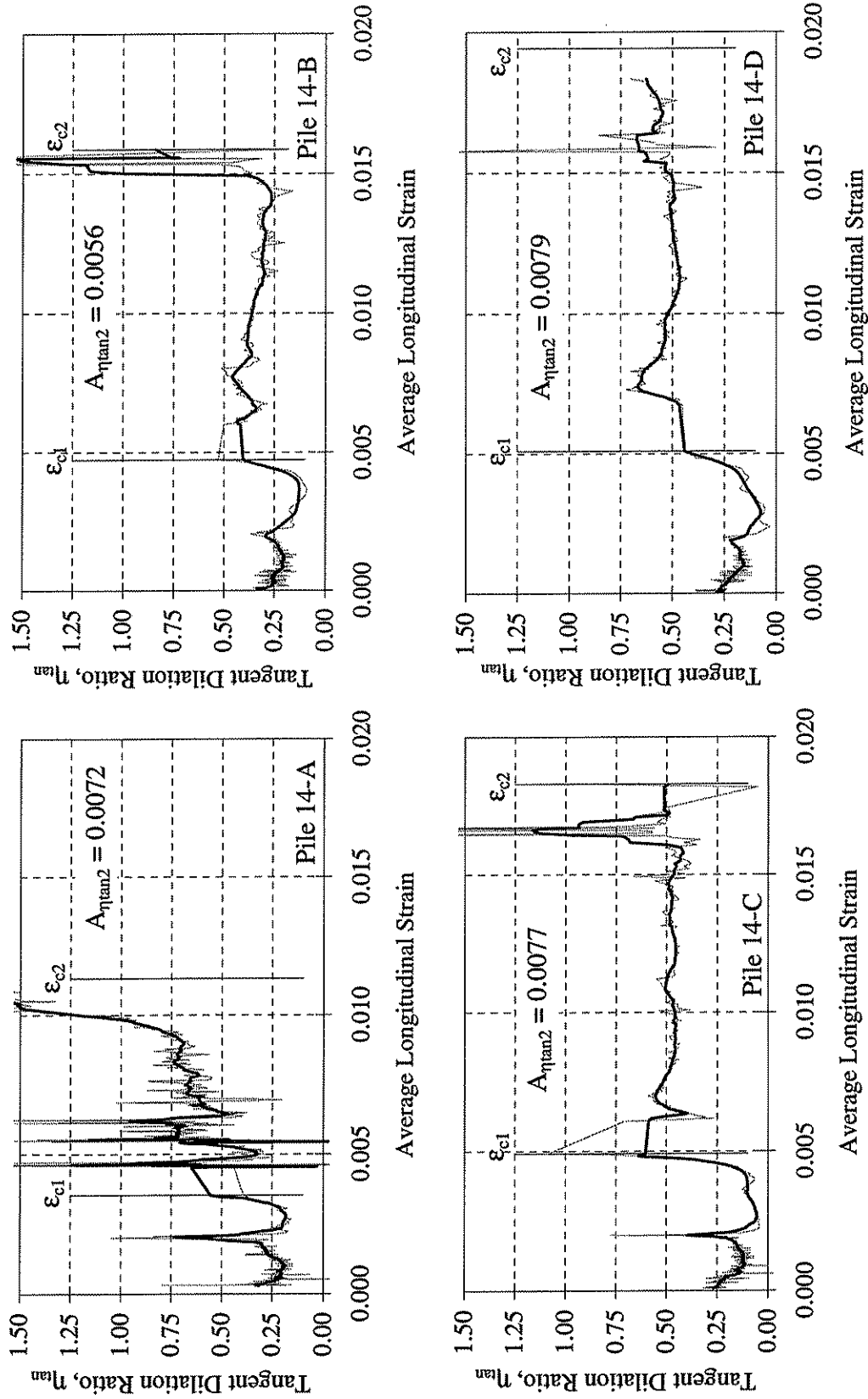
Figure 6.21 Plots of average tangent dilation ratios for 14 in. diameter piles.

149
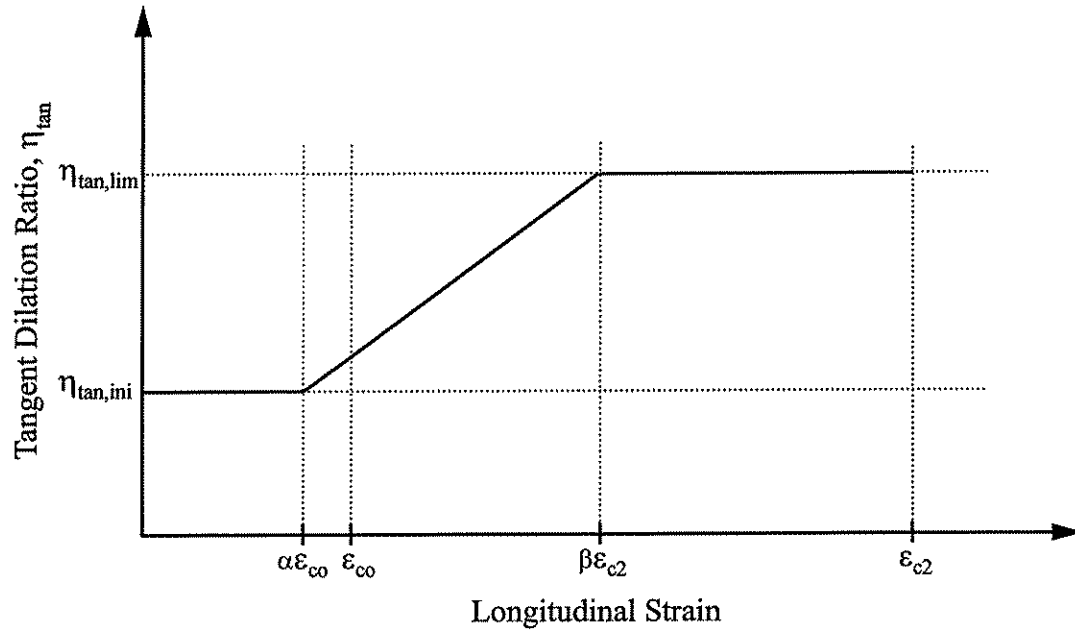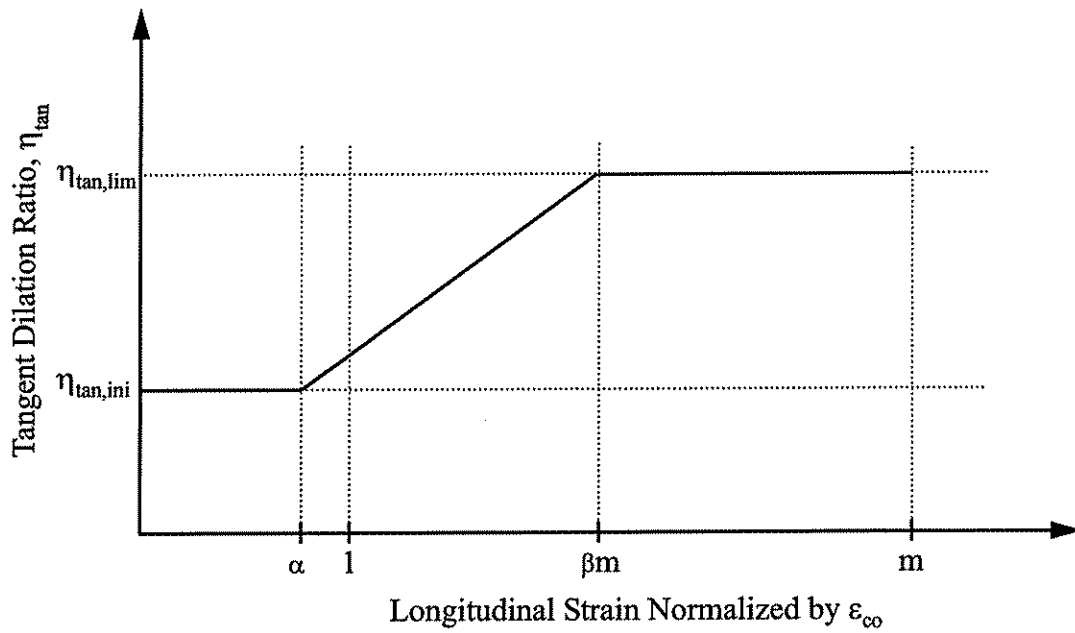
Figure 6.22   Proposed tangent dilation ratio relationship: (a) general form; (b) normalized by ε_{co}.
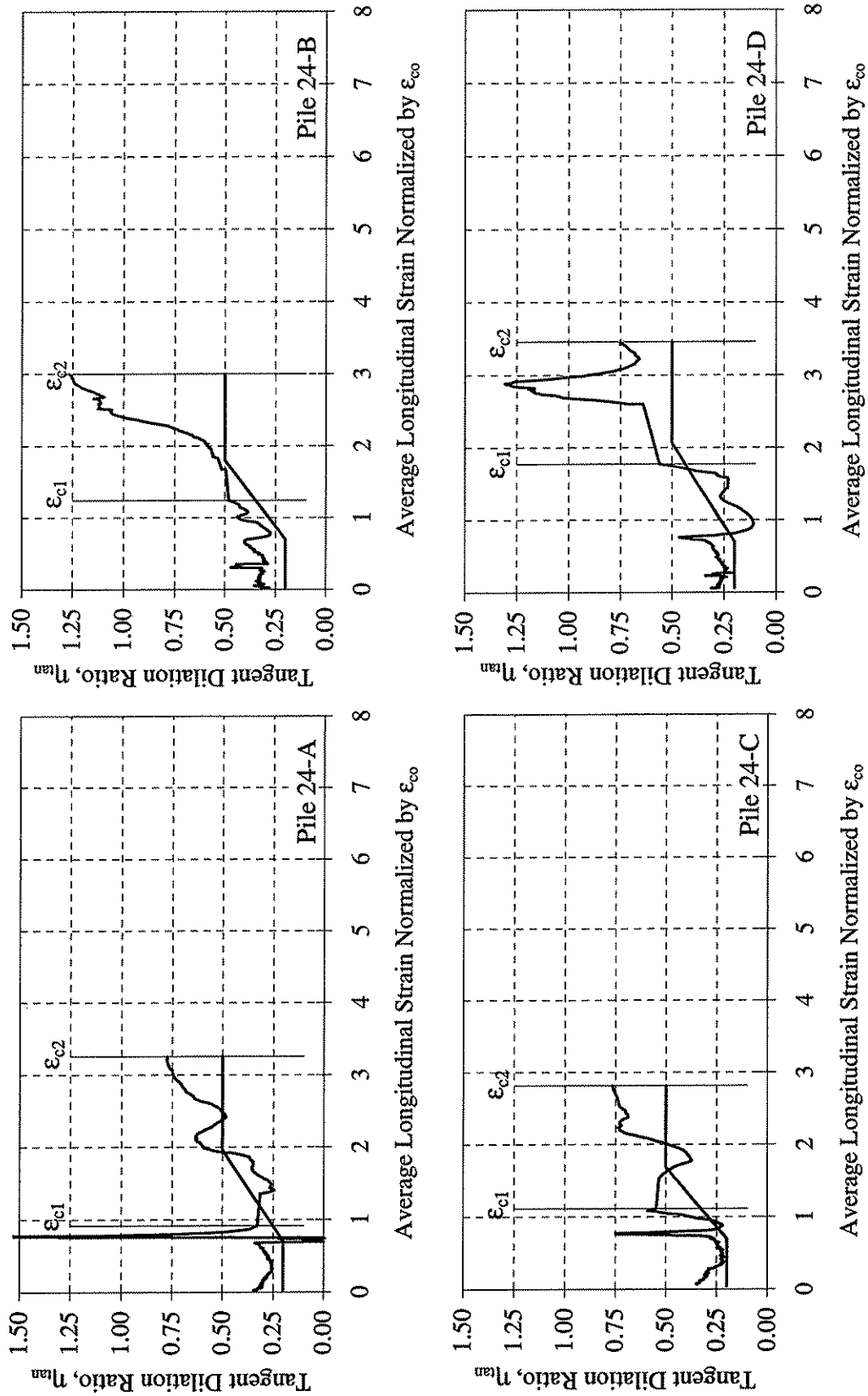
Figure 6.23   Plots of experimental and proposed average tangent dilation ratios for 24 in. diameter piles.

151
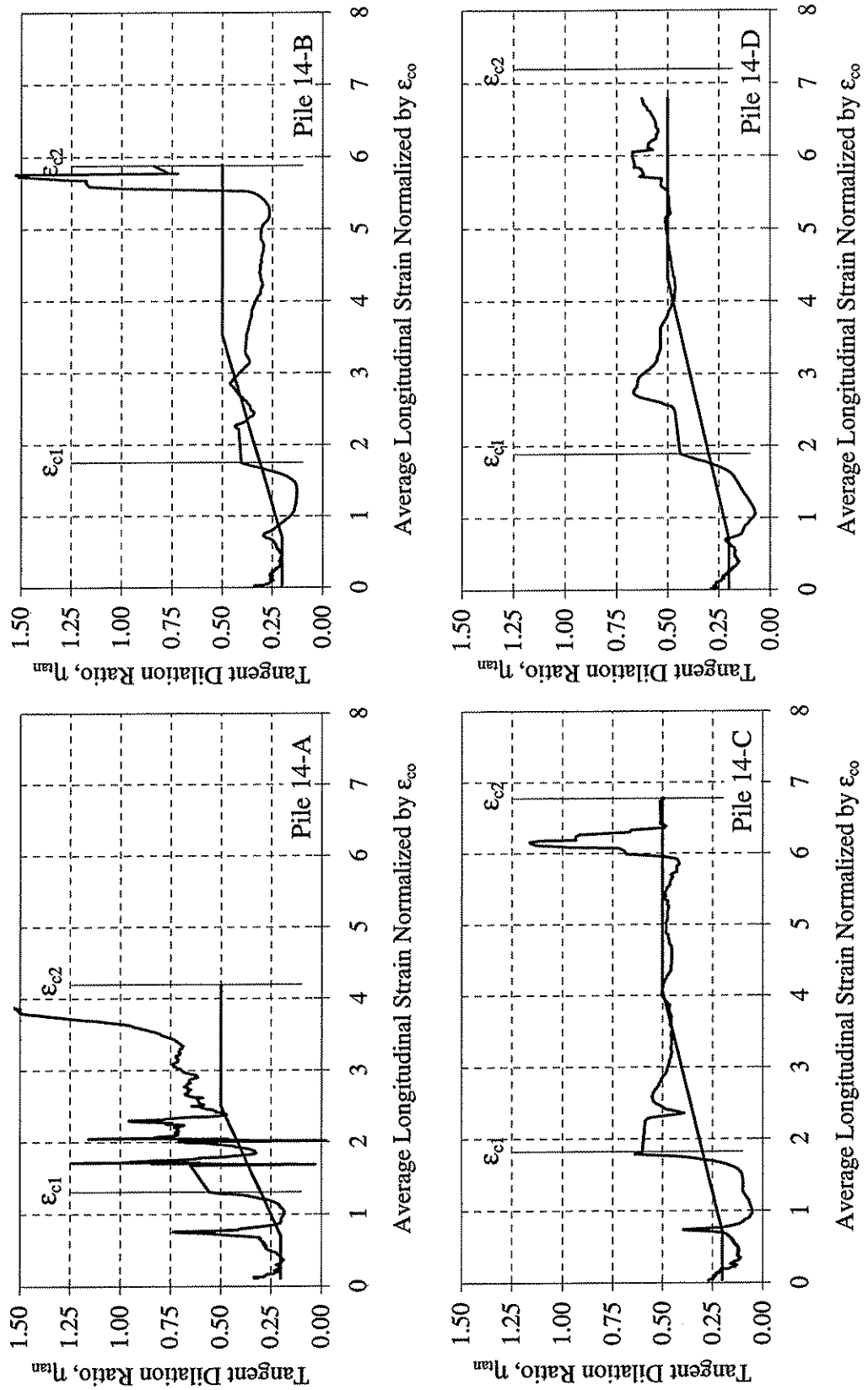
Figure 6.24   Plots of experimental and proposed average tangent dilation ratios for 14 in. diameter piles.

CHAPTER 7
PROPOSED METHOD FOR THE DESIGN OF HIGH STRENGTH
SPIRAL REINFORCEMENT FOR PILES

7.1 INTRODUCTION

This chapter proposes a method for the design of high strength spiral reinforcement for piles. Section 7.2 presents the proposed method. As will be shown in Section 7.2, the proposed method involves the determination of the strain in the spiral at the confined concrete peak strength, ε_{sp2}. The strain in the spiral is determined without prior knowledge of the stress-strain curve of the spiral. However, once ε_{sp2} is determined, knowledge of the *in situ* stress-strain curve is required to design the spiral.

Practical implementation of the proposed method is illustrated in Section 7.3. Using the actual stress-strain curves for the four grades of spiral treated in this study, determined from tension tests of spiraled/straightened wires, spiral reinforcement is redesigned for the 24 in. (610 mm) and 14 in. (356 mm) diameter piles.

Section 7.4 uses the proposed method to determine the maximum useable spiral stress for various pile cross-sectional configurations for a range of pile diameters. Effectively, this is the development of a design aid for high strength spiral reinforcement.

7.2 PROPOSED METHOD FOR SPIRAL DESIGN

Through the combination of a number of the relationships which have been studied throughout this report, a method is proposed which can be used to design high strength spiral reinforcement for piles.

The first step in the method is to determine the level of confined compressive strength which is desired for the core concrete in the pile. This is the core strength at the second peak in the load-shortening response of the pile, and it is thus denoted as f_{c2}. In the usual design of a pile (Section 2.6), this core strength is sufficient to allow the pile to carry the same axial load after the loss of cover concrete that it carried prior to the loss of the cover concrete. With this approach, f_{c2} can be calculated from Equation 7.1.

$$f_{c2} = \frac{f_{co}A_{c,total}}{A_{c,o-o}}$$ (7.1)

However, the proposed method is not limited to f_{c2} computed in this manner, and the desired core strength can be set to any desired value.

After f_{c2} is determined, Equation 7.2 is used to calculate the confining pressure, f_{2-2}, which is required in order for the core concrete to reach the desired strength.

153

$$f_{2-2} = \frac{1}{4.1}\left(f_{c2} - f_{co}\right) \tag{7.2}$$

This equation is a rewritten form of Equation 2.3 which was proposed by Richart et al. As before, the unconfined concrete strength is denoted as f_{co}. In Section 6.5 it was demonstrated that this equation is applicable to the piles treated in this study.

The longitudinal strain at the peak core strength, ε_{c2}, is estimated through Equation 2.4.

$$\varepsilon_{c2} = \varepsilon_{co}\left(5\frac{f_{c2}}{f_{co}} - 4\right) \tag{2.4}$$

This equation was derived by Richart et al. and is presented first in Section 2.2. ε_{co} is the longitudinal strain which corresponds to the peak strength of unconfined concrete. In Section 6.6 it was shown that this equation provides a conservative estimate of the longitudinal strain at the peak core strength.

Next, the transverse core concrete strain, ε_{ct2}, which occurs at the peak confined concrete strength, f_{c2}, is calculated using Equation 6.16.

$$\varepsilon_{ct2} = 0.41\varepsilon_{c2} - 0.105\varepsilon_{co} \tag{6.16}$$

This equation was first presented in Section 6.7.3. For the use of Equation 6.16 presented here, ε_{c2} is determined through the use of Equation 2.4. Section 6.7.4 discusses the validity of Equation 6.16 with regard to the piles tested in this study.

The strain in the spiral reinforcement is the same as the transverse strain in the concrete core. This is true at all strains, including strains at the second peak. Equation 7.3 represents this relationship.

$$\varepsilon_{sp2} = \varepsilon_{ct2} \tag{7.3}$$

Through the use of the equations presented above, the spiral strain, ε_{sp2}, at the confined concrete peak strength, f_{c2}, is determined. This represents the useable strain in the spiral reinforcement. Once ε_{sp2} is known, the stress-strain curve of the spiral is used to determine the stress in the spiral. Two possibilities exist at this point. First, if the *in situ* stress strain curve is available, i.e. the stress-strain curve for the spiral in its spiraled state, then f_{sp2} can be determined directly from the curve. If, as is more likely the case, only the stress-strain curve from a tension test is available, then the value of stress obtained from the curve may need to be modified to account for the differences between the in situ conditions and the tension test conditions.

The required spiral steel ratio is computed using Equation 7.4. This equation is a revised form of Equation 2.7.

$$\rho_{sp} = \frac{2f_{2-2}}{f_{sp2}} \tag{7.4}$$

Finally, using this spiral steel ratio and a given wire diameter, the required pitch is computed through the use of Equation 7.5. This equation is a revised form of Equation 2.8.

$$s = \frac{4A_{sp}}{d_{sp}\rho_{sp}} \tag{7.5}$$

In closing, as was mentioned in Sections 6.6 and 6.7, Equations 2.4 and 6.14 provide conservative estimates of ε_{c2} and ε_{ct2}, respectively. As a result, the design method presented above provides a conservative estimate of ε_{sp2}. A conservative estimate of the useable strain, ε_{sp2}, leads to a conservative value of the useable stress, f_{sp2}, and thus to a conservative design of the spiral for the pile.

7.3 REDESIGN OF THE TEST SPECIMENS USING THE PROPOSED DESIGN METHOD

The spiral reinforcements for the piles treated in this study are redesigned using the design method proposed in Section 7.2. The same general parameters used in the original design of the test specimens are again used here. Specifically, the piles are designed for 24 in. (610 mm) and 14 in. (356 mm) diameters with a 2 in. (51 mm) clear cover. The unconfined concrete compressive strength is 8.0 ksi (55.2 MPa). The strain corresponding to the unconfined peak concrete compressive strength is 0.0027. The piles are designed such that the load carrying capacity lost during cover failure is regained through increased strength of the confined core concrete.

For the 24 in. (610 mm) diameter pile, the level of f_{c2} is calculated using Equation 7.1. This leads to $f_{c2} = 11.53$ ksi (79.50 MPa). Using Equation 7.2, f_2 is calculated to be 0.862 ksi (5.94 MPa). Next, using Equation 2.4, ε_{c2} is calculated to be 0.0087. The value of ε_{ct2} is then calculated through the use of Equation 6.14 to be 0.0033. Thus, $\varepsilon_{sp2} = 0.0033$.

For the 14 in. (356 mm) diameter pile, the same procedure is followed. The only change in the given parameters for this pile is the pile diameter. Using Equation 7.1, $f_{c2} = 15.76$ ksi (108.7 MPa). Subsequently, $f_2 = 1.89$ ksi (13.0 MPa) and then $\varepsilon_{c2} = 0.0158$. Through the use of Equation 6.14, $\varepsilon_{ct2} = 0.0062$ and thus $\varepsilon_{sp2} = 0.0062$.

The ε_{sp2} values calculated above for both diameter piles are shown on Figure 7.1. Also shown on this figure are the stress-strain curves for the four grades of spiral steel as described in Section 5.6. Any of the grades of steel can be used in the design of each pile. However, each of the grades of

155

steel provides a different value of f_{sp2} at ε_{sp2}. Therefore, different volumetric ratios of each grade are required in each pile. For example, for the 14 in. (356 mm) diameter pile, the Grade A reinforcement exhibits a stress of 79 ksi at ε_{sp2}, and thus, from Equation 7.4, requires $\rho_{sp} = 0.0479$ to provide the requisite confining pressure. In this same pile, if Grade C reinforcement is used instead, a stress of 108 ksi is exhibited at ε_{sp2} and thus only $\rho_{sp} = 0.0350$ is required.

Table 7.1 summarizes the volumetric ratio of spiral steel required for the original design of each pile ($\rho_{sp,nom}$) and the volumetric ratio of spiral steel required for the redesign of each pile ($\rho_{sp,redesign}$) using the proposed design procedure. Note that the values of $\rho_{sp,nom}$ are different than the values of ρ_{sp} presented in Table 3.2 due to the slight rounding which is inherent in Equation 2.8, the equation from which the values in Table 3.2 are calculated. Also included in Table 7.1 for comparison purposes is the required volumetric ratio of spiral reinforcement for a 60 ksi yield stress spiral ($\rho_{sp,60}$). Finally, Table 7.1 includes ratios of these steel reinforcement ratios.

Table 7.1 shows that only moderate reductions in the volumetric ratio of spiral reinforcement are achievable for the larger diameter piles. Specifically, for the four grades of reinforcement considered, reductions on the order of 10 to 20 percent are possible. Much greater reductions in spiral reinforcement are possible for the smaller diameter piles as compared to the larger diameter piles. This is because, for a given spiral wire, the smaller diameter piles are able to mobilize a greater useable spiral stress as compared to the larger diameter piles. For the smaller diameter piles and the grades of reinforcement considered, reductions in the required volumetric ratio of spiral reinforcement approaching 45 percent are possible.

Finally, Table 7.1 indicates that for the 24 in. (610 mm) diameter piles, the Grade D wire has a lower value of useable stress than the Grade B and C wires. This is the result of the shape of the stress-strain curves for these three wires. As shown in Figure 7.1, below a strain of about 0.005, the Grade D wire exhibits a lower stress than the Grade B and C wires. Thus, at the useable strain of 0.0033, the Grade D wire exhibits a lower useable stress. The opposite situation occurs in the 14 in. (356 mm) diameter piles, where the useable strain in the spiral reinforcement is 0.0062. At this strain, the useable stress in the Grade D wire is greater than the useable stress in the Grade B and C wires. Thus, in general, a high strength wire with a stress-strain curve characterized by a steep increase in stress with strain is more useful as a spiral material. This is because a higher useable stress may be obtained at any given strain value. This is more important for larger diameter piles, which tend to have a lower strain in the spiral at the second peak.

7.4 DEVELOPMENT OF A DESIGN AID

This section of the report describes the development of a design aid to determine the maximum useable stress, f_{sp2}, for a given spiral stress-strain curve and a range of pile diameters and concrete cover distances. The development of the design aid is presented here for the case of the Grade D spiral in its spiraled/straightened state. It is noted that the results of the development given here would be slightly different for the case of the wire in its spiraled state, since the stress-strain curve for the spiraled/straightened state is slightly different than the in situ stress-strain curve for the

156

spiraled state. However, for the purpose of explaining the development of the design aid, this slight difference is not important.

Figure 7.2 shows the design aid for the Grade D spiral for pile diameters ranging from 12 in. (305 mm) to 58 in. (1470 mm). These piles are all designed with an unconfined concrete compressive strength of 8 ksi (55.2 MPa), a corresponding strain of 0.0027, and no longitudinal steel. Two curves are presented for the range of pile diameters, one representing a 3 in. (76 mm) clear cover and one representing a 1.5 in. (38 mm) clear cover.

These curves were obtained through the use of the proposed method for spiral design as presented in Section 7.2. To summarize the method, first the desired f_{c2} was calculated from Equation 7.1. This desired increase is based on replacing the load carrying capacity which the pile would lose at cover failure. Next, Equation 7.2 was used to calculate the required confining pressure on the confined core. Following this, Equation 2.4 was used to calculate ε_{c2} and then Equation 6.14 was used to calculate ε_{ct2}. Therefore, the value of ε_{sp2} is known since it is equivalent to ε_{ct2}. Using ε_{sp2} and the best-fit stress-strain relation for the Grade D steel as presented in Figure 5.14, the maximum allowable stress in the spiral reinforcement was calculated.

A similar design aid could be obtained for any other set of conditions. For example, through the same procedure, a design aid could be obtained for any other spiral reinforcement stress-strain curve or for any other set of parameters for the pile cross-section. However, it is important to note that the stress-strain relationship for the spiral reinforcement should be the in situ stress-strain relationship for that particular diameter of spiral. In the case presented here, the spiral stress-strain properties were not the in situ properties, but represented the spiraled/straightened properties of steel from a 20 in. (508 mm) diameter spiral.

This design aid clearly shows that as the diameter of the pile increases, the maximum useable f_{sp2} decreases. This is due to the required f_{c2} decreasing because the ratio of $A_{c,o-o}$ to $A_{c,total}$ continues to decrease. A lower f_{c2} requires a lower confining pressure and is accompanied by a lower axial strain, ε_{c2}. In turn, a smaller ε_{ct2} is exhibited and thus the maximum useable f_{sp2} is smaller.

Also note that, depending on the parameters chosen, the maximum useable spiral stress, f_{sp2}, may be lower than 60 ksi (414 MPa). Designing the spiral reinforcement in a pile based on a nominal design yield strength of 60 ksi (414 MPa) may not provide the required response. This is especially the case for both large diameter piles as well as piles which have a relatively small clear cover.

7.5 SUMMARY

The use of a fixed, predefined value of design yield stress for a particular spiral wire reinforcement is not an adequate way to approach the design of a spiral for a pile. This is because the value of stress in the spiral that can be used in design depends upon many factors including the in situ spiral stress-strain curve, pile diameter, cover distance, and concrete strength. The proposed method for the design of high strength spiral reinforcement provides a means to determine the

useable stress in a given spiral wire for a particular combination of pile geometric parameters and material properties. It is recommended that, in the absence of additional research to evaluate the range of applicability of the proposed method, application of the method be limited to piles with similar geometries and material properties as the piles treated in this study.

For the pile geometries and material strengths treated in this study, current code provisions that limit the design yield strength of spiral reinforcement in piles to 60 ksi (414 MPa) are overly conservative. Spiral steel stresses in excess of 60 ksi (414 MPa) can be used to design spiral reinforcement in piles similar to the piles treated in this study.

Finally, the proposed method for the design of high strength spiral reinforcement suggests that for certain combinations of pile geometries and material strengths, current code provisions that limit the design yield strength of spiral reinforcement in piles to 60 ksi (414 MPa) are unconservative. However, this preliminary finding is based in part upon an extension of the proposed design method to a range of pile geometric parameters not treated in the present study, and thus not included in the development of the design method. Additional research is needed to further study this issue before definitive conclusions can be made.

Pile	60 ksi Spiral Steel		Design Yield Strength			Proposed Useable Stress		
	f_{sy} (ksi)	$\rho_{sp,60}$	$f_{sy,nom}$ (ksi)	$\rho_{sp,nom}$	$R(\rho_{sp})_{nom/60}$	$f_{sp2,redesign}$ (ksi)	$\rho_{sp,redesign}$	$R(\rho_{sp})_{redesign/60}$
24-A	60	0.0287	78	0.0221	0.77	68	0.0254	0.88
24-B	60	0.0287	107	0.0161	0.56	74	0.0233	0.81
24-C	60	0.0287	121	0.0142	0.50	76	0.0227	0.79
24-D	60	0.0287	140	0.0123	0.43	71	0.0243	0.85
14-A	60	0.0631	78	0.0485	0.77	79	0.0479	0.76
14-B	60	0.0631	107	0.0354	0.56	104	0.0364	0.58
14-C	60	0.0631	121	0.0313	0.50	108	0.0350	0.56
14-D	60	0.0631	140	0.0270	0.43	110	0.0344	0.55

1 ksi = 6.895 MPa
1 in. = 25.4 mm

Table 7.1   Summary of spiral design for pile specimens treated in this study.

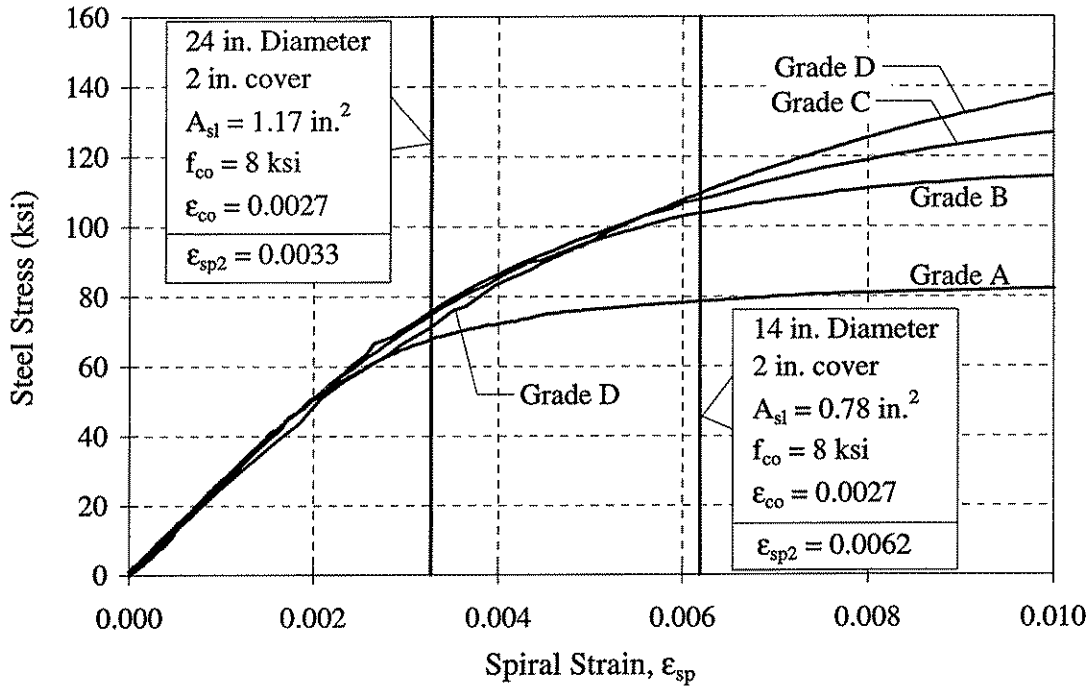Figure 7.1   Plot of ε_{sp2} calculated for the piles tested in this study as compared to the spiral stress-strain curves.
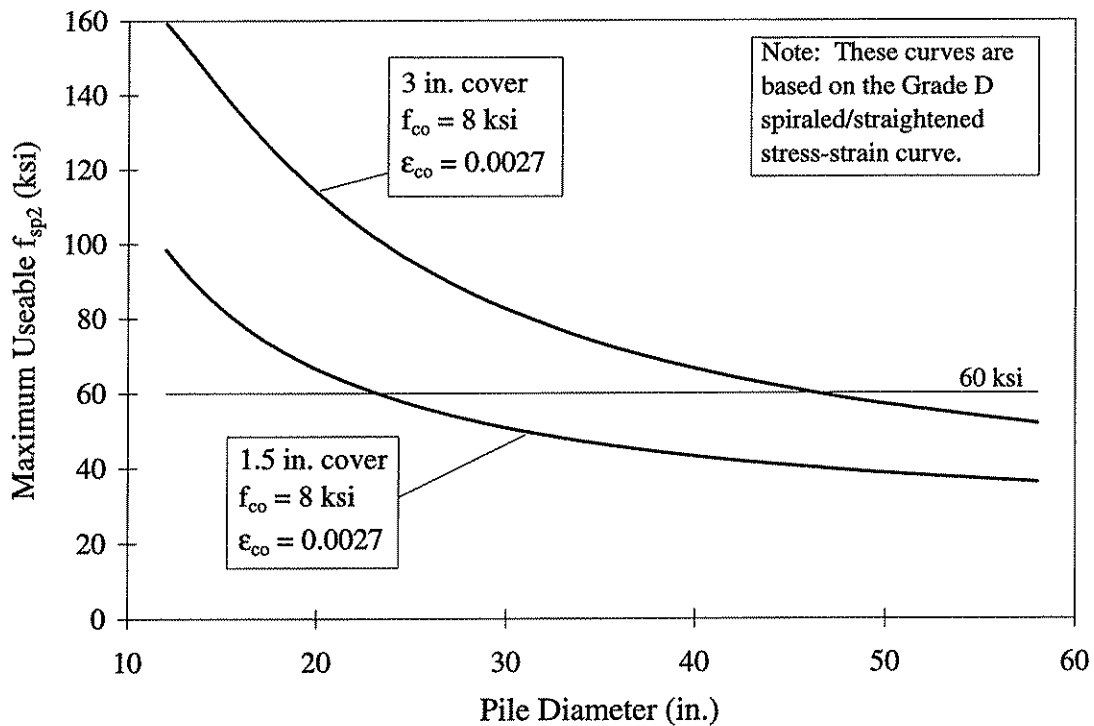

Figure 7.2   Maximum useable spiral stress for two pile configurations for a range of pile diameters for Grade D spiraled/straightened steel.

CHAPTER 8
CONCLUSIONS AND FUTURE RESEARCH

8.1 INTRODUCTION

Spiral reinforcement is often used as transverse reinforcement in precast, prestressed concrete piles. Present design code requirements limit the design yield strength of spiral reinforcement to 60 ksi (414 MPa). The objective of this research is to evaluate the confinement effectiveness of high-strength spiral reinforcement in precast, prestressed concrete piles.

This research involved three phases of work. The first phase involved tests of eight large-scale spirally reinforced concrete piles loaded in concentric axial compression. The test piles were designed according to the requirements of ACI 318 Building Code Requirements for Structural Concrete (1995) and American Association of State Highway and Transportation Officials LRFD Bridge Design Specifications (1994).

The second phase of the research focused on the material properties of the spiral reinforcement. Tension tests were performed on the reinforcement to determine the stress-strain properties, and analytical studies were performed to examine how these stress-strain properties are affected by the residual stresses introduced into the cross-section of the spiral wire as it is turned from a straight length of wire into a spiral.

The final phase of the research focused on the development of a proposed procedure for the design of high strength spiral reinforcement in piles.

The conclusions of this study are presented below. Following the conclusions, recommendations for future research are presented.

8.2 CONCLUSIONS

The following conclusions are made based on the research presented in this report:

1. For the pile geometries and material strengths treated in this study, current code provisions that limit the design yield strength of spiral reinforcement in piles to 60 ksi (414 MPa) are overly conservative. Spiral steel stresses in excess of 60 ksi (414 MPa) can be used to design spiral reinforcement in piles similar to the piles treated in this study. However, the spiral reinforcement should be designed according to the proposed method presented in Chapter 7.

2. The use of a fixed, predefined value of design yield stress for a particular spiral wire reinforcement is not an adequate way to approach the design of a spiral for a pile. This is because the value of stress in the spiral that can be used in design depends upon many factors including the in situ spiral stress-strain curve, pile diameter, cover distance, and concrete strength. The proposed method for the design of high strength spiral reinforcement provides a means to determine the useable stress in a given spiral wire for a particular combination of pile geometric parameters and material properties.

161

It is recommended that, in the absence of additional research to evaluate the range of applicability of the proposed method, application of the method be limited to piles with similar geometries and material properties as the piles treated in this study.

3. For the pile geometries and material properties treated in this study, the amount of reduction of the volumetric ratio of spiral reinforcement attainable through the use of a high strength spiral reinforcement depends in part upon the diameter of the pile. For the larger diameter piles treated in this study, only moderate reductions in the volumetric ratio of spiral reinforcement are achievable through the use of high strength spiral reinforcement. Specifically, for the four grades of reinforcement considered, reductions in the volumetric ratio of spiral reinforcement on the order of 10 to 20 percent are possible. Much greater reductions in spiral reinforcement are possible in the smaller diameter piles as compared to the larger diameters piles. This is because, for a given spiral wire, the smaller diameter piles are able to mobilize a greater useable spiral stress as compared to the larger diameter piles. For the smaller diameter piles and the grades of reinforcement considered, reductions in the required volumetric ratio of spiral reinforcement approaching 45 percent are possible.

4. For the piles treated in this study, the smaller diameter piles exhibit a larger axial strain at the confined concrete peak strength and a larger strain in the spiral reinforcement at the confined concrete peak strength, as compared to the larger diameter piles.

5. In general, a high strength wire with a stress-strain curve characterized by a steep increase in stress with strain is more useful as a spiral material. This is because a higher useable stress may be obtained at any given strain value. This is more important for larger diameter piles, which tend to have a lower strain in the spiral at the second peak in the response.

6. The spiraling process introduces residual stresses into the cross-section of a spiral wire. The magnitude of the residual stresses depends on a number of factors, including the diameter of the spiral, the wire diameter, and the stress-strain relationship of the wire.

7. Residual stresses introduced by the spiraling process change the tension stress-strain properties of the wire. For an unspiraled wire with an elastic-plastic tension stress-strain curve, the residual stresses in the wire introduced by the spiraling process cause a reduction in stress per strain exhibited near the knee of the curve. For a high strength steel wire that already exhibits a rounded stress-strain curve, the residual stresses introduced into the wire by the spiraling process also cause a reduction in stress per strain and a further rounding of the stress-strain curve.

8. For the pile geometries and material properties treated in this study, Equation 2.1 (Richart et al.) provides an accurate means of estimating the confined concrete compressive strength, f_{cc}, from the unconfined concrete compressive strength, f_{co}, and the actual confining stress, f_2. It is emphasized that the equation is accurate only if the actual confining pressure is used. The equation may not provide accurate results if a confining pressure is used which is based on an assumed yield stress in the spiral reinforcement. Equation 2.1 is used in the proposed method for the design of high strength spiral reinforcement in piles.

9. For the pile geometries and material properties treated in this study, Equation 2.2 (Richart et al.) provides a conservative estimate of the strain at the peak compressive stress in confined concrete. This equation is used in the proposed method for the design of high strength spiral reinforcement in piles.

10. For the pile geometries and material properties treated in this study, the proposed tangent dilation ratio relationship provides a reasonably accurate way to approximate the relationship between axial strains and transverse strains in the confined core. This proposed dilation ratio relationship is used in the proposed method for the design of high strength spiral reinforcement in piles.

11. For the pile geometries and material properties treated in this study, failure of the concrete cover occurred in a sudden, brittle manner.

12. For the pile geometries and material properties treated in this study, failure of all piles was precipitated by the failure of the concrete and not of the spiral steel. Evidence to support this conclusion includes the observation that all spiral steel strains were well below the fracture strains for the spirals when pile failure occurred. For the 24 in. (610 mm) diameter piles, failure occurred through the formation of a well defined inclined failure plane. The angle of the failure plane from the horizontal was approximately 60 to 65 degrees in all four specimens. For the 14 in. (356 mm) diameter piles, the failure occurred through either the formation of a poorly defined inclined failure plane or a sudden bulging failure mechanism.

13. The proposed method for the design of high strength spiral reinforcement suggests that for certain combinations of pile geometries and material strengths, current code provisions that limit the design yield strength of spiral reinforcement in piles to 60 ksi (414 MPa) are unconservative. However, this preliminary finding is based in part upon an extension of the proposed design method to a range of pile geometric parameters not treated in the present study, and thus not included in the development of the design method. Additional research is needed to further study this issue before definitive conclusions can be made.

8.3 FUTURE RESEARCH

The results presented in this report suggest a number of topics for future research. A few of these topics are as follows:

1. Perform axial load tests on piles designed using the proposed design method to examine the applicability of the proposed method.

2. Conduct a detailed experimental and analytical investigation of the in situ properties of high strength spiral reinforcement. This work should explore ways to correlate the results of tension tests of unspiraled wire to the in situ stress-strain properties of the spiral wire.

3. Examine the behavior of piles made with high strength spiral reinforcement under the combined action of axial loads and lateral loads.

4. Explore ways to restrain the inclined failure plane that developed in many of the piles treated in this study. This would likely lead to further improvements in pile ductility.

163

REFERENCES

AASHTO, *AASHTO LRFD Bridge Design Specifications*, American Association of State Highway and Transportation Officials, Washington, D.C., First Edition, 1994.

ACI Committee 318, "Building Code Requirements for Structural Concrete (ACI 318-95) and Commentary (ACI 318R-95)," American Concrete Institute, Farmington Hills, MI, 1995.

Collins, M.P., "Stress-Strain Relationships of High-Strength Concrete For Use In Structural Design," *Network of Centres of Excellence on High-Performance Concrete*, Montreal, April 26-28, 1992. 21 pp.

Collins, M.P., and Porasz, A., "Shear Design for High Strength Concrete," *CEB Bulletin d'Information*, No. 193, 1989, pp. 77-83.

Considère, A., "Rèsistance à la compression du bèton armè et du bèton frettè," *Gènie Civil*, 1903.

Cusson, D., De Larrard, F., Boulay, C., and Paultre, P., "Strain Localization in Confined High-Strength Concrete Columns," *Journal of Structural Engineering*, ASCE, Vol. 122, No. 9, September 1996, pp. 1055-1061.

Cusson, D., and Paultre, P., "Stress-Strain Model for Confined High-Strength Concrete," *Journal of Structural Engineering*, ASCE, Vol. 121, No. 3, March 1995, pp. 468-477.

Harries, K.A., Ricles, J.M., Sause, R., and Pessiki, S.P., "Modeling of the Uniaxial Stress-Strain Behavior of Variably Confined Concrete" Report No. 97-08, Center for Advanced Technology for Large Structural Systems, in preparation.

Hsu, T.T., Slate, F.O., Sturman, G.M., and Winter, G., "Microcracking of Plain Concrete and the Shape of the Stress-Strain Curve," *Journal of the American Concrete Institute*, Vol. 60, No. 2, February 1963, pp. 209-224.

Kestner, J.T., Harries, K.A., Pessiki, S.P., Sause, R., and Ricles, J.M., "Rehabilitation of Reinforced Concrete Columns Using Fiber Reinforced Polymer Composite Jackets," Report No. 97-07, Center for Advanced Technology for Large Structural Systems, July 1997, 196 pp.

MacGregor, J.G., *Reinforced Concrete Mechanics and Design*, Prentice-Hall, Inc., 1992, 848 pp.

Madas, P., and Elnashai, A.S., "A New Passive Confinement Model for the Analysis of Concrete Structures Subjected to Cyclic and Transient Dynamic Loading," *Earthquake Engineering and Structural Dynamics*, Vol 21, 1992, pp. 409-431.

Mander, J.B., Priestley, M.J.N., and Park, R., "Observed Stress-Strain Behavior of Confined Concrete," *Journal of Structural Engineering*, ASCE, Vol. 114, No. 8, August 1988, pp. 1827-1849.

Mander, J.B., Priestley, M.J.N., and Park, R., "Theoretical Stress-Strain Model for Confined Concrete," *Journal of Structural Engineering*, ASCE, Vol. 114, No. 8, August 1988, pp. 1804-1826.

Martinez, S., Nilson, A.H., and Slate, F.O., "Spirally Reinforced High-Strength Concrete Columns," *Journal of the American Concrete Institute*, Vol. 81, No. 5, September-October 1984, pp. 431-442.

Mugumura, H., Watanabe, F., Tanaka, H., Sakurai, K., and Nakamura, E., "Effect of Confinement by High Yield Strength Hoop Reinforcement upon the Compressive Ductility of Concrete," *The 22nd Japan Congress on Materials Research - Miscellaneous*, March 1979, pp. 377-382.

PCI Design Handbook - Precast and Prestressed Concrete, Fourth Edition, Precast/Prestressed Concrete Institute, Chicago, IL, 1992.

Pessiki, S., Pieroni, A.M., "Axial Load Behavior of Large-Scale Spirally-Reinforced High-Strength Concrete Columns," *Structural Journal*, American Concrete Institute, Vol. 94, No. 3, May-June 1997, pp. 304-314.

Popovics, S., "A Numerical Approach to the Complete Stress-Strain Curves for Concrete," *Cement and Concrete Research*, Vol. 3, No. 5, September 1973, pp. 583-599.

Prakash, V., Powell, G., and Campbell, S., "DRAIN-2DX Base Program Description and User Guide; Version 1.10," Report No. UCB/SEMM-93/17&18, Structural Engineering Mechanics and Materials, Department of Civil Engineering, University of California, Berkeley, CA, December 1993.

Richart, F.E., Brandzaeg, A., and Brown, R.L., "*A Study of the Failure of Concrete Under Combined Compressive Stresses,*" University of Illinois Bulletin, Vol. XXVI, No. 12, Nov. 20, 1928. 104 pp.

Richart, F.E., Brandzaeg, A., and Brown, R.L., "*The Failure of Plain and Spirally Reinforced Concrete in Compression,*" University of Illinois Bulletin, Vol. XXVI, No. 31, April 2, 1929. 74 pp.

Richart, F.E., Brandzaeg, A., and Brown, R.L., "*An Investigation of Reinforced Concrete Columns,*" University of Illinois Bulletin, Vol. XXXI, No. 40, June 5, 1934. 94 pp.

Sheikh, S.A., and Toklucu, M.T., "Reinforced Concrete Columns Confined by Circular Spirals and Hoops," *Structural Journal*, American Concrete Institute, Vol. 90, No. 5, September-October 1993, pp. 542-553.

Thorenfeldt, E., Tomaszewicz, A., and Jensen, J.J., "Mechanical Properties of High Strength Concrete and Application in Design," *Proceedings of the Symposium on Utilization of High Strength Concrete*, Tapir, Trondheim, 1987, pp. 149-159.

Torrenti, J.M., Desrues, J., Benaija, E.H., and Boulay, C., "Stereophotogrammetry and Localization in Concrete Under Compression," *Journal of Engineering Mechanics*, ASCE, Vol. 117, No. 7, 1991, pp. 1455-1465.

Verbeck, G.J., and Helmuth, R.H., "Structures and Physical Properties of Cement Paste," *Proceedings of the Fifth International Symposium on the Chemistry of Cement, Part 3*, Vol. 3, Tokyo, 1968, pp. 1-32.